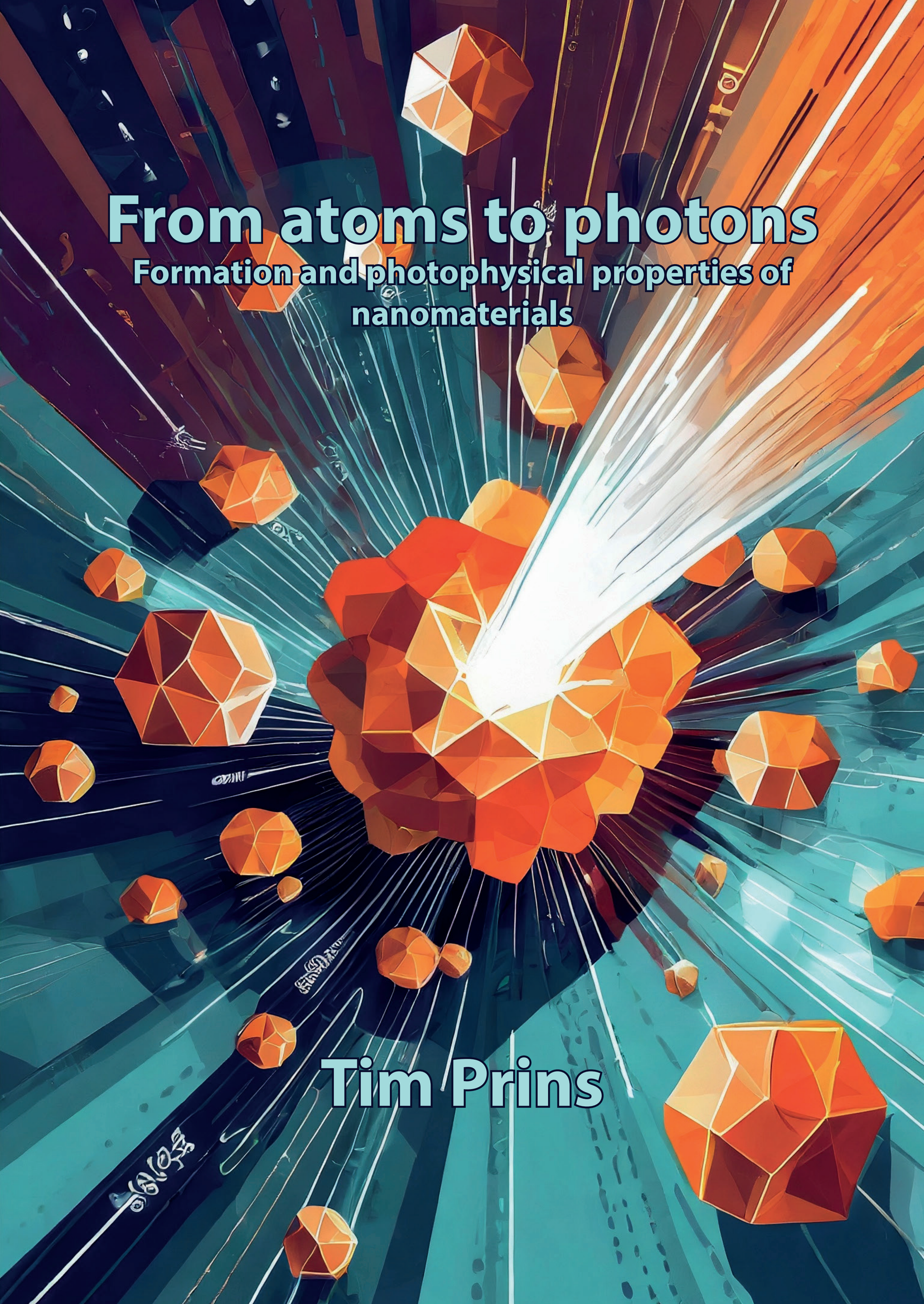

# From atoms to photons

## Formation and photophysical properties of nanomaterials

## Tim Prins

# From atoms to photons

## Formation and photophysical properties of nanomaterials

PhD thesis, Utrecht University
*From atoms to photons: Formation and photophysical properties of nanomaterials*
Paul Timotheüs Prins, 2023

Printed by Ridderprint
ISBN 978-90-393-7611-9
DOI 10.33540/2020

Cover: Artificial artist’s impression of the thesis title using Adobe Firefly

# From atoms to photons

## Formation and photophysical properties of nanomaterials

## Van atomen naar fotonen

De formatie en fotofysische eigenschappen van nanomaterialen

(met een samenvatting in het Nederlands)

Proefschrift

ter verkrijging van de graad van doctor aan de
Universiteit Utrecht
op gezag van de
rector magnificus, prof. dr. H.R.B.M Kummeling,
ingevolge het besluit van het college voor promoties
in het openbaar te verdedigen op

maandag 4 december 2023 des middags te 2.15 uur

door

**Paul Timotheüs Prins**

geboren op 10 februari 1992 te Ermelo

## Promotoren:

Prof. dr. D.A.M. Vanmaekelbergh
Prof. dr. W.G.J.H.M. van Sark

## Copromotor:

Dr. C. de Mello-Donegá

## Beoordelingscommissie:

Prof. dr. A. van Blaaderen
Prof. dr. W.K. Kegel
Prof. dr. A.P. Mosk
Prof. dr. D.J. Norris
Dr. Z. Zanolli

Dit proefschrift maakt deel uit van het onderzoeksprogramma 'Quantum-dot based luminescent solar concentrators' van de Stichting voor de Technische Wetenschappen (STW), die wordt gefinancierd door de Nederlandse Organisatie voor Wetenschappelijk Onderzoek (NWO).

# Contents

# Chapter 1

## Introduction

Light, radiation in the form of *photons*, is essential for life. It serves, for as long as we know, multiple purposes, such as providing warmth, facilitating the production of oxygen and sugar-based structural materials in plants, establishing our day-night rhythm, and enabling us to perceive our surroundings. Our first and still most important source of light is the sun, however, nowadays, we cannot imagine a world without artificial light. We use it to illuminate the world when the sun is down and even when it is up, for communication, and for various other activities. Artificial light became possible due to the ability to synthesize new materials that do not exist in nature. We have also discovered materials that harness the energy of sunlight to generate electricity for powering our devices. Initially, the synthesis of these materials was often a matter of trial and error or good fortune. By combining the right *atoms*, our building blocks, materials can possess the desired properties. Our understanding of this process is ever expanding, enabling us to predict material properties and to synthesize materials while relying on a more rational basis.

## 1.1 Formation and properties of photoactive nanomaterials

There are various methods and processes involved in the formation of photoactive nanomaterials. The specific techniques and conditions used depend on the desired material and its intended application. The synthesis of nanomaterials and the understanding of their optical properties are crucial to fully harness their potential.

In this thesis, our primary focus revolves around nanomaterials and nanoparticles, which typically have dimensions ranging from 1 to 100 nanometers. To provide perspective, a nanometer (nm) corresponds to one billionth of a meter. When a nanoparticle exhibits a solid structure organized in an ordered atomic pattern, they fall into the category known as nanocrystals. Nanocrystals often display distinct properties compared to their larger bulk counterparts. These unique properties have fascinated individuals for centuries,[1] with their exploration dating back to the time of the Egyptian pharaohs[2] (hair dye, Figure 1.1a) and Roman emperors[3] (Lycurgus cup, Figure 1.1b).

For example, let's consider gold in its bulk, macroscopic form. It is known for its yellow color, reflective properties, and resistance to corrosion. However, when the size of the gold crystal is reduced to the nanoscale, it undergoes a significant change in properties.[4] Gold nanocrystals can exhibit various colors depending on their size, ranging from red to purple (Figure 1.1c). This is what gives the reddish color to the light transmitted through the Lycurgus cup.[3] With dimensions on the nanometer scale, gold nanocrystals also exhibit increased reactivity and are therefore used as catalysts in chemical reactions.[5]

Semiconductor materials on a nanometer scale, also known as quantum dots, have revolutionized the understanding and application of semiconductor materials. A macroscopic semiconductor crystal possesses a fixed energy gap between its valence and conduction bands. When a photon carries energy greater than this band gap, it can excite an electron into the conduction band, leaving a hole in the valence band. These excited electron–hole pairs can behave as two free carriers. They can also exist in a bound state due to attractive Coulomb interaction between the electron and hole, known as an exciton. In a solar panel, the excited electron–hole pair is converted into electric work in an external circuit. On the other hand, the electron can also recombine with the hole, resulting in the emission of a photon.

In the past, changing the band gap of semiconductors required altering the type of atoms that make up the material. However, with quantum dots, we have the ability to tune the band gap entirely by adjusting the size of the quantum dots (Figure 1.1d). This size-dependent phenomenon is known as the quantum confinement effect.[6] In bulk materials, the size of an exciton (known as the Bohr radius) is determined by the interplay of electron–hole attraction and the kinetic energy of electron and hole. However, when the physical size of a quantum dot is smaller than the Bohr radius, the exciton is confined by the dimensions of the nanocrystals, and the energy of the exciton increases inversely with the square of the nanocrystal radius. The quantum confinement effect leads to the tunable emission properties of quantum dots. For example, Samsung's QLED televisions use InP-

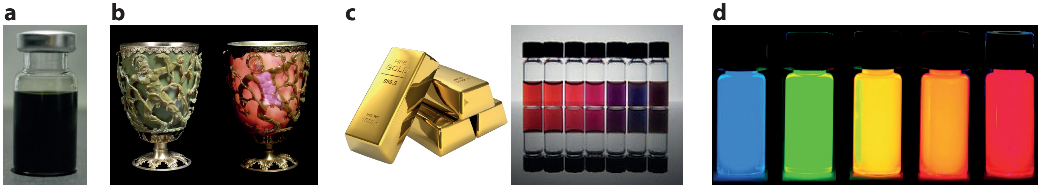

**Figure 1.1 | The appearance of colloidal nanocrystals.** (**a**) More than 4000 years ago the Egyptians used lead salts to dye their hair.[2] Little did they know that the black color was caused by 5 nm PbS nanocrystals embedded inside their hair. The photo shows a dispersion of PbS nanocrystals. (**b**) The Roman Lycurgus cup from the 4th century AC. The cup appears green when illuminated from the front and red or pink when illuminated from the back.[3] This effect is generated by the light absorption of gold nanocrystals embedded in the glass. (**c**) The difference between bulk gold and gold nanocrystals. The size of the gold nanocrystals increases from left to right resulting in a red to purple color.[4] (**d**) CdSe quantum dots under an ultraviolet lamp. The emission is blue for 2 nm quantum dots and shifts towards the red when the quantum dots are 6 nm. This size dependence is due to the quantum confinement effect and enables different emission colors without changing the composition of the quantum dots.

based quantum dots for both green and red emission, but with different diameters of 2 nm and 3.5 nm, respectively.[7]

The tunability of the size of colloidal quantum dots was achieved decades ago by controlling factors such as temperature and the use of specific molecular reagents.[8] However, the formation process of these nanocrystals from their molecular precursors remained unclear. It was hypothesized that the process involves rapid nucleation, where several atoms cluster together, followed by slower growth through the addition of single atoms. The synthesis was optimized through trial and error, aiming to produce a final product consisting mostly of quantum dots with a distinct size, resulting in a specific emission wavelength. This is crucial because emission of quantum dots that is more specific and narrower allows for higher color purity and enhances the television's ability to display accurate colors.

## 1.2 Outline of this thesis

Chapter 2 presents a study of the formation of colloidal CdSe quantum dots using *in situ* X-ray scattering. For the first time, the experimental setup used in the synchrotron is comparable to the one used in the lab for synthesizing these nanocrystals. Contrary to the proposed mechanism of burst nucleation and diffusion-limited growth, our findings reveal extended nucleation and reaction-limited growth. Related to this, we observe a decreasing growth rate with increasing nanocrystal radius, leading to superfocusing and the formation of nanocrystals with distinct sizes.

Chapter 3 focuses on the formation of anisotropic colloidal CdSe nanocrystals, specifically nanoplatelets. These nanoplatelets possess a defined size in one dimension, resulting in emission that is more specific and narrower compared to isotropic nanocrystals. Similar to Chapter 2, we employ a quantitative approach to collect nanocrystal size and concentration information during the synthesis. Our investigation provides insights into the origin of the anisotropic shape and the presence of by-products in the form of isotropic CdSe nanocrystals. We also identify a small population of mini-nanoplatelets in the mixture, whose growth is significantly enhanced when short ligands are introduced.

In Chapter 4, we investigate the formation of insulator $NaYF_4$ nanocrystals doped with photoactive lanthanide ions, specifically $Er^{3+}$ and $Yb^{3+}$, as opposed to semiconductor nanocrystals. Lanthanide ions exhibit even narrower emission lines compared to semiconductor nanocrystals and facilitate a phenomenon known as upconversion, which is a process where two infrared photons are converted into one green photon. Our focus is on the synthesis of hexagonal-phase $NaYF_4$:$Er^{3+}$,$Yb^{3+}$ nanocrystals from cubic-phase precursor nanoparticles, which involves a crystal phase transition. This transition corresponds to a restructuring of the atoms within the crystal lattice. During the synthesis, we observe a bimodal distribution, consisting of two distributions: one of small particles and one of large particles. Contrary to previous assumptions that considered the phase transition as the critical factor in the formation mechanism and the splitting of the particle distribution, our findings demonstrate that the composition of the cubic-phase nanoparticles determines the growth rates of the nanoparticles and thereby the transition from a unimodal to a bimodal size distribution. Subsequently, the larger subset of cubic-phase nanoparticles undergoes a phase transition to the hexagonal phase. This transition is followed by the growth of hexagonal-phase nanocrystals and dissolution of the cubic-phase nanoparticles. Ultimately, this process leads to a unimodal population of hexagonal-phase nanocrystals with a narrow distribution.

Chapter 5 delves into the fundamentals of photon absorption by semiconductor (nano)materials. We uncover an intriguing relationship between the probability of absorption of a resonant photon and the size of the exciton. Whether we consider zero-dimensional nanocrystals, two-dimensional superlattices, or three-dimensional bulk materials, the probability of resonant light absorption per unit time per exciton Bohr diameter is (almost) equal to $\pi\alpha$ (=0.023), where $\alpha$ represents the fine-structure constant. As a consequence, the probability of photon absorption increases with exciton confinement; thus, quantum dots have a stronger absorptance per unit volume *versus* bulk semiconductors. However, quantum dots are typically dispersed or embedded in a medium with a low dielectric constant, resulting in dielectric shielding of the electromagnetic field of light, which, in turn, reduces the absorption probability of a resonant photon. Therefore, it would be interesting to embed the quantum dots in a medium with a high dielectric constant to optimize light absorption per material, for example, in the use of quantum dots as phosphors in lighting and displays, as well as in solar panels.

In Chapter 6, our investigation focuses on the rapid relaxation processes that occur after the absorption of photons by semiconductor nanocrystals. Typically, when a photon carries excess energy beyond the band gap, this surplus energy is dissipated as heat. This limitation on the potential efficiency of solar panels is commonly known as the Shockley-Queisser limit, which, for silicon, is set at 30%. One of the factors that hampers the efficient extraction of carriers is the rapid cooling of photo-generated carriers through Auger cooling, which takes place within a sub-picosecond time-frame. In our study, we conducted a comparison of carrier cooling in Cu-doped InP nanocrystals and undoped InP nanocrystals. By utilizing ultrafast transient absorption spectroscopy, we made an surprising observation that the electron loses energy and cools at a faster rate compared to the hole. This finding suggests that the localization of holes on copper does not impede Auger cooling in Cu-doped InP nanocrystals.

# Chapter 2

## Extended nucleation and superfocusing in colloidal semiconductor nanocrystal synthesis

Hot-injection synthesis is renowned for producing semiconductor nanocolloids with superb size dispersions. Burst nucleation and diffusion-controlled size focusing during growth have been invoked to rationalize this characteristic yet experimental evidence supporting the pertinence of these concepts is scant. By monitoring a CdSe synthesis *in situ* with X-ray scattering, we find that nucleation is an extended event that coincides with growth during 15–20% of the reaction time. Moreover, we show that size focusing outpaces predictions of diffusion-limited growth. This observation indicates that nanocrystal growth is dictated by the surface reactivity, which drops sharply for larger nanocrystals. Kinetic reaction simulations confirm that this so-called superfocusing can lengthen the nucleation period and promote size focusing. The finding that narrow size dispersions can emerge from the counteracting effects of extended nucleation and reaction-limited size focusing ushers in an evidence-based perspective that turns hot injection into a rational scheme to produce monodisperse semiconductor nanocolloids.

### Based on

P.T. Prins, F. Montanarella, K. Dümbgen, Y. Justo, J.C. van der Bok, S.O.M. Hinterding, J.J. Geuchies, J. Maes, K. De Nolf, S. Deelen, H. Meijer, T. Zinn, A.V. Petukhov, F.T. Rabouw, C. de Mello-Donegá, D.A.M. Vanmaekelbergh, Z. Hens

Nano Letters **21**, 2487–2496 (2021)

## 2.1 Introduction

The development of hot-injection synthesis turned colloidal nanocrystals into a widely studied class of nanomaterials with an extensive application potential.[9] The method's central asset is a versatility to produce nanocrystals of very different materials with a variety of morphologies and astonishing precision.[9] The size dispersion (*i.e.*, the ratio between the standard deviation on a characteristic dimension and its mean) can be lower than 5% for the radius $r$ of spherical nanocrystals and zero for the thickness of nanoplatelets.[10] This results in ensembles with optical properties closely resembling those of each individual nanocrystal,[11] which has proven essential for the application of semiconductor nanocrystals in displays,[12,13] lighting,[14,15] photodetection,[16,17] photovoltaics,[18,19] and luminescent solar concentrators.[20,21]

The most-often invoked paradigm to rationalize tight size control by hot injection combines burst nucleation and size focusing.[22–30] Nucleation is then described as a critical process that strongly accelerates above a supersaturation threshold and is quickly arrested by the rapid consumption of the precipitant. As proposed by LaMer *et al.*, the resulting temporal separation of nucleation from growth is what leads to monodisperse colloids.[31] Size focusing refers to the reduction of the standard deviation of the size distribution of a growing nanocrystal ensemble. This absolute focusing happens when small nanocrystals grow faster than large nanocrystals, as is the case for diffusion-limited growth.[32,33] In the case of semiconductor nanocrystal growth, the first observations of size-distribution narrowing were discussed in terms of absolute size focusing.[25,34] Later studies, however, introduced a more relaxed definition of focusing as the reduction of the size dispersion.[35] To attain this relative focusing, a size-independent growth rate, as is often assigned to reaction-limited growth, suffices.[32] Although often invoked and widely accepted, little experimental evidence supports the description of hot injection through burst nucleation and size focusing.[36] Especially for the formation of metal nanoclusters by autocatalytic surface growth, it was claimed that LaMer's paradigm offers little guidance, and alternative synthesis models have been explored.[37–39] However, also in the case of semiconductor nanocrystals, the observation that monodisperse III–V nanocrystals can be formed by continuous precursor injection hints at a more complex mechanism.[40,41]

For the hot-injection synthesis of semiconductor nanocrystals, such as CdSe and PbSe, it was found that the precipitation involves a CdSe[42] or PbSe[43] unit or monomer formed out of the injected metal and chalcogen precursors. Further studies on CdSe,[44,45] PbS,[46] PbSe,[11] InP,[47] and $Cu_2S$[46] showed that the precipitation rate is limited by the precursor to monomer conversion. For such reactions, nucleation and growth become competing pathways of monomer consumption.[44] If the growth rate were zero, then nucleation would continue until monomer generation stopped, which is exactly the opposite from a self-limiting, burst-like event. However, when critical nuclei immediately enter the growth stage, the growth of an increasing number of nanocrystals will lower the super-saturation below the nucleation threshold and arrest nucleation.[44] A central element to understanding the formation of semiconductor nanocrystals by hot-injection synthesis is therefore the rate constant of nanocrystal growth. However, this quantity is unknown, as is the expected nucleation regime in a nanocrystal synthesis.

Here, we analyze nucleation and growth in an established CdSe nanocrystal synthesis.[44,48] Using *in situ* small-angle X-ray scattering (SAXS) measurements and *ex situ* absorbance spectroscopy, we show that this synthesis exhibits a prolonged nucleation stage, active during 15–20% of the reaction time. Nevertheless, we observe that the size distribution narrows over time (absolute size focusing) such that nanocrystals attain a nearly uniform size when the reaction reaches full yield. Even more, we demonstrate that nanocrystal ensembles with a bimodal size distribution exhibit pronounced size focusing that outpaces diffusion-limited focusing. We assign this finding to a strong drop in surface reactivity with size and confirm through kinetic reaction simulations that such plummeting surface reactivity, a property we call superfocusing, extends the nucleation stage. Under such conditions, narrow size dispersions can result from the counteracting effect of extended nucleation and extreme size focusing.

## 2.2 Results and discussion

We monitored *in situ* the formation of CdSe nanocrystals from cadmium oleate and trioctylphosphine selenium (Chapter 2.4 for methods) through SAXS. We reproduced typical laboratory conditions by using a custom-made setup[49,50] consisting of a three-necked flask equipped with an indentation for X-ray scattering and embedded in a heating mantle with active temperature control (Figure 2.1a). As described in Chapter 2.4, the necks enabled us to impose a protective atmosphere, measure the temperature, and inject reagents via a remotely controlled syringe pump, an approach complementary to previous studies where reactions were initiated by heating the entire reaction mixture.[51] SAXS patterns were recorded throughout the synthesis, from which we extracted the size and concentration of the nanocrystals as a function of time (see Chapter 2.4).[52] To rule out the possibility of X-ray-induced changes in the development of the reaction,[53] we performed a similar analysis on the same hot-injection reaction by aliquot-based monitoring (see Chapter 2.4).

Figures 2.1b,c display the temporal evolution of the average nanocrystal radius $r$ and its standard deviation $\sigma_r$, the yield of CdSe formation, and the nanocrystal concentration $c_{\mathrm{NC,tot}}$ as obtained from the *in situ* SAXS data. Clearly, consistent data analysis is possible after ~3 s of reaction time. As shown in Figure 2.1b, the CdSe yield reaches 98% within 400 s, a common time span for this type of reaction.[43] This development concurs with a steady increase in radius from ~1.5 to 2.2 nm. More interesting, however, is the observation that the nanocrystal concentration needs 60 s to reach 98% of the final concentration of ~25 µM. This suggests that nucleation persists during 15% of the reaction time. Despite this prolonged nucleation, the size distribution progressively narrows to reach a size dispersion of ~6% after 400 s. Importantly, this evolution involves absolute size focusing, with the standard deviation of the particle size distribution dropping from ~0.18 nm after 10 s to 0.12 nm after 400 s of reaction time. After the CdSe formation is completed, we observe a gradual decrease in the nanocrystal concentration, a slight increase in radius, and a coarsening of the size dispersion, which

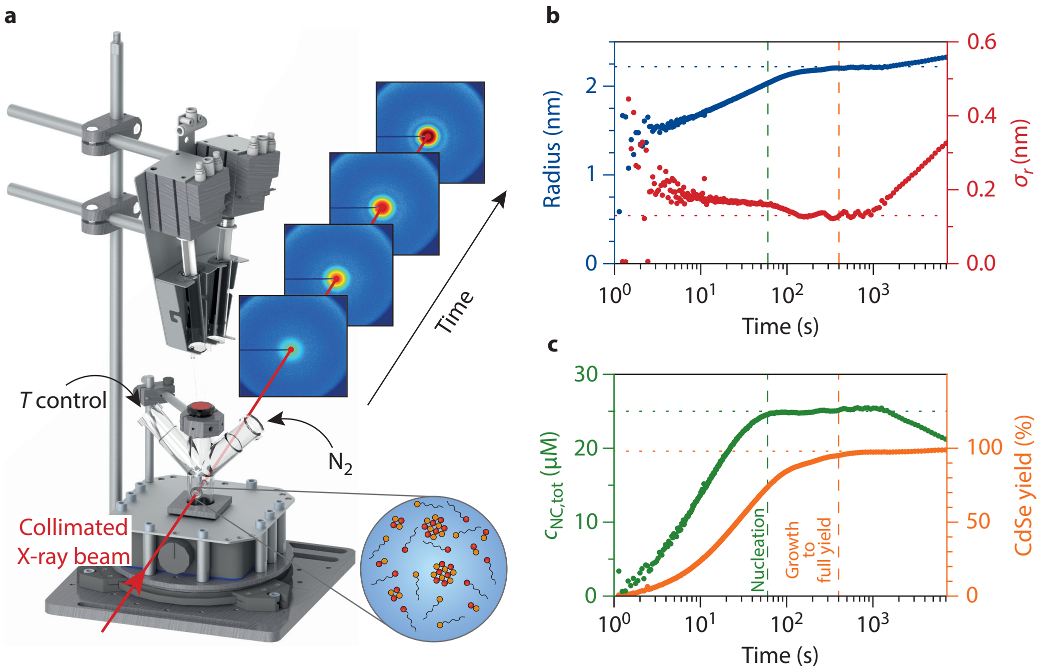

**Figure 2.1 | *In situ* time-resolved small-angle X-ray scattering.** (**a**) Schematic of the experimental setup used for *in situ* monitoring through SAXS of a CdSe hot-injection synthesis based on reacting cadmium oleate with trioctylphosphine selenium. Part of the precursors are loaded into the custom-made three-necked flask, which is heated under a nitrogen atmosphere. The nucleation and growth of the nanocrystals are triggered by the injection of the Cd precursor via the remotely controlled syringe pump placed above the three-necked flask. The reaction is probed with collimated synchrotron-based X-rays through a small indentation in the flask. The 100 ms time resolution of the SAXS detector enables the development of the reaction to be precisely followed. (**b**) Representation of (blue) the average nanocrystal radius and (red) the standard deviation as a function of reaction time as extracted from successive SAXS patterns (see Chapter 2.4). The blue dotted line indicates the final average radius prior to ripening (2.22 nm), and the red dotted line indicates the minimum polydispersity obtained, 0.13 nm (*i.e.*, 6% of the average radius). (**c**) Representation of (green) the concentration of nanocrystals and (orange) the CdSe yield as a function of reaction time as extracted from successive SAXS patterns (see Chapter 2.4). Horizontal dotted lines indicate (green) the nanocrystals' concentration prior to ripening and (orange) the final reaction yield. Vertical dashed lines in **b** and **c** indicate the times at which (green) the concentration of nanocrystals and (orange) the yield attain 98% of the final value.

are three trends characteristic of Ostwald ripening.

We corroborated the *in situ* SAXS observations by monitoring a CdSe synthesis with a similar precursor chemistry (Chapter 2.4 for methods) through the absorbance spectrum of quantitative reaction aliquots.[44] As shown in Figure 2.2, this study confirmed the prolonged buildup of the nanocrystal concentration. By comparing the moments where $c_{\mathrm{NC,tot}}$ and the CdSe yield reach 98% of their final value, we estimate that nucleation continues for about 20% of the reaction time, a number comparable with the outcome of SAXS analysis. A similar conclusion has been recently proposed by

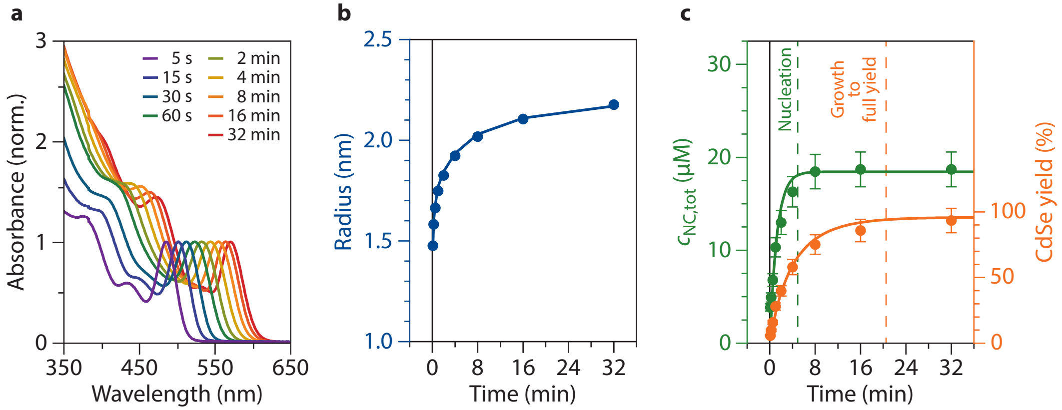

**Figure 2.2 | Time-resolved optical absorption spectroscopy.** (**a**) Absorbance spectra of reaction aliquots taken as indicated after the start of a CdSe synthesis based on reacting cadmium stearate with trioctylphosphine selenium (details in Chapter 2.4).[44] (**b**) Nanocrystal radius estimated from the spectral position of the CdSe NC band-edge transition using a SAXS-based sizing curve.[55] (**c**) (Orange) CdSe yield and (green) concentration of nanocrystals as obtained from the absorbance at 320 nm of quantitative reaction aliquots in combination with the nanocrystal radius. The development of the CdSe yield was fit assuming a second-order monomer generation rate,[44] whereas $c_{\mathrm{NC,tot}}$ was fit to an exponential build-up (see Chapter 2.4). We took the points where the two fits attain 98% of their final value to identify the end of the nucleation and the growth-to-full-yield period as indicated by the green and orange dashed lines, respectively.

Karim and co-workers for Pd nanocrystals[38] and by Owen and co-workers for InP nanocrystals.[54] Despite the lack of a single nucleation event distinct from the growth stage, these syntheses yield monodisperse ensembles in agreement with the *in situ* SAXS study presented in this study. We thus conclude that a prolonged nucleation period is a common feature of hot-injection syntheses, which nevertheless does not prevent such reactions from forming monodisperse nanocrystal sols.

In line with the LaMer model,[31] many hot-injection syntheses involve a sequential mechanism in which injected precursors first react to form a monomer species that is consumed in a second step by the nucleation of new nanocrystals or the growth of already existing ones.[43–46] This precursor/monomer/nanocrystal sequence was explicitly demonstrated for the CdSe synthesis analyzed here.[44] Considering that nanocrystal growth involves the diffusion of the monomer to the nanocrystal followed by monomer adsorption at the nanocrystal (Figure 2.3a), Talapin *et al.* proposed a comprehensive expression for the nanocrystal growth rate $j_G = \mathrm{d}r/\mathrm{d}t$ (see Chapter 2.5):[56]

$$j_G = D V_m [\mathrm{M}]_0 \frac{S - S^{r_c/r}}{r + \frac{D}{k_a(r)}}, \tag{2.1}$$

where $D$ is the monomer diffusion coefficient, $V_m$ is the material's molar volume, $[\mathrm{M}]_0$ is the monomer solubility, $S$ is the supersaturation, $r_c$ is the critical radius, and $k_a(r)$ is the size-dependent rate constant for solute adsorption. Figures 2.3b,c represent $j_G$ under conditions where diffusion ($D/k_a \ll r$) or surface adsorption ($D/k_a \gg r$) limits growth. According to Equation 2.1, diffusion limitation results in absolute size focusing, while reaction limitation yields a gradually increasing growth rate

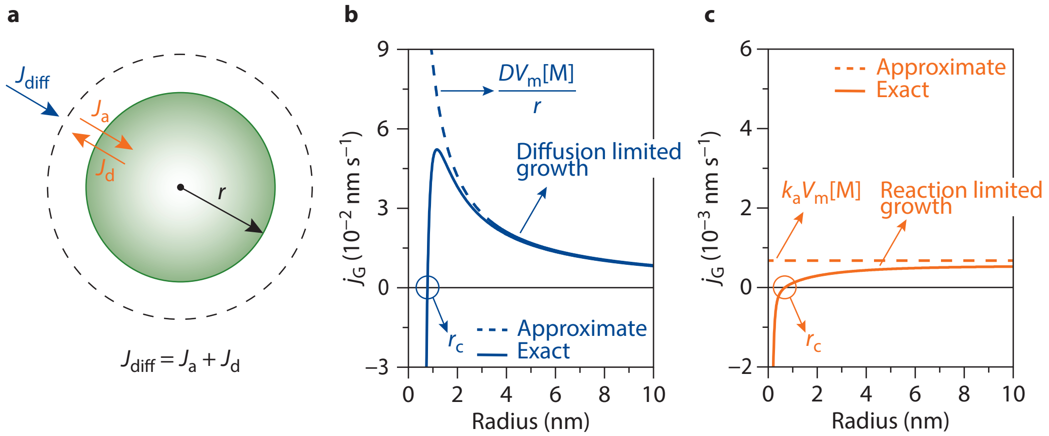

**Figure 2.3 | Nanocrystal growth rate.** (**a**) Cartoon of a nanocrystal with radius $r$ and the monomer flux by (blue) diffusion and (orange) surface reaction leading to nanocrystal growth. (**b**, **c**) Representation of the nanocrystal growth rate as a function of $r$ under conditions of (**b**, blue) diffusion-controlled growth and (**c**, orange) reaction-limited growth. In both cases, the dashed line represents the limiting behavior for large radii used to derive Equation 2.2 and Equation 2.3 and $r_c$ indicates the critical radius. See Chapter 2.5 for an overview of the parameters used.

with nanocrystal size that has the bulk growth rate as an upper limit. This evolution reflects the assumption made in deriving Equation 2.1 that the activation energy for monomer adsorption follows a linear free-energy relation (see Chapter 2.5).[56]

The nanocrystal growth regime is important. Absolute size focusing, for example, is often explained by referring to the characteristic $1/r$ scaling of diffusion-limited growth,[22,25,30,33,56] whereas reaction-limited growth may suffice to attain relative size focusing.[35] Because the growth rate depends on two dynamic variables, the nanocrystal radius $r$ and the supersaturation $S$, the actual growth regime cannot be determined by merely following $\mathrm{d}r/\mathrm{d}t$ during a reaction. This limitation can be overcome by analyzing the evolution of a bimodal size distribution, where different nanocrystal populations grow in a reaction mixture characterized by a single supersaturation, an approach followed before to study Ostwald ripening of CdSe nanocrystals.[57] Under conditions of single supersaturation, radius $r_1$ attained by the first subset in the ensemble can be predicted from radius $r_2$ of the second subset using approximate expressions for growth under diffusion ($j_G \propto S/r$) and reaction ($j_G \propto S$) limitations (Figures 2.3b,c and Chapter 2.5):

$$r_{1,\text{diffusion}} \approx \sqrt{r_2^2 + \left(r_{1,0}^2 - r_{2,0}^2\right)} \tag{2.2}$$

$$r_{1,\text{reaction}} \approx r_2 + \left(r_{1,0} - r_{2,0}\right). \tag{2.3}$$

Here, $r_{1,0}$ and $r_{2,0}$ indicate the radii of either subset at a given time $t_0$. Hence, comparing experimental radii with predictions based on Equation 2.2 and Equation 2.3 provides a straightforward albeit approximate approach to assessing the prevailing growth regime.

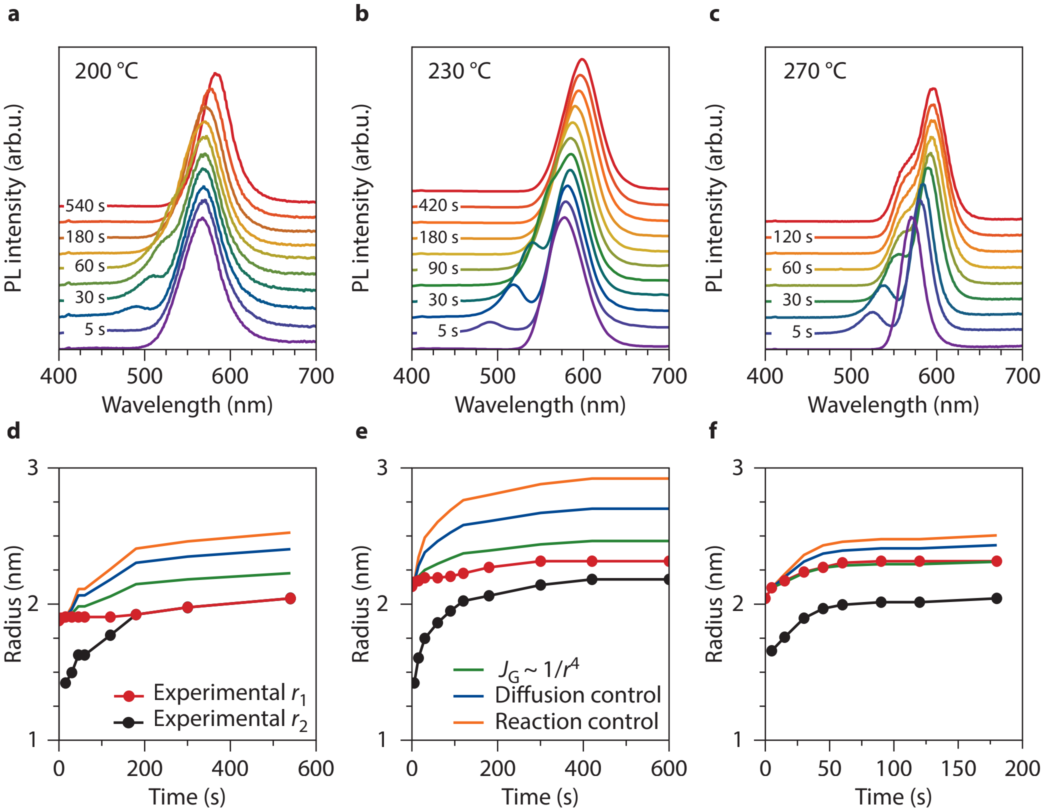

**Figure 2.4 | Bimodal size distribution experiment.** (**a**–**c**) Photoluminescence spectra of reaction aliquots taken at the indicated times after the initiation of a second nucleation in a CdSe reaction mixture. The reaction was carried out using chemistry similar to that in Figure 2.2 at the indicated temperatures. (**d**–**f**) Evolution of the radius of (red dots) the first and (black dots) the second CdSe nanocrystal populations as obtained from the central emission wavelength of both populations. The lines indicate the predicted radius of the first population from the measured radius of the second population assuming (blue) diffusion and (orange) reaction control according to Equation 2.2 and Equation 2.3, respectively. The green lines in panels **d**–**f** represent predicted radii based on a $1/r^4$ scaling of the growth rate (see Chapter 2.4).

To create a bimodal size distribution, we initiated a second nucleation event in a reaction mixture by the additional injection of the cadmium precursor during similar CdSe nanocrystal syntheses as discussed in Figure 2.2 but with a 10-fold initial excess of TOPSe (see Chapter 2.4). We monitored the reaction after the second injection through quantitative aliquots. As shown in Chapter 2.4, this second injection restarts CdSe formation at the same rate as for a single injection and results in a new subset of smaller nanocrystals. As shown in Figures 2.4a–c, the corresponding bimodal size distribution can be identified in the photoluminescence (PL) spectra of reaction aliquots. These spectra feature a second emission band at shorter wavelength, next to the main PL peak of the initial nanocrystal population, that is not formed without the additional Cd injection (see Chapter 2.4).

Fitting of the PL spectra using a double Gaussian fit enabled us to determine the wavelength of maximum PL intensity of both subsets, a number from which we estimated the average nanocrystal radius in each subset (see Chapter 2.4). The resulting band-edge wavelengths agree with the band-edge absorption of the different subsets, insofar as distinct absorption features can be discerned in the absorption spectra of the aliquots (see Chapter 2.4). The resulting radii are represented in Figures 2.4d–f for the different reaction temperatures, together with predicted radii of the initial subset according to Equation 2.2 (red, diffusion control) and Equation 2.3 (blue, reaction control). Remarkably, one sees that at lower temperatures the newly created subset quickly catches up to the initial one. A comparison of the actual and predicted radii makes clear that the larger nanocrystals grow far more slowly than the diffusion-limited and reaction-limited growth predict. This implies that the actual size focusing greatly outpaces the $1/r$ scaling of diffusion-limited growth. This conclusion is supported by the reference line based on a $1/r^4$ scaling of the growth rate, which is reached only for the 270 °C reaction. Importantly, both nanocrystal subsets have the same growth rate once their radii are equal. Hence, the initial sluggish growth of the larger subset is not an artifact due to the poisoning of the CdSe surface during the reaction. We extended this analysis to a different CdSe synthesis, where we used a second injection of black selenium powder to create a bimodal size distribution (see Chapter 2.4). For this reaction, both subsets can be clearly identified in the UV–vis absorption spectra of the aliquots, and we again find that the larger subset grows more slowly than the $1/r^4$ reference scaling used in Figure 2.4.

Whereas little is known as to how the adsorption rate constant $k_\mathrm{a}$ changes with the nanocrystal radius, the $1/r$ dependence of diffusion-limited growth is a relation that relies on few assumptions. The monomer diffusion coefficient may decrease with increasing nanocrystal size due to a more pronounced solvent reorganization around larger nanocrystals,[58,59] yet molecular dynamics simulations show such effects to be minor, even at room temperature.[60] Since the growth of the largest subset at the lower temperatures studied (Figures 2.4a,b) is significantly slower than what diffusion-limited growth predicts, we conclude that growth must be reaction-limited in these cases. Importantly, this implies that $k_\mathrm{a}(r)$ must drop more sharply than $1/r$, a situation we will define as superfocusing. Note that this finding is exactly the opposite of what has been argued based on a linear free-energy relation (Figure 2.3c) and what we implemented in Equation 2.3. Since the growth rate can be expected to increase with temperature more than the diffusion coefficient, higher temperatures can push growth toward diffusion control even for the larger radii, which agrees with our experimental observation at the highest temperature.

To understand the impact of superfocusing on the development of a nanocrystal synthesis, we consider the rate $\mathrm{d}n_\mathrm{M}/\mathrm{d}t$ at which a nanocrystal incorporates monomers under reaction-limited growth:

$$\frac{\mathrm{d}n_\mathrm{M}}{\mathrm{d}t} = \frac{1}{V_\mathrm{m}}\frac{\mathrm{d}V_\mathrm{NC}}{\mathrm{d}t} = 4\pi r^2[\mathrm{M}]\frac{k}{r^n}, \tag{2.4}$$

where $n_\mathrm{M}$ is the number of monomers (in mole) per nanocrystal and $V_\mathrm{NC}$ is the nanocrystal volume.

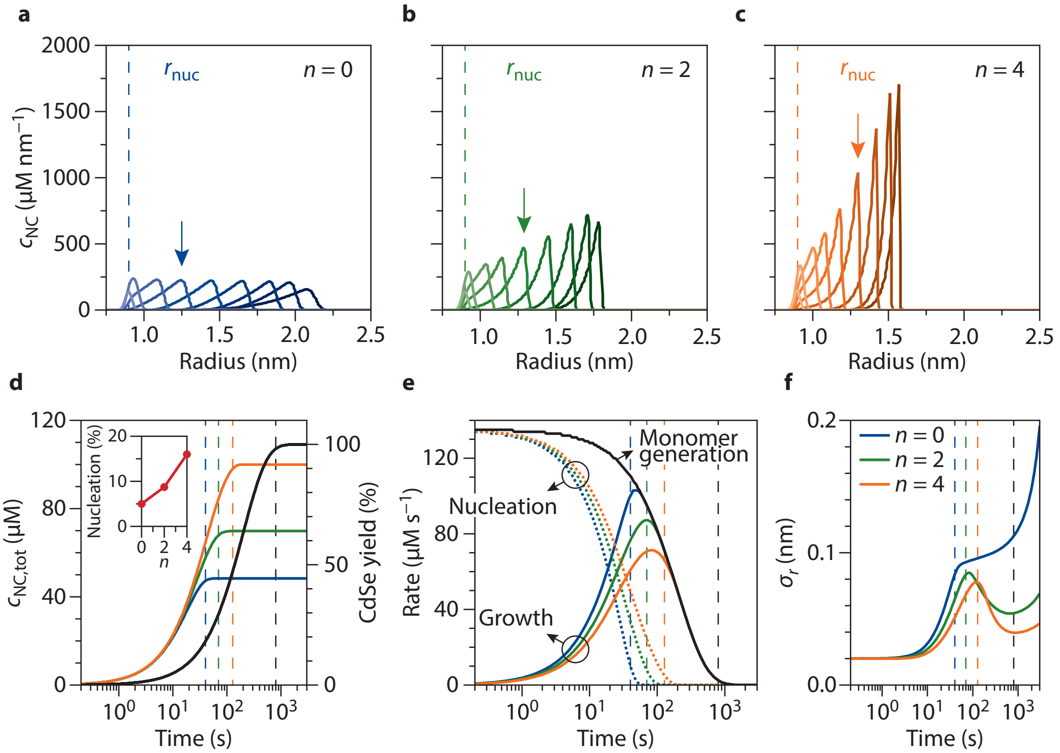

**Figure 2.5 | Kinetic simulations of nanocrystal growth.** (**a**–**c**) Snapshots of the nanocrystal distribution $c_{NC}(r)$ at different times in the synthesis as obtained through kinetic reaction simulations. Plots extend from (lightest trace) 3.16 to (darkest trace) 2275 s for growth exponents of (blue) $n = 0$, (green) 2, and (orange) 4. The vertical line indicates the radius at which nanocrystals initially nucleate for the given parameter settings, whereas the arrows highlight the first distribution shown where nucleation has stopped. (**d**) Time development of the (black) total reaction yield and (colored) total nanocrystal concentration $c_{NC,tot}$ for simulations using different growth exponents as indicated. The vertical lines indicate the moment were (black) the yield and (colored) the nanocrystal concentration attained 98% of the final value. (Inset) Ratio between the time that the concentration and the yield reached 98% of the final value *versus* the growth exponent. (**e**) Rates of (black) monomer generation and monomer consumption by (colored dotted lines) nucleation and (colored solid lines) growth for reaction simulations using different growth exponents. (**f**) Temporal development of the standard deviation of the concentration distribution for reaction simulations with different growth exponents as indicated. The vertical lines in panels **e** and **f** have the same meaning as in **d**.

To explore the impact of superfocusing, we wrote $k_a$ as $k/r^n$ and applied Equation 2.1 in the limit of $r \gg r_c$. Note that the units of $k$ in Equation 2.4 change depending on $n$. While this parametrization may seem arbitrary, any growth rate can be approximated around a given $r$ as $k/r^n$ (details in Chapter 2.5). To understand the evolution of [M] when nanocrystals grow larger, we note that $c_{NC,tot}$ will be constant in the absence of nucleation. Since [M] is quasi-stationary,[44] the rate $dn_M/dt$ is also constant when the monomer generation rate is fixed. Under such conditions, $dn_M/dt$ is independent of any time-dependent variable, including radius $r$. Differentiating both sides of Equation 2.4 with respect to $r$, we find that the monomer concentration then changes with radius as

$$\frac{\mathrm{d}[\mathrm{M}]}{\mathrm{d}r} = (n-2)\frac{[\mathrm{M}]}{r}. \tag{2.5}$$

Hence, with a growth exponent of $n < 2$, growth concurs with a drop in the monomer concentration. On the other hand, if $n > 2$, the dropping growth rate increases the monomer concentration when nanocrystals grow larger. Note that the former growth regime underpins the LaMer model in which growing nanocrystals quickly arrest nucleation by lowering the supersaturation. In Chapter 2.6, we present a more detailed analysis of the development of a nanocrystal ensemble under the aforementioned conditions. These results confirm that growth at constant monomer generation concurs with a decrease in the supersaturation only when $n < 2$. We thus conclude that when $n > 2$, superfocusing can simultaneously promote size focusing and extend nucleation since growth will fail to reduce the supersaturation below the nucleation threshold for a fixed monomer generation rate.

In a real synthesis, the monomer generation rate decreases with time. To further clarify the relationship between size-focusing and extended nucleation, we ran reaction simulations based on a previously published model in which nucleation is described through classical nucleation theory.[44,61,62] We implemented a reaction scheme in which the injected precursors first react to form the actual precipitate or monomer under pseudo-first-order conditions, a process that applies to the CdSe reaction used here (see Chapter 2.4 and Chapter 2.6).[42,45] To evaluate the effect of superfocusing on the reaction development, we modeled the rate constant for monomer adsorption as

$$k_\mathrm{a}(r) = A\frac{(r_{\mathrm{c},0} + B)^n}{(r+B)^n}. \tag{2.6}$$

Equation 2.6 is a heuristic model expression in line with the expression proposed in Equation 2.4. Here, small radial offset $B$ avoids the singularity at $r = 0$ and reference radius $r_{\mathrm{c},0}$ provides a convenient way to change the growth exponent while keeping the rate constant fixed at $r_{\mathrm{c},0}$ (see Chapter 2.5). As outlined in Chapter 2.5 and Chapter 2.6, we implemented this growth rate to analyze a model synthesis under different focusing conditions. Here, model parameters were chosen to have an identical, reaction-limited growth rate at radii close to the critical radius, regardless of the growth exponent, and obtain a reaction development comparable to that in *in situ* SAXS and *ex situ* experiments.

Figures 2.5a–c show the temporal development of the concentration distribution $c_{\mathrm{NC}}(r)$ for three different simulations, where $n$ was set equal to 0, 2 and 4, values that span the presumed range from no superfocusing to superfocusing in agreement with the experimental results shown in Figure 2.4c. As a compromise between the experimental *in situ* SAXS and *ex situ* CdSe synthesis, the simulated syntheses reach a 98% yield after ~800 s (Figure 2.5d). As shown in Figure 2.22 the buildup of the nanocrystal concentration we obtain from these simulations closely follows the single-exponential build-up we used to fit the experimental data in Figure 2.2c. Since this outcome also agrees with the *in situ* SAXS analysis (see Figure 2.12), we conclude that these simulations effectively reproduce the net effect of nucleation, although the molecular aspects of nucleation are not considered.[63] The concentration development plotted in Figure 2.5d directly shows the impact of superfocusing. All simulated reactions exhibit a nucleation period, characterized by an increasing nanocrystal concentration $c_{\mathrm{NC,tot}}$, that gives way to a growth-only regime in which the nanocrystal concentration stays constant. The larger the growth exponent, the longer the nucleation period lasts. The same picture emerges from Figure 2.5e, where we plotted the contribution of nucleation and growth to the monomer consumption. Comparing the moment at which the concentration and yield reach 98% of their final value shows that the nucleation stage lengthens from 5 to 16% of the reaction time when $n$ increases from 0 to 4. Note that such an extended nucleation is close to the experimental values. We thus conclude that superfocusing can indeed extend the nucleation period to 15% or more of the reaction time.

The concentration distribution snapshots highlight a second aspect of superfocusing. When taking $n = 0$, growth leads to a mere translation of the concentration distribution once nucleation is stopped. This evolution is expected since a constant $k_a$ makes all nanocrystals grow at the same rate under reaction control.[32] For $n = 2$ or 4, however, the slower growth rate for larger nanocrystals results in a considerable narrowing of the concentration distribution under conditions of reaction-limited growth. This point is confirmed when we look at the development of the standard deviation $\sigma_r$ of the concentration distribution. While for $n = 0$, $\sigma_r$ becomes nearly constant once nucleation stops, a clear reduction of $\sigma_r$ is realized during the growth stage when $n = 2$ or 4, an evolution that reflects absolute focusing of the concentration distribution. We thus conclude that superfocusing can indeed square a circle, extending the nucleation period on the one hand while promoting narrow size distributions on the other hand.

## 2.3 Conclusion

All syntheses analyzed here exhibit a prolonged nucleation period, while size dispersions can be as low as 6%. Such results indicate that in a hot-injection synthesis, burst nucleation is not required to form monodisperse semiconductor nanocolloids. Interestingly, such extended nucleation periods have also been reported for the formation of metal nanocrystals through nucleation and surface-catalyzed growth.[37,38] For such reactions, a binary distinction between small, rapidly growing and large, slowly growing nanocrystals was introduced to account for the development of the particle size distribution with time.[39,64] In the precursor-driven synthesis of semiconductor nanocrystals, superfocusing solves in a similar way the paradox between extended nucleation and the formation of monodisperse nanocolloids since the plummeting growth rate strongly focuses the size distribution during reaction-limited growth.

The disappearance of reactive crystal facets is a known principle of crystal growth.[65] Although this concept may explain superfocusing in general terms, it does not provide a concrete, atomistic understanding of the growth process for the materials studied here. Interestingly, recent calculations of the binding energies of cadmium salts to CdSe nanocrystals and nanoplatelets indicated that such ligands bind more weakly to sites near edges than to sites in the center of a crystal facet.[66,67] This difference can promote crystal growth at edges in different ways. First, since such sites are more likely to be free of ligands, monomer addition may be kinetically more favorable, as has been recently argued for the autocatalytic reduction of Pd(II) on Pd nanocrystals.[68] Second, if monomer adsorption involves the breaking of the ligand–nanocrystal bond, then weaker binding sites can thermodynamically favor monomer adsorption. Either way, monomer adsorption will slow down when facets become larger and the fraction of edge sites decreases (*i.e.*, for larger nanocrystals). This effect may be even more pronounced since nucleation on plain facets can be highly unfavorable due to the high edge energy of an initial nucleus formed on such a facet.[69]

While showing that an extended nucleation period can lead to a narrow size distribution, the reaction simulations also yield strongly skewed size distributions with a size dispersion of only 1 to 2%. While such narrow distributions have been reported for the case of PbSe nanocrystals,[11] the *in situ* SAXS data presented here yielded a larger size dispersion of ~6%. Hence, the edge of the simulated size distribution at larger radii may especially reflect the limitations of the kinetic model that we implemented. For one thing, we described growth by a single growth exponent *n*, irrespective of the nanocrystal size. In reality, *n* will tend to zero with increasing size as nanocrystals attain the constant growth rate of the bulk material and the resulting loss of focusing will counteract the development of the steep edge in the size distribution at large radii. However, because the simulations cover a range of radii in which we experimentally observe strong focusing, fixing *n* at 4 was a conservative choice that leaves little room for adjustments to broaden the size distribution. A more fundamental limitation is implicit in the description of nanocrystals as spheres. Nanocrystals of the same volume can exist in a variety of structures, exposing different facets, edges, and corners. This structural variety precludes a unique relationship between the nanocrystal radius and the growth rate constant and may lead to a growth-rate heterogeneity that diminishes focusing. Understanding such aspects of nanocrystal growth will require atomistic insight into the adsorption and desorption of monomers to nanoscale surfaces.

Based on our observations, superfocusing under reaction-limited growth appears to be quite a general mechanism by which monodisperse semiconductor nanocolloids are formed in a hot-injection synthesis. Moreover, because such a mechanism does not require burst nucleation, the same interpretation probably applies to syntheses in which monodisperse nanocolloids are formed by gradually heating up a reaction mixture.[70] Interestingly, the bimodal size distribution reactions shown here highlight that superfocusing can lead to monodisperse nanocolloids despite a most disparate nucleation event, and the conclusion that reaction-limited growth can cause pronounced size-distribution focusing could be put into practice in the design of new colloidal synthesis protocols. Even so, superfocusing can be a double-edged sword. The more strongly the growth rate constant decreases with increasing radius, the longer nucleation persists, which increases the degree of focusing needed to attain a narrow size distribution. This point may explain why the lowest-temperature synthesis shown in Figure 2.4 exhibits the strongest growth rate decrease but not the best size distributions. Hence, finding the best reaction conditions will remain a matter of careful synthesis optimization.

On the other hand, introducing coadsorbents into a reaction to slow down monomer adsorption could be a fruitful strategy for tuning and maximizing the impact of superfocusing. Clearly, this variety of possible strategies already highlights that the concept of superfocusing under reaction control provides a much-needed missing link in the mechanistic understanding of nanocolloid synthesis and will prove to be most useful in rationally steering any nanocrystal synthesis to form monodisperse sols.

## 2.4 Methods

*Chemicals.* Trioctylphosphine oxide (TOPO, 90%), octadecylamine (ODA, 90%), oleic acid (OA, 90%), 1-octadecene (ODE, 90%), cadmium acetate dihydrate ($Cd(Ac)_2 \cdot 2H_2O$, 98%), trioctylphosphine (TOP, 90%), 1-butanol (BuOH, anhydrous, 99.8%), methanol (MeOH, anhydrous, 99,8%), and toluene (anhydrous, 99.8%) were all purchased from Sigma-Aldrich® and used as received. Se powder (Se, -200 mesh, 99.999%) was purchased from Brunschwig Chemie.

*Precursor synthesis.* For the preparation of the Cd-precursor, 1.76 g $Cd(Ac)_2 \cdot 2H_2O$, 8.76 g OA and 61.74 g ODE were mixed and degassed in a three-neck flask at 120 °C for three hours to form $Cd(OA)_2$ with 0.1 M concentration. For the preparation of the Se-precursor, 5.15 g Se powder, 27.24

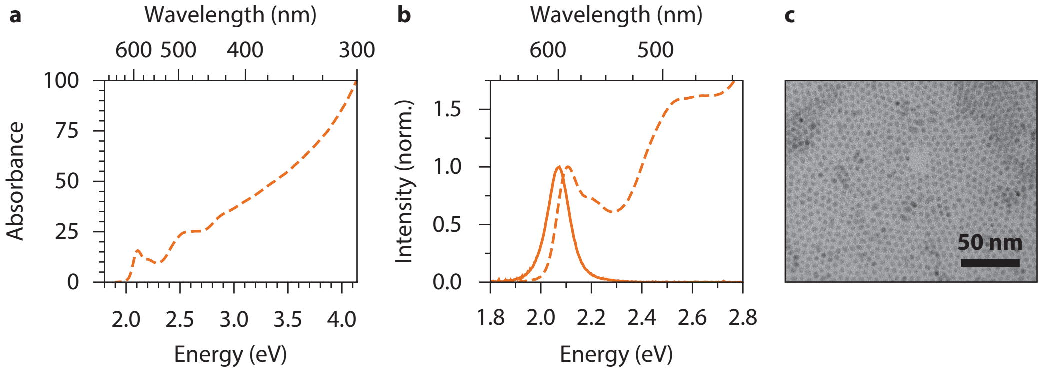

**Figure 2.6 | Optical and structural characterization of CdSe nanocrystals synthesized through hot injection.** (**a**) Absorption spectrum of the purified synthesis products measured in a cuvette with a pathlength of 1 cm. The first exciton transition is clearly visible at 2.10 eV, according to a SAXS-based sizing curve, relating the first excitonic transition to radius,[55] this corresponds to nanocrystals with a radius of 2.36 nm, a close match with the final radius extracted from our *in situ* SAXS measurements (see Figure 2.1b). The concentration nanocrystals can also be obtained, using the Lambert-Beer law and a molar extinction coefficient from literature (3.3 $\mu M^{-1}$ $cm^{-1}$ at 300 nm for CdSe nanocrystals with a radius of 2.36 nm dispersed in toluene[71]) we get 30.6 µM. Considering the 25% thermal expansion of the solvent (see also below), the concentration at 260 °C would be about 24 µM, in good agreement with the final concentration obtained from our *in situ* SAXS measurements (see Figure 2.1c). (**b**) Normalized absorption and emission spectra of the CdSe nanocrystals product. The emission peaks at 2.27 eV and has a full width at half maximum of 105 meV. (**c**) TEM image of the products of the synthesis. The nanocrystals have a quasi-spherical shape with a radius of 2.3 ± 0.3 nm.

g TOP and 43.22 g ODE (previously degassed) were heated to 50 °C and stirred under inert atmosphere in a three-neck flask until complete dissolution of the Se powder. ODA and TOPO were separately degassed at 150 °C for two hours and then kept under inert atmosphere until use.

*Nanocrystal synthesis.* For the synthesis of CdSe nanocrystals, adapted from ref 48, 0.81 g TOPO, 2.33 g ODA, and 3.78 g of the Se-precursor (see Methods 2.4 for precursor preparation) were placed in a custom-made three-neck flask. The content of the flask was heated to 290 °C under nitrogen. At 290 °C, 3.56 g of the Cd-precursor was rapidly injected in the flask via the remotely controlled liquid injector. The temperature, which had dropped to 230 °C after the injection, was set to 260 °C. The mixture reached this temperature within 60 seconds, the solution was kept at this temperature for 120 minutes while stirring. During this time the temperature oscillated around 260 °C with an amplitude of 6.5 °C and a period of 195 seconds. After 120 minutes, the heating was turned off and the reaction was let cool down to room temperature. At room temperature, the crude solution was collected and stored under an inert atmosphere. Optical and structural characterization of the CdSe nanocrystals is shown in Figure 2.6.

*Sample purification.* The samples for *ex situ* TEM and optical absorption analysis were prepared by

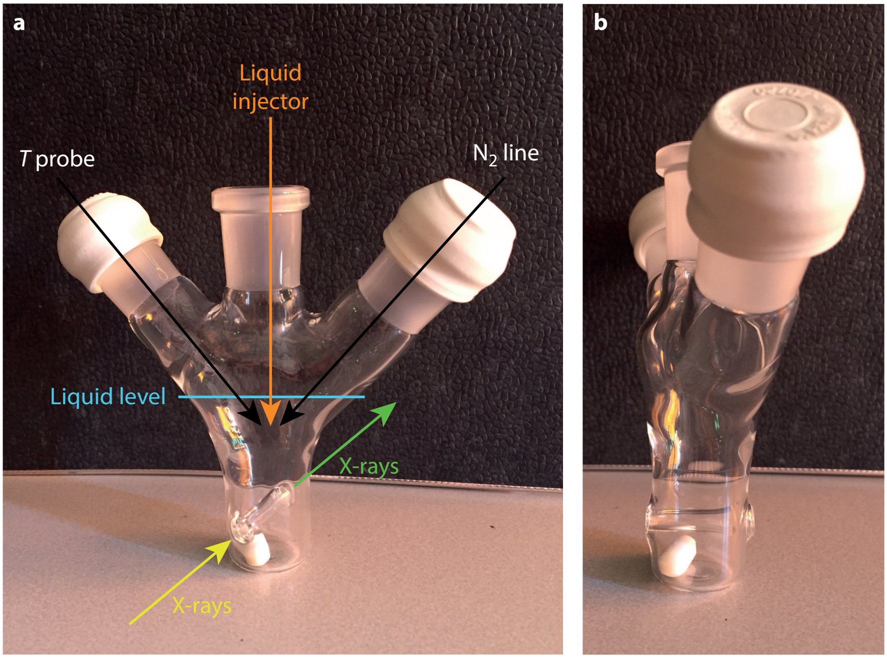

**Figure 2.7 | Custom-made three-neck flask.** (**a**) Front and (**b**) side views of the custom-made three-neck flask used for the SAXS experiments. The flask was equipped with an indentation in its lower part, thus enabling the probing of a small part of the sample during the synthesis. The necks of the three-neck flask were used to insert a temperature probe, to connect the flask to a nitrogen line and to inject the precursors at high temperature.

addition of a mixture of MeOH and BuOH (1:3) to the crude solution and then centrifugation at 2500 rpm for 10 minutes. After centrifugation the supernatant was discarded, the precipitate was redispersed in 6 mL of toluene. The resulting QD solution, red and clear, was then used for the above-mentioned *ex situ* TEM and optical absorption analysis.

*Reaction flask.* The synthesis was performed in a custom-made three-neck flask equipped with an indentation (Figure 2.7). The design of the flask was adapted from literature for our purposes,[50] and it had the advantage of having the same design and structure of the regular three-neck flasks used for the synthesis of colloidal nanocrystals in the chemistry lab, while allowing to probe the sample with X-rays. The flask was carefully designed to allow proper mixing of the reagents, via the presence of a stirring bean at the bottom of it and regardless of the presence of the indentation. The distance between the inner window of the indentation and the outer window of the flask was ~4 mm, and it was designed to allow for the transmission of X-rays without complete absorption from the sample environment. The Duran® borosilicate glass 3.3 windows from Schott had a thickness of 0.7 mm and a diameter of 8 mm. To perform the experiment, the flask was filled with the reagents and connected to the nitrogen supply, thus ensuring that the reaction would be performed under inert atmosphere. The flask was then wrapped with a heating ribbon connected to a thermocouple that probed the temperature of the reagents, thus allowing to reach the temperatures at which the synthesis was performed (260–290 °C).

The flask was then positioned inside a protective aluminum box with holes on both sides, at the same height as the indentation, and wide enough to allow the collection of SAXS and WAXS signals (Figures 2.8a–c). The box had the double purpose of securing the flask and containing potential spillages. The box constituted the upper part of a compact setup which included a stirring plate, in the middle, and an aluminum optical breadboard, at the bottom; this design was characterized by optimal compactness and user-friendliness. To perform the hot injection, the setup was equipped with a remotely controlled liquid injector which was attached to the lower optical breadboard and positioned above the flask (Figure 2.8d). The injector was composed of two pistons, which were actuated by compressed air and that could be activated remotely independently. The pistons pushed on two different syringes which contained the reagents to be injected at high temperature and that were kept in place by rubber bands.

*SAXS/WAXS measurements.* The SAXS/WAXS experiments were performed on the ID02 beamline of the ESRF (European Synchrotron Radiation Facility) at an energy of 18 keV (± 2 eV) with Rayonix MC-170HS detector and a sample-to-detector distance of 1.0 meter. This distance allowed us to probe a scattering vector $q$-range between 0.1 nm$^{-1}$ and 5 nm$^{-1}$. The $q$-range and the scattering intensity were calibrated as described in ref 52. A detailed description of the beamline[52] and the data treatments[72] can be found in literature. Due to the fast kinetics of the reaction in the early stages of the synthesis, and due to the limited storage memory, the patterns were recorded with increasing time in between the patterns. The time in between the measurements followed the formula: $t_i$

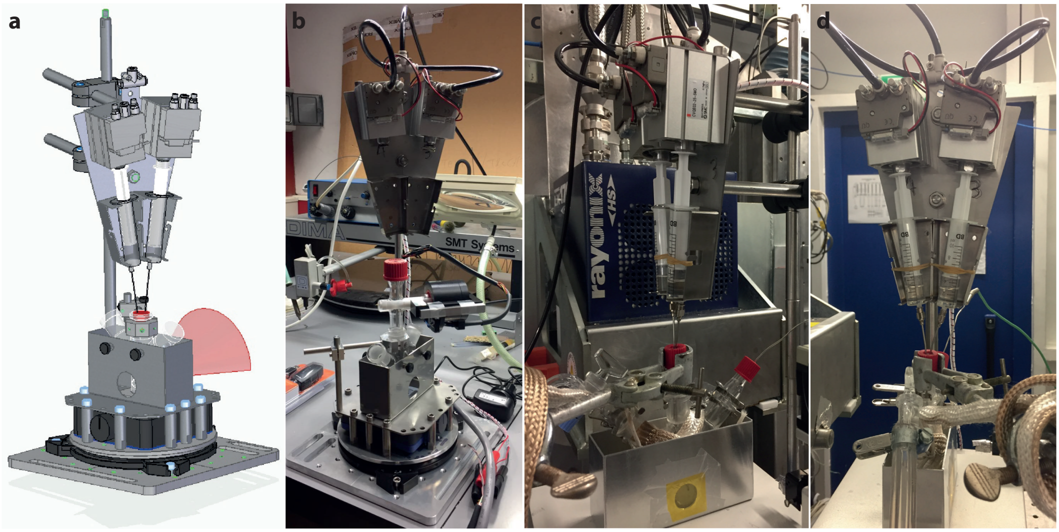

**Figure 2.8 | Custom-made setup for X-ray scattering experiments.** (**a**) Scheme of the setup for X-ray scattering experiments. The custom-made flask was positioned inside a protective aluminum box with two holes at the same height as the indentation, so to allow collection of the SAXS/WAXS signal (red cone). The box was welded to a structure composed of a stirring plate and an aluminum optical breadboard. Above the flask, and connected to it through two metallic needles, were two syringes containing the reagents for the hot injection. The syringes were pressed by two pistons which could be activated remotely. (**b**) Digital photo of the setup in the workshop during manufacturing. (**c**) Digital photo of the setup, ready for an experiment, in the experimental hutch of ID02 at ESRF. (**d**) Digital photo of the custom-made liquid injector.

+ $t_w 1.015^{n-1}$, where $t_i$ is the integration time (75 ms), $t_w$ the initial waiting/dead time (22 ms, the shortest time possible for the detector with 8x8 pixel binning), and $n$ the number of the frame with a maximum of 575. This resulted in a temporal resolution of 100 ms at the beginning of the experiment and about 100 seconds at the end of the experiment.

*Ex situ reaction development by quantitative aliquots.* As a benchmark of the *in situ* SAXS study, we carried out the same synthesis of CdSe nanocrystals as described in S.1.2 in a standard lab set-up and monitored the reaction development by means of the UV–vis absorption spectrum of quantitative reaction aliquots (Figure 2.9). More details on the quantitative analysis of absorption spectra are provided below.

*Analysis of SAXS patterns.* For isotropic samples, the scattering intensity does not depend on the azimuthal angle of the detector. For this reason, we only discuss the data analysis of the one-dimensional (1D) scattering patterns obtained by azimuthal integration of the 2D scattering patterns, performed by a procedure specific for the used beamline, ID02 at the ESRF, as described by ref 72. Examples of the 1D scattering patterns are shown in Figure 2.10a for different times after the hot injection. From these scattering patterns the background (scattering pattern at time 1 s) is already subtracted. Abso-

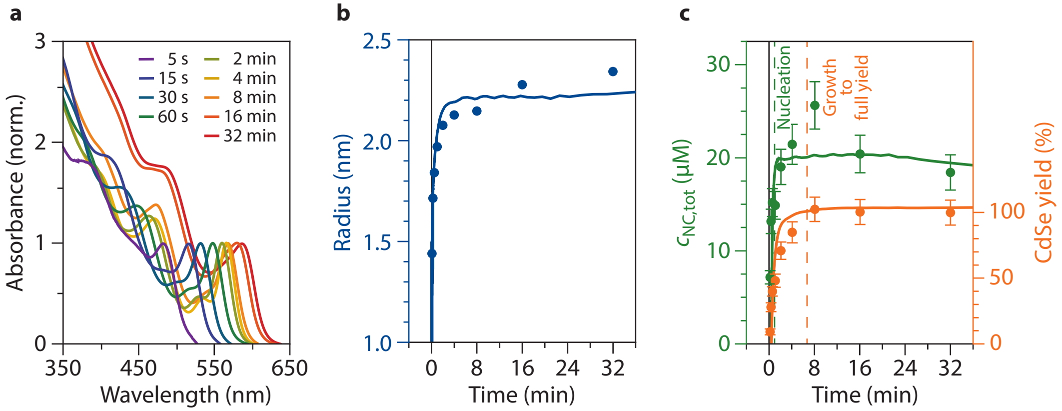

**Figure 2.9 | Aliquots during CdSe synthesis.** (**a**) Absorbance spectra of reaction aliquots taken as indicated after the start of a CdSe synthesis following the method used for the *in situ* SAXS study. (**b**) (markers) Nanocrystal radius as obtained from the central wavelength of the first exciton transition in the absorption spectrum, using a SAXS-based calibration curve.[55] (line) Development of the nanocrystal radius as obtained from the *in situ* SAXS analysis, *i.e.*, the same data as in Figure 2.1. (**c**) (green dots) Yield of CdSe and (orange dots) nanocrystal concentration as obtained from the aliquot analysis. In both cases, the full lines represent the data obtained from the *in situ* SAXS analysis. Note that we multiplied the *in situ* SAXS based concentration by 0.8 to account for the slight underestimation of the reaction yield in the aliquot analysis.

lute intensities were obtained by correcting for the pathlength, ~4 mm, calibrated by measuring the scattering intensity of water (absolute scattering cross section $1.65 \cdot 10^{-3}$ mm$^{-1}$).[73] A comprehensive overview of common protocols for the handling of scattering patterns on semiconducting nanocrystals is described by ref 55. Figure 2.10c shows the scattering patterns with background subtracted and absolute intensities collected during the hot injection synthesis as used for further data analysis.

*Assumptions*. Since the reaction mixture is a diluted mixture of nanocrystals with a volume fraction $f \approx 7 \cdot 10^{-4}$ at the end of the synthesis, we analyzed the SAXS patterns assuming that there is no interaction between the nanocrystals, *i.e.*, the structure factor is equal to 1. *Ex situ* transmission electron microscopy images show that the nanocrystals are quasi-spherical (Figure 2.6c). In reality the nanocrystals are faceted as shown in Figure 2.11a. However, the difference in SAXS between a perfect sphere and a multifaceted and isotropic nanocrystal is minimal (Figure 2.11b). Hence, we use the assumption that the nanocrystals are spherical with a radius $R$, which follows a Gaussian distribution.

*Model scattering pattern*. The scattering pattern of a mixture of nanocrystals with an isotropic form factor $P_{\text{sphere}}$ and a Gaussian distribution of radii reads:[75]

$$I(q) = c_{\text{NC,tot}} N_{\text{A}} P_{\text{sphere}}(q), \tag{2.7}$$

where $c_{\text{NC,tot}}$ is the molar concentration of nanocrystals, $N_{\text{A}}$ the Avogadro constant, and the isotropic form factor $P_{\text{sphere}}$ for a spherical object is given by

$$P_{\text{sphere}}(q) = 36\pi \Delta\rho^2 V_{\text{sphere}}^2 \left[ \frac{\sin(qR) - qR\cos(qR)}{(qR)^3} \right]^2 . \tag{2.8}$$

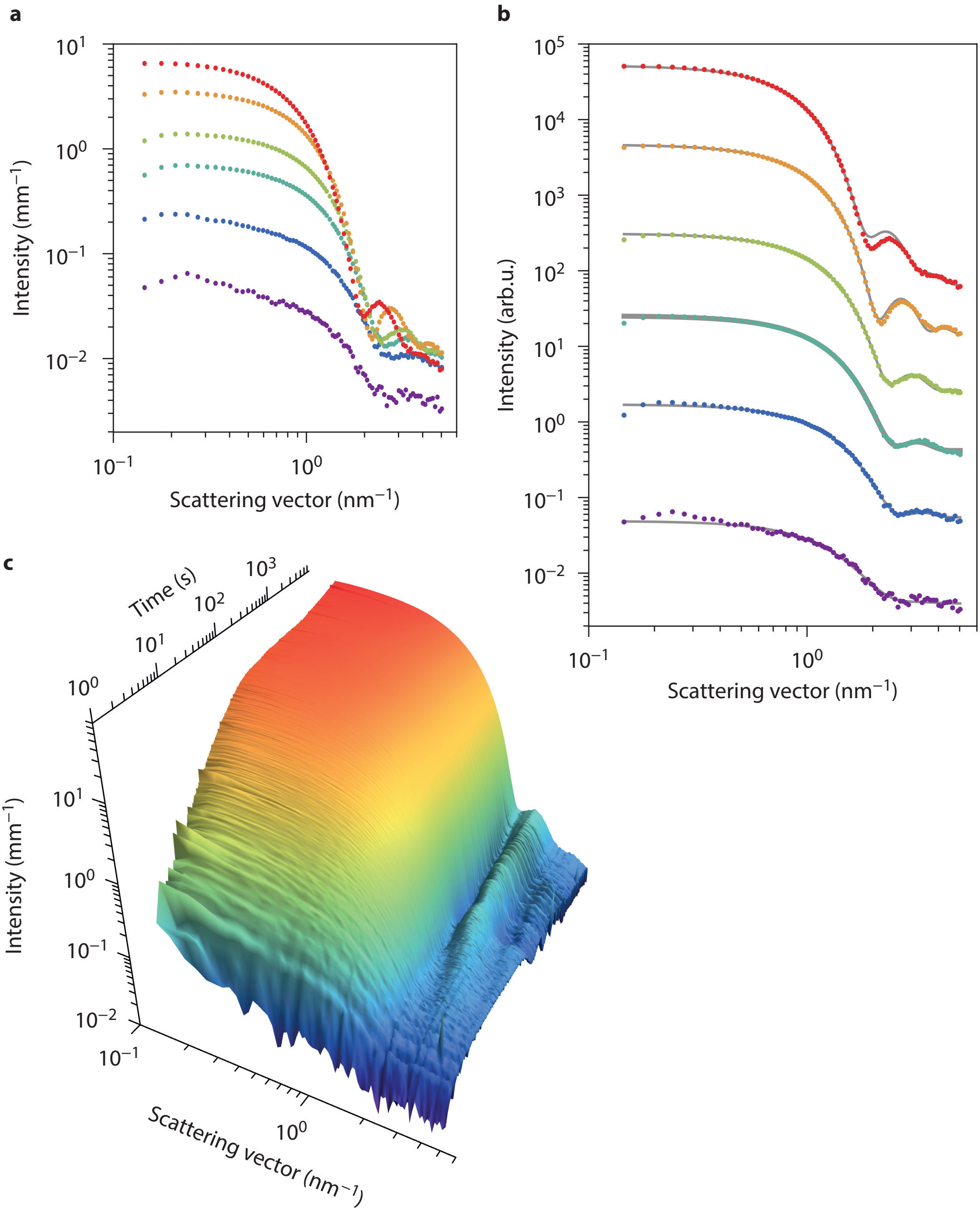

**Figure 2.10 | 1D scattering patterns extracted from the 2D scattering patterns and their corresponding fits.** From purple to red are respectively corresponding to the times 1.8 s, 5.3 s, 11 s, 22 s, 76 s, and 78 min after the hot injection. (**a**) The 1D scattering patterns with absolute intensity and background subtracted at the selected times. (**b**) The scattering patterns from panel **a** but now shifted for clarity (with $6^{n-1}$, $n$ the number of the scattering pattern) and their corresponding fits. (**c**) All 1D scattering patterns collected during the hot injection synthesis with background subtracted and absolute intensities.

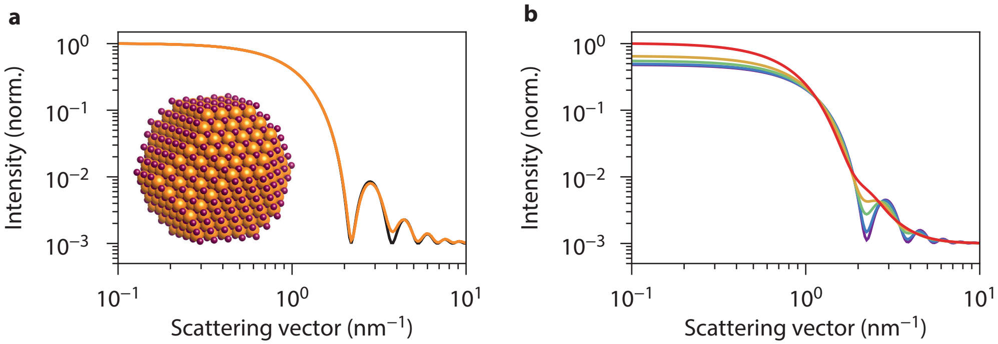

**Figure 2.11 | SAXS modeling and fitting.** (**a**) Schematic representation of a faceted CdSe nanocrystal, cadmium atoms are depicted red and the selenium atoms orange (produced with Vesta).[74] The nanocrystal has a zinc blende crystal structure with six [100] and eight [111] facets at the surface, its shape is that of a truncated cube. This representation is closer to the real shape of the nanocrystals prepared in our work than the perfectly spherical shape used to fit the SAXS data. (**b**) Scattering curve of the nanocrystal shown in panel **a**, taking into account all the individual atoms, *i.e.,* the exact shape represented in panel **a** (orange curve), and all orientations. The black curve is the theoretical scattering curve of a perfect sphere with a radius of 2.06 nm. It is clear that approximating the shape of the nanocrystals to a perfect sphere does not induce significant differences in the scattering curve with respect to the more realistic multifaceted and isotropic shape depicted in panel **a**. (**c**) Theoretical scattering patterns of an ensemble of nanocrystals with average radius of 2 nm and polydispersities of 2.5%, 5%, 10%, 15%, and 25% for respectively purple to red.

The average form factor for spheres with a Gaussian distribution of radii $R$ is then obtained as

$$\left\langle P_{\text{sphere}}(q)\right\rangle_R = 36\pi\Delta\rho^2 \frac{1}{\sqrt{2\pi\sigma_R}} \int_0^\infty \mathrm{e}^{-\frac{(R-R_0)^2}{2\sigma_R^2}} V_{\text{sphere}}^2 \left[\frac{\sin(qR) - qR\cos(qR)}{(qR)^3}\right]^2 \mathrm{d}R. \qquad (2.9)$$

Here, $R_0$ is the mean radius and $\sigma_R$ the standard deviation. Figure 2.11c shows the influence of the standard deviation on the theoretical scattering pattern. The increase in intensity at small scattering vector values is due to the increase in the average volume of the nanocrystals. $\Delta\rho$ is the scattering length density contrast between the medium and the nanocrystals, *i.e.*, $\Delta\rho = \rho_{\text{CdSe}} - \rho_{\text{reaction mixture}}$.

According to the scattering length density calculator provided by the National Institute of Standards and Technology (NIST, https://www.ncnr.nist.gov/resources/activation/), we have $\rho_{\text{CdSe}} = 40.7 \cdot 10^{-6}$ Å$^{-2}$ and $\rho_{\text{reaction mixture}} = 5.5 \cdot 10^{-6}$ Å$^{-2}$ at 18 keV and 260 °C. Note: At room temperature the density of the reaction mixture is 0.8 g cm$^{-3}$. However, for organic materials the thermal expansion is significant, and based on refs 51,76 we estimated a thermal expansion of 25% from room temperature to 260 °C. For that reason, a density of 0.6 g cm$^{-3}$ was used to calculated $\rho_{\text{reaction mixture}}$.

*Fitting procedure*. Fitting of the experimental data was done following a weighted least squares fitting procedure in a custom script. It was weighted with $1/\sigma^2$, $\sigma$ the standard deviation on the measured intensity values provided in the processed data from the beamline, ID02 at the ESRF. The standard deviation is influenced by the number of counts on a pixel and the number of pixels corresponding to a certain $q$ bin.[77] Propagation of error was considered when rebinning the data and subtracting the background. Equation 2.7 with Equation 2.9 were used as model, integrated by summation with steps of 0.02 nm, plus an additional constant background. From this fitting procedure we extracted the molar concentration, average radius, standard deviation, and background as function of time as shown in Figures 2.1b,c. Examples of the obtained fits are shown for selected times in Figure 2.10b.

*Reaction yield calculation.* From the fits to the SAXS scattering pattern, we obtained the molar concentration and the average radius of the CdSe nanocrystals in the reaction mixture. To calculate from these data the reaction yield, we first determined the average number of $Cd^{2+}$ cations in a single nanocrystal from the ratio between the average nanocrystal volume $\langle V_{\mathrm{sphere}} \rangle_R$ and the volume of the CdSe zinc blende unit cell ($a$: lattice parameter):

$$n_{\mathrm{Cd}^{2+}} = 4\frac{\left\langle V_{\mathrm{sphere}} \right\rangle_R}{a^3}. \tag{2.10}$$

The reaction yield $Y$ is then obtained from the ratio between the total amount of $Cd^{2+}$ cations incorporated in the nanocrystals and the amount of $Cd^{2+}$ cations initially present in the reaction mixture:

$$Y = c_{\mathrm{NC,tot}}\frac{n_{\mathrm{Cd}^{2+}}}{c_{\mathrm{Cd},0}}, \tag{2.11}$$

where $c_{\mathrm{NC,tot}}$ is the molar nanocrystal concentration as deduced from the SAXS analysis, and $c_{\mathrm{Cd},0}$ is the initial molar concentration of the Cd precursor.

*Synthesis method for aliquot-analysis of reaction development*. CdSe nanocrystals were synthesized as described in ref 44. In brief, a 10 mL mixture of 0.2 mmol cadmium stearate, 0.4 mmol stearic acid, and 1.6 mmol hexadecylamine (HDA) in ODE was loaded in a 25 mL three-neck flask. The reaction mixture was degassed for 30–60 min at room temperature and 60 min at 100 °C under a nitrogen flow. Afterwards, the temperature was raised to an injection temperature of 245 °C and 2 mL of a solution of 0.5 mmol Se in TOP (TOP-Se) was injected. After injection, the reaction temperature was stabilized at 230 °C. The reaction was monitored by means of successive aliquots and finally quenched by cooling with a water bath.

*Aliquots*. During the reaction, aliquots were taken and quenched in a 1:5 mixture of OA and toluene with a known weight. After determining the mass of the aliquot by weighting, the nanocrystals were precipitated with a 1:1 mixture of methanol and 2-propanol. The precipitate was redissolved in toluene, precipitated a second time with methanol, and again redissolved in toluene. As demonstrated in the literature, this synthesis yields quasi-spherical CdSe nanocrystals with a zinc blende structure.[44,78]

*Aliquot analysis.* To determine the amount of CdSe in a given aliquot, we used an average determined by combining the absorbance at 340, 320, and 300 nm with published respective intrinsic absorption coefficients at these wavelengths and we assumed a fixed 1.2:1 Cd:Se ratio in the nanocrystals.[71] The radius was determined from the wavelength where the exciton absorbance peaks using a published, SAXS-based calibration curve.[55] Both numbers were combined to determine the CdSe nanocrystal concentration.

*Data analysis – CdSe formation.* It has been shown in the literature that the time development of the amount of CdSe $n_{\mathrm{CdSe}}$ in the reaction is in line with a rate-determining monomer generation rate that is first order in the cadmium and first order in the selenium concentration:[44]

$$n_{\mathrm{CdSe}}(t) = n_{\mathrm{Cd},0}\left(1 - \frac{(\beta - 1)\mathrm{e}^{-k_2(\beta-1)c_0 n_{\mathrm{Cd},0} t}}{\beta - \mathrm{e}^{-k_2(\beta-1)c_0 n_{\mathrm{Cd},0} t}}\right). \tag{2.12}$$

Here, $n_{\mathrm{Cd},0}$ is the amount of the Cd precursor in the reaction mixture, $\beta$ is the molar ratio of the selenium and cadmium precursor, $k_2$ is the second-order rate constant of the monomer formation reaction and $c_0$ is the inverse of the reaction volume of 12 mL. For reactions at 230 °C, the rate constant $k_2$ was determined at 0.14 L mol$^{-1}$s$^{-1}$.[44]

*Data analysis – nanocrystal concentration.* To estimate the moment the NC concentration reaches 98% of its final value, we fitted the NC concentration as obtained for *in situ* SAXS data and the aliquots by means of a single exponential build-up:

$$n_{\mathrm{NC}}(t) = n_{\mathrm{NC},\infty}(1 - \mathrm{e}^{-kt}). \tag{2.13}$$

This expression can be obtained by considering the monomer mass balance. Under conditions where monomer generation is rate determining, the number of monomers used for nucleation should equal the difference between the monomer generation rate and the monomer consumption by growth. Hence

$$\frac{V_\mathrm{c}}{V_\mathrm{m}}\frac{\mathrm{d}n_{\mathrm{NC}}}{\mathrm{d}t} = G_\mathrm{M} - Kn_{\mathrm{NC}}, \tag{2.14}$$

where $V_\mathrm{c}$ is the volume of a critical nucleus, $V_\mathrm{m}$ the molar volume of the material precipitating, $G_\mathrm{M}$ is the monomer generation rate and $K$ is the rate at which monomers adsorb at a single nanocrystal.

Under conditions where $V_\mathrm{c}$, $G_\mathrm{M}$, and $K$ are constant, the exponential build-up (Equation 2.13) we used for fitting purposes is obtained. Interestingly, this exponential build-up provides a satisfactory fit to the time development of the nanocrystal concentration we obtained from the SAXS analysis (see Figure 2.12). Considering the assumptions under which the exponential build-up was derived, a constant $V_\mathrm{c}$ and $G_\mathrm{M}$ do not seem problematic in the beginning of the reaction. The assumption of a constant rate constant $k$, on the other hand, is less obvious. Probably, the correspondence between the data and the exponential build-up results from an average over all existing nanocrystals. Even so, the correspondence between the *in situ* SAXS and the simple exponential build-up warrants the use

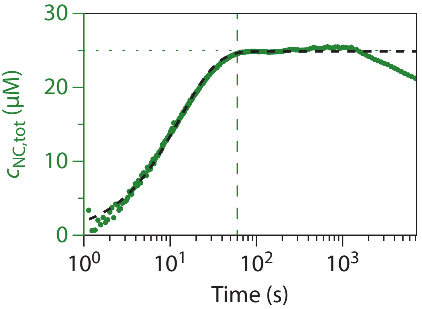

**Figure 2.12 |** Best fit of an exponential build-up (dashed black line) to the time-dependent nanocrystal concentration as measured by *in situ* SAXS (see Figure 2.1).

of Equation 2.13 to determine the moment at which a synthesis attains 98% of its final concentration.

*Experimental method bi-modal size distribution experiments.* A mixture with a total volume of 10 mL containing 0.2 mmol $Cd(OA)_2$, 0.6 mmol HDA, 0.8 mmol OA, and ODE was stirred under a nitrogen flow for 1 h at 120 °C. The nitrogen flow was stopped, and still under nitrogen, the temperature was raised to $X + 15$ °C and 2 mL of a 1 M TOP-Se solution (Cd:Se 1:10) was injected. After injection, the reaction temperature was stabilized at $X$ °C. After 4 min, an additional 0.4 mmol of $Cd(OA)_2$ was injected and aliquots were taken at different reaction times from 5 s to 600 s after this second injection step. The same reaction was carried out at $X = 200$, 230, and 270 °C.

Note that this procedure is highly similar to what has been discussed above. In this case, however, oleic acid instead of stearic acid was used as the carboxylic acid and the molar excess of the selenium precursor was increased to 10:1, such that the second injection of cadmium oleate can effectively start a highly similar nucleation event as the first injection.

*Bi-modal reaction procedure without additional injection.* Figure 2.13 represents the reaction development for the synthesis as described above, carried out at respectively 245 °C and 230 °C as injection and growth temperature. The absorbance spectra give no indication of the formation of a second population. In this case, 98% of the final yield is reached after 2.5 minutes, while the nanocrystal concentration takes 0.3 min to reach a constant value. Hence, we estimate that the nucleation period for this reaction lasts for ~12% of the reaction time.

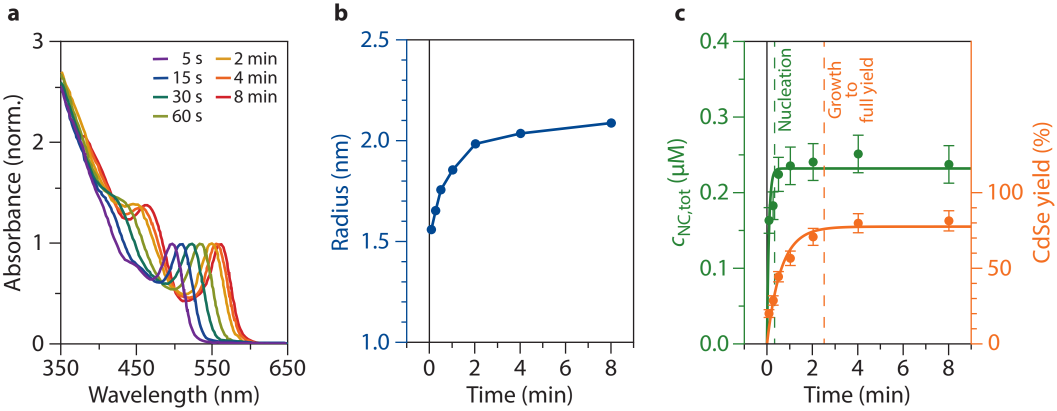

**Figure 2.13 |** (**a**) Normalized absorbance of aliquots taken at the indicated times from the CdSe reaction mixture. (**b**) Development of the nanocrystal radius as estimated from the absorbance spectra shown in panel **a** using a SAXS-based sizing curve.[55] (**c**) Development of the amount of (blue) CdSe and (red) nanocrystals as estimated from the absorbance spectra shown in panel **a**. The green and orange dashed lines respectively indicate the times at which the nanocrystal concentration and the CdSe yield attain 98% of the final value.

*Bi-modal reaction procedure after additional injection.* Figure 2.14a represents the absorption spectra of reaction aliquots taken at the indicated time after the second injection of $Cd(OA)_2$ for the reaction carried out at 230 °C injection/growth temperature. The corresponding photoluminescence spectra have been represented in Figure 2.4b. In particular in the spectra recorded until 60 s after the second injection, the band-edge absorption feature of the smaller subset can be identified. However, an accurate determination of the band-edge position from these spectra is difficult, a result that motivated us to analyze the bimodal size distribution by photoluminescence spectroscopy. The thus obtained band-edge positions have been added as markers to the spectra shown in Figure 2.14a.

Through the absorption of each quantitative aliquot, we could also determine the additional amount of CdSe formed by the second injection. As shown in Figure 2.14b one sees that the second injection leads to a conversion yield of 70%, slightly smaller than typically found for a single injection reaction. Moreover, a fit to Equation 2.13 yields a second-order rate constant $k_2 = 0.125 \pm 0.015$ L mol$^{-1}$ s$^{-1}$. This rate constant coincides within the measurement error with the published value of $k_2 = 0.14 \pm 0.01$ L mol$^{-1}$ s$^{-1}$.[44] Given these observations, we conclude that the CdSe formation is indeed independent of the presence of nanocrystals.

*Luminescence calibration.* To establish a calibration curve linking the wavelength of maximum exciton emission to the wavelength of maximum exciton absorbance, we used two CdSe syntheses as shown in Figure 2.13, where we changed the oleic acid to cadmium oleate ratio to have a sufficiently wide span of the exciton peak absorbance and emission. As shown in Figure 2.15, by taking different aliquots during such a synthesis, a relation between the wavelength where the exciton absorbance and the emission peak can be established. A linear fit to such data points yields a calibration curve

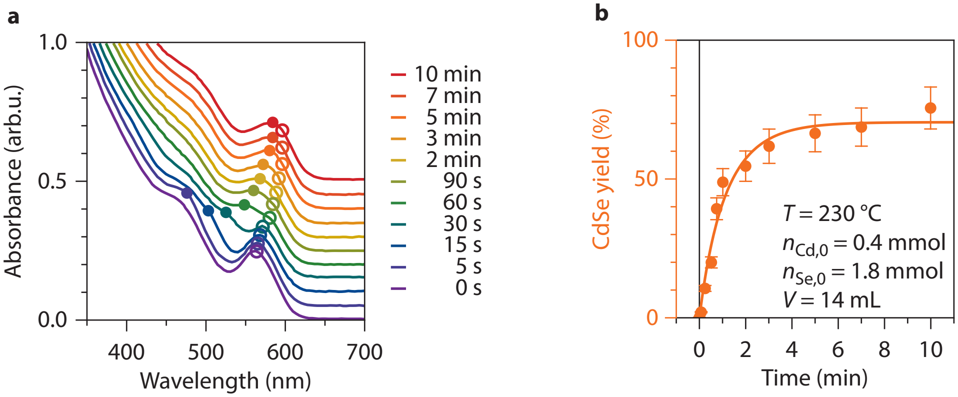

**Figure 2.14 |** (**a,b**) Absorbance spectra of aliquots for the bimodal distribution experiment at 230 °C, corresponding to Figure 2.4b. The spectra are recorded on quantitative aliquots taken at the indicated moment after the second injection of $Cd(OA)_2$. (**b**) (markers) Yield of CdSe obtained from the absorbance spectra shown in **a** and (full line) fit of these data to Equation 2.13 from which we obtain a second-order rate constant $k_2 = 0.125 \pm 0.015$ L mol$^{-1}$ s$^{-1}$.

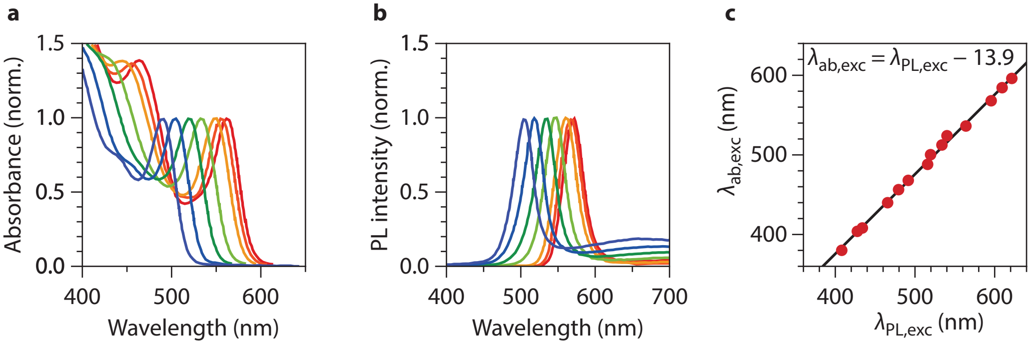

**Figure 2.15 |** (**a**,**b**) Absorbance spectra of aliquots for the CdSe synthesis used to determine the exciton peak absorbance wavelength *versus* peak emission wavelength calibration curve. The same color is used to represent absorbance and emission from the same aliquot. (**c**) Resulting calibration curve, including an expression for the best fitting linear trend line.

that we used to turn the emission wavelength in an absorbance wavelength. The latter was recalculated as a nanocrystal radius using a published, SAXS-based calibration curve.[55]

*Superfocusing analyzed by UV–vis absorption spectroscopy.* As shown in Figure 2.14a, the bimodal distribution created by the second injection of $Cd(OA)_2$ is difficult to quantify by means of UV–vis absorption spectra for the synthesis as described above, hence our use of photoluminescence spectroscopy to determine the average radius of both sets of nanocrystals in Figure 2.4. While band-edges obtained from photoluminescence correspond to the few identifiable features of both sets of nanocrystals in the absorption spectra shown in Figure 2.14a, a photoluminescence analysis may create artifacts since only emissive nanocrystals are measured.

To avoid such issues, we extended the study on bimodal size distributions and superfocusing to a different CdSe synthesis, first described by ref 79. Here, 0.4 mmol CdO was added to 10 mL of ODE together with 1.2 mmol of OA in a three-neck flask with cooler under air. The mixture was heated up to 270 °C to dissolve the red CdO in ODE by the formation of a cadmium carboxylate complex. The formation of CdSe nanocrystals was initiated by injecting a 2 mL solution of ODE containing 0.05 mmol of black Se powder. The growth temperature was set at 260 °C. After 20 s of reaction, a similar injection of 0.05 mmol followed, while keeping the reaction temperature at 260 °C, and aliquots were taken at regular intervals.

As can be seen in Figure 2.16, the second injection creates in this case a clearly identifiable absorption feature of the smaller subset that stands out relative to the shorter wavelength absorption features of the larger subset. Identifying the average radius of the initial and the newly formed subset from these absorption spectra, we again find that the smaller subset grows significantly faster than the larger set than predicted based on the $1/r$ dependence of diffusion-limited growth, *i.e.*, superfocusing.

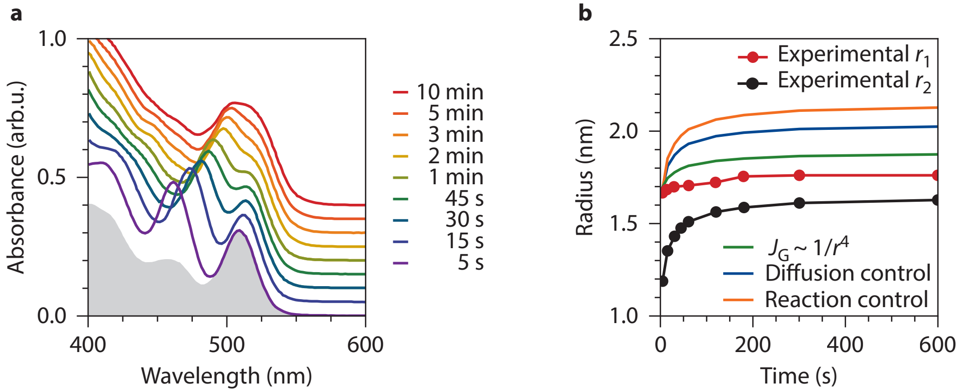

**Figure 2.16 | Observation of superfocusing in a CdSe synthesis based on the reaction between cadmium oleate and black selenium.** (**a**) (colored lines) Absorbance spectra recorded at the indicated times after a second injection of black selenium and (filled gray trace) reference spectrum of a CdSe nanocrystal batch obtained with the same synthesis after a single precursor injection. Given this reference spectrum, we attribute the two absorption features at ~510 nm and ~460 nm in the UV–vis spectrum obtained 5 s after the second precursor injection to the initial and newly formed set of nanocrystals, respectively. (**b**) Variation of the nanocrystal diameter as a function of time for the (red) initial set and (black) newly formed set of nanocrystals in the reaction mixture. The blue and orange line indicate the expected evolution of the diameter of the large set under diffusion and reaction control respectively. The green line represents the evolution expected for a growth exponent $n = 4$.

## 2.5 Theory of nanocrystal growth

*The nanocrystal growth rate.* We define the NC growth rate $j_G$ as the rate of change of the nanocrystal radius $r$:

$$j_G = \frac{\mathrm{d}r}{\mathrm{d}t}. \tag{2.15}$$

To obtain an expression for $j_G$ as a function of the NC radius, we assume that growth involves the diffusion of monomers to the NC surface, and the adsorption or desorption of monomers at the NC surface, see Figure 2.17. Considering spherical NC, the concomitant fluxes $J_{\mathrm{diff}}$, $J_a$, and $J_d$ [mol s$^{-1}$] can be written as:

$$J_{\mathrm{diff}} = 4\pi r D([\mathrm{M}] - [M(r)]) \tag{2.16}$$

$$J_a = 4\pi r^2 k_a(r)[M(r)] \tag{2.17}$$

$$J_d = -4\pi r^2 k_d(r). \tag{2.18}$$

Here, $D$ is the monomer diffusion coefficient, [M] and [M($r$)] are the monomer concentration in the reaction mixture and at the surface of the nanocrystal, respectively. The respective symbols $k_a(r)$ and $k_d(r)$ denote the rate constants for monomer adsorption and desorption, which are explicitly seen as radius dependent quantities. Note that in writing Equation 2.18, we assumed that the diffusion layer thickness strongly exceeds the NC radius.

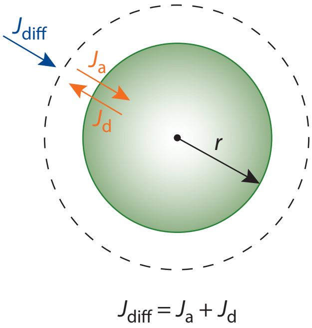

**Figure 2.17 |** Representation of the different fluxes involved in nanocrystal growth. The dashed line represents the surface at which boundary condition $J_{\mathrm{diff}} = J_{\mathrm{a}} + J_{\mathrm{d}}$, which was artificially displaced from the true nanocrystal surface to highlight the interrelation between the fluxes.

At the NC surface, the different fluxes are related by a boundary condition $J_{\mathrm{diff}} = J_{\mathrm{a}} + J_{\mathrm{d}}$. Accordingly, we obtain $[\mathrm{M}(r)]$ as:

$$[M(r)] = \frac{D[\mathrm{M}] + rk_{\mathrm{d}}(r)}{D + rk_{\mathrm{a}}(r)}. \tag{2.19}$$

Hence, the net monomer flux $J$ towards the NC surface can be written as:

$$J = J_{\mathrm{a}} + J_{\mathrm{d}} = 4\pi r^2 D \frac{k_{\mathrm{a}}(r)[\mathrm{M}] - k_{\mathrm{d}}(r)}{D + rk_{\mathrm{a}}(r)} = 4\pi r^2 D[\mathrm{M}]_0 \frac{S - \frac{k_{\mathrm{d}}(r)}{k_{\mathrm{a}}(r)[\mathrm{M}]_0}}{\frac{D}{k_{\mathrm{a}}(r)} + r}. \tag{2.20}$$

In Equation 2.20, we have introduced the monomer solubility $[\mathrm{M}]_0$ and the supersaturation $S$ as the ratio $[\mathrm{M}]/[\mathrm{M}]_0$ between the actual monomer concentration and the solubility. From Equation 2.20, the growth rate is eventually obtained as:

$$j_{\mathrm{G}} = \frac{V_{\mathrm{m}}}{4\pi r^2} J = DV_{\mathrm{m}}[\mathrm{M}]_0 \frac{S - \mathrm{e}^{\frac{2\gamma V_{\mathrm{m}}}{rRT}}}{\frac{D}{k_{\mathrm{a}}(r)} + r}. \tag{2.21}$$

Here, we have introduced the relation between the adsorption and desorption rate constants that follows from equilibrium considerations, where $\gamma$ is the surface tension, $V_{\mathrm{m}}$ the molar volume of the condensed phase, $R$ the gas constant and $T$ the absolute temperature. Indeed, when the monomer concentration is equal to the nanocrystal solubility $[\mathrm{M}]_0(r)$, the adsorption and desorption flux should balance. Hence, using the Kelvin equation, we have:

$$\frac{k_{\mathrm{d}}(r)}{k_{\mathrm{a}}(r)} = [\mathrm{M}]_0(r) = [\mathrm{M}]_0 \mathrm{e}^{\frac{2\gamma V_{\mathrm{m}}}{rRT}}. \tag{2.22}$$

*Rate constants based on a linear free-energy argument.* To use Equation 2.21 for the growth rate, an explicit expression of the radius-dependence of $\mathrm{k_a}(r)$ is needed. Here, a possible answer follows from extending the Kelvin equation with a linear free energy argument. The argument goes as follows. As indicated in Equation 2.22, the solubility of small nanocrystals increases with decreasing radius. This can be interpreted as an increase of the chemical potential of the monomers in a nanocrystal solid as compared to a bulk solid. As outlined in Figure 2.18, a linear free energy argument states that this increase of the free energy of the final state induces a proportional increase of the activation energy of the forward reaction, *i.e.*, the adsorption reaction. We thus have:

$$k_{\mathrm{a}}(r) = k_{\mathrm{a}}(\infty)\mathrm{e}^{-\alpha\frac{2\gamma V_{\mathrm{m}}}{rRT}}. \tag{2.23}$$

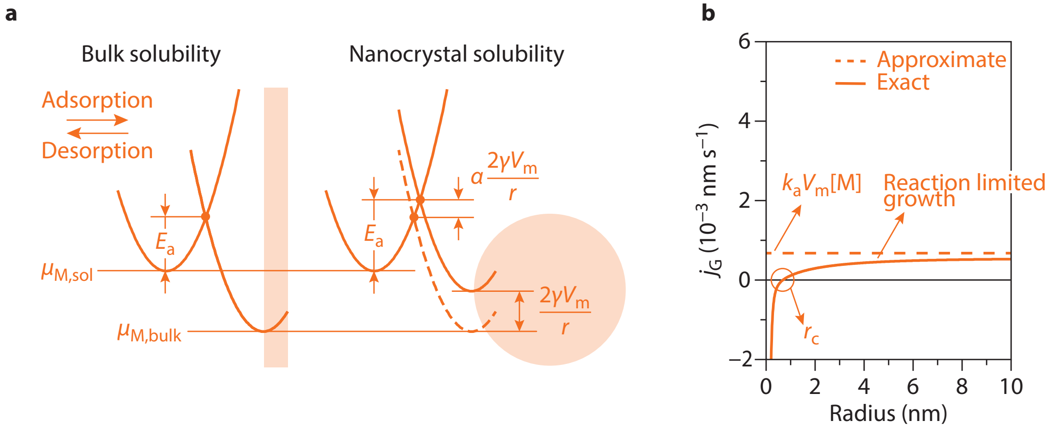

**Figure 2.18 |** (**a**) Representation of bulk and nanocrystal solubility, where the enhanced solubility of the nanocrystals is related to an increased chemical potential of the monomers incorporated in nanocrystals as compared to bulk. Through a linear free energy argument, the activation energy for monomer adsorption changes proportionally with this increase of the chemical potential,[56] as described by the transfer coefficient $\alpha$. (**b**) Growth rate obtained in a reaction-limited regime using an adsorption rate constant as described by a linear free energy relationship.

Using this relation, we obtain the expression of the growth rate as proposed by Talapin *et al.*, which predicts a gradual increase of $k_a(r)$ with increasing radius that levels of at $k_a(\infty)$ in the bulk limit.[56] Note that by introducing the critical radius $r_c = 2\gamma V_m/RT\ln S$, Equation 2.21, Equation 2.22, and Equation 2.23 can be combined to write the growth rate as:

$$j_G = DV_m[M]_0 \frac{S - S^{\frac{r_c}{r}}}{r + \frac{D}{k_a(r)}} = DV_m[M]_0 \frac{S - S^{\frac{r_c}{r}}}{r + \frac{D}{k_a^{\infty}} S^{\alpha \frac{r_c}{r}}}. \tag{2.24}$$

Combined with Equation 2.21, Equation 2.23 yields a growth rate that increases with increasing radius as shown in Figure 2.18b and Figure 2.3c. Here, the calculation was done with parameters as summarized in Table 2.1.

| Symbol | Parameter description | Value | Unit |
|---|---|---|---|
| $D$ | Monomer diffusion coefficient | $5 \cdot 10^{-10}$ | $m^2\,s^{-1}$ |
| $v_0$ | Volume per CdSe unit cell | $5.59 \cdot 10^{-29}$ | $m^3$ |
| $[M]_0$ | Monomer solubility | $1 \cdot 10^{-7}$ | $mol\,m^{-3}$ |
| $k_a(\infty)$ | Rate constant for monomer adsorption, bulk limit | $4 \cdot 10^{-3}$ | $m\,s^{-1}$ |
| $\gamma$ | Surface tension | 0.2 | $J\,m^{-2}$ |
| $S$ | Supersaturation | 50 | - |

**Table 2.1 |** Parameter setting for the calculation of the growth rate under diffusion and reaction control as shown in Figures 2.3b,c and Figure 2.18b.

*Growth of a bimodal size distribution.* We write the growth rate under conditions that the desorption reaction is negligible in a generic way as:[32]

$$j_{\mathrm{G}}(r) = \frac{A}{r^n} S. \tag{2.25}$$

Here, $A$ is a rate constant, and $S$ is the supersaturation. In Equation 2.25 is a convenient way of expressing the growth rate, since the situation $n = 0$ would correspond to reaction limited growth in the limit of large nanocrystals, whereas $n = 1$ would yield diffusion limited growth under the same conditions. Since $j_{\mathrm{G}}(r) = \mathrm{d}r/\mathrm{d}t$, we have:

$$r^n \mathrm{d}r = AS(t)\mathrm{d}t. \tag{2.26}$$

Integration left and right thus yields:

$$\frac{1}{n+1}\left(r^{n+1} - r_0^{n+1}\right) = \int_0^t AS(t)\mathrm{d}t. \tag{2.27}$$

Since Equation 2.27 applies to both sets of nanocrystals in a bimodal ensemble, we have:

$$r_1^{n+1} - r_{0,1}^{n+1} = r_2^{n+1} - r_{0,2}^{n+1}. \tag{2.28}$$

So, for $n = 1$ and $n = 0$, we obtain:

$$r_{1,\mathrm{diffusion}} \approx \sqrt{r_2^2 + \left(r_{1,0}^2 - r_{2,0}^2\right)} \tag{2.2}$$

$$r_{1,\mathrm{reaction}} \approx r_2 + \left(r_{1,0} - r_{2,0}\right). \tag{2.3}$$

Similar expressions for any value of $n$ are readily obtained.

*Local approximation of functions as $1/r^n$.* Equation 2.4 writes the growth rate in general as:

$$\frac{\mathrm{d}n_{\mathrm{M}}}{\mathrm{d}t} = \frac{1}{V_{\mathrm{m}}}\frac{\mathrm{d}V_{\mathrm{NC}}}{\mathrm{d}t} = 4\pi r^2 [\mathrm{M}] \frac{k}{r^n}, \tag{2.4}$$

where we use this relation as a heuristic model to explore different degrees of superfocusing, as characterized by the exponent $n$. While heuristic, this approach has general relevance since any function $f(r)$ can be locally approximated by means of Equation 2.4 by an appropriate choice of $n$. To understand this, we start by introducing a local approximation for $f(r)$ as:

$$f(r) = \frac{A}{r^n}. \tag{2.29}$$

Replacing both sides of Equation 2.29 by a first-order Taylor expansion, we obtain:

$$f(r) + \frac{\mathrm{d}f}{\mathrm{d}r}\mathrm{d}r = \frac{A}{r^n} - n\frac{A}{r^{n+1}}\mathrm{d}r. \tag{2.30}$$

Hence, an expression of the kind $A/r^n$ will locally describe $f(r)$ if we take the exponent $n$ as:

$$n = -\frac{r}{f}\frac{\mathrm{d}f}{\mathrm{d}r}. \tag{2.31}$$

## 2.6 Kinetic reaction modeling

*The reaction chemistry of CdSe formation.* According to literature, the formation of CdSe from a cadmium carboxylate and trioctylphosphine selenium takes place by means of a two-step mechanism in which both precursors first react to form a compound typically referred to as the monomer.[42,45] This monomer is the actual solute or precipitant. The following chemical reactions equations for the precursor conversion have been proposed:[42,45]

$$\mathrm{TOPSe} + \mathrm{Cd(RCOO)_2} \rightleftharpoons \mathrm{(TOP)Se{-}Cd(RCOO)_2} \longrightarrow \mathrm{CdSe} + \mathrm{TOPO} + \mathrm{RCOOOCR}. \quad (2.32)$$

Here, the CdSe formula unit represents the CdSe monomer in the reaction mixture. Moreover, it was found that the byproducts of the precursor conversion — in particular TOPO — are produced at the same rate as the solid CdSe is formed. Therefore, several authors proposed that the conversion reaction from precursors to monomers determines the overall rate at which solid material is formed through nucleation and growth.[44,45] This conclusion was confirmed in the case of CdS formation by the finding that the formation rate of CdS was independent of the presence of seed nanocrystals in the reaction mixture or not.[80] Building on this insight, Abe *et al.* analyzed the CdSe formation rate as a function of the concentration of the $\mathrm{Cd(RCOO)_2}$ and TOPSe in the reaction mixture and showed that the formation rate follows a simple rate law that is first order in the concentration of either precursor.[44] Importantly, the buildup of CdSe after the second injection in the bimodal size distribution experiments yields the same second-order rate constant as published previously by Abe *et al.*[44] This observation confirms that the formation of CdSe is determined by the monomer formation rate and is independent of the presence or not of CdSe nanocrystals.

*Modeling colloidal crystallization.* In the literature, two main approaches have been developed to describe nucleation and growth in crystallization reactions.[62] A first alternative — referred to as the population balance equation model in ref 62 — involves a continuous approach in which the nanocrystal population balance is expressed through a partial differential equation that takes time and the nanocrystal radius as independent variables. A second — dubbed the kinetic rate equation method — translates nucleation, growth, and dissolution into a set of discrete ordinary differential equations, each addressing a single, discrete nanocrystal size. For computational convenience, both methods can be coupled by using separate rate equations for small nanocrystals, and a continuous approach for larger nanocrystals. In the case of precipitation reactions involving a homogeneous monomer formation, the continuous approach has been used to describe nucleation and growth of iron oxide[61] and CdSe[44] nanocrystals, while a hybrid methodology was implemented by Rempel *et al.*[35] For reactions involving surface-catalyzed growth, extensive modeling of nucleation and growth has been accomplished by the kinetic rate equation method.[39,64]

Vetter *et al.*, in ref 62, stated: “We have confirmed for every mechanism separately that the KRE and PBE model deliver similar descriptions of the process and that the dependence of the two models on the key parameters given above is consistent. Nevertheless, the KRE model in general allows obtaining deeper insight into the behavior of both sub- and supercritical crystals.” (Page 4904)

This statement aligns with the observation that the continuous simulations of a hot injection synthesis carried out by Abe *et al.*[44] and the hybrid simulations proposed by Rempel *et al.*[35] yield a comparable development of the concentration distribution as a function of time and particle size. Even so, one should realize that a continuous approach in which nucleation is modeled by means of classical nucleation theory will not give atomistic insight into the nucleation process.

*The population balance equations.* All simulations are based on the model equations reported and explained previously.[44] Based on the literature insight in the CdSe synthesis, the modeling approach is based on a kinetic scheme where injected precursors P react to form a solute or monomer M, which precipitates to form nanocrystals either by nucleation or growth, a mechanism we succinctly represent as:

$$\mathrm{P} \longrightarrow \mathrm{M} \rightleftharpoons \mathrm{NC}. \tag{2.33}$$

While the formation of a compound such as CdSe requires multiple precursors, we will only consider a single precursor species for the reaction simulations. This approach reflects the finding that the CdSe synthesis can be carried out under pseudo first-order conditions, for example by using a substantial excess of the selenium precursor.

Following Equation 2.33, the central quantities in the modeling are (1) the concentration distribution $c(r,t)$ of NCs in [m$^{-4}$] — where the product $c(r,t)\mathrm{d}r$ yields the concentration of NCs with a radius between $r$ and $r + \mathrm{d}r$ at time $t$, (2) the supersaturation $S(t)$, which is defined as the ratio between the actual concentration of the solute or monomer and its equilibrium concentration $[\mathrm{M}]_0$ and (3) the precursor concentration [P]. For simplicity, the model assumes a single precursor.

The concentration distribution $c(r,t)$ changes with time since new NCs nucleate (index N) and existing NCs grow (index G):

$$\frac{\partial c}{\partial t} = \left.\frac{\partial c}{\partial t}\right|_{\mathrm{N}} + \left.\frac{\partial c}{\partial t}\right|_{\mathrm{G}} = J_{\mathrm{N}}\delta(r - r_{\mathrm{c}}) - \frac{\partial(j_{\mathrm{G}}c)}{\partial r}. \tag{2.34}$$

In the above expression, we describe nucleation as the formation of NCs with the critical radius $r_{\mathrm{c}}$ [m] at a rate $J_{\mathrm{N}}$ [m$^{-3}$ s$^{-1}$], both given by classical nucleation theory:

$$r_{\mathrm{c}} = \frac{2\gamma V_{\mathrm{m}}}{RT \ln S} \tag{2.35}$$

$$J_{\mathrm{N}} = \frac{2D}{v_0^{5/3}} \exp\left(-\frac{16\pi\gamma^3 V_{\mathrm{m}}^2 N_{\mathrm{A}}}{3(RT)^3(\ln S)^2}\right), \tag{2.36}$$

where $v_0$ is the monomer volume and $N_{\mathrm{A}}$ is Avogadro's constant. The growth term in Equation 2.34 is written in terms of the NC growth rate $j_{\mathrm{G}}$, see Equation 2.21.

Regarding the supersaturation $S$, we assume that its time-dependence is governed by the generation of monomers from the precursors $G_{\mathrm{M}}$ [m$^{-3}$ s$^{-1}$] and by their consumption through the nucleation and the growth of nuclei. $\mathrm{d}S/\mathrm{d}t$ thus reads:

$$\frac{\mathrm{d}S}{\mathrm{d}t} = \frac{1}{[\mathrm{M}]_0}\left\{G_{\mathrm{M}} - \frac{4\pi r_{\mathrm{c}}^3}{3v_0}J_{\mathrm{N}} + \int_0^{\infty} \frac{4\pi r^3}{3v_0}\frac{\partial(j_{\mathrm{G}}c)}{\partial r}\mathrm{d}r\right\}. \tag{2.37}$$

Finally, the monomer generation rate $G_M$ is determined by the reaction of the precursor, and therefore the change of the precursor concentration [P] with time. For simplicity, we assume a first-order rate equation:

$$\frac{d[P]}{dt} = -G_M = -k_1[P]. \tag{2.38}$$

*Mathematical analysis growth-only reaction development*. Following Equation 2.37, the supersaturation changes in the absence of nucleation according to:

$$\frac{dS}{dt} = \frac{1}{[M]_0}\left\{G_M + \int_0^\infty \frac{4\pi r^3}{3v_0}\frac{\partial(j_G c)}{\partial r}dr\right\}. \tag{2.39}$$

The second part of the right-hand side can be rewritten using integration by parts:

$$\int_0^\infty \frac{4\pi r^3}{3v_0}\frac{\partial(j_G c)}{\partial r}dr = \left[\frac{4\pi r^3}{3v_0}j_G c\right]_0^\infty - \int_0^\infty \frac{4\pi r^2}{v_0}j_G c dr. \tag{2.40}$$

To evaluate the first term on the right-hand side, we express the total number of monomers $n_M$ incorporated in the nanocrystals as:

$$n_M = \int_0^\infty \frac{4\pi r^3}{3v_0}c(r)dr. \tag{2.41}$$

To have a finite integral, the *integrandum* should drop to zero for $r \to \infty$ faster than $1/r$, hence $c(r)$ must be $O(1/r^4)$. Hence, even for $j_G$ $O(1)$, the first term on the right-hand side of Equation 2.40 will always be zero. To evaluate the second term in Equation 2.40 in view of the growth exponent, we write the growth rate as:

$$j_G = \frac{dr}{dt} = V_m[M]_0 S\frac{k_a}{r^n}. \tag{2.42}$$

We obtain accordingly:

$$\frac{dS}{dt} = \frac{1}{[M]_0}\left\{G_M - \frac{4\pi V_m[M]_0 k_a}{v_0}S\int_0^\infty \frac{c(r)}{r^{n-2}}dr\right\}. \tag{2.43}$$

For $n = 2$, the integral in Equation 2.43 yields the total nanocrystal concentration $c_{tot}$. Since any radius dependence is eliminated, the supersaturation can settle for a time independent value of:

$$S = \frac{G_M v_0}{4\pi N_A[M]_0 k_a c_{tot}}. \tag{2.44}$$

Hence, when $n = 2$, growth occurs at constant supersaturation as long as $G_M$ is constant. In general, the integral in Equation 2.43 is proportional to the ensemble average $\langle 1/r^{n-2}\rangle$. In the case of a quasi-stationary supersaturation, we thus have:

$$S = \frac{G_M v_0}{4\pi N_A[M]_0 k_a c_{tot}\left\langle 1/r^{n-2}\right\rangle}. \tag{2.45}$$

When $n < 2$, $\langle 1/r^{n-2}\rangle$ will increase for an ensemble of growing nanocrystals while this average will decrease when $n > 2$. As a result, nanocrystals growth reduces the supersaturation when $n < 2$, while the supersaturation will increase by nanocrystal growth when $n > 2$.

*Simulated growth-only development*. To illustrate the role of the growth exponent in keeping up the supersaturation and promoting persistent nucleation, we implemented the kinetic reaction simulations for an existing concentration distribution under growth-only conditions. Neglecting monomer diffusion and desorption, we implemented the growth rate as (see Figure 2.19):

$$j_\mathrm{G} = \frac{\mathrm{d}r}{\mathrm{d}t} = V_\mathrm{m}[\mathrm{M}]_0 S k_\mathrm{g}(r). \tag{2.46}$$

The adsorption rate constant $k_\mathrm{g}(r)$ was taken as:

$$k_\mathrm{g}(r) = A\left(\frac{r_{\mathrm{c},0}}{r}\right)^n \theta(r-r_0). \tag{2.47}$$

Here, $\theta(r-r_0)$ is the Heaviside step function, which we implement with $r_0 = 0.5$ nm to prevent that simulations become unstable at radii close to 0.

As argued before, growth-only reaction development at constant monomer generation rate will concur with a decrease of the supersaturation only when the growth exponent $n < 2$. We analyzed this point by modeling the growth-only reaction development of an initial concentration distribution corresponding to a Gaussian centered around $r = 1.2$ nm with a $\sigma_r$ of 0.1 nm and a total concentration of 830 µM. Figure 2.20 depicts snapshots of the concentration distribution during this development for $n = 0$, 2, and 4. A growth exponent $n = 0$ results in a mere displacement of the distribution to larger radii with time, as expected for a radius-independent growth rate, while growth exponents $n = 2$ and $n = 4$ result in a marked focusing of the size distribution. More interesting is the variation of the supersaturation with time, which indeed drops for $n = 0$, stays put for $n = 2$ and increases for $n = 4$. These simulations thus confirm the general point that focusing with a growth exponent $n > 2$ will increase the supersaturation during growth-only reaction development; a mechanism that can prolong nanocrystal nucleation during an actual synthesis.

*Synthesis simulations under reaction-limited conditions.* The coupled differential Equation 2.34, Equation 2.37, and Equation 2.38 were implemented in COMSOL Multiphysics® 5.4. A one-dimensional simulation domain for the NC radius ranging from 0 to 4 nm was divided into 502 elements. From 0 to 0.2 nm, an absorbing boundary condition was implemented for computational stability. The nucleation rate $J_\mathrm{N}$ was implemented as a Gaussian function with a width of 0.02 nm, centered 0.3 nm

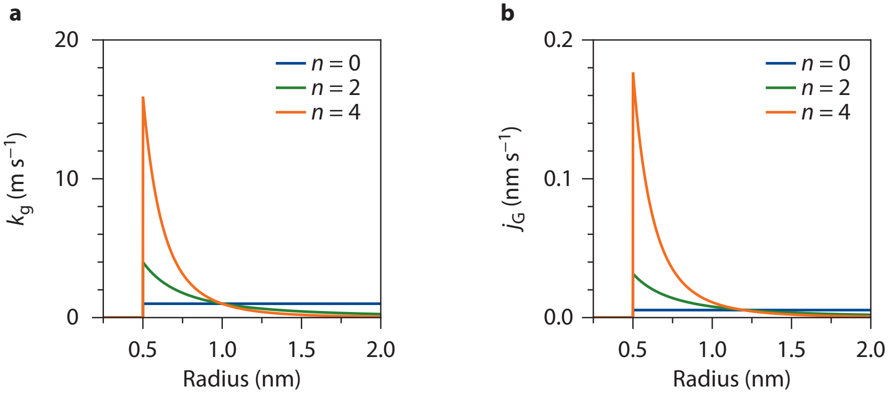

**Figure 2.19 |** (**a**) Adsorption rate constants $k_\mathrm{g}(r)$ for growth exponents as indicated used to simulate growth-only reaction development. (**b**) Shows the growth rates $j_\mathrm{G}$ for the same growth exponents after 1 ms. For the simulations we used $r_{\mathrm{c},0} = 1$ nm, $A = 1$ m s$^{-1}$, $V_\mathrm{m} = 3.3 \cdot 10^{-5}$ m$^3$ mol$^{-1}$, and $[\mathrm{M}]_0 = 4 \cdot 10^{-8}$ mol m$^{-3}$.

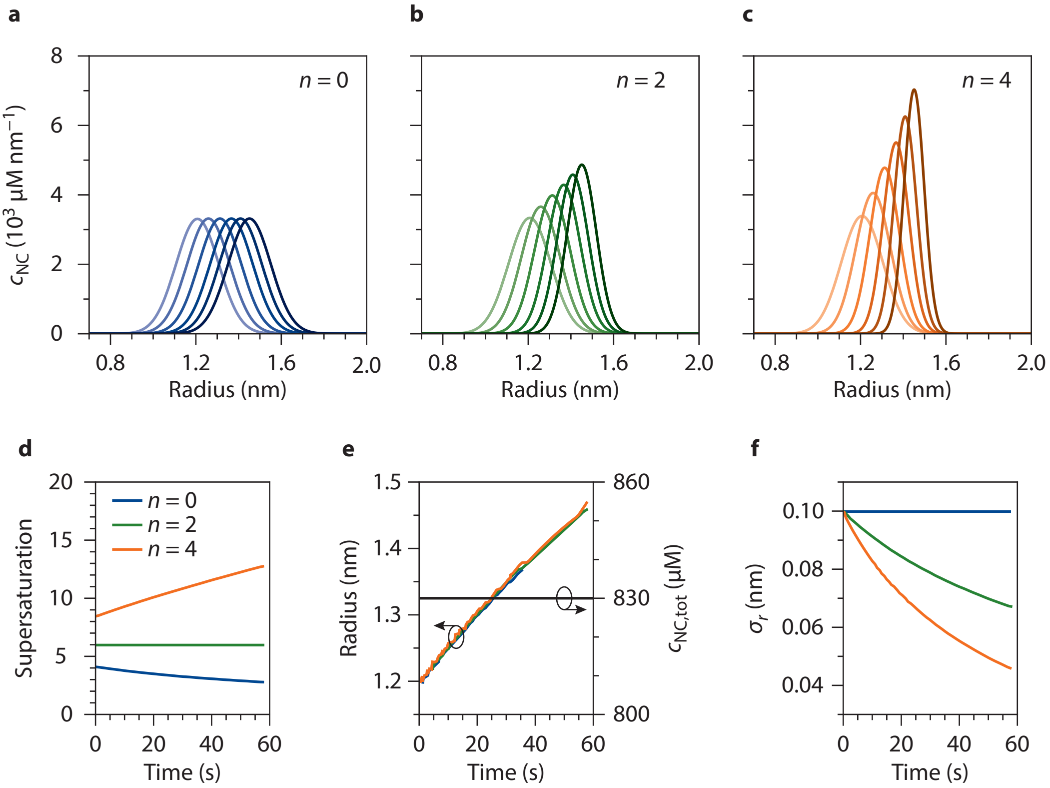

**Figure 2.20 |** (**a**–**c**) Evolution of a nanocrystal concentration distribution under growth-only conditions for different growth exponents as indicated. Size distribution focusing for *n* = 2 and *n* = 4 is clearly visible. (**d**) Simulated evolution of the supersaturation for the synthesis shown in panels **a**–**c**. (**e**) Simulated evolution of the average radius and the nanocrystal concentration. The concentration is the same for all three and therefore indicated with a black line. (**f**) Simulated evolution of the standard deviation on the average radius, clearly showing the impact of size focusing.

above the critical radius.

Table 2.2 provides an overview of the different values we used for the model parameters (see Equations 2.34–2.38). Measurable numbers were used for the monomer volume $v_0$, which was taken as the volume of a single spherical CdSe unit in the zincblende CdSe unit cell, the monomer diffusion coefficient $D$, which was chosen according to literature values for free oleic acid ligands obtained from diffusion NMR,[81] and the initial precursor concentration, which was taken in agreement with the cadmium concentration in the *in situ* SAXS experiment. Moreover, the first-order rate constant was set in line with the experimental reaction rate, whereas an initial precursor concentration was taken in agreement with the concentration of the limiting reagent in a real hot injection synthesis. Other parameter values, most notably the monomer solubility $[M]_0$, the surface tension $\gamma$, and the adsorption rate parameter $A$ were set to obtain simulated concentrations and radii in agreement with experimental reactions. Because of the nature of the reaction, the chemical meaning of these parameter values is limited. Since the monomer concentration is quasi-stationary, monomer consumption by growth depends on the product of the rate constant and the monomer concentration. Hence, while this monomer consumption rate can be measured, its factorization in a rate constant and a monomer concentration requires an independent determination of the monomer concentration. Such measurement, however, has remained elusive in the case of a hot injection synthesis. The result is that reaction simulations with somewhat different combination of parameter settings may yield a synthesis development with a similar outcome in terms of nanocrystal concentration and radius. Note that alternative reaction simulation methods will face similar issues when describing reactions in which precursor conversion is the rate determining step.

To implement superfocusing, the adsorption rate constant $k_\mathrm{a}(r)$ appearing in Equation 2.22 was taken as:

$$k_\mathrm{a}(r) = A\frac{(r_{\mathrm{c},0}+B)^n}{(r+B)^n}. \tag{2.6}$$

This expression ensures that regardless of the growth exponent $n$, the same rate constant is obtained at a radius $r = r_{\mathrm{c},0}$. This point is exemplified in Figure 2.21. In this way, the balancing between nucleation and growth is not changed artificially by a change in initial growth rate for different growth exponents. In addition, the small radial offset $B$ avoids the singularity at $r = 0$ that renders expressions such as Equation 2.24 difficult to implement numerically, while preserving the role of the growth exponent. As outlined in Table 2.2, we set $B$ fixed to 0.2 nm and took $r_{\mathrm{c},0}$ equal to 0.8 nm, in close agreement with the critical radius observed throughout the simulations. Finally, $A$ was chosen such that growth is limited by the surface reaction, not by monomer diffusion, and that in combination with all other parameters, the nanocrystal radius reaches ~2 nm at the end of the reaction; a number in line with the CdSe synthesis studied through *in situ* SAXS. Concentration snapshots in Figures 2.5a–c were taken at 3.16, 9.47, 28.34, 49.03, 84.83, 146.78, 253.96, 439.4, and 2275.8 s.

| Symbol | Parameter description | Value | Unit |
|---|---|---|---|
| $D$ | Monomer diffusion coefficient | $5\cdot10^{-10}$ | $\mathrm{m^2\,s^{-1}}$ |
| $v_0$ | Volume per CdSe unit cell | $5.59\cdot10^{-29}$ | $\mathrm{m^3}$ |
| $[\mathrm{M}]_0$ | Monomer solubility | $1\cdot10^{-7}$ | $\mathrm{mol\,m^{-3}}$ |
| $k_\mathrm{a}(\infty)$ | Rate constant for monomer adsorption, bulk limit | $4\cdot10^{-3}$ | $\mathrm{m\,s^{-1}}$ |
| $\gamma$ | Surface tension | 0.2 | $\mathrm{J\,m^{-2}}$ |
| $[\mathrm{P}]_\mathrm{i}$ | Initial precursor concentration | 27 | $\mathrm{mol\,m^{-3}}$ |
| $A$ | Adsorption rate parameter 1 | $4.5\cdot10^{-2}$ | $\mathrm{m\,s^{-1}}$ |
| $B$ | Adsorption rate parameter 2 | $2\cdot10^{-10}$ | m |
| $r_{\mathrm{c},0}$ | Adsorption rate parameter 3 | $8\cdot10^{-10}$ | m |

**Table 2.2 |** Parameter setting for the kinetic reaction simulations shown in Figure 2.5.

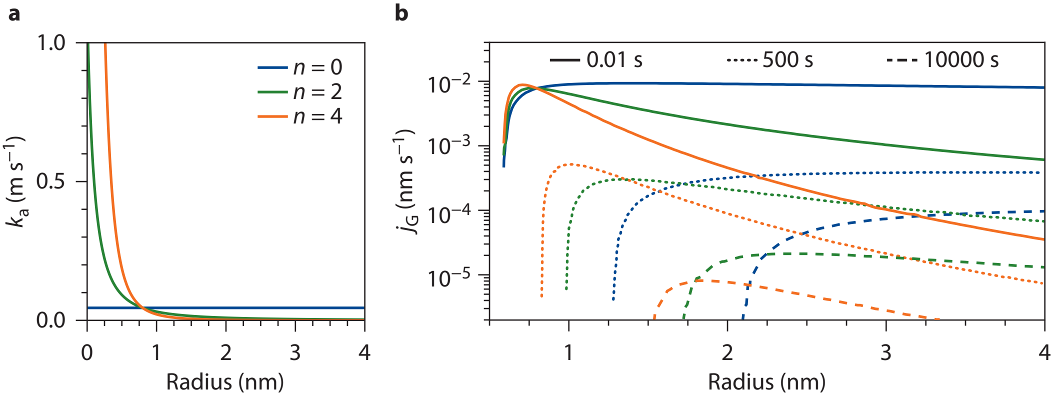

**Figure 2.21 |** (**a**) Representation of the rate constant of monomer adsorption $k_a$ for different values for the growth exponent as indicated, and $A$, $B$, and $r_{c,0}$ parameters as listed in Table 2.2. One sees that the same growth rate is obtained at $r = r_{c,0}$, regardless of the growth exponent. (**b**) Nanocrystal growth rate linked to the rate constant plotted in panel **a** at different moments during a reaction simulation. The identical growth rate at $r = r_{c,0}$ in the initial stage of the reaction and the pronounced difference in focusing as a function of the growth exponent are clearly visible.

*Nanocrystal concentration build-up*. In Chapter 2.4, we showed that the buildup of the nanocrystal concentration $n_{\mathrm{NC}}(t)$ can be approximated by a single exponential:

$$n_{\mathrm{NC}}(t) = n_{\mathrm{NC},\infty}(1 - \mathrm{e}^{-kt}). \tag{2.13}$$

In addition, we found that the experimental buildup of the nanocrystal concentration from *in situ* SAXS measurements fits this expression well (Figure 2.12). As shown in Figure 2.22, the same conclusion applies to the results of the reaction simulations. For the different choices of the growth exponent $n$, we find that Equation 2.13 yields a reasonable fit for the evolution of the nanocrystal concentration with time. Hence, while the description of nucleation through classical nucleation theory discards the underlying chemistry of the nucleation process, the modeling approach provides a good description of the net effect of nucleation, which is the appearance of growing nanocrystals.

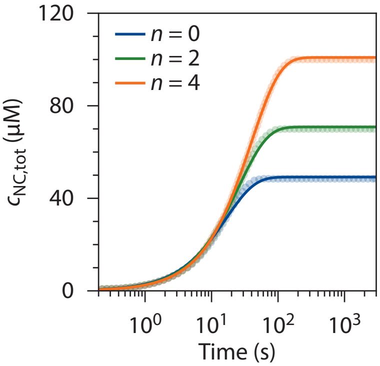

**Figure 2.22 |** (markers) Simulated nanocrystal concentrations for the different growth exponents as indicated and (lines) best fit to a single exponential build-up.

# Chapter 3

## *In situ* optical spectroscopy and X-ray scattering reveals evolution toward mature CdSe nanoplatelets by synergetic action of myristate and acetate ligands

The growth of two-dimensional platelets of the CdX family (X = S, Se, or Te) in an organic solvent requires the presence of both long- and short-chain ligands. This results in nanoplatelets of atomically precise thickness and long-chain ligand-stabilized Cd top and bottom surfaces. The platelets show a bright and spectrally pure luminescence. Despite the enormous interest in CdX platelets for optoelectronics, the growth mechanism is not fully understood. Riedinger *et al.* studied the reaction without a solvent and showed the favorable role for short-chain carboxylates for growth in two dimensions. Their model, based on the total energy of island nucleation, shows favored side facet growth *versus* growth on the top and bottom surfaces. However, several aspects of the synthesis under realistic conditions are not yet understood: Why are both short- and long-chain ligands required to obtain platelets? Why does the synthesis result in both isotropic nanocrystals and platelets? At which stage of the reaction is there bifurcation between isotropic and 2D growth? Here, we report an *in situ* study of the CdSe nanoplatelet reaction under practical synthesis conditions. We show that without short-chain ligands, both isotropic and mini-nanoplatelets form in the early stage of the process. However, most remaining precursors are consumed in isotropic growth. Addition of acetate induces a dramatic shift toward nearly exclusive 2D growth of already existing mini-nanoplatelets. Hence, although myristate stabilizes mini-nanoplatelets, mature nanoplatelets only grow by a subtle interplay between myristate and acetate, the latter catalyzes fast lateral growth of the side facets of the mini-nanoplatelets.

### Based on

J.C. van der Bok, P.T. Prins, F. Montanarella, D.N. Maaskant, F.A. Brzesowsky, M.M. van der Sluijs, B.B.V. Salzmann, F.T. Rabouw, A.V. Petukhov, C. De Mello-Donegá, D.A.M. Vanmaekelbergh, A. Meijerink

Journal of the American Chemical Society **144**, 8096–8105 (2022)

## 3.1 Introduction

Over the past decades, CdSe nanoparticles with a wide variety of shapes have been synthesized, for instance quantum dots (QDs),[8] nanorods,[82] and nanoplatelets (NPLs). The latter family is of particular interest because CdSe NPLs exhibit by far the narrowest-band emission of them all.[83] This remarkable property makes CdSe NPLs of interest for implementation in displays, as narrow-band emitters are needed to achieve higher energy efficiency and a wider color gamut.[84,85] The narrow band emission arises from the atomically accurate thickness of these quasi-two-dimensional nanoparticles resulting in strongly reduced inhomogeneous broadening of the emission spectra compared to QDs and nanorods.[86–88]

Implementation of NPLs in applications is only viable if high-quality NPLs are synthesized with high yield and post-synthesis purification steps are minimized. This can only be achieved if the formation of NPLs proceeds with a higher yield than is currently obtained with state-of-the-art synthesis protocols. The synthesis protocol typically used for CdSe NPLs is a solution-based method, similar to the first reported method,[89] where cadmium myristate and elemental selenium are heated in octadecene, and cadmium acetate is introduced in the reaction mixture at elevated temperature. Both CdSe QDs and NPLs form and must be separated by size-selective precipitation of the NPLs at a later stage.[66,69,90–93] This is often not clear from reports on the synthesis and optical properties of CdSe NPLs. The NPL yield, if reported, is low; Moreels *et al*. reported an increase in yield for 3.5 ML NPLs using an alternative propionic acid-based method, while the authors reported a chemical yield of 40% when they used the standard method of Ithurria and Dubertret.[93] Moreover, we find that, with the standard CdSe NPL synthesis, the concentration of NPLs formed is far below that of QDs. Platelets are thus formed as a side product, and the low reaction yield and necessity of a purification step form a severe drawback for commercial application.

An improved synthesis method can resolve these issues but requires a better understanding of the reaction mechanism. Even though the first reports on the syntheses of zinc blende CdSe NPLs date from 2008,[89,94] the formation mechanism of these NPLs is still under debate. Mechanisms proposed for zinc blende CdSe NPL formation include oriented attachment,[95–97] templated growth,[98] and continuous lateral growth.[69,90,99] Because experimental data on nanocrystal nucleation and the evolution of (an)isotropic growth under realistic synthesis conditions are lacking, consensus on the formation mechanism has not yet been established. In addition, it is not clear why both long-chain and short-chain ligands are imperative for NPL formation, what controls the growth of both isotropic QDs and 2D NPLs, and how acetate catalyzes the formation of large NPLs in the widely used CdSe NPL synthesis method pioneered by Ithurria and Dubertret.[89] In this study, we provide answers to these questions by studying CdSe QD and NPL nucleation and growth under realistic synthesis conditions.

It is challenging to study nanocrystal growth under reaction conditions that mimic the standard laboratory synthesis, and this has, so far, never been reported for CdSe NPLs. Previous studies on the growth of NPLs have either used *ex situ* analysis of aliquots taken during the reaction or *in situ* probing of the synthesis performed in capillaries.[90,95,99] The pitfalls of the first approach are the low temporal resolution and disturbance of the reaction by taking aliquots. Furthermore, aliquots are not fully representative of the reaction mixture, and collecting quantitative aliquots is challenging. The second approach suffers from higher size polydispersity than for a synthesis performed in a flask due to insufficient mixing of reagents and temperature inhomogeneity. Additionally, the difference in reaction volume and diffusion rates in a capillary compared to a reaction flask can influence the reaction. Moreover, and this is crucial for the CdSe NPL synthesis, no additional reactants can be introduced during the reaction when using capillaries.

To resolve these issues and to allow *in situ* probing of the NPL growth, we used a specially designed three-neck flask adapted from a design in the literature with an indentation in the glass (Figure 3.1a).[49,50] This indentation enables *in situ* UV–vis absorption spectroscopy and small-angle X-ray scattering (SAXS) studies because it reduces the pathlength from the entire flask (leading to saturation of absorption) to a few millimeters. Hence, the intensity of transmitted light and X-rays is sufficient to conduct meaningful spectroscopy and scattering experiments. The use of this adapted three-neck flask also enables studies under standard reaction conditions, *i.e.,* inert atmosphere, high temperatures, and sufficient stirring, identical to the conditions used in the practical synthesis of CdSe NPLs. Moreover, a powder or liquid injector can be installed on top of the flask to remotely add other precursors during the synthesis. Therefore, no adaptations need to be made to the synthesis method for CdSe NPLs, where cadmium acetate is added at elevated temperatures. The growth of high-quality CdSe QDs has previously been investigated for a hot-injection synthesis demonstrating the unique capabilities of this home-built setup for *in situ* monitoring of nanocrystal formation.[100]

Here, we first follow and quantify the formation of CdSe NPLs and QDs and show that the currently used synthesis method yields CdSe NPLs in a much lower concentration with respect to CdSe QDs. A separation step is required to obtain nearly homogeneous solutions of NPLs, and the chemical yield is low, typically less than 50%. Then, we report on *in situ* UV–vis absorption spectroscopy and SAXS measurements to monitor and quantify the formation of CdSe NPLs and QDs under different synthesis conditions with and without addition of acetate. By combining the results from both techniques, insights into the growth mechanism and the role of the ligands are obtained. Oriented attachment and lateral extension at the expense of QDs could be excluded as a formation mechanism. Our results show that both myristate and acetate play a pivotal role in the formation of NPLs. In the presence of long myristate ligands, a small concentration of mini-CdSe NPLs nucleates in addition to QDs, even without addition of acetate. In the continued absence of acetate, isotropic growth of QDs dominates. However, the addition of cadmium acetate triggers fast anisotropic growth of the mini-NPLs along the side facets which almost completely outcompetes further QD growth. The results are explained by a subtle interplay between long-chain myristate and short-chain acetate ligands in the formation and growth of QDs and NPLs. These insights can help adapt the synthesis to better control the interplay between ligands and favor the nucleation and growth of 2D NPLs to improve the yield of CdSe NPLs.

## 3.2 Results and discussion

The formation of NPLs was followed *ex situ* and *in situ* for the widely used synthesis method[89] for CdSe NPLs which is described in detail in Chapter 3.4. Briefly, it involves a solution-based reaction by heating Cd myristate and elemental Se in octadecene (ODE) typically to 240 °C with the addition of Cd acetate at a specific temperature. The home-built experimental setup for *in situ* measurements is depicted in Figure 3.1. The setup allows for the addition of cadmium acetate at any time and temperature during the synthesis without opening the reaction vessel. First, the optimal addition temperature was determined by adding cadmium acetate at 190, 220, or 240 °C. All experiments were performed in duplicate to verify reproducibility (Figure 3.6). The addition of cadmium acetate at 220 °C resulted in the formation of QDs (3.4 nm diameter[55]) and monodisperse 4.5 monolayer (ML) NPLs. Other temperatures yielded more than one NPL population or a higher fraction of QDs, as can be deduced from the *ex situ* absorption (Figure 3.6). For this reason, we focus here on the CdSe NPL

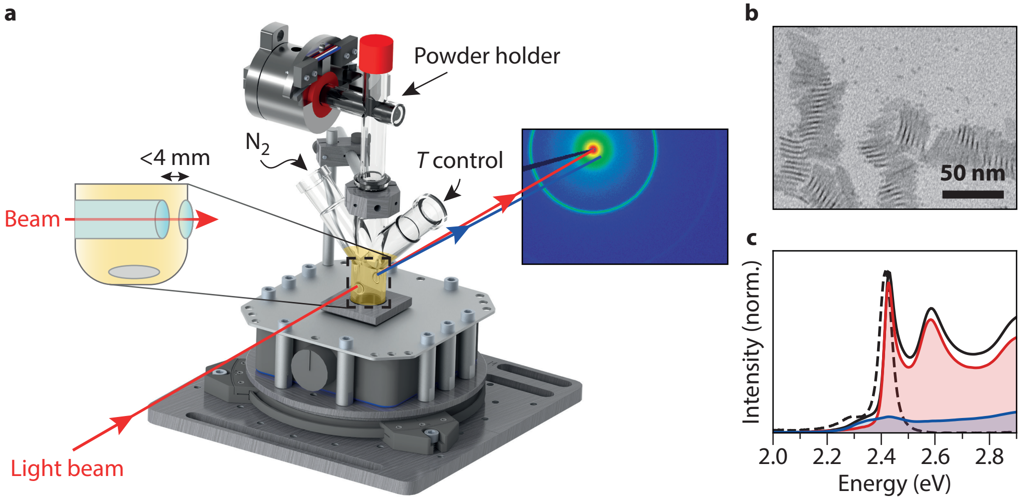

**Figure 3.1 |** (**a**) Schematic of the experimental setup for *in situ* absorption spectroscopy and X-ray scattering experiments, containing a magnetic stirrer, a custom-made flask, and a powder injector. A protective container and heating ribbon are omitted from the image for clarity. A Teflon™ rod with small cavity functions as a powder holder. This rod can be rotated remotely, upon which the powder falls into the reaction mixture. The flask can be connected to a nitrogen outlet. The reaction mixture is probed with either a collimated X-ray beam or UV–vis light beam. An indentation in the reaction flask reduces the pathlength to less than 4 mm. (**b**) TEM image of the product obtained during the *in situ* SAXS experiment with the addition of cadmium acetate at 220 °C. Both NPLs and QDs are formed. The NPLs agglomerate into long stacks. (**c**) Room-temperature absorption (solid) and emission (dashed) spectra of the same product confirm that both NPLs (2.43 eV) and QDs (~2.3 eV) are formed during the reaction. The contribution of the NPLs and QDs is shown in red and blue respectively. These spectra of the separate contributions were obtained after size-selective precipitation.

synthesis with the addition of cadmium acetate at 220 °C.

A transmission electron microscopy (TEM) image of the product using these reaction conditions (Figure 3.1b) shows the presence of both NPLs and QDs in the final product. The NPLs have a rectangular shape, typical for when anhydrous cadmium acetate is used,[101] with lateral dimensions of 27 ± 2.2 nm by 7.5 ± 1.2 nm (Figure 3.1b and Figure 3.8b). The NPLs tend to form large stacks. *Ex situ* absorption and emission spectra at room temperature are shown in Figure 3.1c. The contribution of the NPLs is highlighted in red and features the characteristic heavy- and light-hole transitions of 4.5 ML NPLs at ~2.4 eV (~510 nm) and ~2.6 eV (~480 nm).[89] The QDs produce a relatively weak absorption and emission feature near 2.3 eV. The contribution of the QDs to the total absorption is indicated in blue.

The fractions of QDs and NPLs in the absorption spectrum were determined with the absorption spectra obtained after size-selective precipitation. From this, we estimated (Figure 3.7) concentrations of QDs and NPLs in the reaction mixture of 2.9 μM and 0.35 μM, respectively. This is a rough estimate because the QD fraction still contains residual NPL absorption. Furthermore, the QD concentration is underestimated by the scattering of stacked NPLs at 2.35 eV. This scattering also affects the absorbance at 300 nm. Nevertheless, this rough estimate reveals that the NPL concentration is an order of magnitude lower than the QD concentration. This may seem surprising considering the weak absorption feature of the QDs in Figure 3.1c but it is a consequence of the much lower QD extinction coefficient due to the difference in the volume (21 $\text{nm}^3$ for the QDs compared to 263 $\text{nm}^3$ for the NPLs) and intrinsic absorption coefficient $\mu_\text{i}$ ($2 \cdot 10^5\ \text{cm}^{-1}$ compared to $6 \cdot 10^5\ \text{cm}^{-1}$) at a wavelength of 300 nm.[91,102,103] Note that even though the concentration of NPLs is about ten times lower, the CdSe yield for the QDs and NPLs is similar due to the large volume difference. The difficulty in extracting the absolute concentrations and the relatively low NPL concentration stresses the importance of exploring the reaction mechanism using *in situ* studies.

The temperature and time evolution of the absorption spectra and SAXS data of the *in situ* measurements are shown in Figures 3.2a,b. The colors reflect the time relative to the cadmium acetate addition at $t = 0$ min, as is specified by the legend on the left. Both data sets show the formation of QDs starting from ~170 °C (dark blue) by the increase in UV absorption and scattering. The $q^0$ slope extending to 1 $\text{nm}^{-1}$ and shape of the early X-ray scattering patterns match the form factor of spherical particles (Figure 3.12), *i.e.*, the QDs. These QDs grow over time shifting the absorption maximum to lower energies and slightly shifting the scattering minimum to smaller $q$-values (compare the dark blue and dashed scattering pattern around $q = 3\ \text{nm}^{-1}$). These features are consistent with the theoretical scattering patterns for growing QDs, but a minor contribution of small anisotropic nanostructures cannot be excluded.

The evolution of the QD growth in the scattering patterns is shown in more detail in Figure 3.2e. A shallow minimum is visible at $q \sim 3\ \text{nm}^{-1}$ and shifts to $\sim 2.8\ \text{nm}^{-1}$ over time. The minimum is shallow because of the polydispersity in size. The intense scattering at $q < 0.2\ \text{nm}^{-1}$ in the first few frames

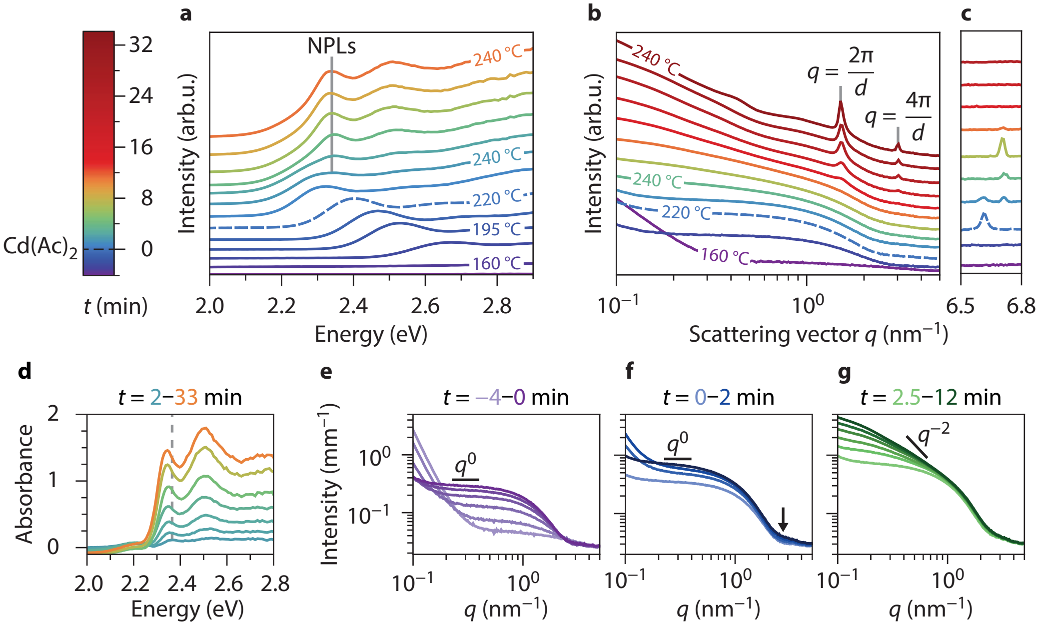

**Figure 3.2 |** Absorption spectra (**a**) and scattering patterns (**b** and **c**), shifted for clarity, obtained *in situ* during the synthesis of CdSe NPLs. The colors of all curves correspond to the times indicated in the legend. Temperature increases from ~160 to 240 °C and is then kept at 240 °C. Cadmium acetate is added at 220 °C (dashed line, $t = 0$ min). Blue to cyan absorption spectra show growth of QDs. The absorption features of the NPLs (2.35 eV) become visible shortly after addition of the acetate. The SAXS data also indicate growth of isotropic particles (purple to blue, scattering intensity scaling as $q^0$), followed by growth of NPLs after addition of acetate (blue to red, $q^0$ regime disappears). Structure factor peaks are observed, due to stacking of the formed NPLs ($d = 2\pi/q = 4.2$ nm). In C, the atomic scattering peak of solid cadmium acetate can be observed. The peak shifts around 230 °C, probably due to a change in the crystal structure. After ~10 min at 240 °C the acetate is completely dissolved. (**d**) The QD absorbance (a spectrum at 230 °C) is subtracted from the data in **a**. The resulting spectra show the heavy- and light-hole transition of 4.5 ML NPLs at 2.35 and 2.52 eV, respectively, shifted to lower energies compared to room temperature due to temperature effects (see text). A dashed gray line is added to emphasize the shift of the absorption maximum in the first few frames due to quantum confinement in the lateral dimensions. (**e**) SAXS patterns until addition of the acetate. (**f**) SAXS patterns shortly after addition of acetate. The scattering increases at $q = 2$–$3$ nm$^{-1}$, but still, a $q^0$ regime is observed. (**g**) SAXS patterns 2.5–12 min after the acetate addition, reflecting particle growth at 240 °C. The slope at $q < 1$ nm$^{-1}$ becomes steeper than the previous $q^0$ scaling, indicating growth of anisotropic particles.

is caused by the scattering of undissolved μm-large selenium particles (Figure 3.11f). The additional scattering reduces when the selenium dissolves and is not significant anymore at $t \approx 0$ min. No lamellar phase is observed in the SAXS data when nanoparticles start to form. The cadmium myristate dissolves around 100 °C (Figure 3.11a), well before the onset of nucleation. This rules out templated NPL growth on a lamellar Cd myristate phase and is consistent with other reports.[69,99,104]

The absorption spectra in Figure 3.2a show that after the addition of cadmium acetate at 220 °C (dashed), the existing QDs continue to increase in size over the first minute (*i.e.*, the absorption feature shifts to lower energy). Within one minute after the acetate addition, a new absorption feature appears at 2.35 eV, quickly outgrowing the QD absorption. In the scattering data, the growth of small particles is apparent from the increase in intensity at $q = 2–3\ \mathrm{nm}^{-1}$ (Figure 3.2f, arrow). The slope at $q < 1\ \mathrm{nm}^{-1}$ still scales with $q^0$, typical for isotropic particles. After several minutes (Figure 3.2b, yellow and orange), the slope starts to deviate from $q^0$ which shows that anisotropic particles have formed. The slope is not equal to a $q^{-2}$ slope expected for 2D materials (Figure 3.2g) because the scattering pattern originates from QD and NPL scattering resulting in a slope between $q^0$ and $q^{-2}$.

To monitor the growth of the NPLs, the QD contribution was subtracted from the absorption spectra. The resulting spectra are shown in Figure 3.2d and clearly contain the heavy- and light-hole transitions characteristic of 4.5 ML NPLs (at 2.35 and 2.52 eV, respectively). Note that at elevated temperatures, the peak position shifts to lower energies, and the peak width increases compared to room temperature (Figure 3.1c). The peak maximum shifted from 2.43 eV at room temperature to 2.35 eV at 240 °C, corresponding to a shift of 0.37 meV $°\mathrm{C}^{-1}$, which matches values of 0.31–0.44 meV $°\mathrm{C}^{-1}$ reported for the emission of 4.5 ML NPLs.[105,106]

The intensity of the NPL absorption in Figure 3.2d increases over time. In addition, the absorption maximum shifts noticeably between the first few displayed spectra (light blue to green), more than expected from temperature effects. Both the increase in intensity and the shift in position are evidence of the growth in the NPL lateral dimensions.[107] At first, the still laterally small NPL dimensions lead to three-dimensional confinement of the exciton. As the NPLs grow, the lateral dimensions quickly exceed the confinement regime, and consequently, the peak does not shift any further. The small fluctuations of the absorption maxima (green to orange) are caused by temperature fluctuations, varying between 235 and 245 °C.

Overall, the evolution of absorption spectra in the different synthesis stages is consistent with the scattering data. Additionally, the scattering data show the stacking of NPLs after ~12 minutes as structure factor peaks begin to appear at $q = 1.5\ \mathrm{nm}^{-1}$ and $q = 3.0\ \mathrm{nm}^{-1}$.[108] These $q$-values are consistent with linear stacks of NPLs with a center-to-center distance as $d = 2\pi n/q = 4.2$ nm (with $n = 1$ or 2). This distance is set by twice the length of the myristate ligand plus the thickness of a 4.5 ML NPL (1.3 nm).[109] Thus, the length determined for the myristate ligands is 1.45 nm, slightly shorter than the 1.7 nm expected for myristate with a fully extended carbon chain.[110] This means that the ligands are not fully extended, or they slightly interpenetrate.

The scattering data further reveal the presence and slow dissolution of solid cadmium acetate crystallites. The reappearance of strong scattering at $q < 0.2\ \mathrm{nm}^{-1}$ at $t = 0$ min in Figure 3.2e and the appearance of a peak in the scattering pattern at $q = 6.63\ \mathrm{nm}^{-1}$ (Figure 3.2c) indicate the presence of undissolved cadmium acetate crystallites (Figure 3.11e). The peak's intensity decreases at 230 °C, and a new peak appears at $q = 6.71\ \mathrm{nm}^{-1}$. This shift is probably caused by a change of the cadmium acetate crystal structure.[111,112] The signal disappears completely after ~10 min at 240 °C. Similar behavior is observed when cadmium myristate and cadmium acetate are heated without the presence of selenium (Figure 3.11d). When cadmium acetate is heated in the absence of cadmium myristate, the peak in Figure 3.2c does not disappear until a temperature of 255 °C (Figure 3.11e), *i.e.*, the melting temperature of cadmium acetate.[111] We conclude that the dissolution of cadmium acetate is assisted by reaction with cadmium myristate forming $\mathrm{Cd(Ac)}_{2-x}\mathrm{(Myr)}_x$. These results show that NPLs start forming when cadmium acetate is still, at least partly, present as a solid (compare lemon-colored lines in Figures 3.2a,d with that in Figure 3.2c).

The size, aspect ratio, and concentration of the QDs and NPLs can be extracted by fitting the SAXS data in Figure 3.2b, this makes it possible to follow the formation of QDs and NPLs over time. The scattering patterns were carefully corrected for background effects and analyzed to obtain information on the size and shape evolution of nanostructures in the reaction mixture, as described in detail in Chapter 3.6. This analysis gave a NPL aspect ratio of 1:3 and a concentration of 0.6 μM. The evolution of size and concentration for the QDs is shown in Figure 3.3a in blue and orange, respectively. The length of the largest lateral dimension $L$ of the NPLs is shown in Figure 3.3b in red. The scattering patterns were fitted until the NPLs started to stack at $t = 12$ min. The oscillation in the data is caused by a temperature fluctuation during the synthesis.

Figure 3.3a shows that the QD concentration quickly increases to ~11 μM during the heat-up from 170 to 220 °C and remains constant afterward. The QD diameter increases during this period as well. In the first 1.5 min following cadmium acetate addition, the QDs continue growing from 3.16 to 3.36 nm, consistent with the analysis of the absorption spectra discussed earlier. After 1.5 min, the QD growth stops.

Immediately after the cadmium acetate addition, the lateral dimensions of the NPLs grow, as shown in Figure 3.3b. Within half a minute after the addition of cadmium acetate, NPLs with lateral dimensions of 5.0 by 1.7 nm are visible. This indicates that small NPLs are present before the acetate addition (*vide infra*) but not easily observed because the scattering is negligible compared to the QD scattering (Figure 3.14b). The edge lengths rapidly increase after acetate addition to 26 by 8.7

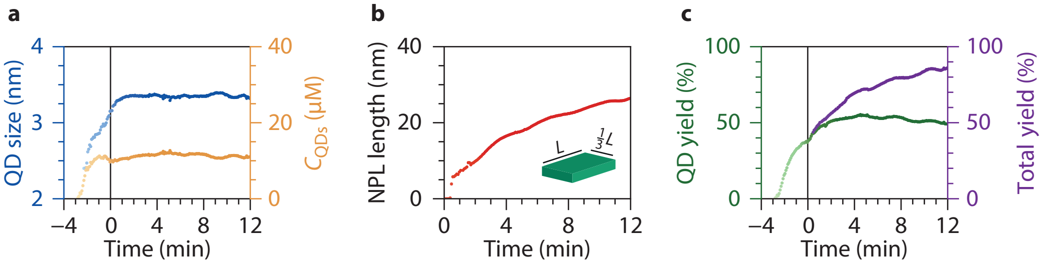

**Figure 3.3 |** Fit results extracted from the SAXS patterns in Figure 3.2b. (**a**) QD diameter (blue) and QD concentration (orange). (**b**) Length *L* of the longest edge of the NPLs. The aspect ratio of the lateral dimensions is 1:3. *L* could be underestimated in the first few minutes because the concentration of the NPLs was kept at a constant value of 0.6 μM during the fitting procedure. (**c**) Percentage of CdSe consumed by the formed QDs in green and by the QDs and NPLs in purple.

nm after 12 min, just before the NPLs start to stack. TEM analysis gives lateral dimensions of 27 ± 2.2 by 7.5 ± 1.2 nm (Figure 3.1b and Figure 3.8b), which matches the SAXS results and confirms the reliability of the fitting procedure. The constant concentration of QDs after the cadmium acetate addition indicates that NPL formation is not due to attachment of seed QDs. Moreover, the diameter of the QDs is already 3.16 nm when cadmium acetate is added, by far exceeding the NPL thickness of 1.3 nm. The constant QD radius and concentration show that the growing NPLs do not consume existing QDs, but the CdSe monomers that are still present in the reaction mixture. The CdSe yield of the reaction, calculated from the incorporated amount of selenium in the nanoparticles (Chapter 3.7) with respect to the selenium added in the reaction mixture, as shown in Figure 3.3c supports this. The available CdSe units are far from depleted at $t = 0$ min: the total yield (purple) is only 40%. Over the 12 min following cadmium acetate addition, an additional 10% of the available CdSe is incorporated in the QDs. Simultaneously, 40% of the CdSe is incorporated in the NPLs. Hence, the growth of the NPLs is much faster than that of the QDs after the addition of cadmium acetate.

Additionally, the 10% increase in yield due to QD growth indicates that the QDs do not dissolve in favor of NPL growth. The QDs are an undesired by-product of the reaction and consume roughly half of the available precursors. The concentration of QDs (~11 μM) is much higher than the NPL concentration (0.6 μM), as was also estimated from the *ex situ* absorption spectrum. Although most QDs formed before cadmium acetate addition induces the growth of NPLs, they still form when cadmium acetate is added much earlier (Figure 3.8a), and such procedures produce 3.5 ML NPLs instead of 4.5 ML NPLs.

To study the role of cadmium acetate further, we compare the results discussed above with a synthesis using the same reaction conditions but without the addition of cadmium acetate. The *in situ* absorption spectra and SAXS patterns are shown in Figures 3.4a,b, respectively. They show, up until 220 °C, a similar QD evolution compared to the results in Figures 3.2a,b. In contrast to the experiment of Figure 3.2, we add no acetate at 220 °C at $t = 0$. Nevertheless, a new absorption feature still arises around $t = 2$ min. The feature, labeled with “NPLs” in Figure 3.4a, is first visible at 2.34 eV (light blue) and later shifts to 2.28 eV (green). Clearly, a mixture of two types of nanoparticles still forms in the absence of acetate (Figure 3.19).

The presence of two populations of nanoparticles is evident in the *ex situ* absorption and emission spectra as well (Figure 3.4c). The luminescence and absorption spectra at room temperature show, in addition to the QD absorption and emission, a peak of a second population of nanoparticles at 2.47 eV. These two populations could be separated with size-selective precipitation. The high-angle annular dark-field scanning transmission electron microscopy (HAADF-STEM) image in Figure 3.4d reveals that the two species of nanoparticles are spherical QDs and small anisotropic nanoparticles. The anisotropic nanoparticles appear as rod-like structures in the HAADF-STEM image with the largest lateral dimension equal to ~5 nm.

These nanoparticles stack during the synthesis, which results in the structure factor peaks in the

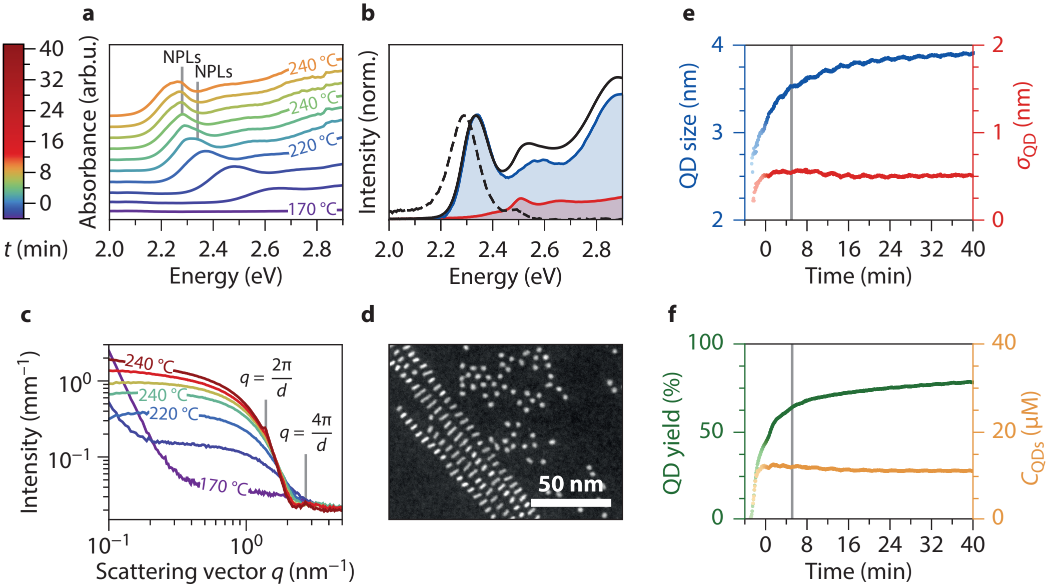

**Figure 3.4 |** Absorption spectra (**a**) and scattering patterns (**b**) of *in situ* experiments when no acetate is added to the reaction mixture. In **a**, the spectra are shifted in intensity for clarity. The weak absorption features of 4.5 mini-NPLs at 2.34 eV and 5.5 ML mini-NPLs at 2.28 eV are labeled with NPLs for clarity. Features shift to lower energies compared to room temperature due to temperature effects. The structure factor peaks of the stacked 5.5 ML mini-NPLs are labeled in **b** (d = 4.5 nm). (**c**) Absorption (solid) and emission (dashed) spectra at room temperature of the product obtained during the *in situ* SAXS experiment. Next to QD absorption and emission (2.3 eV), also a second population of nanoparticles is present: mini-NPLs (2.47 eV). The blue and red curves represent contributions from the supernatant (QDs, blue) and precipitate (predominantly mini-NPLs, red) after selective precipitation. (**d**) HAADF-STEM image of the reaction product showing stacked mini-NPLs and QDs. (**e**) Diameter (blue) and polydispersity (red) of the QDs extracted from fitting the SAXS data in **b**. (**f**) QD concentration during the reaction (orange) and the reaction yield (green). This yield only accounts for the CdSe consumed by the QDs. The total yield, including the mini-NPLs, is ~3% higher than the yield in **f**. The gray line in **e** and **f** at ~5 min indicates when the stacking of the mini-NPLs starts to contribute to the total scattering.

SAXS data at $q = 1.5$ nm$^{-1}$ and $q = 3$ nm$^{-1}$. These $q$-values are due to stacking at a center-to-center distance of 4.5 nm, which is larger than the center-to-center distance found above for the stacked 4.5 ML NPLs (Figure 3.2b) by 0.3 nm. This difference matches the thickness of one CdSe monolayer, *i.e.*, half a unit cell. The anisotropic nanoparticles are thus likely “mini-NPLs” of 5.5 ML thickness. They appear as rod-like structures on (S)TEM images and in a HAADF-STEM tilt series (Figure 3.9) because the shortest lateral dimension is not much larger than the thickness of the mini-NPLs, when assuming a similar aspect ratio as that of the large NPLs (3:1).

Heating the reaction mixture to 240 °C results in the formation of 5.5 ML mini-NPLs. Mini-NPLs with a thickness of 4.5 ML can also be synthesized by lowering the final reaction temperature to 190 °C instead of 240 °C. Structure factor peaks at the same position as in Figure 3.2b were observed in

SAXS data obtained using these reaction conditions (Figure 3.18). In the reaction with acetate, the 4.5 ML mini-NPLs rapidly grow to form 4.5 ML NPLs. Without acetate, 5.5 ML mini-NPLs form upon heating to 240 °C. This temperature dependence suggests that the two absorption features in Figure 3.4a, labeled with NPLs, correspond to mini-NPLs with a thickness of 4.5 ML formed below 240 °C (2.34 eV, slightly higher energy than that of large 4.5 ML NPLs) and 5.5 ML mini-NPLs formed after a temperature of 240 °C is reached (2.28 eV). Note that the stronger confinement for the small lateral dimension of the 5.5 ML mini-NPLs results in stronger temperature dependence of the absorption maximum, shifting it to a higher energy (2.47 eV) at room temperature compared to the thinner but larger 4.5 ML NPLs (2.43 eV).

The size, polydispersity, and concentration of the QDs and mini-NPLs and the reaction yield were extracted from the SAXS data as well (Chapter 3.6).[113] The form factor of a disk was used to approximate the mini-NPLs shape. An average radius for the mini-NPLs of 3.5 nm was obtained with 4.5% polydispersity and a concentration of ~0.25 μM. The fit results for the QDs are shown in Figures 3.4e,f. The evolution of the QD concentration in the cases with and without cadmium acetate is very similar, (orange, Figure 3.3a and Figure 3.4f). The polydispersities are also similar, reaching a value of ~0.5 nm after an initial increase. However, the increase in QD size over time is strikingly different between the experiments. While acetate addition leads to stagnating QD growth shortly after $t = 0$ (Figure 3.2), the growth continues until a final size of 3.8 nm at $t = 10$ min in the absence of acetate. The 0.4 nm difference in final size shows that without cadmium acetate, more CdSe precursor is available for QD growth. In other words, the presence of cadmium acetate results in precursor consumption by the growth of the second population of nanocrystals, *i.e.*, the NPLs.

The same conclusion can be drawn by comparing the reaction yields with and without the addition of cadmium acetate. The yield of the reaction without cadmium acetate is given in Figure 3.4f in green. The yield in Figure 3.4f accounts only for the CdSe incorporated in the QDs and can therefore directly be compared to the corresponding results of the experiment with acetate (green in Figure 3.3c). Similar values for the yield are obtained until $t = 0$ min (38%). However, without the addition of cadmium acetate, the final CdSe consumption by QDs is much higher (70% compared to 50% after 12 min). Without acetate, the anisotropic particles (mini-NPLs) take up 3% of the total CdSe content (Chapter 3.7), compared to 40% CdSe incorporated in NPLs in the experiment with acetate. We verified the yield derived from the SAXS results by inductively coupled plasma optical emission spectrometry (ICP-OES) analysis. Yields of 47 ± 1.5% and 75 ± 1% were obtained with ICP-OES at reaction times corresponding to $t = 10$ minutes and $t = 30$ minutes in Figure 3.4f, respectively. This matches well with the SAXS results. The results from optical absorption, SAXS, and ICP-OES are consistent and show that the contribution of the stacked and individual mini-NPLs to the total yield for the synthesis without acetate is low.

We learn from these experiments that the addition of acetate strongly enhances the growth rate of already existing anisotropic particles (mini-NPLs) but not the growth rate of the QDs. The presence of acetate promotes the lateral growth of already existing NPLs so strongly that almost no reactants are used in the further growth of the QDs. The question arises if acetate also affects the nucleation of mini-NPLs *versus* small QDs in the initial stage of the reaction. From the fit, we estimate a mini-NPL concentration of 0.25 μM without and a NPL concentration of 0.6 μM with acetate. The 0.25 μM is a lower limit as only the stacked mini-NPLs contribute, while the 0.6 μM is a more reliable estimate of the total concentration of NPLs. Both concentrations of (mini)-NPLs are very small compared to the QD concentration. Hence, acetate does not strongly affect the initial ratio between QDs and mini-NPLs, but its role is to favor very strongly the lateral growth of already existing mini-NPLs.

Figure 3.5 gives a schematic overview of the reaction mechanism based on the data discussed in this work. In the early stage of the reaction, both QDs and mini-NPLs with small lateral dimensions form. The mini-NPLs have an order of magnitude lower concentration than the QDs. Once formed, the mini-NPLs are likely stabilized by strong Van der Waals interactions between the long alkyl chains of the ligand layers on the top and bottom facets. The stability of the myristate layers on the large facets is evidenced by the center-to-center distances observed for (mini-)NPL stacks by *in situ* SAXS. Even at high temperatures, these distances are consistent with a spacing created by slightly interpenetrating myristate layers. Furthermore, a higher concentration of long-chain ligands results in increased NPL absorption relative to QD absorption.[104]

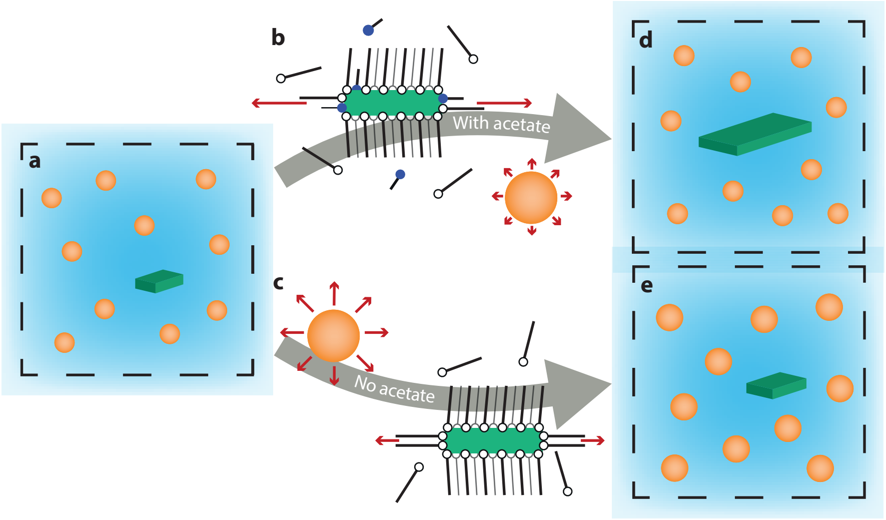

**Figure 3.5 | Schematic overview of the CdSe NPL growth mechanism.** (**a**): Nanoparticles nucleate and grow. An order of magnitude more QDs are formed than NPLs. Middle (**b**): The addition of acetate results in faster monomer consumption. With the reaction conditions used here, most monomers are consumed by growth of the small facets of the NPL (red arrows). As a result, the NPLs grow laterally, and the QDs do not grow much (**d**). The concentration of QDs and NPLs is unaffected by the addition of an acetate. Middle (**c**): If no acetate is added, both QDs and mini-NPLs grow with a comparable monomer consumption (red arrows). This way the NPLs remain small, and slightly larger QDs are obtained compared to with the addition of acetate (**e**).

When solid cadmium acetate crystallites are added to the reaction mixture, the solution concentration of cadmium acetate is initially low as the crystallites dissolve slowly. As the concentration of acetate in solution increases, the monomer consumption by the small facets of the NPL starts to outcompete the monomer consumption by the QDs. Importantly, our work demonstrates that the conditions under which NPLs grow are not required to make NPLs nucleate. Indeed, we observe mini-NPLs even if we do not add acetate to the reaction and at approximately the same final concentration as for the large NPLs. On the other hand, the formation of mini-NPLs seems to be disrupted if too much acetate is available too early in the reaction. For example, when cesium acetate (melting point 195 °C) instead of cadmium acetate is added at 190 °C while heating to 240 °C, only 3D particles are formed (Figure 3.10a). Under these conditions, the concentration of acetate in solution is too high immediately after addition. On the other hand, NPLs are formed when cesium acetate is added at 190 °C without further heating to 240 °C (Figure 3.10b). The results are in line with previous reports on acetates catalyzing NPL growth.[89] All reported acetates have melting points well above 190 °C (see Chapter 3.4). Note that the addition of different acetates also affects the lateral shape of the NPLs. Likely other factors next to the melting point, such as the reactivity of the cation acetate, also affect the growth of the NPLs.

The model proposed by Norris *et al.*[69,114] explains anisotropic 2D growth of (mini-)NPLs by a lower activation energy for island nucleation on side facets compared to top and bottom facets. This activation energy is determined by the volume, area, and line energies of zinc blende CdSe. The synthesis condition used to construct the model, *i.e.*, NPLs formed in a melt of cadmium acetate and selenium, deviates significantly from the solution-based synthesis studied here. Furthermore, the work of Norris *et al.* considers constant reaction conditions, while in our and standard experiments, the conditions are changed midway by addition of cadmium acetate. The presence of acetate affecting the CdSe monomer consumption stresses the importance of including the effect of the surfactants on anisotropic growth.

The effect of cadmium acetate addition can be included in a NPL growth model as a drop in the values for area, line, and volume energies. Lowering any of these energies results in a decrease in the activation energy for "island nucleation", *i.e.*, the formation of a new monolayer on an existing facet, and hence an acceleration of crystal growth. With the right combination of energy values, island nucleation rates on the narrow facets outpace those on the top and bottom facets. The fastest growing facets can consume available monomers so quickly that growth on other facets effectively stops. Interestingly, further lowering area, line, and volume energies decreases the difference in the activation energies between narrow and large facets. This explains why the addition of too much acetate early in the reaction results in isotropic growth, as it decreases the anisotropy in growth rates.

The middle part of Figure 3.5 gives a molecular picture of the potential effects of cadmium acetate on the volume, surface, and line energies. The volume energy may become more negative when cadmium acetate is present in the reaction mixture by lowering the solubility of the cadmium precursor. The surface and line energies decrease due to changes in the ligand coverage of the NPL by exchanges of myristate ligands with acetate. The reaction rate for all NPL and QD facets will likely increase. However, as the activation energy for island nucleation on narrow NPL facets is the lowest, the effective monomer consumption by the narrow facets of the NPL will outcompete the monomer consumption by the QDs and large facets (red arrows). A higher ligand exchange of the side facets by short acetate ligands, due to weaker binding sites at the edges,[66] may further enhance the 2D growth by lowering the steric barrier for monomer attachment on side facets.

The formation of large NPLs, using the standard CdSe NPL reaction protocol, thus ultimately relies on the synergy between cadmium myristate and cadmium acetate ligands, where the cadmium myristate reduces isotropic growth by stabilizing mini-NPLs at the early stages of the reaction, and addition of cadmium acetate results in faster growth on the small side facets. The molecular picture that we present is in line with the model of Norris, which emphasizes that an appropriate balance of surface and line energies is required for two-dimensional growth. When no acetate is added, both the QDs and mini-NPLs grow with a comparable monomer consumption (Figure 3.5c). This can be deduced from the similar ratio between the concentrations and contributions to the total yield (11 μM compared to 0.25 μM and 75% yield compared to 3% yield after 12 min). The presence of acetate favors lateral growth of the platelets and, by precursor consumption, impedes further growth of the QDs. Acetate addition determines the sizes but not the final concentrations of the two types of particles (Figures 3.5d,e).

## 3.3 Conclusion

With our home-built setup, we were able to probe *in situ* the formation of CdSe NPLs with (or without) the addition of cadmium acetate for the standard NPL synthesis under realistic reaction conditions. Analysis of *in situ* absorption and scattering experiments shows that both isotropic and anisotropic particles form at an early stage of the reaction even without short-chain ligands. NPLs with large lateral dimensions (~27 by 7.5 nm) are formed due to a synergy between the long myristate ligands stabilizing top and bottom facets of the 2D structures and short acetate ligands that promote fast growth of the NPL side facets but do not affect the NPL concentration. The concentration of NPLs (~0.6 μM) is low compared to the QDs (~11 μM), which are always formed as a prominent and undesired side product. These QDs are responsible for a low NPL reaction yield and have to be removed using size-selective precipitation. The new insights in the mechanism of CdSe NPL formation can help improve the synthesis conditions (such as type and concentration of ligands, reaction temperature, etc.) to optimize the mini-NPL *versus* QD formation and NPL growth to improve the NPL yield.

## 3.4 Methods

*Chemicals.* 1-butanol (anhydrous, 99.8%), 1-octadecene (ODE, 90%), cadmium(II) acetate anhydrous (99.995%), cadmium(II) nitrate tetrahydrate (99,99%, trace metal basis), cesium(I) acetate (99.999%, trace metal basis), hexane (anhydrous, 95%), methanol (anhydrous, 99,8%), methanol (hydrous, 100%), oleic acid (OA, 90%), sodium myristate (≥99%), and toluene (anhydrous, 95%) were all purchased from Sigma-Aldrich®. Selenium powder (-200 mesh, 99.999%) was purchased from Brunschwig Chemie. ODE and OA were degassed at 100 °C under vacuum for 3h and the other chemicals were used without further purification.

*Cadmium myristate precursor.* Cadmium myristate precursor was prepared by dissolving 1.23 g cadmium nitrate tetrahydrate (4 mmol) in 40 mL methanol and 3.13 g sodium myristate (12.5 mmol) in 250 mL methanol. The cadmium nitrate solution was added to the sodium myristate solution while stirring. A white precipitate was visible. The precipitate was vacuum filtrated using a Büchner flask and rinsed with 1 L of methanol (hydrous). The cadmium myristate was dried overnight under vacuum to remove methanol and water.

*NPLs synthesis.* 4.5 ML CdSe NPLs were synthesized as reported by Ithurria *et al.*[90] For the *in situ* measurements, the synthesis was scaled down by a factor of two. 85 mg of cadmium myristate (0.15 mmol), 6.0 of mg elemental selenium (0.075 mmol) and 7.5 mL of ODE were loaded in a specially designed three-neck flask and degassed under vacuum at room temperature for 1 h. After degassing, the mixture was put under a nitrogen atmosphere, and the powder injector (Figure 3.1a) was attached with 26 mg of cadmium (0.11 mmol) acetate in the powder holder. The system was flushed three times by applying a vacuum or nitrogen flow. Then, the mixture was heated to 240 °C with a rate of 15 °C $\text{min}^{-1}$ using a heating ribbon around the flask. For the *in situ* absorption measurements, a transparent medium was needed to align the flask with the UV–vis light beam. Therefore, an additional heating step to ~110 °C, before heating to 240 °C, was implemented to melt and dissolve the cadmium myristate.

A series of experiments was conducted to investigate the role of acetate in the formation of CdSe NPLs. In the various experiments, the flask with the reaction mixture was heated to 240 °C. Cadmium acetate was added at 190, 220, or 240 °C by rotating the powder holder. Furthermore, an experiment without the addition of acetate was performed. During the reaction, UV–vis absorption spectra or X-ray scattering patterns were recorded. After heating up and a reaction time of 10–45 min at 240 °C the mixture was let to cool down to room temperature. 0.5 mL of oleic acid was added at 70 °C and 7 mL hexane at room temperature. The product was purified twice by adding 45 mL of methanol/butanol mixture (1:2) and centrifuged at 3000 rpm. Special care was taken to precipitate all the product to ensure that the absorption spectra give a reliable view of the ratio QDs-to-NPLs. If the supernatant was not transparent, more methanol was added. Finally, the product was redispersed in 4 mL of hexane.

*NPLs synthesis with cesium acetate.* The synthesis method for NPLs with the addition of cesium acetate is similar to the method above. The amounts were not halved for these experiments and were performed in a standard 100 mL three-neck round-bottom flask. 86 mg cesium acetate (0.44 mmol) was added at 190 °C. A twice as high amount in mmol of cesium(I)acetate compared to cadmium(II) acetate was added to ensure that an equal amount of acetate was present during the reaction.

*SAXS.* The SAXS experiments were conducted at the SWING beamline of synchrotron Soleil at an energy of 16 keV and a sample-to-detector distance of 1.83 m. This allowed us to probe a $q$-range of 0.05 $\text{nm}^{-1}$–8 $\text{nm}^{-1}$. 2D scattering patterns were recorded every 5 s with an exposure time of 3 s. The background scattering of the solvent, reactants and flask was subtracted from the azimuthally integrated 2D scattering patterns (Chapter 3.6). Models for the fitting of the scattering patterns are also discussed in Chapter 3.6.

*UV–vis absorption.* The *in situ* absorption experiments were performed using a DH-2000-BAL lamp as the excitation source, 200 μm core solarization resistant fibers, and a USB4000 spectrometer all from Ocean Optics. To obtain a collimated light beam with a diameter smaller than 5 mm, the diameter of the indentation in the glass, the following optics was used: 14 mm focal point (f14) VIS achromatic lens, 350 nm long pass filter, f30 VIS aspherical achromatic lens, 200 μm pinhole, and f14 VIS aspherical achromatic lens. The light bundle after the sample was coupled into a fiber using a f14 VIS aspherical achromatic lens. The lenses and filter were obtained from Edmund Optics. Spectra were recorded with an integration time of 100 ms. The absorbance was calculated afterward, taking an $I_0$ spectrum just before nanoparticles started to form.

*TEM.* The TEM images and HAADF-STEM images were either recorded on a FEI Tecnai 20 operating at 80 keV or a FEI Talos F200X operating at 200 keV. Samples were made by drop-casting a dilute dispersion of nanoparticles on a TEM grid.

*Preparation and measurement method ICP-OES.* To prepare the inductively coupled plasma optical emission spectrometry (ICP-OES) samples, first, the unreacted precursors were removed after a synthesis using the standard washing method discussed above. The total mass of the product in hexane was weighted (~10 g). 2 grams of the whole product was taken and put under vacuum to remove hexane. 2 mL 65% nitric acid was added to dissolve the CdSe nanoparticles. After the solution was clear, it was diluted with Milli-Q® water to a total volume of 10 mL. The samples were diluted at least 500 times with a 5% nitric acid in Milli-Q® water solution to obtain a cadmium concentration of ~0.5 ppm. The exact cadmium concentration was determined with a 0–1 ppm cadmium in a 5% nitric acid calibration curve made using standard solution 3 of PerkinElmer®. Measurements were conducted with a PerkinElmer® ICP-OES Optima™ 8300. The cadmium concentration was measured using the emission lines at 228.8, 214.4, and 226.5 nm. The yield was calculated using the average ppm values obtained with measurements on these three emission lines.

*Melting point other acetate salts.* In the literature other acetate salts have been reported, including $Mn(Ac)_2 \cdot 4H_2O$, $Zn(Ac)_2$, $Mg(Ac)2 \cdot 4H_2O$, $Co(Ac)_2 \cdot 4H_2O$, and Na(Ac), to promote formation of CdSe NPLs.[89] All these mentioned acetates resulted in the formation of NPLs in our own experiments as well (addition temperature of 190 °C). The melting temperature of all these acetates is higher than 190 °C: $Co(Ac)_2$ (298 °C), $Mn(Ac)_2$ (210 °C), $Zn(Ac)_2$ (257 °C), and $Na(Ac)_2$ (324 °C). For $Mg(Ac)_2 \cdot 4H_2O$, a melting point of 90 °C is often reported. However, $Mg(Ac)_2$ dissolves in the water incorporated in the crystal at this temperature, giving a seemingly lower melting temperature. A melting temperature of ~230 °C is reported by Jiang *et al.* for $Mg(Ac)_2$.[115] In this respect, it is worth noting that we only observe anhydrous cadmium acetate in the scattering patterns (peak at $q = 6.63$ $nm^{-1}$) when we either add anhydrous or hydrous cadmium acetate. The water incorporated in the crystal is apparently quickly evaporated. Therefore, we consider the melting points of the anhydrous salt even if the hydrous version is added.

## 3.5 Additional figures

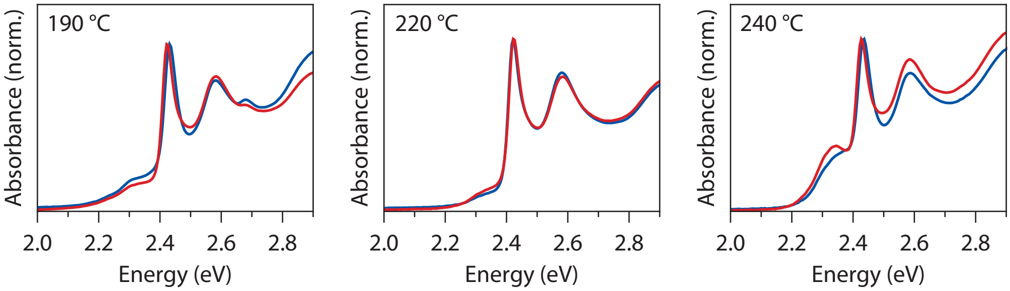

**Figure 3.6 | Absorption spectra products *in situ* SAXS experiments in homebuilt setup.** *Ex situ* absorption spectra of the product from *in situ* SAXS experiments where cadmium acetate is added at 190, 220, and 240 °C. Experiments were performed in duplicate (blue and red). These *ex situ* results verify that synthesis is reproducible in our homebuilt setup. NPLs emitting at 2.7 eV (460 nm) are obtained next to NPLs emitting at 2.45 (510 nm) and QDs at ~2.3 eV (~540 nm) when acetate is added at 190 °C. When cadmium acetate is added at 240 °C, more QDs compared to NPLs are formed. Addition at 220 °C results in the formation of only one population of NPLs and a smaller amount of QDs. For these reasons we used the 220 °C procedure in Chapter 3.2.

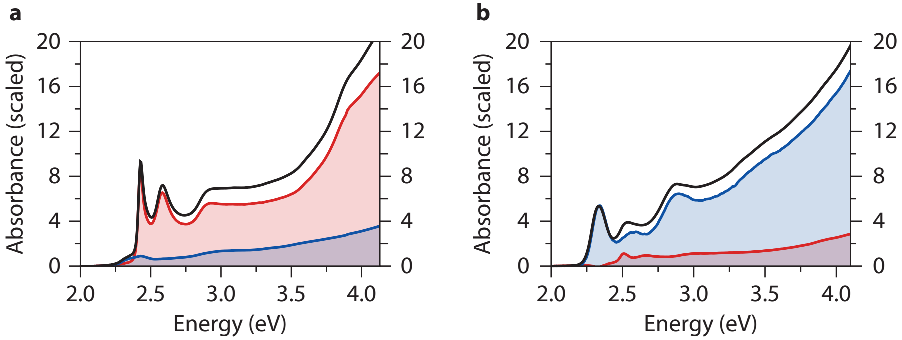

**Figure 3.7 | Concentration QDs and NPLs from *ex situ* absorption spectra.** (**a**) Synthesis with addition of cadmium acetate (Figure 3.1c). NPLs (red) and QD (blue) contributions were extracted using size-selective precipitation. (**b**) Synthesis without addition of cadmium acetate (Figure 3.4c), mini-NPLs and QD contribution are shown in red and blue, respectively. No pure mini-NPL fraction could be extracted, the spectrum in red therefore contains a little contribution of absorption by QDs. The NPL and QD concentration were estimated from the *ex situ* spectra using Lambert-Beers law. The contribution of the NPLs or QDs absorbance to the total absorbance at 300 nm (4.13 eV) was determined by fitting the spectra with the QD and NPL fractions obtained with size-selective precipitation. The absorption coefficients well above the band edge absorption were calculated for the NPLs and QDs as described in literature.[55,102,116] For these calculations, the QD volume was extracted from the absorption spectra using the sizing curve by Maes *et al*.[55] and the volume of the NPLs was obtained from TEM analysis. The resulting concentrations of the product dispersions were scaled to match the volume during the synthesis at 240 °C, *i.e.*, scaled to a total volume of 9.4 mL (7.5 mL ODE and a volume expansion of 25% at 240 °C.[76]) This ensures that the calculated concentrations can directly be compared to the concentrations obtained from the *in situ* SAXS analysis. A QD and NPL concentration of 2.9 µM and 0.35 µM were obtained for the synthesis with addition of cadmium acetate. A QD concentration of 11.2 µM was extracted for the synthesis without addition cadmium acetate.

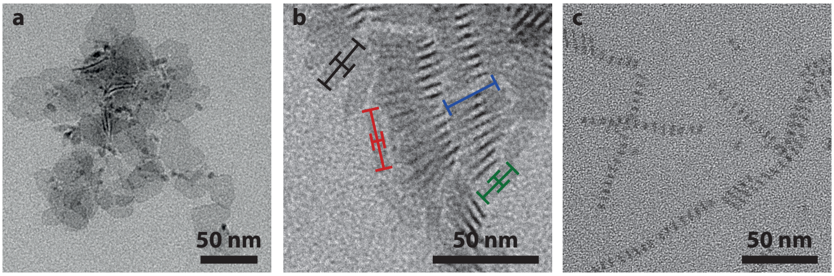

**Figure 3.8 | TEM images of 3.5 ML NPLs, 4.5 ML NPLs, and 5.5 ML mini-NPLs.** (**a**) TEM image displaying 3.5 ML NPLs and QDs obtained when cadmium acetate is added at room temperature and the reaction mixture is heated to 240 °C for 10 minutes in a standard three-neck flask. (**b**) TEM image of 4.5 ML NPLs obtained during SAXS experiment in homebuilt setup with addition of cadmium acetate at 220 °C. The lateral dimensions of a few NPLs are indicated in the image. The average lateral dimensions, 27 ± 2.2 nm by 7.5 ± 1.2 nm, were determined by measuring >100 NPLs. (**c**) Bright-field TEM image 5.5 ML mini-NPLs obtained when no cadmium acetate is added. Synthesis performed in homebuilt setup.

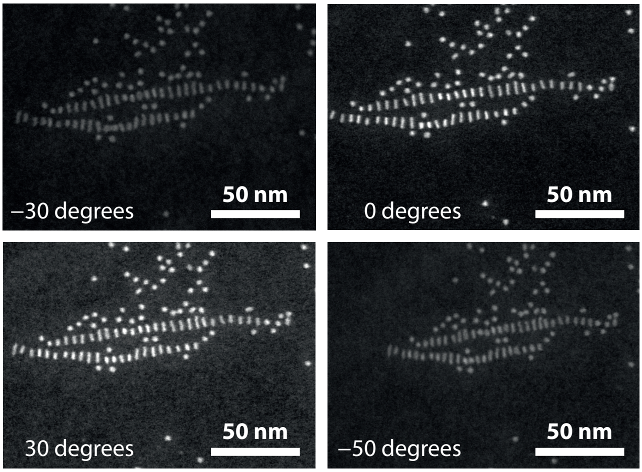

**Figure 3.9 | Tilt series HAADF-STEM 5.5 ML mini-NPLs.** Tilt series of the reaction product without addition of cadmium acetate. The HAADF-STEM images were measured for the reaction product without size-selective precipitation and show the presence of both mini-NPLs and QDs.

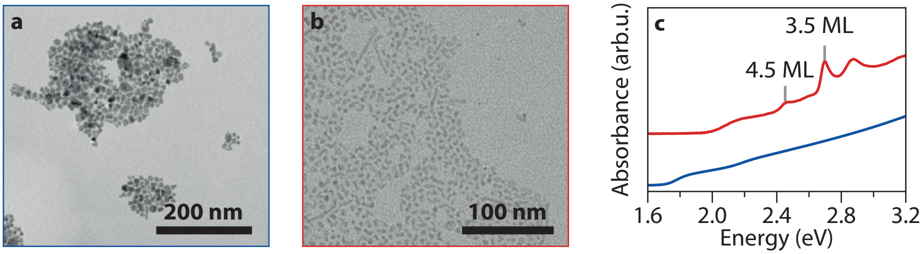

**Figure 3.10 | TEM images and absorption spectra cesium acetate experiments.** TEM images of the synthesis product when cesium acetate is added at 190 °C and temperature is increased to 240 °C (**a**) or cesium acetate is added at 190 °C without increasing the temperature (**b**). The absorption spectra are shown in blue and red, respectively (**c**). NPLs are only observed on TEM images and in absorption spectra when the temperature is not increased above the melting temperature of cesium acetate (195 °C).

## 3.6 Data analysis

*SAXS data processing.* We obtained the 1D scattering curves of the growing nanocrystals by azimuthal integration of the patterns recorded on the 2D detector. The curves were processed by subtracting the temperature-dependent scattering of a cadmium myristate precursor solution in the reaction flask (Figure 3.11, top row) and the scattering of the empty flask

$$I_{\mathrm{proc}}(T) = I_{\mathrm{raw}}(T) - aI_{\mathrm{flask}} - b\left[I_{\mathrm{Cd(Myr)_2inODE}}(T) - I_{\mathrm{flask}}\right]. \tag{3.1}$$

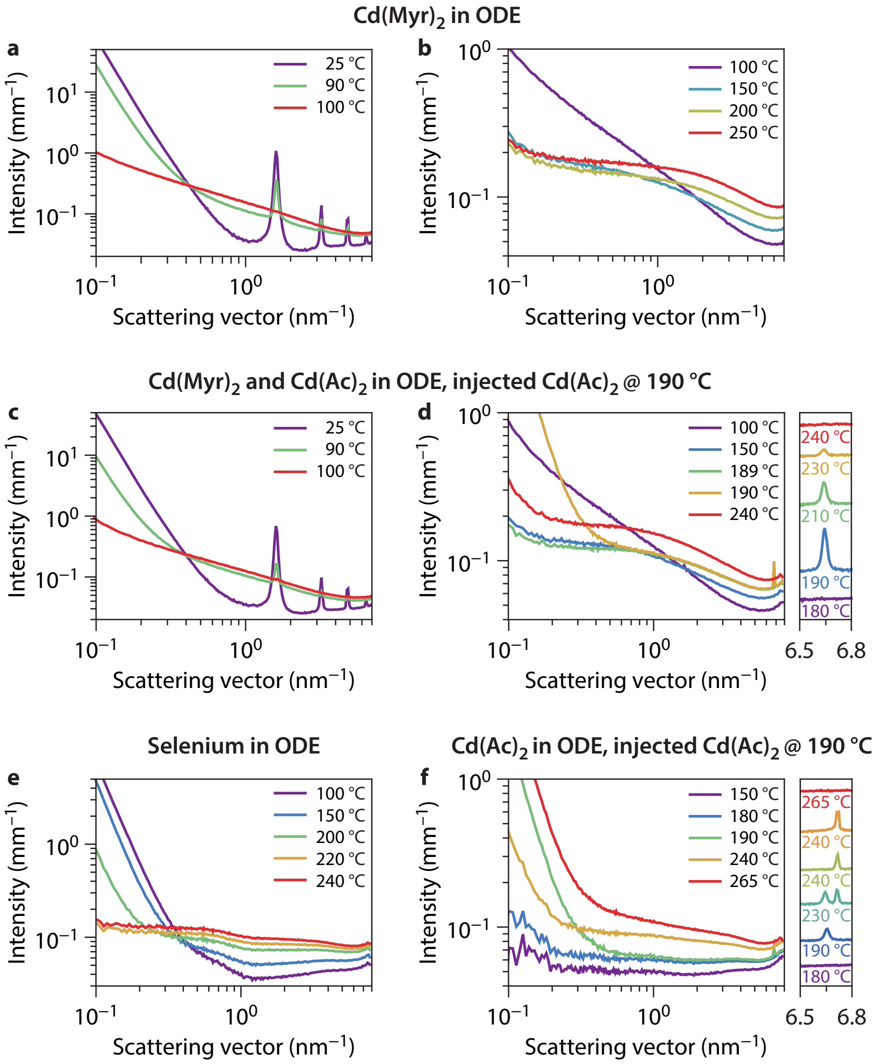

**Figure 3.11 | SAXS patterns of the precursors. Top:** Scattering patterns of cadmium myristate in ODE at low (**a**) and high (**b**) temperatures. At low temperatures a lamellar phase is observed, which melts around 100 °C. The scattering patterns of experiments discussed in Chapter 3.2 were corrected using these scattering patterns. **Middle:** scattering patterns of cadmium myristate in ODE with the addition of cadmium acetate at 190 °C. The addition of cadmium acetate can be observed by the increase in scattering at small $q$-values ($q < 0.2$ nm$^{-1}$) and by a peak at ~6.7 nm$^{-1}$ (orange, **d**). The scattering peak is plotted more clearly next to the bottom image. These scattering patterns are shifted for clarity. The increase in intensity at $q <$ 0.2 nm$^{-1}$ and the peak at ~6.7 nm$^{-1}$ disappear upon heating the mixture to 230 °C. Note: This temperature is lower compared to when the acetate is injected at 220 °C (experiment in Chapter 3.2) because the acetate is introduced earlier. **Bottom:** (**e**) scattering patterns of cadmium acetate in ODE at different temperatures (acetate injected at 190 °C). The increase in scattering at small $q$ and the appearance of a peak at ~6.7 nm$^{-1}$ upon addition of the acetate is also observed here. Around 230 °C, the peak shifts to higher $q$-values, similar to what was observed during the experiment in Chapter 3.2. The cadmium acetate salt does not melt/dissolve at temperatures lower than its melting temperature (255 °C) without the presence of cadmium myri-

state in the mixture. In the right panel, where the cadmium acetate peak is shown, the peak is still observed after prolonged heating at 240 °C. The two plots at 240 °C are 20 min apart. This indicates that the cadmium acetate reacts with cadmium myristate when both are present in the reaction mixture. (**f**) Scattering patterns at different temperatures of selenium in ODE (selenium added at room temperature). The presence of large selenium clumps results in scattering at small $q$-values. Selenium starts to dissolve after reaching 150 °C. Selenium in ODE gives an almost constant background at 220 °C and higher.

The values for $a$ varied between 0.95 and 1.05. A constant value of ~0.8 was used for $b$ for all temperatures. This value was determined at 240 °C. After this processing, $I_{\mathrm{proc}}(T)$ still contained some residual cadmium myristate scattering before the temperature reached 240 °C because less myristate precursor had reacted. This additional scattering was accounted for during the fit by approximating the scattering, arbitrarily, with the form factor of a sphere with a radius of ~0.7 nm ($P_{\mathrm{sphere,myr}}$ in text below). Figure 3.12 shows that the scattering of cadmium myristate resembles that of a sphere (red) for $q > 1$ nm$^{-1}$. At these $q$-values, cadmium myristate background is the dominant contribution to the scattering signal in the initial stages of our *in situ* synthesis experiments. The strength of this background signal decreases as the reaction mixture is heated and is negligible when the temperature hits 240 °C. Selenium does not produce any significant background at intermediate $q$-values, and it fully dissolves in ODE at the temperatures of interest.

The absolute scattering intensity was corrected for the pathlength of X-rays through the reaction flask, which ranged from 3.4 mm to 3.8 mm, and was determined by measuring the scattering intensity of water for each of the different flasks used during our experiments. The scattering intensity could then be calibrated using the known absolute scattering cross section of water ($1.65 \cdot 10^{-3}$ mm$^{-1}$ at 16 keV).[73]

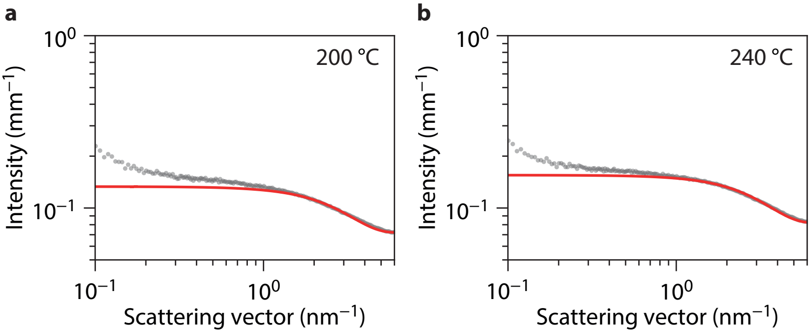

**Figure 3.12 |** The scattering of cadmium myristate (gray) at 200 °C (**a**) and 240 °C (**b**) can be approximated with the scattering pattern of a spherical particle with a radius of 0.7 nm (red). This calculated scattering curve was used during the fitting procedure to fit the initially higher scattering of cadmium myristate, which was underestimated by the correction described above.

*Model for QDs.* CdSe quantum dots (QDs) have a quasi-spherical shape. Good fit results can be obtained from SAXS data of CdSe QDs by assuming spheres with a Gaussian size distribution. The scattering intensity of spherical particles with a Gaussian distribution of radii is given by

$$I(q) = n_1 \Delta\rho^2 \left\langle P_{\text{sphere}}(q) \right\rangle_R S_{\text{spheres}}(q), \tag{3.2}$$

where $n_1$ is the number density, $\Delta\rho$ the scattering length density (SLD) contrast, $\langle P_{\text{sphere}}(q)\rangle_R$ the average form factor for spherical particles with average radius $R_0$ and standard deviation $\sigma_R$. $S_{\text{spheres}}(q)$ is the structure factor due to positional order between the particles. In our experiments, the QD density remains low and the inter-QD interactions are weak, so $S_{\text{spheres}}(q) = 1$. The form factor of a sphere of radius $R$ is

$$P_{\text{sphere}}(q) = 36\pi \Delta\rho^2 V_{\text{sphere}}^2 \left[ \frac{\sin(qR) - qR\cos(qR)}{(qR)^3} \right]^2. \tag{3.3}$$

Averaging over a Gaussian size distribution is described by

$$\left\langle P_{\text{sphere}}(q) \right\rangle_R = 36\pi\Delta\rho^2 \frac{1}{\sqrt{2\pi}\sigma_R} \int_0^\infty e^{-\frac{(R-R_0)^2}{2\sigma_R^2}} V_{\text{sphere}}^2 \left[ \frac{\sin(qR) - qR\cos(qR)}{(qR)^3} \right]^2 \mathrm{d}R, \tag{3.4}$$

where $V_{\text{sphere}}$ is the volume of a sphere with radius $R$. $\Delta\rho$ is calculated by subtracting the SLD of the reaction mixture from that of CdSe: $\Delta\rho = \rho_{\text{CdSe}} - \rho_{\text{reaction mixture}}$. Using the SLD calculator provided by the National Institute of Standards and Technology (NIST, https://www.ncnr.nist.gov/resourses/activation/) we obtained $\rho_{\text{CdSe}} = 40.6 \cdot 10^{-6}$ Å$^{-2}$ for CdSe at 16 keV. For the organic reaction mixture, we considered a mass density of 0.63 g cm$^{-3}$ at 240 °C [76] due to thermal expansion. With this density, we obtain $\rho_{\text{reaction mixture}} = 6.1 \cdot 10^{-6}$ Å$^{-2}$ at 16 keV.

*Model for the experiments without acetate addition: stacked mini-NPLs.* The scattering intensity of a stack of NPLs can be approximated by[117]

$$I(q) = n_2 \Delta\rho^2 \langle P_{\text{NPLs}}(q)\rangle_R F_{\text{stacking}}(q), \tag{3.5}$$

where $n_2$ is the number density of the NPLs, $\Delta\rho$ the SLD contrast between the NPL and the reaction mixture (see above), $\langle P_{\text{NPLs}}(q)\rangle_R$ the average form factor of the lateral shape of the NPLs and $F_{\text{stacking}}(q)$ the shape factor for the structure in the perpendicular direction. The mini-NPLs were, for simplicity, fitted with the form factor of a disk with radius $R$

$$P_{\text{mini-NPL}}(q) = 16\pi\Delta\rho^2 A_{\text{NPL}}^2 \frac{2J_1(qR)^2}{(qR)^2}. \tag{3.6}$$

With a Gaussian distribution in the radii of the disk, this becomes

$$\langle P_{\text{mini-NPL}}(q)\rangle_R = 16\pi\Delta\rho^2 \frac{1}{\sqrt{2\pi}\sigma_R} \int_0^\infty e^{-\frac{(R-R_0)^2}{2\sigma_R^2}} A_{\text{NPL}}^2 \frac{2J_1(qR)^2}{(qR)^2} \mathrm{d}R, \tag{3.7}$$

with $A_{\text{NPL}}$ the area of a disk with radius $R$, $J_1(qR)$ the first-order Bessel function, $R_0$ the average radius and $\sigma_R$ the standard deviation in $R$.

The shape factor $F_{\text{stacking}}(q)$ is the Fourier transform of the electron density profile in the stacking direction and is given by[113]

$$F_{\text{stacking}}(q) = NL^2 \frac{\sin(qL/2)}{qL/2} \frac{\sin(qNd/2)}{\sin(qd/2)}, \tag{3.8}$$

where $L$ is the thickness of the 5.5 ML mini-NPLs which is 1.6 nm, $d$ the spacing between two NPLs which could be determined by the position of the structure factor peaks ($d$ = 4.5 nm), $N$ is the num-

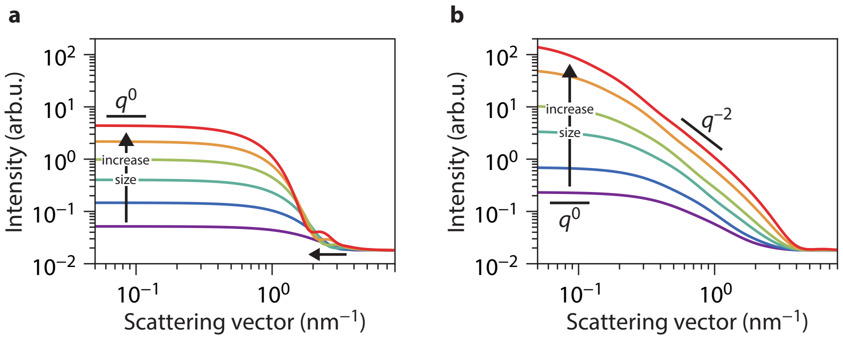

**Figure 3.13 |** Theoretical form factor of (**a**) spheres and (**b**) rectangular 2D particles with a thickness of 1.3 nm. A similar polydispersity of the particles and amount of background scattering are used as in the experiments. The number density of the rectangular particles is one order of magnitude lower than the QDs. QD diameters considered in the panel **a** range from 2 to 4.5 nm. For larger QDs, the minima shift to smaller $q$-values. The lateral dimensions of the NPLs in panel **b** range from 1.5 nm by 4.5 nm to 8 nm by 24 nm. Qualitatively, NPLs and QDs can easily be distinguished in SAXS; both have a regime where the scattering is independent of $q$ (indicated with $q^0$), but the NPLs also have a range where the slope scales with $q^{-2}$. Additionally, the minima for rectangular particles are less pronounced due to rotational averaging.

ber of NPLs in a stack. A Gaussian distribution was also used for the number of NPLs in a stack

$$\left\langle F_{\text{stacking}}(q)\right\rangle_N = \frac{L^2}{\sqrt{2\pi\sigma_N}}\int_0^\infty \mathrm{e}^{-\frac{(N-N_0)^2}{2\sigma_N^2}}\, N\,\frac{\sin(qL/2)}{qL/2}\,\frac{\sin(qNd/2)}{\sin(qd/2)}\,\mathrm{d}N. \tag{3.9}$$

The complete model, used for the synthesis where no acetate is added, is

$$I(q) = B + n_0 P_{\text{sphere,myr}}(q) + n_1\Delta\rho^2\left\langle P_{\text{sphere}}(q)\right\rangle_R + n_2\Delta\rho^2\left\langle P_{\text{mini-NPL}}(q)\right\rangle_R\left\langle F_{\text{stacking}}(q)\right\rangle_N. \tag{3.10}$$

The first term is background scattering and the second accounts for the additional scattering of cadmium myristate during the heat-up. The scattering patterns were fitted using this model, with $B$, $n_0$, $n_1$, $n_2$, $R_{\text{mini-NPLs}}$, $R_{\text{QDs}}$, $\sigma_{R,\text{mini-NPLs}}$, $\sigma_{R,\text{QDs}}$, $N$, and $\sigma_N$ as free fit parameters. An example of a fit with the contribution of the QDs and stacked NPLs is shown in Figure 3.14.

*Model for the experiments with acetate addition: large rectangular 4.5 ML NPLs.* The large 4.5 ML NPLs obtained when cadmium acetate is added during the reaction could not be fitted well with the form factor of a disk (in contrast to the 5.5 ML mini-NPLs). These scattering patterns were fitted using the form factor of a rectangular-shaped particle with a thickness of 1.3 nm, corresponding to 4.5 ML NPLs. The form factor, averaged over all orientations, for this anisotropic particle is given by[118]

$$P_{\text{NPL}}(q) = \int_0^{2\pi}\int_0^{\pi}\left|4RWd\,\frac{\sin(q_xR)}{q_xR}\,\frac{\sin(q_yW)}{q_yW}\,\frac{\sin(q_zd/2)}{q_zd/2}\right|^2\sin\theta\,\mathrm{d}\theta\,\mathrm{d}\phi, \tag{3.11}$$
$$q_x = q\sin\theta\cos\phi,\ q_y = q\sin\theta\sin\phi,\ q_z = q\cos\theta,$$

where $R$, $W$, and $d$ are the half-length, half-width, and thickness of the particles, respectively. Best fits were obtained with $W$ equal to $3R$. Again, a Gaussian distribution in $R$ was used.

The complete model to fit the scattering data for experiments with acetate addition is

$$I(q) = B + n_0 P_{\text{sphere,myr}}(q) + n_1\Delta\rho^2\left\langle P_{\text{sphere}}(q)\right\rangle_R + n_2\Delta\rho^2\left\langle P_{\text{NPLs}}(q)\right\rangle_R + aI_{\text{Cd(Ac)}_2\text{inODE}}. \tag{3.12}$$

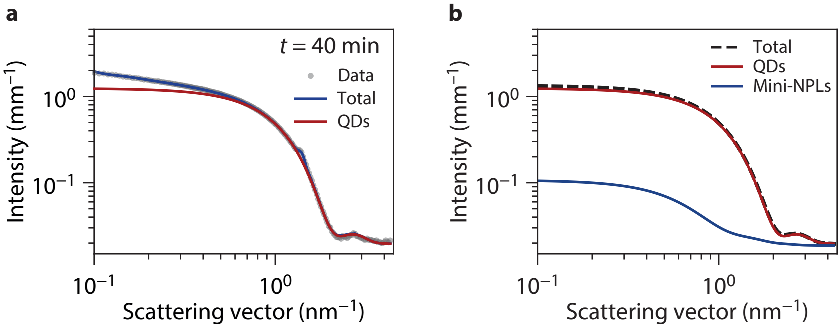

**Figure 3.14 |** (**a**) Fit (blue) of scattering pattern 40 min after reaching a temperature of 220 °C using a model for scattering of QDs and stacked 5.5 ML mini-NPLs. The contribution of the QDs is shown in red. (**b**) Scattering intensity of unstacked 5.5 ML mini-NPLs compared to the fitted QD-scattering in **a**. In blue the scattering of 5.5 ML mini-NPLs with a 3.5 nm radius, thickness of 1.6 nm, and a concentration of 0.25 µM. These values were extracted from the fit in **a**. The effect of unstacked mini-NPLs on the total scattering (black dashed) is neglectable. The same holds for NPLs with small lateral dimensions in a synthesis with addition of cadmium acetate. The increase in scattering at small *q* in **a** is mainly caused by the stacks of mini-NPLs, not by the scattering of individual mini-NPLs.

The first term accounts for background scattering and the second for the additional myristate scattering during the heat-up. The last term accounts for the scattering of the cadmium acetate crystallites in the reaction mixture. The ratio between the lateral dimension, $W/R = 3$, and the NPL concentration, $n_2/N_A = c_{NPL} = 0.6$ µM, were determined from a fit to the scattering curve at an experiment time where the cadmium acetate has melted, *i.e.*, $t = 9$ min. The values were fixed for the fits to the curves at all other times.

Both experiments (with and without acetate addition) saw the polydispersity of the QDs ($\sigma_{R,\mathrm{QDs}}$) increase to a value of 0.5 nm during the heat-up to 220 °C. Background scattering from cadmium acetate, following addition at 220 °C, complicated reliable fitting of the scattering contribution from QDs. We therefore fixed the QD polydispersity at $\sigma_{R,\mathrm{QDs}} = 0.5$ nm for the analysis of all scattering curves following acetate addition. Examples of fitted data before and after cadmium acetate dissolution are shown in Figure 3.15.

*Variations fitting procedure SAXS data with acetate addition.* In Figure 3.17, we check that our fit results are robust to slight variations of the model used. We compare the fit results obtained with a fixed time-independent NPL concentration $c_{NPL}$ to those obtained when $c_{NPL}$ is a free parameter, and the results obtained with and without the inclusion of a background contribution due to cadmium acetate. The estimated lateral dimensions are similar at $t > 7.5$ min for three variations considered to the model (blue, red, and green). The variation where both the NPLs concentration and cadmium acetate background was fitted (orange) gives slightly smaller values because it overestimates the cadmium acetate background. However, if no cadmium acetate background is included in the model, the NPL concentration shows an unrealistic peak in the NPL concentration around $t = 2$ min and the

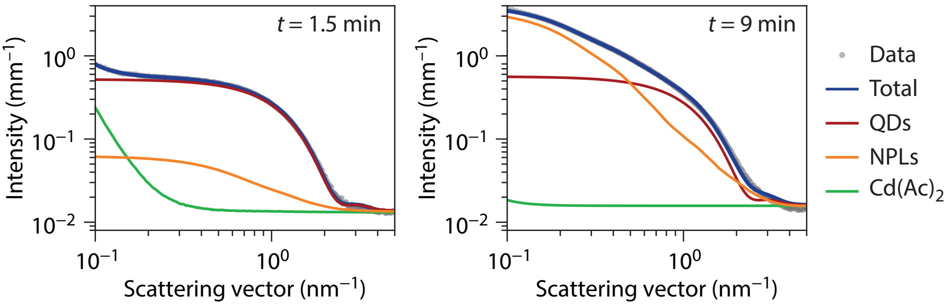

**Figure 3.15 |** Fitted scattering patterns at $t$ = 1.5 min and $t$ = 9 min with the contribution of QD, NPL and cadmium acetate scattering to the total scattering. The fitted intensity of the flat background scattering B (~0.015 mm$^{-1}$) is added to the fits shown in blue, red, orange, and green.

lateral dimensions are very large at $t < 2.5$ min (Figure 3.17, green). This is likely an artifact due to the false assignment of the sloping background scattering of cadmium acetate to NPLs. We resolve this difficulty by fixing $c_{\mathrm{NPL}} = 0.6$ µM, which is the constant value extracted for $t > 5$ min (Figure 3.17b). This might give rise to a slight overestimation of the lateral dimension in the first minutes after the addition of cadmium acetate. The value of 0.6 µM is similar to the concentration of mini-NPLs obtained when no acetate is added and therefore is likely a good estimate of the NPL concentration around $t$ = 0–5 min.

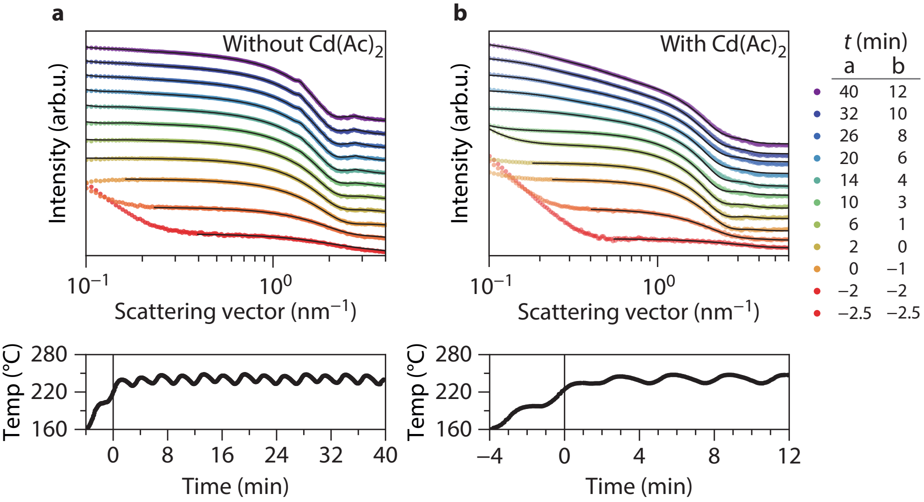

**Figure 3.16 | Fit results SAXS with and without cadmium acetate addition.** Selection of scattering patterns with fit (black) obtained using the models described above. Synthesis (**a**) without and (**b**) with the addition of cadmium acetate at $t$ = 0. Scattering patterns are shifted in intensity for clarity. Below the temperature profiles are given of the respective experiments.

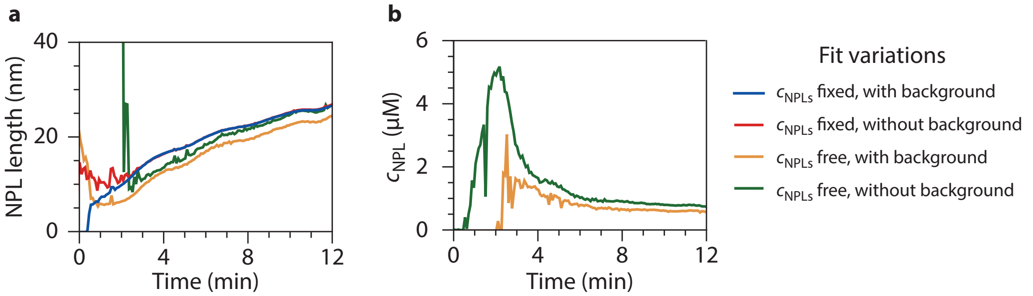

**Figure 3.17 |** Fit results of the synthesis with cadmium acetate addition (Figure 3.16b) using four variations to the model. (**a**) the NPL size, expressed in terms of the longest edge length while the aspect ratio is fixed at 3:1, and (**b**) NPL concentration. We kept the NPL concentration fixed at $c_{NPL} = 0.6$ µM (blue and red) or used it as a free fit parameter (orange and green). We did (blue and orange) or did not (red and green) include a background contribution of Cd acetate.

*SAXS data formation mini-NPLs at 190 °C followed with addition cadmium acetate.* The data in Chapter 3.2 shows that 5.5 ML mini-NPLs form when the reaction mixture is heated to 240 °C without adding cadmium acetate at 190 °C. Thinner mini-NPLs can be synthesized when the reaction temperature is kept at 190 °C instead. The structure factor peaks in Figure 3.18a show that 4.5 ML mini-NPLs form after prolonged heating at 190 °C. Large 4.5 ML NPLs can still be formed when cadmium acetate is added after 35 min at 190 °C. The reaction temperature is also increased to 240 °C as for a standard 4.5ML NPLs synthesis (Figure 3.18b).

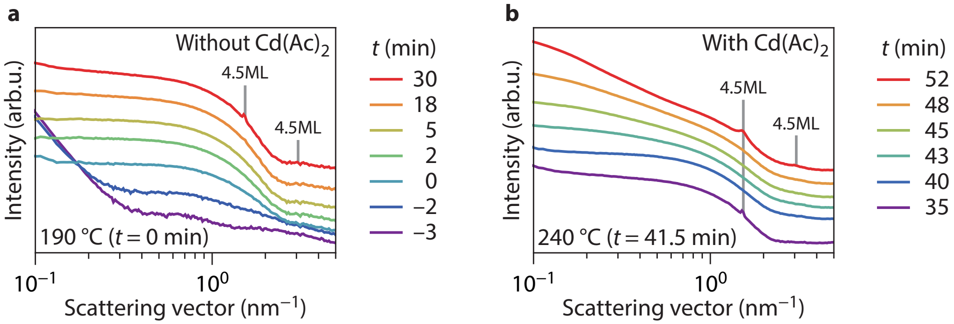

**Figure 3.18 |** (**a**) Scattering data without adding cadmium acetate with a reaction temperature of 190 °C instead of 240 °C as in Chapter 3.2. The scattering data corresponds to the form factor of spherical NCs, but after prolonged heating, structure factor peaks appear corresponding to 4.5ML mini-NPLs (red). (**b**) Upon addition of cadmium acetate ($t = 35$ min), the mini-NPLs first unstack (purple to blue spectrum), and the lateral dimension of the NPLs increase (green to orange), which can be deduced from the change in slope for $q < 1$ nm$^{-1}$. At the end of the reaction, the large NPLs also form stacks, indicated by the structure factor peaks. The peaks' positions correspond to 4.5 ML NPLs.

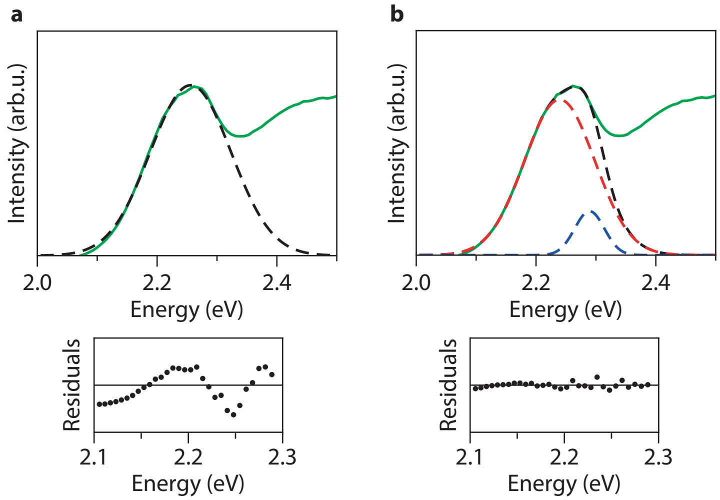

**Figure 3.19 | Fit *in situ* absorption synthesis without addition acetate.** Single Gaussian (**a**) and double Gaussian (**b**) fit of first exciton transition in the *in situ* absorption spectrum at *t* = 10 min and *T* = 240 °C for the synthesis without addition of cadmium acetate (orange spectrum Figure 3.4a). The fit and the fit residuals of the single Gaussian fit (**a** and **c**) show a systematic deviation and reveal an additional feature on the high energy side. The double Gaussian fits the data well (see fit residuals, **d**) and reveals a small extra absorption peak at the position of the 5.5 ML mini-NPLs (at ~2.28 eV).

## 3.7 Comparison SAXS and ICP-OES results

*Calculation yield from SAXS data.* The yields of the reaction displayed in Figure 3.3c and Figure 3.4f were determined from the SAXS data by calculating the amount of selenium incorporated into the QDs and (mini-)NPLs and the amount of selenium added at the start of the reaction (6 mg) because selenium is the element in deficit. From the SAXS scattering patterns, we extracted the molar concentration ($n_{\mathrm{NP}}/N_{\mathrm{A}} = c_{\mathrm{NP}}$) and average volume $\langle V_{\mathrm{NP}}(q)\rangle_R$ of the nanoparticles (NPs), where $R$ are the radii (QDs and mini-NPLs) or edge lengths (NPLs). The yield can be obtained by calculating the average amount of selenium in a NP

$$N_{\mathrm{Se}} = \frac{4\,\langle V_{\mathrm{NP}}\rangle_R}{a^3}, \tag{3.13}$$

where $a^3 = 0.22\ \mathrm{nm}^3$ is the volume of the cubic unit cell of zinc blende CdSe. The 4 comes in because a unit cell contains four Se atoms. The yield can then be expressed as:

$$Y = c_{\mathrm{NC}}\frac{N_{\mathrm{Se}}}{c_0}, \tag{3.14}$$

where $c_0$ is the initial concentration of selenium ($8.2 \cdot 10^{-3}$ M), *i.e.*, 6 mg in a total reaction volume of 9.4 mL, taking the thermal expansion of the reaction mixture into account.

Note that for the volume of the NPLs and mini-NPLs a thickness of 1.2 nm and 1.5 nm is used instead of the actual thickness (1.3 nm and 1.6 nm) to account for the additional cadmium layer. The number of selenium atoms in a (mini-)NPL would be overestimated without this adjustment.

*Yield and concentration synthesis without addition Cd(Ac)$_2$.* Figure 3.4f shows the CdSe consumption by the QDs (CdSe yield by QDs) when no cadmium acetate is added. For the total yield of the synthesis the CdSe consumption by the mini-NPLs should also be considered. The concentration and size of the mini-NPLs could be extracted from the SAXS data when the mini-NPLs started to stack. The reaction yield as a function of reaction time was then calculated as

$$Y = \frac{4\left\langle V_{\text{mini-NPL}}\right\rangle_R}{a^3}\frac{c_{\text{mini-NPLs}}}{c_0}, \tag{3.15}$$

where $\langle V_{\text{mini-NPL}}(q)\rangle_R$ is the NPL volume averaged over the fitted distribution of disk radii, $a^3 = 0.22$ nm$^3$ is the volume of the cubic unit cell of zinc blende CdSe, and $c_0$ is the initial concentration of Se (the element in deficit) in the reaction mixture. The 4 comes in because a unit cell contains four Se atoms. To calculate the volume relevant for Se consumption, a thickness of 1.5 nm instead of 1.6 nm was used to compensate for the additional cadmium layer as both top and bottom facets are Cd-terminated.

The concentration and yield of the stacked mini-NPLs are shown in Figure 3.20. After 30–40 min, the concentration was ~0.25 μM and the yield ~3%. This results in a total yield, QD and mini-NPLs CdSe consumption of 81% after a reaction time of 40 min.

The concentration and yield of the mini-NPLs could be underestimated because only the concentration of the stacked mini-NPLs could be extracted from the SAXS data. Therefore, the total reaction yield was also determined *ex situ* with ICP-OES. The selenium concentration (element in deficit) in a sample cannot be determined directly with ICP-OES because sample preparation with an strong acid results in the formation of $H_2Se$, which escapes. Instead, the cadmium concentration was measured and a molar ratio of Cd:Se = 1 in the QDs and mini-NPLs was assumed to determine the yield of the reaction. The sample preparation is discussed below. The yields obtained after a reaction time of 10 min and 30 min are shown in Table 3.1.

The yield obtained via ICP-OES is similar to the SAXS results. After 30 min, the total yield is ~75% and ~79%, respectively. After 13 min, the yield is a bit lower in the ICP-OES analysis (~47% compared to ~72%), which is likely due to the heat-up difference in a standard three-neck flask compared to the flask used for SAXS analysis. Overall, the comparison of ICP-OES and SAXS results shows that the mini-NPL concentration and yield are not heavily underestimated with only probing the stacked mini-NPLs.

*Yield synthesis with addition Cd(Ac)$_2$.* The SAXS yield was also verified with ICP-OES for the synthesis with addition of cadmium acetate. The comparison is shown below in Table 3.2. The ICP-OES yield was measured thrice. For the ICP-OES results, a molar ratio of Cd:Se = 1 in the QDs and NPLs was used. Due to the additional cadmium layer, this ratio will deviate for the NPLs. Also here, the yield around 13 minutes is slightly lower, likely due to the heat-up difference in a standard three-neck flask compared to the flask used for SAXS analysis. Both the SAXS and ICP-OES results show that at 13 min a higher total reaction yield is obtained when cadmium acetate is added to the reaction mixture.

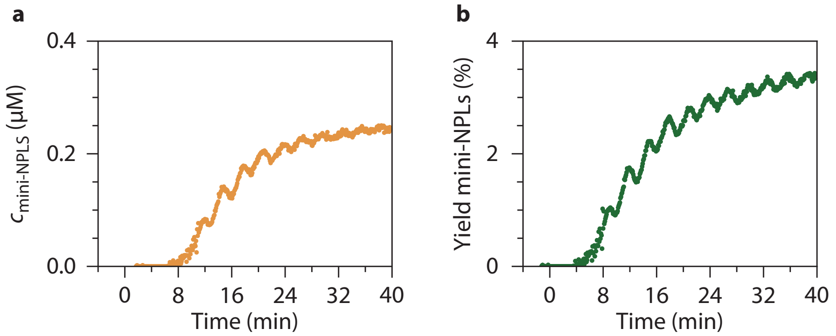

**Figure 3.20 |** Concentration (**a**) and yield (**b**) of 5.5 ML mini-NPLs as a function of reaction time for synthesis without addition cadmium acetate. The oscillations are caused by temperature oscillation (Figure 3.16) affecting the expansion of the reaction flask and reaction volume. The concentration and yield plotted are underestimated values because only the scattering of stacking mini-NPLs is visible over scattering of QDs, while scattering of individual mini-NPLs is too weak. The growth of mini-NPL concentration and yield between $t = 5$ min and 30 min reflect that more and longer stacks are formed. Starting from $t = 30$ min, the NPL concentration levels off to a constant value of 0.25 µM. Table 3.1 shows the total yield determined with ICP-OES and SAXS for reactions without addition of cadmium acetate. The values represent the selenium consumption by QD and mini-NPLs. At 13 min, there is not much stacking of the mini-NPLs yet. The yield is estimated to be between 1.5% and 3%.

| ICP-OES | | SAXS | | | |
|---|---|---|---|---|---|
| *t* (min) | Total yield (%) | *t* (min) | Total yield (%) | QD yield (%) | NPL yield (%) |
| 13 | 52 ± 0.8 | 13 | 71.5–73 | 70 | 1.5–3 |
| 13 | 44 ± 0.8 | 30 | 79 | 76 | 3 |
| 13 | 42 ± 2.7 | 40 | 81 | 78 | 3 |
| 13 | 49 ± 0.9 | | | | |
| 30 | 74 ± 1.0 | | | | |
| 30 | 75 ± 0.9 | | | | |

**Table 3.1 |** Yield ICP-OES and SAXS without addition $Cd(Ac)_2$.

| ICP-OES | | SAXS | | | |
|---|---|---|---|---|---|
| *t* (min) | Total yield (%) | *t* (min) | Total yield (%) | QD yield (%) | NPL yield (%) |
| 13 | 63 ± 1.4 | 13 | 88 | 50 | 38 |
| 13 | 76 ± 1.5 | | | | |
| 13 | 70 ± 1.0 | | | | |

**Table 3.2 |** Yield ICP-OES and SAXS with addition $Cd(Ac)_2$.

# Chapter 4

## The formation of $NaYF_4:Er^{3+},Yb^{3+}$ nanocrystals studied by *in situ* X-ray scattering: phase transition and size focusing

$\beta$-$NaYF_4$ nanocrystals are a popular class of optical materials. They can be doped with optically active lanthanide ions and shaped into core-multi-shell geometries with controlled dopant distributions. Here, we follow the synthesis of $\beta$-$NaYF_4$ nanocrystals from $\alpha$-$NaYF_4$ precursor particles using *in situ* small-angle and wide-angle X-ray scattering and *ex situ* electron microscopy. We observe an evolution from a unimodal particle size distribution to bimodal, and eventually back to unimodal. The final size distribution is narrower in absolute numbers than the initial distribution. These peculiar growth dynamics happen in large part *before* the α-to-β phase transformation. We propose that the splitting of the size distribution is caused by variations in the reactivity of $\alpha$-$NaYF_4$ precursor particles, potentially due to inter-particle differences in stoichiometry. Rate equation modeling confirms that a continuous distribution of reactivities can result in the observed particle growth dynamics.

**Based on**

P.T. Prins, J.C. van der Bok, T.P. van Swieten, S.O.M. Hinterding, A.J. Smith, A.V. Petukhov, A. Meijerink, F.T. Rabouw

Angewandte Chemie International Edition **62**, e202305086 (2023)

## 4.1 Introduction

Lanthanide ions are used for their light-emitting properties in a variety of applications. They are attractive because of their many options for color conversion, producing narrow-band emissions with long excited-state lifetimes. In particular, upconversion of light is possible with lanthanide ions, *i.e.*, the conversion of low energy into high-energy photons. This phenomenon is useful for background-free imaging,[119–121] security inks,[122,123] solar-energy conversion,[124,125] and other applications.[126] It often relies on energy-transfer processes between lanthanide dopants in a crystalline host material. The most popular host material for this purpose is β-phase $NaREF_4$, with RE = Y, Gd, or Lu, because it makes high upconversion efficiencies possible and reproducible synthesis procedures for high-quality nano[127,128] and bulk materials[129] are available. Where bulk materials are usually superior in terms of quantum efficiency,[127,128,130] colloidal nanocrystals (NCs) are non-scattering and solvent-dispersible, which makes them preferable for various applications[126] and processing methods.[131,132]

$NaREF_4$ NCs of the cubic α-phase were first reported in 2004.[133] A synthesis procedure for NCs of the hexagonal β-phase followed in 2006.[134] The latter procedure did not use molecular precursors but small α-$NaREF_4$ precursor particles for the nucleation and growth of β-$NaYREF_4$ NCs. This peculiar strategy has since been further developed to produce bright and highly monodisperse batches of β-$NaREF_4$ NCs for a wide variety of compositions.[135,136] It has also been employed for the synthesis of core–shell or core–multi-shell geometries with improved properties due to a designed dopant distribution.[127,137–142]

The intriguing formation of large monodisperse β-$NaREF_4$ NCs from smaller α-$NaREF_4$ precursor particles has triggered studies into the growth mechanism. The studies involve, for example, *ex situ* electron microscopy and X-ray scattering/diffraction on aliquots taken during synthesis.[143–146] Such techniques provide insight into the intermediate stages of the reaction, but they offer limited time resolution and limited possibilities for quantitative analysis. Other studies have used *in situ* photoluminescence to study the growth mechanism from α-$NaREF_4$ to β-$NaREF_4$ NCs,[144,145] which enhances the time resolution but quantitative interpretation remains difficult. Models for the synthesis mechanism are sometimes directly contradictory. For example, one model proposes that α-$NaREF_4$ precursor particles dissolve, after which β-$NaREF_4$ NCs nucleate and grow,[143] while an alternative model proposes that α-$NaREF_4$ particles grow, after which an α-to-β phase transition occurs at a specific size.[147] One of the most thorough studies, using a combination of *in situ* photoluminescence and multiple *ex situ* techniques, concludes: “It is still not completely clear where the β-phase seeds originate from.”[145]

In this work, we follow the formation of β-$NaYF_4$ NCs from α-$NaYF_4$ precursor particles using *in situ* X-ray scattering. A home-built adaptation of a three-neck flask ensures similar reaction conditions—temperature, volume, stirring—to common lab-based syntheses, while allowing X-ray access.[148] Small-angle X-ray scattering (SAXS) reveals the size distribution of NCs, while wide-angle

X-ray scattering (WAXS) on crystal planes shows the α-to-β phase transition.[149] Surprisingly, we observe a small subensemble of rapidly growing α-$NaYF_4$ precursor particles, while the rest remains small and eventually dissolves. This produces a striking bimodal particle size distribution midway during the reaction. The α-to-β phase transition does not occur until the growing particles are >4 nm radius. This disproves earlier models of dissolution of α-$NaYF_4$ particles followed by nucleation of β-$NaYF_4$ NCs, as well as the idea that the phase transformation triggers rapid growth.[143,147] We hypothesize that variations in surface reaction rate of the α-$NaYF_4$ precursor particles trigger faster growth of a small subensemble, which eventually transforms into β-$NaYF_4$ NCs. This idea is corroborated by population-balancing simulations. We propose that the distribution of surface reaction rates of the α-$NaYF_4$ precursor particles is due to variations in Na/RE ratio. Indeed, the average stoichiometry is known to affect the growth kinetics of $NaYF_4$ NCs on the ensemble scale.[150] These insights could lead to new synthesis strategies for bright NCs or intricate core–shell geometries.

## 4.2 Results and discussion

We study the state-of-the-art synthesis procedure for upconversion NCs of β-$NaYF_4$ doped with 2% $Er^{3+}$ and 18% $Yb^{3+}$,[150] which is schematically visualized in Figure 4.1a. For brevity, we will omit the specification of dopant content in the rest of the text. The used method is hydroxide-free and thereby avoids the incorporation of $OH^-$ at $F^-$ positions in the lattice, significantly improving the upconversion quantum efficiency.[127,151] The first step of the procedure is the formation of cubic α-$NaYF_4$ particles (Figures 4.1b,c) at 200 °C from a solution of oleate salts and $NH_4F$ in oleic acid and 1-octadecene (see Chapter 4.5 for details). Transmission electron microscopy (TEM; Figure 4.1c) shows small particles with ill-defined shapes. The SAXS pattern of our α-$NaYF_4$ particles (Figure 4.1b; left) matches spherical particles with radius 2.2 ± 0.5 nm (volume-weighted mean ± standard deviation) and the WAXS pattern (Figure 4.1b; right) confirms the cubic crystal phase. In the second step, the purified α-$NaYF_4$ precursor particles are heated to 300 °C in a mixture of oleic acid and 1-octadecene, transforming into β-$NaYF_4$ NCs (Figures 4.1d,e) over the course of 90 minutes. The SAXS pattern of our final NCs (Figure 4.1d; left) shows that they are 5.7 ± 0.3 nm in radius (volume-weighted), while the WAXS pattern (Figure 4.1d; right) matches the hexagonal crystal phase. Indeed, TEM (Figure 4.1e) shows larger, monodisperse, and well-defined NCs with a radius of 5.5 ± 0.4 nm (number-weighted; Figure 4.6a).

We followed the second step of the synthesis *in situ*, *i.e.*, the transformation from α-$NaYF_4$ to β-$NaYF_4$, using SAXS and WAXS at beamline I22 of Diamond Light Source, United Kingdom (see Chapter 4.5 for details).[152] The high X-ray photon flux enabled scattering measurements through approximately 4 mm of reaction mixture in our custom three-neck flask at an integration time as short as 1 second. Scattering patterns were recorded continuously every 5 s while the dispersion of purified α-$NaYF_4$ particles was heated from room temperature to 300 °C at a rate of 10 °C $min^{-1}$. The moment the reaction mixture reached 300 °C is defined as $t = 0$ (Figure 4.2a). In the following, we will discuss the evolution of scattering patterns after $t = 0$. The early patterns at 300 °C are already

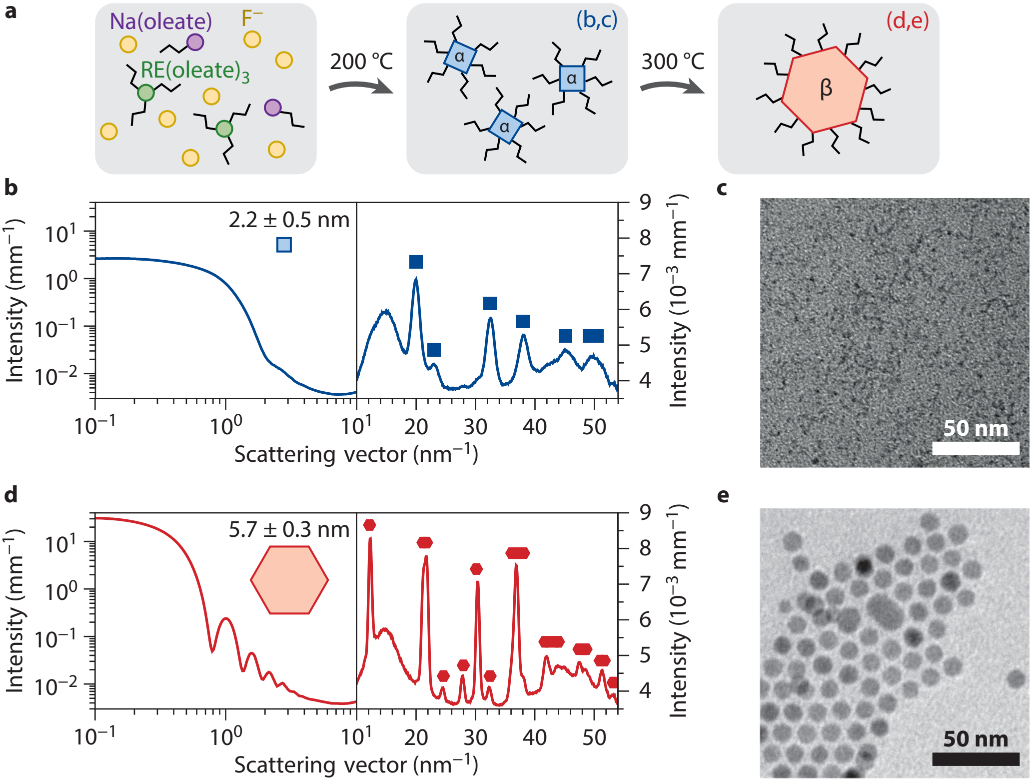

**Figure 4.1 | Synthesis of β-$NaYF_4$:$Er^{3+}$,$Yb^{3+}$ NCs from α-$NaYF_4$:$Er^{3+}$,$Yb^{3+}$ precursor particles.** (**a**) Schematic of the synthesis procedure. Step 1: Na(oleate), $F^-$, and RE$(oleate)_3$ (with RE = Y, Er, Yb) form small α-$NaYF_4$ precursor particles. Step 2: The precursor particles transform into larger β-$NaYF_4$ NCs. (**b**) SAXS and WAXS patterns of the α-$NaYF_4$ particles at 300 °C. Diffraction peaks expected for α-$NaYF_4$ are indicated with blue squares.[153] (**c**) TEM image of the α-$NaYF_4$ particles before heating. (**d**) Same as in panel **b** but for the β-$NaYF_4$ product NCs measured after 60 min at 300 °C. The reference for β-$NaYF_4$ in WAXS is shown with red hexagons.[154] (**e**) TEM image of the final β-$NaYF_4$ NCs after 90 min of reaction.

somewhat different from the patterns at room temperature, most likely reflecting a slight increase in crystallinity and/or size of the α-$NaYF_4$ precursor particles upon heating.

Figures 4.2b,c show the scattering patterns recorded *in situ* at different times during the synthesis. In the WAXS pattern (Figure 4.2b), a narrow peak at 30.38 $nm^{-1}$ due to β-$NaYF_4$ appears, while a broader peak at 32.53 $nm^{-1}$ due to α-$NaYF_4$ goes down. This shows the formation of large β-$NaYF_4$ NCs with narrow diffraction peaks from smaller α-$NaYF_4$ precursor particles with broader diffraction peaks. The SAXS patterns (Figure 4.2c) show a shift of the first dip from 2 $nm^{-1}$ at $t = 10$ min to 0.7 $nm^{-1}$ at $t = 60$ min, confirming the growth of particles. Simultaneously, multiple pronounced minima are evident at $t > 40$ min. This highlights the narrowing of the size distribution of the particles. These results are qualitatively consistent with the *ex situ* TEM data of Figure 4.1.

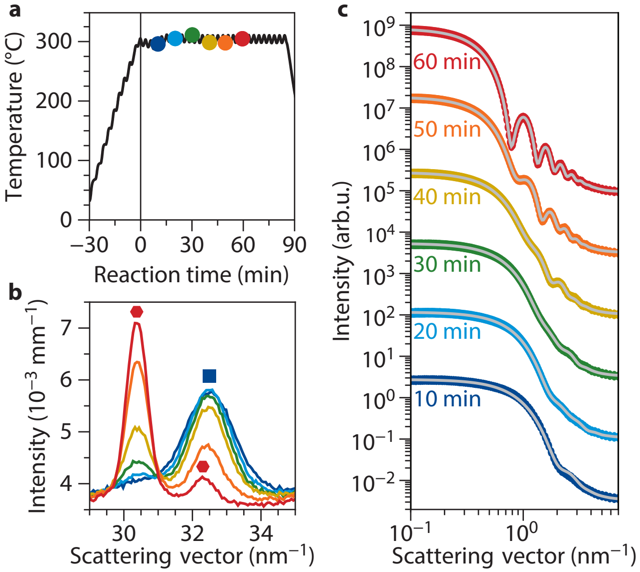

**Figure 4.2 | *In situ* measurements of phase transformation and growth.** (**a**) The temperature recorded by a thermocouple during the synthesis procedure as a function of reaction time. Colored dots highlight moments of the recordings shown in panels **b** and **c**. (**b**) WAXS patterns recorded at various times (see panel **a**), showing the phase transition from α- to β-NaYF$_4$. Diffraction peaks due to the α- and β-phases are indicated with a blue square and red hexagons, respectively: the 220 (32.53 nm$^{-1}$) reflection of α-NaYF$_4$ and the 201 (30.38 nm$^{-1}$) and 210 (32.35 nm$^{-1}$) reflections of β-NaYF$_4$. Nanocrystal growth is evident from the peak narrowing of both the α- and β-peak. (**c**) SAXS patterns recorded at the same times as the data in panel **b**. The NCs are more monodisperse and larger at later times, as evidenced by the sharper dips in the pattern occurring at lower scattering vector. The gray lines are fits to a model of spherical particles with a distribution of radii, optimized using McSAS.[155] A model for polydisperse spherical particles is a good approximation for the slightly faceted but randomly oriented particles that we measure in reality (Figure 4.1e). See Figure 4.7 for full-range WAXS and unshifted SAXS patterns.

For a quantitative analysis of the *in situ* scattering, we first focus on the SAXS data. We fit the patterns with $t > 5$ min to an ensemble of polydisperse spherical particles with a distribution of radii using the open-source program McSAS.[155,156] This model of polydisperse spherical particles approximates our slightly faceted and randomly oriented particles (Figure 4.1e) well. This program can retrieve size distributions using a Monte Carlo rejection sampling approach (see Chapter 4.6 for details). The patterns at $t < 5$ min are very complex because of particle aggregation (Figure 4.8) and are therefore disregarded in our quantitative analysis. The gray lines in Figure 4.2c show best fits to the SAXS patterns at six different reaction times, as found by McSAS. The fitted size distributions as a function of reaction time are presented in the color map of Figure 4.3a. The initially unimodal size distribution with radii of 2.2 ± 0.5 nm (volume-weighted; mean ± standard deviation) splits into two peaks at $t = 17$ min. The mean radius in both peaks increases with time and the small-particle peak disappears around $t = 57$ min. The final distribution is again unimodal, with radii 5.7 ± 0.3

nm (volume-weighted). Our fitting procedure thus shows that the absolute size dispersity decreases during the reaction, from 0.5 to 0.3 nm. Such size focusing has been known but a decrease in absolute values for size dispersion is remarkable, especially considering that a crystal phase transition occurs simultaneously.

Figures 4.3b–f are different visualizations of the particle size distributions during the reaction. The size distributions in terms of volume fraction (Figure 4.3b) show that the total volume of $NaYF_4$ material (*i.e.*, the area under the curves) remains approximately constant during the transition from a unimodal to a bimodal distribution and back. The size distributions in terms of number of particles (Figure 4.3c) show that, meanwhile, the particle concentration decreases by a factor 25. This is a necessary consequence of particle growth at a constant amount of material. We distinguish between the kinetics of "small" and "large" particles by integrating the size distributions using a threshold radius of 3.5 nm (Figure 4.3d). Evaluating the particle concentration as a function of time (Figure 4.3e) shows that the number of large particles grows until $t = 35$ min and then remains constant. Meanwhile, the reaction yield as a function of time (Figure 4.3f) shows that the transfer of material from small to large particles is quantitative and complete at $t = 55$ min. This is the moment when the small particles have completely disappeared (Figure 4.3e).

It is tempting to interpret the bimodal size distribution from the SAXS analysis (Figures 4.3a–f) as due to small $\alpha$-$NaYF_4$ precursor particles and large $\beta$-$NaYF_4$ NCs. Indeed, we know from *ex situ* analysis (Figure 4.1) that the initial precursor particles are small and $\alpha$-$NaYF_4$, while the product NCs are larger and $\beta$-$NaYF_4$. The SAXS data suggest a mechanism where some precursor particles undergo an $\alpha$-to-$\beta$ phase transition that triggers their further growth at the expense of the dissolution of remaining precursor particles. This simple and attractive model, previously suggested in the literature,[147] is however inconsistent with the kinetics in the WAXS data. We see that at moments when the size distribution is already distinctly bimodal (e.g., green line in Figure 4.3b; $t = 30$ min), the corresponding *in situ* diffraction (green line Figure 4.2b) shows only a minor reflection from $\beta$-$NaYF_4$. If the large particles were $\beta$-$NaYF_4$ already at $t = 20$–$40$ min, we should observe strong $\beta$-$NaYF_4$ reflections in WAXS, even more so because diffraction intensity scales with the square of a crystallite's volume. Instead, we observe that the amplitude of the $\beta$-$NaYF_4$ WAXS peak (Figure 4.3g) grows more slowly than the amount of material in large particles (Figure 4.3f). A significant portion of the large particles must be $\alpha$-phase particles. We thus have to conclude that splitting of the size distribution is *not* triggered by an $\alpha$-to-$\beta$ phase transition in a subset of particles but is instead due to differences in growth rate among the $\alpha$-phase particles.

To confirm that some of the large particles midway during the reaction are $\alpha$-phase, we turn to *ex situ* high-resolution TEM. Figure 4.4 shows TEM images of aliquots taken midway during the synthesis of $\beta$-$NaLuF_4$ NCs. We were able to obtain high-resolution TEM images of $NaLuF_4$ particles but not of $NaYF_4$. The two materials are chemically similar (Figure 4.10), but $NaLuF_4$ contains the heavy element Lu (atomic number $Z = 71$ *versus* $Z = 39$ for Y), which provides the critical advantage

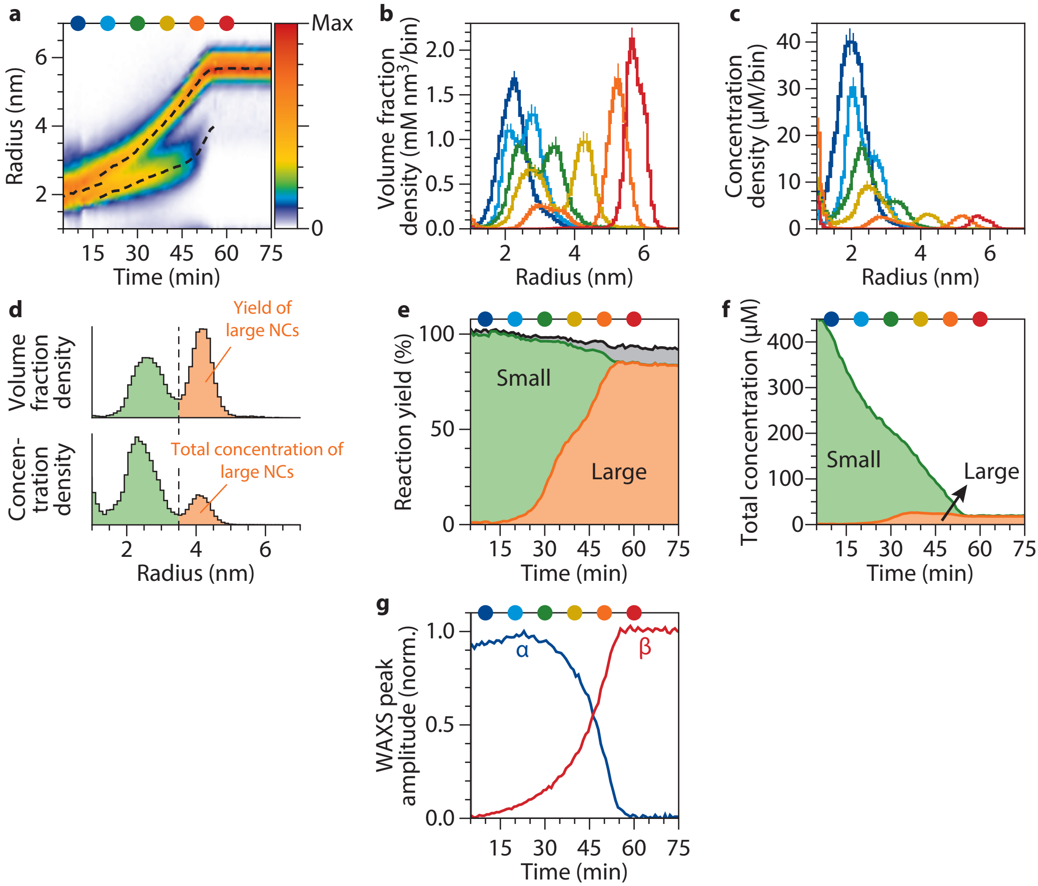

**Figure 4.3 | Growth dynamics from *in situ* X-ray scattering.** (**a**) Size distribution as a function of reaction time, determined from fitting SAXS patterns. The color scale shows the size distribution in terms of volume fraction density per unit of radius. The dashed lines highlight the modes of the distributions, which are unimodal in the initial ($t < 17$ min) and final ($t > 57$ min) stages of the reaction, and bimodal midway. (**b**) Six size distributions picked at specific times from Figure 4.3a on a one-dimensional scale. Colors correspond to the same times as in Figure 4.2c and those highlighted by colored disks in panel a. The *y*-axis shows volume fraction density, *i.e.*, the particle volume per unit of volume of reaction mixture per unit of radius. The bin width on the *x*-axis is 0.1 nm. (**c**) The same size distributions as in panel **b** but converted to a *y*-axis showing concentration density, *i.e.*, number of particles per unit of volume of reaction mixture per unit of radius. (**d**) Schematic of our procedure to obtain total concentrations and yields, using the distributions at $t = 40$ min (yellow in panels **b** and **c**) as an example. Integrating volume fraction density (top), we obtain the reaction yield while integrating concentration density (bottom), we obtain the total concentration. Setting the upper (lower) integration bound at a radius of 3.5 nm yields the reaction yield of small (large) NCs or the total concentration of small (large) NCs. (**e**) The total reaction yield (black line), reaction yield of small NCs (green area; note the cumulative presentation), and reaction yield of large NCs (orange area) as a function of time, where we set the threshold between small and large at 3.5 nm (panel **d**). The gray area is small material with a fitted radius of <1 nm, perhaps incorporating excess Na provided by off-stoichiometric α-$NaYF_4$ precursor particles (Figure 4.9). The yield is defined with respect to the total amount of α-$NaYF_4$ precursor material at $t = 0$. (**f**) Same as in **e** but in terms of concentration. (**g**) Amplitude of the WAXS peaks at 19.92 nm$^{-1}$ (blue; α-$NaYF_4$, 111 reflection) and 30.38 nm$^{-1}$ (red; β-$NaYF_4$, 201 reflection) as a function of reaction time.

of strong interaction with the electron beam. *In situ* SAXS and WAXS (Figure 4.11 and Figure 4.12) and *ex situ* TEM analysis (Figures 4.13c,d) show that the synthesis mechanism of β-$NaLuF_4$ NCs is the same as for β-$NaYF_4$ NCs, except that full conversion takes 30 minutes longer and the final size is larger (15.7 ± 1.0 nm). Quantitative analysis of the SAXS patterns of $NaLuF_4$ particles is more challenging because of aggregation resulting in additional scattering.

The TEM images (Figure 4.4a) of an aliquot taken midway during the reaction confirm that it contains a mixture of small and large particles. This is visible in the particle size distribution obtained from the TEM analysis (Figures 4.13a,b). In Figures 4.4b,c we magnify two regions of the TEM image and highlight four larger particles with radii of 4–5 nm. The atomic lattice planes of these particles are visible. Fast Fourier transforming the images (Figures 4.4d,e) helps us determine the lattice spacings of the particles. Based on this, we can identify one large α-phase and one large β-phase particles in each image. More examples of large α-phase and β-phase particles are given in Figure 4.14. The simultaneous presence of large α- and large β-phase particles supports our interpretation of the *in situ* SAXS and WAXS data: a subset of the α-phase particles grows *before* they transform into the β-phase. Growth of α-phase particles is also consistent with the narrowing of the diffraction peak of the α-phase in Figure 4.2b; compare dark blue, cyan, and green diffraction patterns.

Now the question arises: What causes the differences in reaction rate among initial α-phase precursor particles that triggers the splitting of the size distribution? First, the α-phase precursor particles differ in terms of surface faceting and ligand coverage. This is however not a likely cause for the differences in reaction rate because the surface of NCs is highly dynamic, and fluctuations average out the reaction rates of any particular surface structure. Instead, we propose that differences in stoichiometry determine which α-phase precursor particles grow faster than others. Indeed, the overall Na/RE ratio in a reaction mixture has been used as a parameter to control the reaction kinetics and final product size in synthesis procedures.[150] Our results suggest that variations in—rather than the average—Na/RE ratio among particles is a hidden but key aspect enabling this size control. The small materials produced during the synthesis (<1 nm diameter; gray area in Figure 4.3e; see also Figure 4.9) might be left-over NaF from the conversion of partially off-stoichiometric α-$NaYF_4$ to stoichiometric β-$NaYF_4$.

On the ensemble scale, the average stoichiometry of α-phase particles can vary continuously between a RE excess (Na/RE = 0.6) and a Na excess (Na/RE = 1.2), which affect the reaction kinetics.[150] Stoichiometries likely vary continuously on the single-particle scale as well. Yet the size distribution midway during the synthesis is distinctly bimodal (Figures 4.3a–c). To reconcile the seeming contradiction between a continuous stoichiometry distribution and bimodal growth, we constructed a simple mathematical model for nanoparticle growth with a continuous distribution of growth rates. This model and its results are presented below. It produces an evolution from a unimodal to a bimodal and back to a unimodal size distribution, in qualitative agreement with the experiment, and helps us explain these unusual size dynamics.

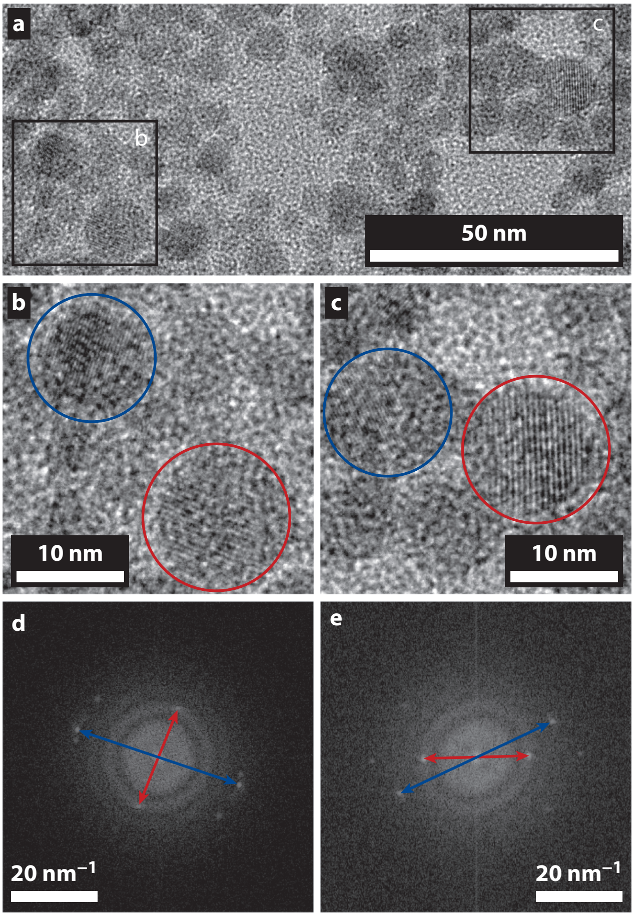

**Figure 4.4 | *Ex situ* electron microscopy of an aliquot taken midway during the reaction.** These experiments were performed on $NaLuF_4$ particles, which are chemically similar to $NaYF_4$ (Figure 4.40). (**a**) TEM image of an aliquot taken 30 min after the reaction mixture reached 300 °C. (**b,c**) Zooms of the areas highlighted with black squares in panel **a**. Blue and red circles highlight α- and β-phase particles, respectively. (**d,e**) Fast Fourier transforms of panels **b** and **c**, respectively. The spots highlighted with blue arrows are at a distance of $2\pi/d = 20\ \mathrm{nm}^{-1}$ from the origin, matching the {111} lattice spacing, $d_{111} = 0.31$ nm, of α-$NaLuF_4$.[153] The red arrows highlight spots matching the {100} lattice spacing, $d_{100} = 0.51$ nm, of β-$NaLuF_4$.[154] Comparing the orientation of the lattice planes in panels **b**,**c** with the angle of the spots in panels **d**,**e**, we identify the particles circled in blue as α-phase and those circled in red as β-phase. The additional peaks in the patterns, not indicated by arrows, are likely due to some small particles in the same region shown in panels **b**,**c**. See Figure 4.14 for more examples.

Our model simulates the evolution of the radii of spherical α-$NaYF_4$ particles as they exchange monomers with the surrounding solution. It thus focuses on the surprising evolution of the size distribution of α-$NaYF_4$ particles rather than on the transformation into the β-phase. Release of monomers results in particle shrinking, while uptake results in growth. The growth rate of a particle of radius $r$ is

$$\frac{\mathrm{d}r}{\mathrm{d}t} = f(r)\left(S - \mathrm{e}^{2\gamma/k_\mathrm{B}T\rho r}\right). \tag{4.1}$$

The factor between brackets describes how the growth rate depends on monomer concentration. It contains the surface energy $\gamma$ and number density $\rho$ of the particles, the thermal energy $k_\mathrm{B}T$, and the supersaturation $S$, defined as the monomer concentration normalized to the concentration of a solution in equilibrium with bulk α-$NaYF_4$. The prefactor $f(r)$ describes the radius dependence of the reaction rate. We take $f(r) = A/r^2$, which reflects a size-dependent rate constant for monomer uptake/release[100] and allows for straightforward tuning of a particle's reaction rate through the value of $A$. Slightly different expressions for $f(r)$ have been used for the cases of diffusion- or reaction-limited growth with size-independent rate constants.

We model the simultaneous growth of particles with uniformly distributed rate constants $A$. This tests whether α-$NaYF_4$ particles with a continuous distribution of reaction rates can evolve from a unimodal to a bimodal and back to a unimodal size distribution (Figure 4.5a). We approximate the continuous distribution with 80 different types of particles, having values of $A$ of $\{A_\mathrm{max}/80, 2A_\mathrm{max}/80, 3A_\mathrm{max}/80, \ldots, A_\mathrm{max}/80\}$. We start off the simulation with the same number of each type of particle (Figure 4.5b; top) and initiate each type with Gaussian distribution in radius with mean 2 nm and standard deviation 0.25 nm (Figure 4.5c; top). We discretize the radius distributions and make the radii evolve according to Equation 4.1. The time dependence of $S$ is tracked simultaneously, as it changes because of monomer uptake and release by the particles. The value of $S$ is initiated such that at $t = 0$ the monomers are in equilibrium with particles of the mean radius (2 nm). This means that particles smaller than the mean tend to dissolve, while larger particles grow. Chapter 4.7 provides more details on the algorithm of this simplified reaction model, while the text below presents the results and interpretation.

Figures 4.5b–e show the simulation results. Midway during the reaction, half of the particles with the fastest reaction rate have dissolved (Figure 4.5b; mid, purple) while the other half have significantly grown (Figure 4.5c; mid, purple). Meanwhile, particles with an intermediate reaction rate dissolved more (Figure 4.5b; mid, blue) and grew less (Figure 4.5c; mid, blue) than the fast-reacting particles. Slowly reacting particles hardly dissolved (Figure 4.5b; mid, green) nor changed size (Figure 4.5c; mid, green). At late stages of the reaction, particles of intermediate and slow reaction rates have dissolved nearly completely, while the fast-reacting particles survive (Figures 4.5b,c; bottom). This evolution of number of particles is summarized in Figure 4.5d. It produces an overall particle size distribution that is unimodal initially, is bimodal midway during the reaction, and then returns to unimodal (Figure 4.5e). Hence, a continuous distribution of reaction rates (through parameter $A$)

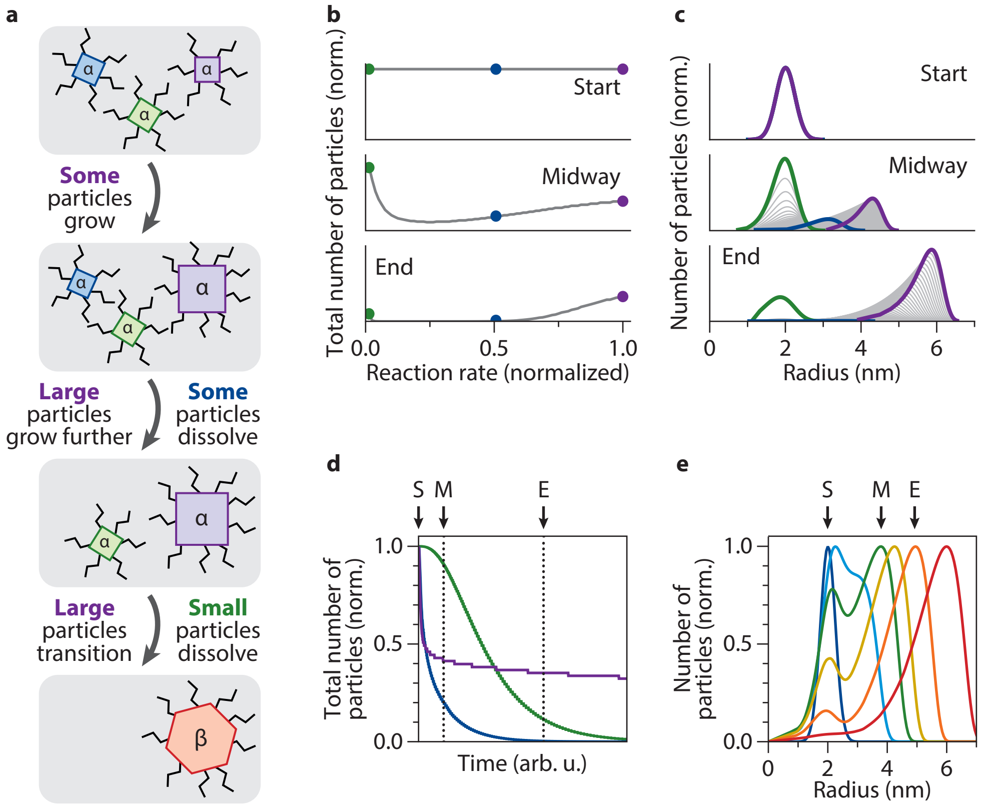

**Figure 4.5 | Simulation of the splitting size distribution of α-phase particles.** (**a**) Schematic of the proposed synthesis mechanism, based on *in situ* SAXS and WAXS. Some of the initial α-phase precursor particles grow, while the others remain small, producing a bimodal size distribution midway during the reaction. The large particles transform into β-phase while the small particles dissolve eventually. (**b**) Our rate equation model couples particles of different reaction rates through uptake and release of monomers in the solution. From top to bottom: the number of particles at different reaction rates at different stages of the reaction. In our model, particles can grow or dissolve, while the reaction rate constant $A$ (see text) is fixed. (**c**) From top to bottom: size distributions of particles of 80 different reaction rates (gray lines) at different stages of the reaction. Highlighted are the size distributions of the particles reacting most slowly (in green), at the mean rate (in blue), and fastest (in purple). (**d**) Time evolution of the number of particles reacting most slowly (green), at the mean rate (blue), and fastest (purple). The times denoted "Start" (S), "Midway" (M), and "End" (E) in panels **b** and **c** are indicated. (**e**) Total simulated size distribution (number of particles per unit of radius) at increasing reaction time, going from blue to red.

can naturally produce a bimodal size distribution of particles coupled through monomer exchange.

The simulation results of Figures 4.5b–e help us explain the evolution of the particle size distribution intuitively. The size distribution is bimodal midway during the reaction because: (1) particles with fast reaction rates grow rapidly, (2) particles with slow reaction rates have not had sufficient time to change size, (3) particles with intermediate reaction rates are too slow to keep up with the growth of the fastest particles, but sufficiently fast to dissolve as the few growing particles reduce the monomer concentration. The distinct minimum in the growth rate distribution (Figure 4.5b; mid) results in the bimodal size distribution in the simulation (Figure 4.5e), which we also observe experimentally (Figure 4.3b).

## 4.3 Conclusion

Our combined *in situ* scattering experiments, *ex situ* electron microscopy, and kinetic modeling provide a new mechanistic picture of the synthesis of β-$NaYF_4$ NCs. As the reaction temperature is reached, a subensemble of the α-$NaYF_4$ precursor particles with higher reactivity starts growing. Whether or not an α-$NaYF_4$ precursor particle grows may be determined by its stoichiometry. While stoichiometry likely varies continuously across the ensemble of particles, the simulation shows that this can produce the bimodal size distribution that we observe midway during the reaction. The subensemble of α-$NaYF_4$ particles largest in size then transforms into β-$NaYF_4$, likely because of a size-dependent balance between surface and bulk free energies of the two phases.[157] Meanwhile, the smaller α-$NaYF_4$ particles dissolve as larger particles (α- or β-phase) consume monomers from solution. The consumption of smaller α-$NaYF_4$ particles might accelerate as the larger particles transition into the thermodynamically more stable β-phase. Our experiments show that, if this happened, it would be *after* the bimodal size distribution appears (Figure 4.2).[158] The simulation does not include this phase transformation and its potential effect on growth rates explicitly, because it aims to test the origin of the bimodal size distribution conceptually.

The sequence of events we uncovered here is markedly different from commonly considered reaction mechanisms for NC synthesis. In particular, a mechanism of dissolution of α-phase and simultaneous nucleation of β-phase particles is excluded by the observation of growing α-$NaYF_4$ particles (Figures 4.3e,g). Non-classical mechanisms of growth by attachment or coalescence are unlikely given the continuously shifting peaks in the size distribution (Figures 4.3a–c). The proposed role of stoichiometry variations offers a new handle to optimize synthesis outcomes. Indeed, existing synthesis procedures have used the overall stoichiometry in a reaction mixture to, for example, tune particle size[150] or prevent secondary nucleation.[135] Clever strategies with intentional stoichiometry variations among precursor particles might enable the one-pot synthesis of core–shell or gradient-composition β-$NaREF_4$ NCs, using rapidly reacting precursors with high Na/RE ratio[150] for the core and slowly reacting precursors with (gradually) lower Na/RE ratio[150] for the (graded) shell. Such procedures might not only be more time-efficient, but also lead to a less defective core–shell interface or doping concentration gradients that guide the internal energy flow in the NCs.[137–142] Beyond Na-$REF_4$, stoichiometry-dependent reaction rates could be key in the synthesis mechanisms of various other material classes with loose stoichiometries, including hybrid organic/inorganic perovskites, Cu- and Ag-containing semiconductors, or metal alloys.

## 4.4 Additional figures

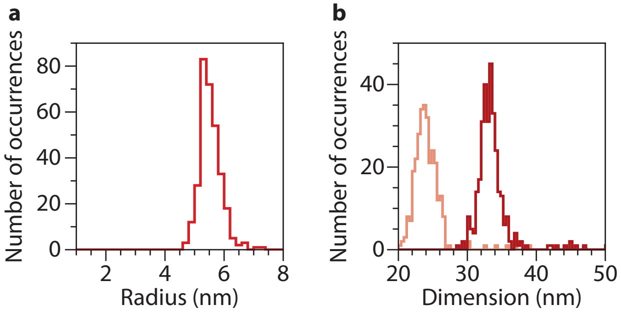

**Figure 4.6 |** (**a**) Statistical analysis of particle sizes as observed by TEM on the final β-$NaYF_4$:$Er^{3+}$,$Yb^{3+}$ NCs synthesized during *in situ* SAXS and WAXS experiments. These as the experiments discussed in Chapter 4.2. A representative TEM image is shown in Figure 4.1e. The number-weighted radii are 5.5 ± 0.4 nm (mean ± standard deviation). (**b**) Same as **a**, but for β-$NaLuF_4$:$Er^{3+}$,$Yb^{3+}$ NCs. A representative TEM image is shown in Figure 4.10e. The final product is non-spherical, with number-weighted axis lengths of 24.2 ± 2.2 nm and 33.5 ± 2.5 nm. *In situ* SAXS and WAXS results are shown in Figures 4.11,4.12.

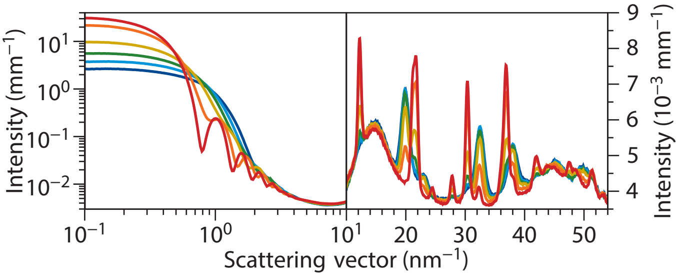

**Figure 4.7 |** Unshifted SAXS patterns and full-range WAXS patterns on the formation of β-$NaYF_4$:$Er^{3+}$,$Yb^{3+}$ NCs at the same times as the data in Figure 4.2 in panels **b** and **c**. See Chapter 4.2 for the discussion of the data.

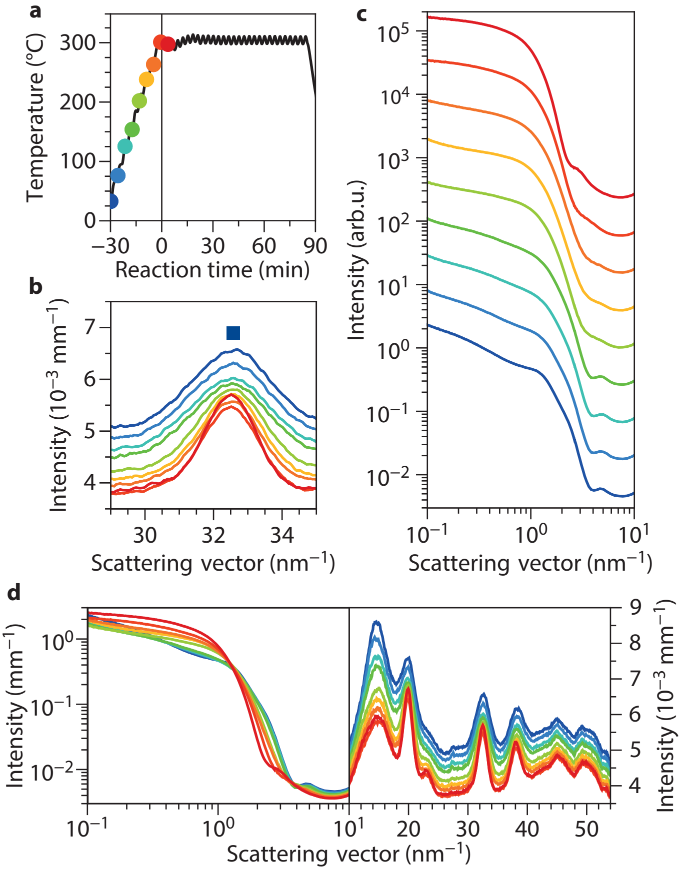

**Figure 4.8 | *In situ* measurements on the formation of β-$NaYF_4$:$Er^{3+}$,$Yb^{3+}$ NCs during heat-up to 300 °C until *t* = 5 min.** (**a**) The temperature recorded by a thermocouple during the synthesis procedure as a function of reaction time. Colored dots highlight moments of the recordings shown in panels **b**–**d**. (**b**) Wide-angle X-ray scattering (WAXS) patterns recorded at times defined in panel **a**. The diffraction peak due to the α-phase is indicated with a blue square:[153] Although less evident due to changing background scattering, the peak narrows indicating some particle growth and/or increase in crystallinity during heat-up. (**c**) Small-angle X-ray scattering (SAXS) patterns recorded at the same times as the data in panel **b**. (**d**) Unshifted SAXS patterns and full-range WAXS patterns same times as the data in panels **b** and **c**. Initially, the SAXS patterns do not match the form factor scattering as expected for isolated spherical particles; the particles are clustered, resulting in structure factor scattering. The presence of structure factor scattering is especially clear at low scattering vectors where the scattering pattern is not flat, and at $q = 1$ $nm^{-1}$ where there is a structure factor peak. After reaching 300 °C around $t = 5$ min, the scattering patterns become flat at low scattering vectors, and it is possible to fit the patterns with a model of spherical particles with a distribution of radii, as discussed in Chapter 4.2.

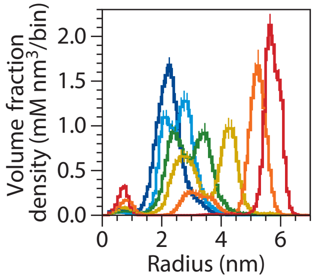

**Figure 4.9 |** Six size distributions as obtained from the Monte Carlo fitting procedure. Colors correspond to the same times as in Figure 4.2c and those highlighted by colored disks in Figure 4.2a and Figure 4.3. The *y*-axis shows volume fraction density, *i.e.*, the particle volume per unit of reaction mixture volume per unit of radius. The bin width on the *x*-axis is 0.1 nm. This plot includes the material with radius <1 nm, the gray area in Figure 4.3e.

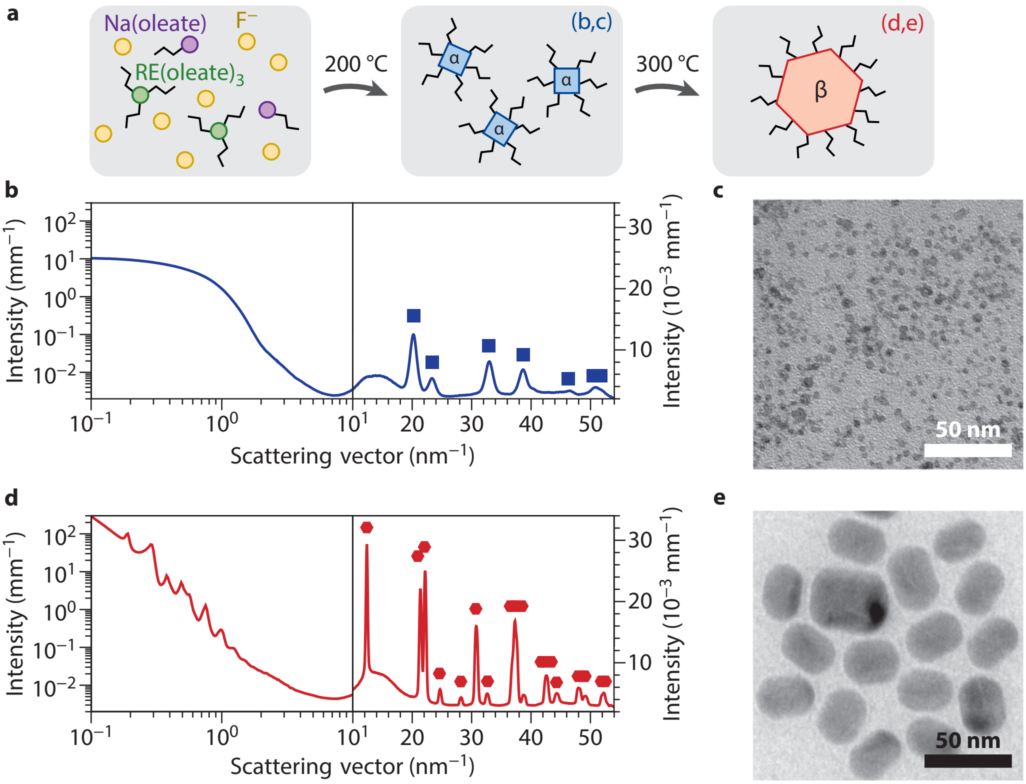

**Figure 4.10 | Synthesis of β-$NaLuF_4$:$Er^{3+}$,$Yb^{3+}$ NCs from α-$NaLuF_4$:$Er^{3+}$,$Yb^{3+}$ precursor particles.** (**a**) Schematic of the two-step synthesis procedure. Step 1: Na(oleate), $F^-$, and RE(oleate)$_3$ (with RE = Lu, Er, Yb) form small α- $NaLuF_4$:$Er^{3+}$,$Yb^{3+}$ precursor particles. Step 2: The precursor particles transform into larger β-$NaLuF_4$:$Er^{3+}$,$Yb^{3+}$ NCs. (**b**) SAXS and WAXS patterns of the α-$NaLuF_4$:$Er^{3+}$,$Yb^{3+}$ particles at 300 °C. Diffraction peaks expected for α-$NaLuF_4$ are indicated with blue squares.[153] A fit of the SAXS pattern with the McSAS method described below, gives a radius of 2.5 ± 0.9 nm. (**c**) Transmission electron micrograph on the α-$NaLuF_4$:$Er^{3+}$,$Yb^{3+}$ particles before heating to 300 °C. (**d**) Same as in panel **b** but for the β-$NaLuF_4$:$Er^{3+}$,$Yb^{3+}$ product NCs measured after 131 min at 300 °C. The reference for β-$NaLuF_4$ in WAXS is shown with red hexagons.[154] (**e**) Transmission electron micrograph on an aliquot taken at 150 min. The β-$NaLuF_4$:$Er^{3+}$,$Yb^{3+}$ NCs are anisotropic with dimensions 24.2 ± 2.2 nm and 33.5 ± 2.5 nm (Figure 4.6b).

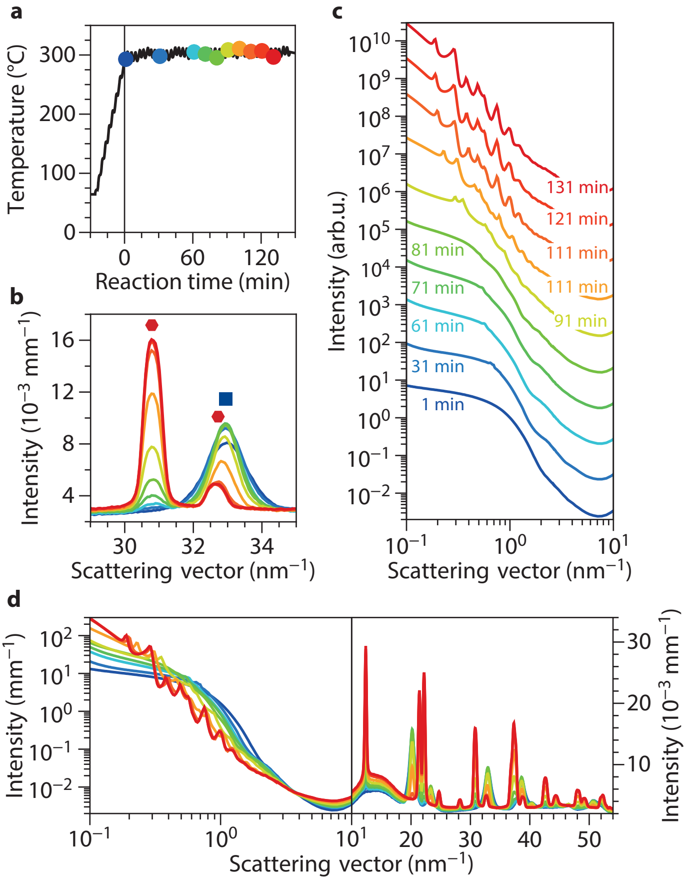

**Figure 4.11 | *In situ* measurements of phase transformation and growth during the formation of β-$NaLuF_4$:$Er^{3+}$,$Yb^{3+}$ NCs.** (**a**) The temperature recorded by a thermocouple during the synthesis procedure as a function of reaction time. Colored dots highlight moments of the recordings shown in panels **b**–**d**. (**b**) Wide-angle X-ray scattering (WAXS) patterns recorded at different times (see panel **a**), showing the phase transition from α- to β- $NaLuF_4$:$Er^{3+}$,$Yb^{3+}$. Diffraction peaks due to the α- and β-phases are indicated with a blue square and red hexagons, respectively: the 220 (32.96 nm$^{-1}$) reflection of α-$NaLuF_4$ and the 201 (30.81 nm$^{-1}$) and 210 (32.66 nm$^{-1}$) reflections of β-$NaLuF_4$. Nanocrystal growth is evident from the peak narrowing. (**c**) Small-angle X-ray scattering (SAXS) patterns recorded at the same times as the data in panel **b**. (**d**) Unshifted SAXS patterns and full-range WAXS patterns same times as the data in panels **b** and **c**. Early in the synthesis, sharp features arise in the SAXS patterns around 0.6 nm$^{-1}$, indicative of structure factor scattering due to clustering of the NCs. The slope at lower scattering vectors also indicates the presence of clusters; the clusters have sizes larger than the NCs resulting in scattering at lower scattering vectors. At the end of the synthesis, the features shift and become more apparent, most likely due to both NC growth and cluster size growth. The peak positions indicate hexagonally packed columns of stacked NCs with a stacking distance of 33 nm and an intercolumn separation of 22 nm. These dimensions correspond well to the sizes obtained from the TEM analysis in Figure 4.6b, 33.5 ± 2.5 nm and 24.2 ± 2.2 nm, respectively.

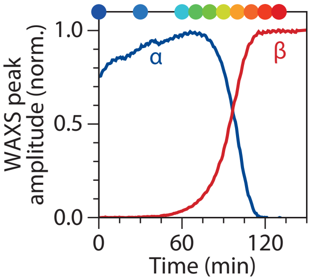

**Figure 4.12 |** Amplitude of the WAXS peaks at 20.19 $nm^{-1}$ (blue; α-$NaLuF_4$, 111 reflection) and 30.81 $nm^{-1}$ (red; β-$NaLuF_4$, 201 reflection) as a function of reaction time. Colors correspond to the same times as in Figure 4.11. The conversion takes longer for $NaLuF_4$ than for $NaYF_4$, as discussed in Chapter 4.2.

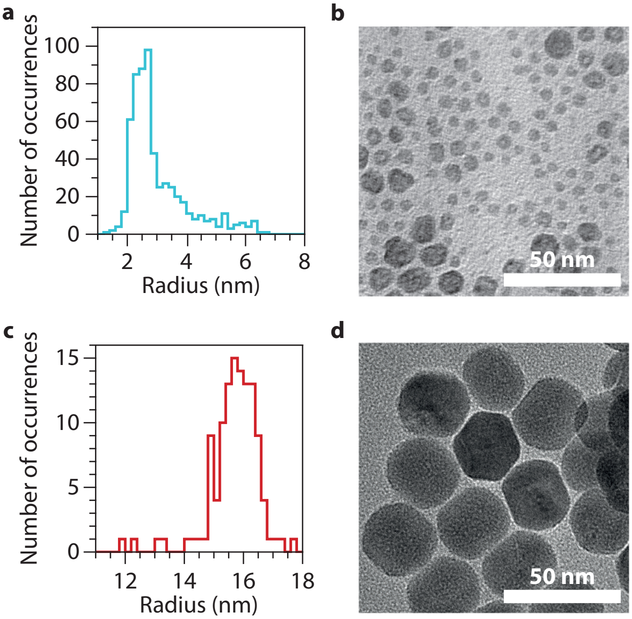

**Figure 4.13 |** TEM analysis on the β-$NaLuF_4$:$Er^{3+}$,$Yb^{3+}$ NCs synthesis with aliquots. (**a**,**b**) Histogram and TEM of aliquot taken after 60 min at 300 °C. The sample is highly polydisperse with number-weighted radii of 3.0 ± 1.0 nm. (**c**,**d**) Histogram and TEM of product obtained after heating for 2 h at 300 °C. The number-weighted radii are 15.7 ± 1.0 nm.

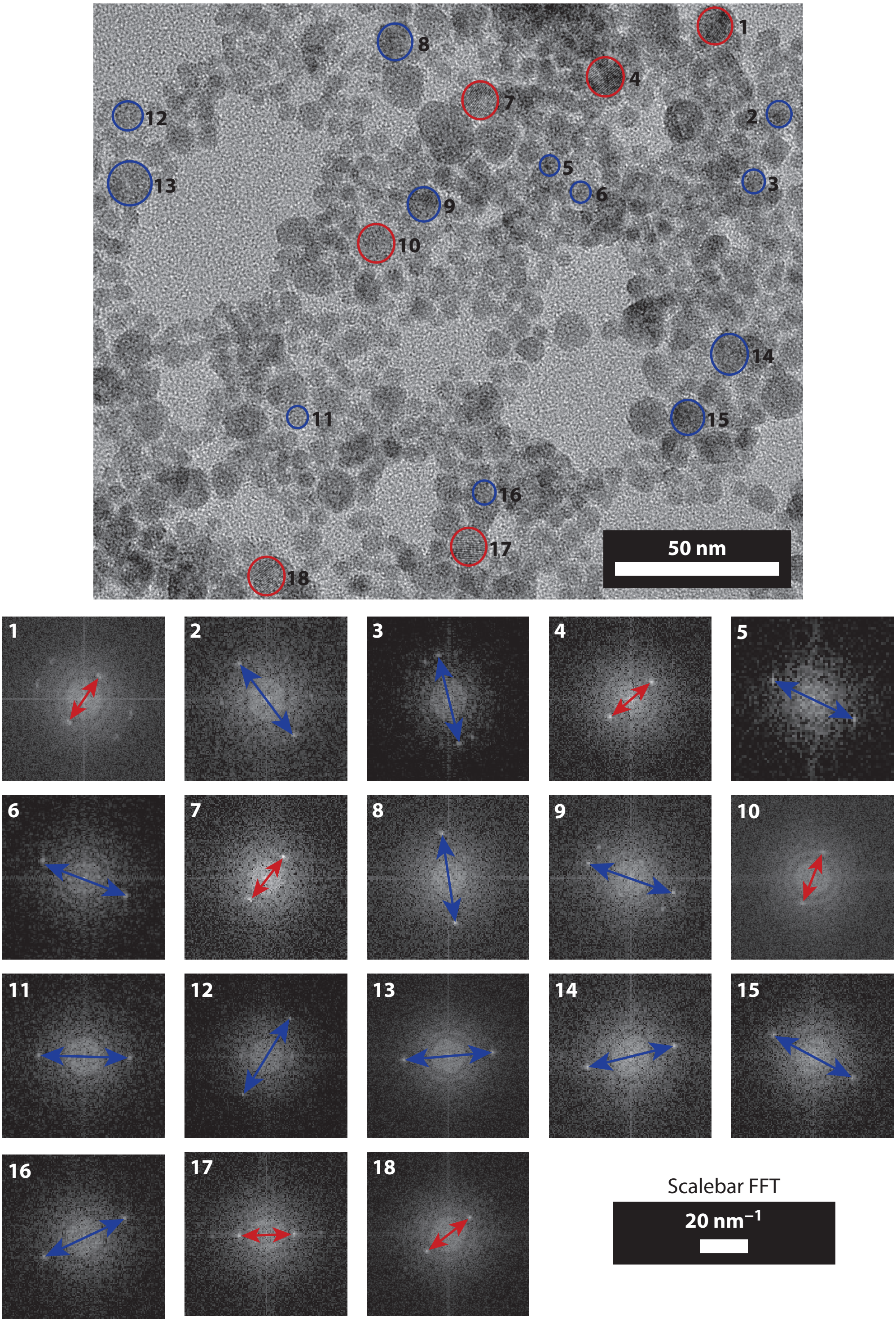
1
4
7
8
2
12
5
13
6
3
9
10
14
11
15
16
17
18
50 nm
1
2
3
4
5
6
7
8
9
10
11
12
13
14
15
16
17
18
Scalebar FFT
20 nm$^{-1}$

**Figure 4.14 (left page) | *Ex situ* electron microscopy of an aliquot taken midway during the formation of β-$NaLuF_4$:$Er^{3+}$,$Yb^{3+}$ NCs.** Panels display an extended analysis of the sample discussed in Figure 4.4. Below fast Fourier transforms of the circled and numbered areas in the TEMs are given. The particles highlighted in blue are identified as α-phase particles and in red as β-phase. As in Figure 4.4, the spots highlighted with blue arrows are at a distance of $2\pi/d = 20\ \text{nm}^{-1}$ from the origin, matching the {111} lattice spacing, $d_{111} = 0.31$ nm, of α-$NaLuF_4$. The red arrows highlight spots matching the {100} lattice spacing, $d_{100} = 0.51$ nm, of β-$NaLuF_4$.

## 4.5 Methods

*Synthesis of α-$NaYF_4$:$Yb^{3+}$,$Er^{3+}$ and α-$NaLuF_4$:$Yb^{3+}$,$Er^{3+}$ precursor particles.* α-$NaYF_4$:$Er^{3+}$,$Yb^{3+}$ precursor particles were synthesized using the protocol by Homann *et al.*[127] For the first step, the synthesis of the α-$NaYF_4$:$Er^{3+}$,$Yb^{3+}$ particles, 4.06 g (12 mmol) yttrium acetate tetrahydrate, 1.14 g (2.7 mmol) ytterbium acetate tetrahydrate, and 0.126 g (0.3 mmol) erbium acetate tetrahydrate were combined with 150 mL oleic acid and 150 mL 1-octadecene in a 1 L flask. The mixture was kept under vacuum for 1 h at room temperature followed by 2 h at 100 °C to degas and remove the acetic acid. Next, 13.7 g (45 mmol) sodium oleate was added under a nitrogen flow, and the vacuum was reapplied while the sodium oleate dissolved. Afterward, 3.33 g (90 mmol) ammonium fluoride was added under nitrogen flow, and subsequently, the reaction vessel was flushed three times to eliminate oxygen by alternating a short vacuum and refilling with nitrogen. The mixture was heated to 200 °C under a nitrogen atmosphere and kept at this temperature for 1 h. After letting the reaction mixture cool down to room temperature, the nanoparticles were extracted from the reaction mixture by a few purification steps. First, ethanol was added with a ratio of 1:2 of reaction mixture to ethanol, and the mixture was centrifuged at 2750 rpm for 5 min. The precipitate was redispersed in 100 mL hexane and centrifuged at 1000 rpm for 10 min. The sediment, the byproduct NaF, was discarded. The nanocrystal dispersion was washed once more with a 1:2 ratio of reaction mixture to ethanol and centrifuged at 3000 rpm. The precipitate was redispersed in 10 g hexane. The dispersion contains 17.4 wt% of α-$NaYF_4$:$Er^{3+}$,$Yb^{3+}$ material, as determined by thermal gravimetric analysis (TGA) measurements showing a weight loss of 40% due to the ligands.

$NaLuF_4$:$Er^{3+}$,$Yb^{3+}$ nanocrystals were synthesized using the method described above with 3.66 g (8.64 mmol) lutetium acetate tetrahydrate, 0.820 g (1.94 mmol) ytterbium acetate tetrahydrate, 0.090 mg (0.22 mmol) erbium acetate tetrahydrate, 108 mL oleic acid and 108 mL 1-octadecene. The mixture was degassed overnight at 120 °C. In the subsequent steps, 9.84 g (32.4 mmol) sodium oleate and 2.40 g (64.8 mmol) ammonium fluoride were added. The dispersion contains 14.1 wt% α-$NaLuF_4$:$Er^{3+}$,$Yb^{3+}$ material, as determined by TGA showing a weight loss of 22.6% due to the ligands.

*Formation of β-$NaYF_4$:$Yb^{3+}$,$Er^{3+}$ and β-$NaLuF_4$:$Yb^{3+}$,$Er^{3+}$ nanocrystals.* The β-$NaYF_4$:$Er^{3+}$,$Yb^{3+}$ nanocrystals were synthesized *in situ* at the beamline in a custom designed flask[100,148] with a reduced volume compared to the protocol by Homann *et al.*[127] Therefore, the synthesis was down-scaled to three-tenth of the standard reaction volume. 1.78 g of the hexane dispersion containing 1.5 mmol of $NaYF_4:Er^{3+},Yb^{3+}$ units, 3 mL oleic acid, and 3 mL 1-octadecene were combined in this flask and put under vacuum for 30 min at room temperature and at least 1 h at 50 °C to degas the mixture and remove the hexane. The mixture was then put under a nitrogen atmosphere and heated to 300 °C with a ramp rate of 10 °C $min^{-1}$. After 90 min, the mixture was cooled down to room temperature. The reaction mixture was purified twice with ethanol (1:4 ratio of reaction mixture to ethanol, 3000 rpm) and redispersed in 6 g hexane.

For the $\beta$-$NaLuF_4:Er^{3+},Yb^{3+}$ synthesis at the beamline, 2.42 g of the hexane dispersion containing 1.25 mmol of $NaLuF_4:Er^{3+},Yb^{3+}$ units was combined with 2.5 mL oleic acid and 2.5 mL 1-octadecene. The same procedure was used as for the synthesis of $\beta$-$NaYF_4:Er^{3+},Yb^{3+}$ nanoparticles. Reaction time at 300 °C was 180 min.

2.92 g (1.5 mmol) of the $\alpha$-$NaLuF_4:Er^{3+},Yb^{3+}$ nanoparticles dispersed in hexane was combined with 3 mL oleic acid and 3 mL 1-octadecene for the $\beta$-$NaLuF_4:Er^{3+},Yb^{3+}$ with aliquots synthesis. The reaction time for this synthesis was 120 min at 300 °C. The aliquot of Figure 4.4 was taken at 60 min at 300 °C.

*Small- and wide-angle X-ray scattering measurements.* The SAXS and WAXS experiments were performed at I22 of synchrotron Diamond at an energy of 20 keV ± 2.3 eV using a Pilatus P3-2M SAXS detector and a P3-2M-DLS L-shaped WAXS detector. The sample-to-detector distance to the SAXS and WAXS detectors was 216 mm and 9776 mm, respectively. This enabled us to probe a $q$-range of 0.023–3.1 $nm^{-1}$ for SAXS and a range of 2.4–61 $nm^{-1}$ for WAXS. The scattering patterns were collected with an exposure time of 1 s followed by a waiting time of 4 s. The beamline setup and data acquisition of I22 are discussed in ref 152.

The SAXS and WAXS experiments were conducted under nitrogen flow in a custom-made three-neck flask and setup discussed in detail in refs 100,148. In these experiments, a Vigreux was added on top of the flask instead of an injector.

*TEM measurements.* TEM samples were prepared by drop-casting a diluted (100–1000 times) dispersion of NCs onto a copper TEM grid. The TEM grids of the $NaLuF_4:Er^{3+},Yb^{3+}$ aliquots, which were not purified, were treated with a mixture of ethanol and activated carbon as described in ref 159 to reduce contamination by hydrocarbons during imaging. The measurements on $NaLuF_4:Er^{3+},Yb^{3+}$ were performed on a FEI Talos F200X operating at 200 keV, and other TEM measurements were performed on a FEI Tecnai 20 operating at 200 keV.

## 4.6 Data analysis

*Data preparation for fitting.* The SAXS and WAXS patterns contain the scattering of the NCs but also from additional components. This background scattering needs to be removed before the data can be analyzed. Background scattering originates from the setup, flask, and the mixture of oleic acid and 1-octadecene (OA/ODE). The isolated scattering of these components is obtained by measuring

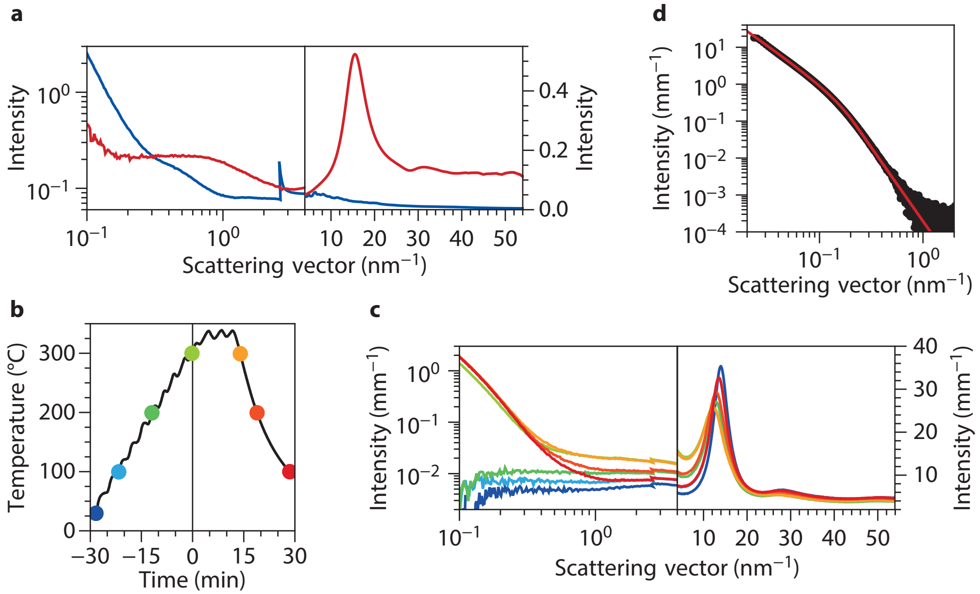

**Figure 4.15 |** (**a**) SAXS and WAXS from the empty beam path (blue) and an empty reaction flask (red). (**b**–**d**) Temperature dependence of the SAXS and WAXS from a mixture of 3 mL oleic acid (OA) and 3 mL octadecene (ODE). (**b**) Temperature recorded with a thermocouple during the heating of a solvent mixture of OA and ODE as a function of time. Colored dots highlight moments of the recordings shown in panel **c**. (**c**) SAXS and WAXS patterns recorded at times defined in panel **b**. The scattering intensity at $q < 1\ nm^{-1}$ is not reversible when cooling down. (**d**) Component of the SAXS that is time-dependent, extracted from the patterns shown in panel **c**. The red line is a fit with a general model for the Guinier and Porod regime (see text below). The best fit is obtained with a radius of gyration of 4.5 nm. The temperature dependence of the WAXS pattern is fully reversible and only depends on temperature.

---

an empty beam path, an empty flask, and a flask with OA/ODE inside, respectively. The SAXS and WAXS patterns of the empty beam and empty flask are shown in Figure 4.15a. The scattering of OA/ODE is temperature dependent and was for that reason measured as a function of temperature. The temperature-dependent patterns are shown in Figures 4.15b–d.

When measuring the temperature-dependent SAXS and WAXS of the solvent mixture without any nanoparticles, *i.e.*, 3 mL OA and 3 mL ODE, we observed that part of the SAXS did not depend on temperature alone but also on time. Additional scattering, noticeable from $q = 0.03–0.5\ nm^{-1}$, appears after 260 °C, increases with time, and remains when cooling down to room temperature. We could isolate the additional scattering by comparing the scattering before and after heating and subtracting the temperature-dependent contribution. The time-dependent scattering pattern, shown in Figure 4.15d, has a slope of $q^{-2}$ in the Guinier regime (low $q$) and $q^{-4}$ in the Porod regime (high $q$). This is the same pattern that would be produced by Gaussian polymer chains or randomly oriented two-dimensional structures (lamellae or platelets). We thus used scattering models of these structures to obtain an analytical model for the background signal. When performing a least square fitting with the shape-specific model from ref 160, we obtain a radius of gyration of 4.5 nm. We hypothesize that the scattering originates from polymerized 1-octadecene, as discussed in ref 161.

In total we consider five contributions to the *in situ* SAXS and WAXS patterns: the nanocrystals, the setup, the flask, the OA/ODE mixture, and the polymer structures

$$I(q,t,T) = I_{\mathrm{NC}}(q,t,T) + I_{\mathrm{setup}}(q) + a_1 I_{\mathrm{flask}}(q) + a_2 I_{\mathrm{OA+ODE}}(q,T) + a_3(t) I_{\mathrm{polymer}}(q). \tag{4.2}$$

Values of 0.9 and 0.65 were obtained for the prefactors $a_1$ and $a_2$, respectively. These values are independent of time and temperature. The prefactor $a_3$ is determined by a least-square fitting method for every scattering pattern. Specifically, as the polymer structures are the only contribution that produces a sloped SAXS pattern at low $q$, the low-$q$ region is a sensitive probe for $a_3(t)$. Since we now know all factors involved, we can obtain $I_{\mathrm{NC}}(q, t, T)$. To speed up the fitting process in the next step, we rebinned the data to 162 data points on the interval $q = 0.1–7\ \mathrm{nm}^{-1}$.

Lastly, we have to correct the intensity for the pathlength of the flask to obtain the intensity in units of $\mathrm{mm}^{-1}$. The pathlength of the flasks was acquired by measuring the transmission through the flask with and without chloroform. Using the known attenuation length of chloroform at 20 keV, 1.01 mm, we obtained a pathlength of 4.5 mm and 4.1 mm through the flasks used for the $NaYF_4:Er^{3+},Yb^{3+}$ and $NaLuF_4:Er^{3+},Yb^{3+}$ synthesis, respectively.

The curve of $I_{\mathrm{NC}}(q, t, T)$ corrected for pathlength was provided to the McSAS program for further analysis of particle size distributions.

*Thermal expansion.* The amount of starting material in the synthesis is 1.5 mmol of $\alpha$-$NaYF_4:Er^{3+},Yb^{3+}$ units as discussed above. At room temperature, the volume of the mixture is 3 mL OA and 3 mL ODE. However, at 300 °C this volume will expand due to thermal expansion of OA and ODE, following

$$V_2 = V_1 \exp\left[\int_{T_1}^{T_2} \alpha_V(T)\mathrm{d}T\right], \tag{4.3}$$

with $V_1$ and $V_2$ the volume at 20 °C ($T_1$) and 300 °C ($T_2$), respectively. $\alpha_V(T)$ is the temperature-dependent volume-expansion coefficient obtained from Yaws.[162] The obtained volumes are 3.9 mL OA and 4.1 mL ODE at 300 °C. With a total volume of 8 mL, we obtain a concentration of $\alpha$-$NaYF_4:Er^{3+},Yb^{3+}$ units at $t = 0$ of $c_{\mathrm{NaYF_4}} = 0.19\ \mathrm{mol\ L^{-1}}$.

The thermal expansion of $\alpha$-$NaYF_4:Er^{3+},Yb^{3+}$ is less compared to the reaction mixture but was still taken into account. The unit cell volume increases from 0.551 $\mathrm{nm}^3$ at 20 °C to 0.555 $\mathrm{nm}^3$ at 300 °C using a volume thermal expansion coefficient of $81.68 \cdot 10^{-6}\ \mathrm{K}^{-1}$.

In relation to the volume changes calculated above, the densities of OA, ODE, and $\alpha$-$NaYF_4:Er^{3+},Yb^{3+}$ decrease due to thermal expansion from 0.888, 0.785, and 4.062 g $\mathrm{cm}^{-3}$ at 20 °C to 0.570, 0.690, and 3.970 g $\mathrm{cm}^{-3}$ at 300 °C respectively. These values were used to calculate the theoretical scattering length density (SLD), see text below.

*Data fitting with McSAS.* The particles investigated here are quasi-spherical, and for that reason, we used a model for spheres with a distribution of radii. The scattering intensity for spheres with a discrete distribution of radii

$$I(q) = \Delta\rho^2 \sum_{k=R_{\min}}^{R_{\max}} \frac{\phi_k}{V_k} \left[ \frac{3V_k(\sin(qR_k) - qR_k\cos(qR_k))}{(qR_k)^3} \right]^2 + B, \tag{4.4}$$

where $\Delta\rho$ is the SLD difference between the spheres and the medium, $R_{\min}$ and $R_{\max}$ are the radius of the smallest (0.05 nm) and largest (7.95 nm) bin respectively, $\phi_k$ is the volume fraction of nanocrystals in bin $k$, $V_k$ is the volume of particles in bin $k$, and $B$ is a constant background contribution. When optimizing the model, the McSAS code, discussed in ref 155, adjusts $\phi_k$ and $B$ to obtain a good fit. We used the following settings: 50,000 as maximum number of iterations, 2000 as number of contributions, 2/3 as compensation component, 20 as number of repetitions, and a convergence criterion of 3.5. This convergence criterion was too low for the early scattering patterns; a successful fit was not obtained within the maximum number of iterations. Thus, the convergence criterion was slightly increased to still obtain fitting results for the first few patterns.

*Scattering length densities.* When taking the limit $q \to 0$ of the Equation 4.4 above we obtain

$$\lim_{q\to 0} I(q) = \Delta\rho^2 \sum_{k=R_{\min}}^{R_{\max}} \phi_k V_k + B. \tag{4.5}$$

Given that at $t = 0$, the amount of α-$NaYF_4$:$Er^{3+}$,$Yb^{3+}$ is expected to be equal to the amount added, we get

$$\sum_{k=R_{\min}}^{R_{\max}} \phi_k = \frac{c_{NaYF_4} N_A V_{\mathrm{unitcell}}}{z_{\mathrm{unitcell}}}. \tag{4.6}$$

By inserting the number of units in a unit cell $z_{\text{unit cell}} = 2$, $c_{NaYF_4}$, and $V_{\text{unit cell}}$ as discussed above we obtain $\Delta\rho = 22.8 \cdot 10^{-6}$ Å$^{-2}$. To obtain this value we used the first 15 scattering patterns after $t = 0$, a period in which the yield does not change. This calculated value for $\Delta\rho$ corresponds well to the theoretical $\Delta\rho = 24.5 \cdot 10^{-6}$ Å$^{-2}$, calculated on the National Institute of Standards and Technology (NIST) website (https://www.ncnr.nist.gov/resources/activation/) using the densities of OA, ODE, and α-$NaYF_4$ at 300 °C specified above. For the reaction mixture, we used the volume weighted SLD using $6.58 \cdot 10^{-6}$ Å$^{-2}$ for OA and $5.55 \cdot 10^{-6}$ Å$^{-2}$ for ODE resulting in $6.05 \cdot 10^{-6}$ Å$^{-2}$. The calculated SLD for α-$NaYF_4$ is $30.58 \cdot 10^{-6}$ Å$^{-2}$.

We used $\Delta\rho = 22.8 \cdot 10^{-6}$ Å$^{-2}$ as an input parameter in the McSAS fitting procedure. Thereby, the fitting resulted in absolute volume fractions and NC concentrations. These results are shown and discussed in Chapter 4.2.

## 4.7 Simulation of particle growth

We simulate particles that change their radius $r$ in time $t$ according to

$$\frac{\mathrm{d}r}{\mathrm{d}t} = f(r)\left(S - \mathrm{e}^{2\gamma/k_\mathrm{B}T\rho r}\right), \tag{4.1}$$

where $\gamma$ and $\rho$ are the surface energy and density of the particles, and $k_\mathrm{B}T$ is the thermal energy. The supersaturation $S$ is the monomer concentration in solution normalized to the monomer concentration of a solution in equilibrium with a macroscopic crystal. We choose

$$f(r) = \frac{A}{r^2}. \tag{4.7}$$

This describes growth with a stronger size dependence than expected for diffusion- or reaction-limited growth with a size-independent rate constant. Such stronger size dependence is necessary to produce absolute size focusing in a synthesis where particles nucleate over a prolonged period.[100] The continuous distribution of reaction rate constants in our model makes size-dependent rate constants necessary to keep a narrow size distribution.

We initiate the model with a flat distribution of reaction rate constants $A$ uncorrelated with a Gaussian distribution of particle radii. To solve the evolution of sizes from Equation 4.7, we discretize the distribution of rate constants, the distribution of radii, and time. More precisely, we consider $M$ types of particles with reaction rate constants

$$A_j = \frac{j+1}{M} A_\mathrm{max}, \tag{4.8}$$

where $j \in \{0, 1, 2, \ldots M-1\}$. For each type $j$ of particle, we initiate the number of particles $n_{i,j}$ of radius $r_{i,j,0}$ (where 0 denotes start of the simulation; time $t = 0$) according to a Gaussian size distribution

$$n_{i,j} = \frac{8n_\mathrm{tot}}{\sqrt{2\pi MN}} \exp\left[-\frac{1}{2}\left(\frac{i-N/2}{N/8}\right)^2\right], \tag{4.9}$$

where $N$ is the number of discrete radii considered and $n_0$ is the total number of particles in the system

$$n_\mathrm{tot} = \sum_{j=0}^{M-1}\sum_{i=0}^{N-1} n_{i,j}. \tag{4.10}$$

The initial radii are uniformly distributed between $r_\mathrm{min}$ and $r_\mathrm{max}$

$$r_{i,j,0} = r_\mathrm{min} + \frac{i}{N-1}(r_\mathrm{max} - r_\mathrm{min}) \tag{4.11}$$

with $i \in \{0, 1, 2, \ldots N-1\}$. We see that the initial radii are independent of particle type $j$. We initiate the super-saturation at a value of

$$S_0 = \exp\left(\frac{2\gamma}{k_\mathrm{B}T\rho r_{N/2,M/2,0}}\right), \tag{4.12}$$

where again the subscript 0 denotes the start of the simulation ($t = 0$). The value of $S_0$ is such that particles at the peak of the size distribution, *i.e.*, those with radius $r_{N/2,j,0}$ (for any $j$), are stable at $t = 0$. Indeed, Equation 4.7 shows that $\mathrm{d}r/\mathrm{d}t = 0$ for these particles at $t = 0$.

Next, we let the particle radii evolve in discrete time steps

$$r_{i,j,t+1} = r_{i,j,t} + \frac{A}{r_{i,j,t}^2}\left(S_t - e^{2\gamma/k_B T \rho r_{i,j,t}}\right) \tag{4.13}$$

for all $i$ and all $j$. We update the supersaturation using

$$S_{t+1} = S_t + \frac{4\pi}{3}\rho \sum_{j=0}^{M-1}\sum_{i=0}^{N-1} n_{i,j}(r_{i,j,t}^3 - r_{i,j,t+1}^3). \tag{4.14}$$

If any of the radii $r_{i,j,t}$ ever drops below a threshold value $r_{\mathrm{th}}$, we immediately dissolve these particles ($n_{i,j} \to 0$) and no longer track this subset $(i, j)$. This step minimizes numerical errors as the radii of shrinking particles could otherwise go below zero.

From the simulation output we calculate particle size distributions as a function of time. The number $n_{i,j}$ of particles of type $j$ at time $t$ is converted into a 'density' $x_{i,j,t}$ of particles of type $j$ per unit of radius:

$$x_{i,j,t} = \frac{n_{i,j}}{r_{i+1,j,t} - r_{i-1,j,t}}. \tag{4.15}$$

This conversion is necessary because the radii become nonuniformly distributed as time progresses. We assign the value of density $x_{i,j,t}$ to a radius value of $r_{i,j,t}$. The particle size distributions presented in Figures 4.5c,e show these densities of particles per unit of radius.

For the simulation results in Figure 4.5, we used the following input values: $M = 80$, $N = 200$, $A_{\max} = 8 \cdot 10^{-5}$, $n_{\mathrm{tot}} = 0.31$, $r_{\min} = 1$, $r_{\max} = 3$, $r_{\mathrm{th}} = 0.1$, $\gamma/k_B T = 10$, and $\rho = 10$.

# Chapter 5

# The fine-structure constant as a ruler for the band-edge light absorption strength of bulk and quantum-confined semiconductors

Low-dimensional semiconductors have found numerous applications in optoelectronics. However, a quantitative comparison of the absorption strength of low-dimensional *versus* bulk semiconductors has remained elusive. Here, we report generality in the band-edge light absorptance of semiconductors, independent of their dimensions. First, we provide atomistic tight-binding calculations that show that the absorptance of semiconductor quantum wells equals $m\pi\alpha$ ($m = 1$ or 2 with $\alpha$ as the fine-structure constant), in agreement with reported experimental results. Then, we show experimentally that a monolayer (superlattice) of quantum dots has similar absorptance, suggesting an absorptance quantum of $m\pi\alpha$ per (confined) exciton diameter. Extending this idea to bulk semiconductors, we experimentally demonstrate that an absorptance quantum equal to $m\pi\alpha$ per exciton Bohr diameter explains their widely varying absorption coefficients. We thus provided compelling evidence that the absorptance quantum $\pi\alpha$ per exciton diameter rules the band-edge absorption of all direct semiconductors, regardless of their dimension.

**Based on**

P.T. Prins, M. Alimoradi Jazi, N.A. Killilea, W.H. Evers, P. Geiregat, W. Heiss, A.J. Houtepen, C. Delerue, Z. Hens, D.A.M. Vanmaekelbergh

Nano Letters **21**, 9426–9432 (2021)

## 5.1 Introduction

Low-dimensional semiconductors and quantum wells play a key role in optoelectronic devices, such as infrared photodetectors, solar cells, lasers, and phosphors in displays and LEDs.[9,163–168] Optical transitions over the fundamental gap involve the valence hole and conduction electron states. The absorption and emission spectra depend on the semiconductor band structure and thus on the degree of electron (hole) confinement. Regarding the *energetics* of optical transitions, the effects of quantum confinement have been extensively studied, and this knowledge has resulted in a tremendous series of applications. The effects of confinement on the rate or *strength* of optical transitions are less documented and especially for band-edge absorption, a quantitative comparison between semiconductor nanostructures and bulk semiconductors is still very much needed. For one thing, such an analysis is hampered by the impact of dielectric screening on transition rates. For instance, for zero-dimensional (0D) quantum dots (QDs), the dielectric contrast between the semiconductor and its surroundings leads to a substantial reduction of the incident electromagnetic field within the QD, which lowers the effective transition rates.[116,169–171] Considering quasi-spherical QDs, a systematic correction for screening effects made clear that QDs exhibit similar absorption coefficients as the corresponding bulk semiconductors at energies where quantum confinement is negligible.[116] But a quantitative comparison on the strength of band-edge absorption and the effects of quantum confinement on this is lacking, although semiconductor QDs are often qualified as “strong” absorbers and emitters. The band-edge transition in QDs is typically characterized by an oscillator strength or integrated cross section, not unlike a two-level system (see Chapter 5.4). These quantities are valid as descriptors. However, these quantities obscure possible similarities or differences with band-edge absorption in bulk semiconductors, which is typically described by an absorption coefficient.

Here, we use the notion of absorptance per active element, *i.e.*, the volume of the electron–hole exciton, to compare the band-edge absorption strength of a wide variety of direct semiconductors from three-dimensional (3D) bulk semiconductors to 0D QDs. This means that for 0D QDs we measure the absorptance of a compact monolayer of QDs to obtain the absorptance per confined exciton volume; for bulk semiconductors, we derive the absorptance per bulk exciton volume from the absorption coefficient spectrum and the exciton Bohr diameter, obtained from the effective electron and hole mass. As a starting point, we reconsider the absorptance of two-dimensional (2D) semiconductors (quantum wells) in which the exciton experiences confinement in the direction perpendicular to the well. The absorptance of InAs quantum wells of different thicknesses has been reported to increase in steps of $\pi\alpha$, with $\alpha = e^2/4\pi\varepsilon_0\hbar c$ being the fine-structure constant.[172] We show by means of atomistic tight-binding calculations that this “quantum of absorption” characterizes the absorptance of a multitude of 2D semiconductors, which invariably exhibits steps with increasing photon energy of $m\pi\alpha$, with $m$ = 1 or 2, depending on the nature of the conduction- and valence-band valleys. By generalizing literature results,[171–174] this outcome urged us to investigate the absorptance of 0D QDs; we therefore designed QD samples in which the absolute band-edge absorptance can be measured in the same way as for the 2D quantum wells. After correction for photonic effects, we report that the absorptance per QD is close to $m\pi\alpha$. Finally, we develop a heuristic model to frame these remarkable results. For bulk semiconductors, the model suggests an absorptance of $m\pi\alpha$ per Bohr exciton diameter. We confirm this by using reported values of the band edge absorption coefficients for many different semiconductors spread over 2 orders of magnitude. We thus show empirically that the absorptance quantum $\pi\alpha$ is a good ruler to estimate the band-edge absorption strength of all direct semiconductors, independent of the degree of quantum confinement, if we consider the exciton volume as the elementary optically active volume.

## 5.2 Results and discussion

With InAs quantum wells as an example, it was experimentally shown that the absorptance increases stepwise with the photon energy with steps equal to $\pi\alpha$,[172] see Figure 5.1a. The InAs quantum wells of different thickness were grown on a $CaF_2$ substrate, each showing pronounced steps equal to 1.6% in the absorptance spectrum. To address intrinsic material properties, however, this result has to be corrected for reflection from the substrate by a factor $4n_m^2/(n_s + n_m)^2$, where $n_m$ is the refractive index of the medium (air, $n_m = 1$) and $n_s$ the refractive index of the substrate ($CaF_2$, $n_s = 1.43$), see Figure 5.1b. Each step in the absorptance amounts then to $\pi\alpha$, *i.e.*, $\pi/137 = 2.3\%$. Importantly, in this quasi-2D configuration, the semiconductor itself does not screen the electromagnetic field, for light perpendicularly incident on the quantum well surface.

In ref 172 it was argued that this remarkably simple result follows from applying Fermi's golden rule within a $k \cdot p$ description of a set of nondegenerate energy bands for which many factors in the transition dipole matrix element and the joint density of states mutually cancel, see also Chapter 5.5. However, we found that this result has a more general meaning and is not due to coincidental simplifications in the effective mass theory. We performed atomistic tight-binding calculations for an InAs quantum well (of varying thickness) in the single-particle regime (see Chapter 5.5). As shown in Figure 5.1a, the tight-binding calculated absorptance spectra (thick solid lines) show overall steps of close to $\pi\alpha$. However, a close watch shows some fine structure in the first plateau, due to the transitions of the heavy-hole, light-hole, and spin–orbit split-off band to the lowest conduction band, all three transitions contribute to an overall absorptance of close to $\pi\alpha$. With the understanding of these features in the atomistic tight-binding calculations, we now also recognize these features in the experimental data from ref 172. The inset in Figure 5.1a shows the experimental and calculated absorptance spectra of a 6 nm thick InAs quantum well in more detail. Atomistic tight-binding calculations account for deviations of parabolicity of the bands, for the existence of heavy- and light-hole bands with anisotropic warping, and for the mixing of these band states due to the quantum confinement. In order to find out if this result is independent of the semiconductor material, we have calculated the absorptance for specific II–VI and IV–VI compounds as well. As shown in Figure 5.7, CdSe quantum wells also feature absorptance steps of $\pi\alpha$, while the absorptance of PbSe quantum wells is characterized by steps of $2\pi\alpha$ (see Figure 5.8a). We assign the latter finding to a combination

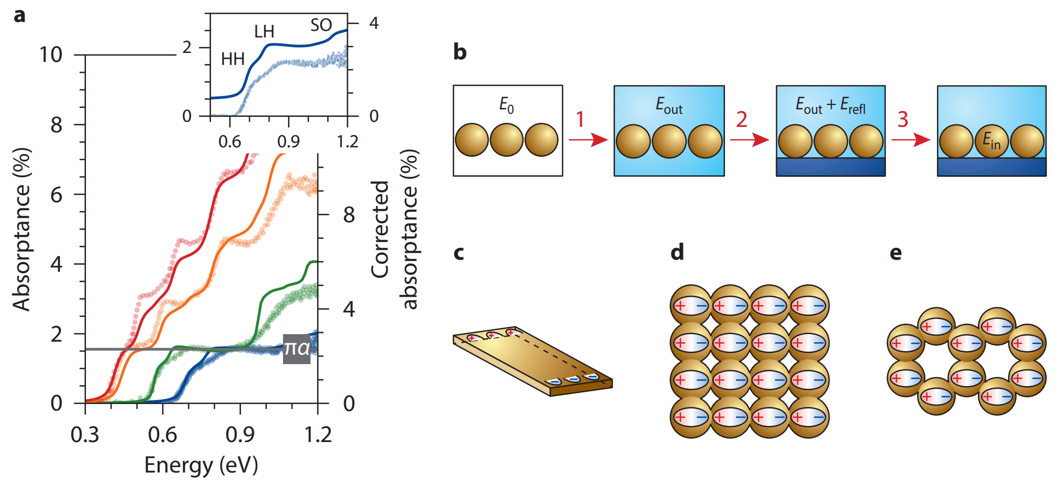

**Figure 5.1 | Measured and calculated absorptance of InAs quantum wells, and a schematic representation of the screening of the electromagnetic field in a quantum well and a QD monolayer.** (**a**) Measured absorptance spectra of InAs quantum wells with variable thickness; 6 nm (blue), 9 nm (green), 14 nm (orange), and 19 nm (red) (data from ref 172). The thick solid lines represent the absorptance spectra calculated with an atomistic tight-binding model in which we have slightly adjusted the quantum well thickness to match the optical threshold with the measured one (details and justification in Chapter 5.5). The right axis provides the absorptance corrected for substrate reflection (see text and below). For all experimental and calculated spectra, the absorptance of the first allowed transition (and subsequent steps) is equal to $\pi\alpha$. The inset shows the experimental and calculated absorption spectra for a 6 nm thick InAs quantum well in more detail. The calculated spectrum is shifted with 0.5% for clarity. The labels are the transitions from the heavy-hole (HH), light-hole (LH), and spin–orbit split-off band (SO) to the lowest conduction band. (**b**) A schematic overview of the photonic effects that results in a screening of the electromagnetic field. Step 1 induces a factor $1/n_m$ on the absorptance, $n_m$ the refractive index of the surrounding medium. Step 2 includes the effect of reflection in case a substrate with refractive index $n_s$ is present, resulting in a factor $4n_m/(n_s + n_m)^2$. The third step is the screening of the dielectric field inside the QDs, reducing the squared field strength with a factor $|F|^2$. (**c**–**e**) Comparison of the reduction of the electromagnetic field by dynamic charge accumulation (dielectric screening) in a quantum well (no screening $|F|^2 = 1$), a square quantum dot superlattice $|F|^2 = 0.59$, and a honeycomb quantum dot superlattice, $|F|^2 = 0.36$.

of a 4-fold degenerate bandgap at the L points of the Brillouin zone and the quasi-linear dispersion relation of the valence and conduction bands around the L points (see Figure 5.8b). We thus find in general that the absorptance of direct 2D semiconductors equals $A_{2D} = m\pi\alpha$, with $m = 1$ or $m = 2$, depending on the nature of the band edges.

In the very active field of *colloidal* QDs, the size-dependence and inhomogeneous broadening of the band-edge absorptance as measured on QD suspensions has been extensively investigated. However, the absorption of light resonant with the band-edge transition was rarely compared quantitatively to the corresponding bulk semiconductor. This is partly due to dielectric screening of the electromagnetic field by QDs, which obscures the underlying optical transition rate, and partly to different quantification of band-edge absorption by an absorption coefficient for bulk semiconductors and an oscillator strength or integrated absorption coefficient for QDs, see Chapter 5.4. To minimize the impact of dielectric screening, we analyzed the absolute absorptance of a series of QD superlattices built from PbSe or CdSe QDs.[175–177] Such samples combine a 0D confinement with a 2D geometry,[178] which makes that only minor corrections are needed for the screening of the electromagnetic field (see also Figures 5.1b–e). More precisely, we calculated for the different QD samples the local field factor $F$, which is the ratio between the external and the local electric field using atomistic dielectric modeling (see Chapter 5.6), and found that $|F|^2$ ranges between 0.4 and 0.8. Hence, in terms of dielectric screening, such superlattices indeed form a bridge to quantum wells (Figure 5.1c), which do not screen the electric field ($|F|^2 = 1$) for perpendicular incidence and exhibit an absorptance $m\pi\alpha$ per allowed transition.

Figures 5.2a,b present two monolayer superlattices of epitaxially connected PbSe QDs, one with a square and the other with a silicene-type honeycomb geometry. The high-angle annular dark-field scanning transmission electron microscopy (HAADF-STEM) images of the lattices (in lower right insets) show the atomic connection of QDs via their [100] facets. The electron diffraction patterns (upper right insets) reveal that the structures have a high degree of crystallinity, as observed by the occurrence of four and six sharp spots in electron diffraction patterns recorded on a selected area (see Figure 5.10) for the honeycomb and square superlattices, respectively. The width of the electron diffraction patterns reflects a slight disorder in the alignment of the QDs, as discussed elsewhere.[179] The absorptance spectra of both superlattices are presented in Figures 5.2c,d. These spectra were measured by placing the samples under a small angle inside the integrating sphere of a UV–vis–NIR spectrometer (see Chapter 5.6 for more details). The absorptance spectra shown here are representative for a series of measurements recorded independently by different research groups, see Figure 5.11. The results are summarized in Table 5.1. The first absorption feature at ~0.7 eV is indicative of the bandgap transition. As an aside, we remark that two monolayer superlattices stacked on top of each other show an absorptance increased by a factor 2. The right axis of Figures 5.2c,d present the absorptance corrected for the photonic effects, where the screening of the electromagnetic field is accounted for by the factor $|F|^2$, and reflectance by the factor $4n_m^2/(n_s + n_m)^2$. The maximum absorptances reaches about 3.8 and 4.5%, for square and honeycomb superlattices respectively. Thus, this is close to two times the absorptance quantum $\pi\alpha$, which is in agreement with the steps calculated for a PbSe quantum well. The absorptance spectra for CdSe honeycomb and square superlattices are presented in Figure 5.12. In those cases, a first absorptance peak occurs at 2.0 eV, typical for superlattices consisting of CdSe QDs.[176] The absorptance lies between $\pi\alpha$ and $2\pi\alpha$; we expect $m = 1$ for the fundamental absorption in CdSe. It is remarkable that, despite their very different bandgap, degree of quantum confinement, and electronic structure, the absorptance of PbSe and CdSe superlattices at the band-edge transition is very well quantified by $\pi\alpha$.

Above, we showed that the reported absorptance of semiconductor quantum wells, increasing with $m\pi\alpha$ per allowed optical transition, is corroborated by atomistic tight-binding theory. The ab-

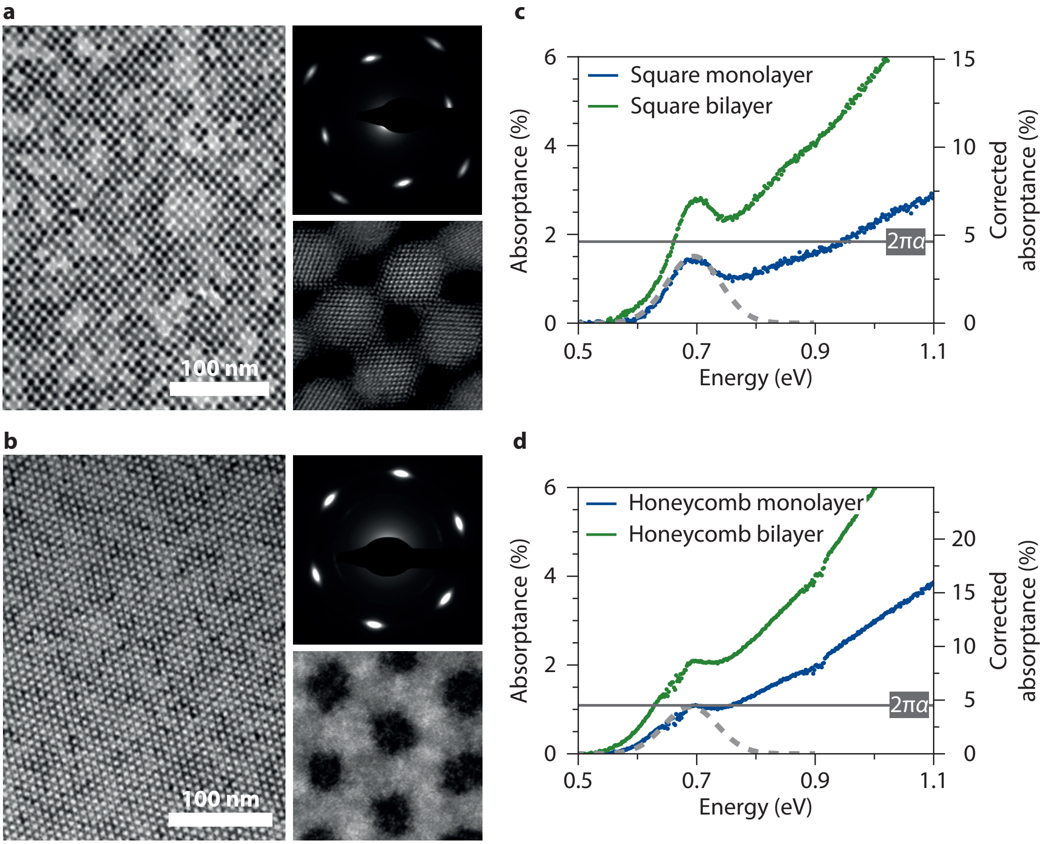

**Figure 5.2 | Absorptance of quantum dot monolayer superlattices.** (**a**) TEM image of a part of a PbSe square superlattice taken from the sample also used in the absorptance measurements. Lower right insert: HAADF-STEM images of the superlattice showing the epitaxial connection of the QDs. Top right insert: Electron diffraction pattern showing atomic alignment between the QDs. (**b**) TEM image of a part of a PbSe superlattice with silicene-type honeycomb geometry. Lower right inset: HAADF-STEM image showing the epitaxial connection between the QDs and the hexagonal array of voids in the superlattice. Top right inset: Electron diffraction pattern showing atomic alignment between the QDs, oriented with the [111] axis upward. (**c**) Absorptance (%) as a function of photon energy for a square PbSe superlattice (blue, one monolayer in thickness) present on a quartz substrate, the absorptance is 1.5% at 0.7 eV. The green spectrum shows the absorptance when a second PbSe square superlattice is stacked on the first one. (**d**) Absorptance for one layer of the honeycomb superlattice (blue); the absorptance is 1.1% at a photon energy of 0.7 eV. The addition of one more honeycomb monolayer (green) adds a similar contribution to the absorptance as the first monolayer. In both panels **c** and **d**, the right *y*-axis shows the bare absorptance, thus corrected for photonic effects. In both cases, the bare absorptance at 0.7 eV is close to $2\pi\alpha$. This is very similar to the result calculated with an atomistic tight-binding model for PbSe quantum wells. The light gray dashed lines in panels **c** and **d** show the absorptance feature calculated from the known integrated absorption cross section (Chapter 5.4).

| **Configuration** | **Compound** | $A_{exp}$ **(%)** | $A_{corr}$ **(%)** | $\|F\|^2$ | **Surrounding** |
|---|---|---|---|---|---|
| Honeycomb superlattice | PbSe | 1.1 | 4.5 | 0.36 | $4/(1.44+1)^2$ |
| Square superlattice | PbSe | 1.5 | 3.8 | 0.59 | $4/(1.44+1)^2$ |
| Quantum Well | PbSe | - | 4.6[a] | 1 | - |
| Honeycomb superlattice | CdSe | 1.7 | 3.4 | 0.66 | $4/(1.46+1)^2$ |
| Square superlattice | CdSe | 1.4 | 3.2 | 0.75 | $4/(1.46+1)^2$ |

**Table 5.1 |** Overview of the experimental parameters as discussed in the text. [a]Calculated with tight-binding approach.

sorptance quantum also rules the band-edge absorptance of a monolayer of QDs present in a superlattice. We now present a heuristic model that shows that *the absorptance quantum per exciton volume* is a ruler that unifies the experimental results obtained for 0D quantum dots, 2D quantum wells, and even 3D bulk semiconductors.

We start with the effective mass two-band model for 2D quantum wells,[172] see Chapter 5.4. We consider light absorption from free carrier states $|\, v \,\rangle$ of the highest valence sub-band induced by the vertical confinement to free carrier states $|\, c \,\rangle$ of the lowest conduction sub-band. Excitation involves a monochromatic beam with energy density $I$, linearly polarized, and normal incidence on the 2D semiconductor, and couples to states resonant with the photon energy ($\hbar\omega = E_c - E_v = E_{cv}$). The absorptance $A$ is the ratio of the energy absorbed by optical transitions in the semiconductor *versus* the incident energy, and can be written as

$$A(\hbar\omega) = \frac{E_{cv}W(\hbar\omega)}{I} = (\pi\alpha)4\pi E_{cv}|\langle\, c \,|\, \mathbf{x} \,|\, v \,\rangle|^2 \rho_{2D}(\hbar\omega) = \sigma_i \rho_{2D}(\hbar\omega). \tag{5.1}$$

In Equation 5.1, $W(\hbar\omega)$ is the transition rate between the states $|\, v \,\rangle$ and $|\, c \,\rangle$, $\rho_{2D}(\hbar\omega)$ is the joint density of states of optical transitions, and $\sigma_i$ is the integrated absorption cross section of a single transition (see Chapter 5.4). Within $k \cdot p$ theory, the dipole matrix element $|\langle\, c \,|\, \mathbf{x} \,|\, v \,\rangle|^2$ is given by $\hbar^2/4\mu E_{cv}$, while $\rho_{2D}$ amounts to $\mu/\pi\hbar^2$, with $\mu$ being the reduced effective mass of an electron–hole pair. Substitution of these elements in Equation 5.1 results in the absorptance being equal to $\pi\alpha$ within a single quantum-well sub-band, in agreement with the experimental steps observed for InAs quantum wells.

The density of states $\rho_{2D}(\hbar\omega)$ measures a number of states per unit area and per unit of energy. Interestingly, one can rewrite $\rho_{2D}(\hbar\omega)$ using the Bohr radius $r_X$, in fact $\sqrt{2}r_X$, as a unit of length and the exciton binding energy $E_X$ as a unit of energy

$$\rho_{2D}(\hbar\omega) = \frac{\mu}{\pi\hbar^2} = \frac{1}{2\pi r_X^2 E_X}. \tag{5.2}$$

Equation 5.2 suggests that a given 2D semiconductor attains steps $\pi\alpha$ in the absorptance by having $n = 1/2\pi r_X^2$ absorbing transitions per unit area in an energy range $E_X$. In this regard, a quantum well can thus be represented by a set of active elements, each measuring $2r_X^2$ in area (edges $\sqrt{2\pi}r_X$

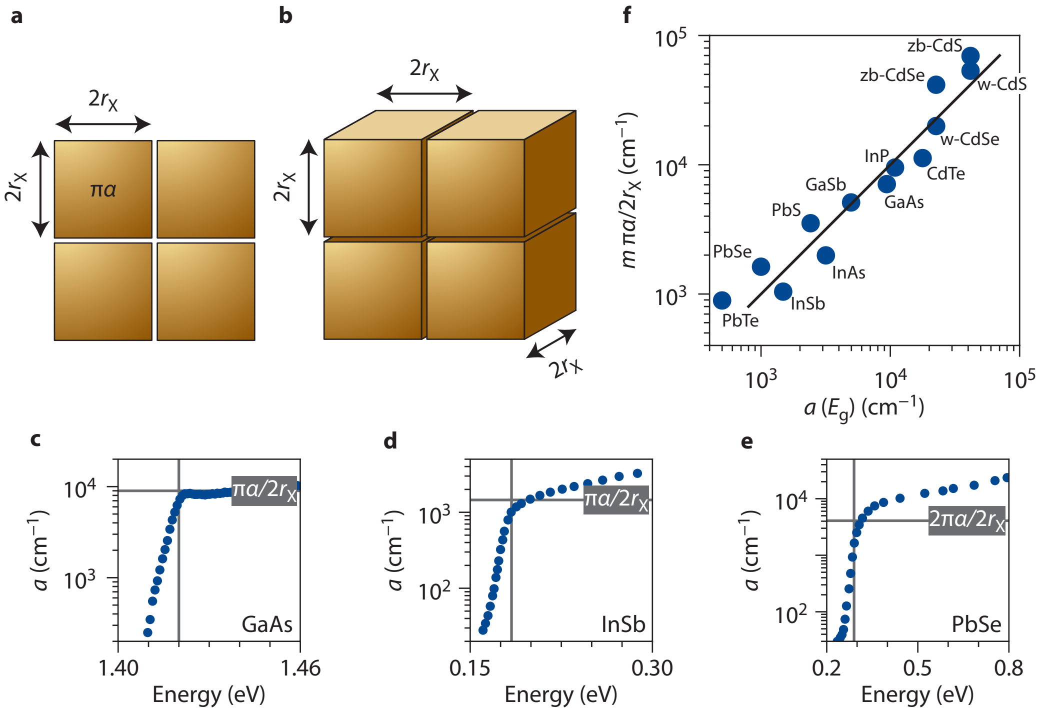

**Figure 5.3 |** Schematic representation of the heuristic model, and its evaluation for bulk semiconductors. (**a**) The band edge light absorptance of a quantum well, equal to $m\pi\alpha$ per allowed transition, can be interpreted by dividing the quantum well in square regions with area approximately $4r_X^2$ having an absorptance $m\pi\alpha$ across the exciton binding energy range $E_X$, see text and Equations 5.1–5.3. (**b**) Extension of this proven concept in the case of bulk semiconductors; this would mean that cubes with edge equal to $2r_X$ have each an absorptance equal to $m\pi\alpha$ per allowed transition, see text and Equation 5.4. (**c**–**e**) Experimental check of the above concept by presenting the experimental absorption coefficient spectra for the bulk semiconductors GaAs,[180] InSb,[181] and PbSe, [182] respectively; the vertical gray line shows the bandgap taken from ref 183, the horizontal line shows the value of $m\pi\alpha/2r_X$ with $r_X$ being the bulk exciton Bohr radius taken from ref 183. (**f**) Experimental check of the concept for a large variety of semiconductors, by plotting $m\pi\alpha/2r_X$ *versus* the absorption coefficient $a(E_g)$ at the band edge. The black line shows $a(E_g) = m\pi\alpha/2r_X$ with $m$ equal to 1 except for the IV–VI semiconductors for which it is 2.

$\approx 2r_X$, *i.e.*, the exciton Bohr diameter) and exhibiting an absorptance $\pi\alpha$ (or $2\pi\alpha$) across the energy range $E_X$, see Figure 5.3a. While different 2D semiconductors will be represented by squares of different sizes, the interplay between the integrated cross section and the 2D density of states always yields the same absorptance steps $\pi\alpha$ (or $2\pi\alpha$). Hence, $\pi\alpha$ can be used as a ruler to quantify $\sigma_i$

$$\sigma_i = \frac{\pi\alpha}{\rho_{2D}(\hbar\omega)} = \pi\alpha\frac{\pi\hbar^2}{\mu}. \tag{5.3}$$

Extending this approach to *3D (bulk) semiconductors*, we conjecture that for such materials the *bulk* Bohr diameter of the electron–hole exciton similarly sets the physical volume contributing to a single optical transition. In the heuristic model, this physical volume can be approximated by a cube with edges equal to the Bohr diameter $2r_\mathrm{X}$, see Figure 5.3b. If correct, the absorption coefficient $a$, *i.e.*, the absorptance per unit length, would be given by

$$a = \frac{A}{2r_\mathrm{X}} = \frac{m\pi\alpha}{2r_\mathrm{X}}. \tag{5.4}$$

The above relation can be tested by analyzing experimental absorption coefficient spectra for bulk semiconductors from the literature. In Figures 5.3c–e, we plot such spectra for GaAs,[180] InSb,[181] and PbSe.[182] Similar plots for other semiconductors are collected in Figure 5.13, ($E_\mathrm{CV}$ and $r_\mathrm{X}$ are from ref 183). It is clear that the crossing of the gray lines ($E_\mathrm{CV}$, $\pi\alpha/2r_\mathrm{X}$), indicates a point very close to the saturated absorption coefficient at the band edge. For bulk PbSe, we took the value of $2\pi\alpha$ to account for the degeneracy of the band edges (see above). Furthermore, Figure 5.3f represents $\pi\alpha/2r_\mathrm{X}$ *versus* the absorption coefficient at the band edge for a large variety of semiconductors with very different bandgaps, effective electron and hole mass, and crystal structures. Very remarkably, for a large variety of direct bulk semiconductors with the absorption coefficient spanning over 2 orders of magnitude, $\pi\alpha/2r_\mathrm{X}$ is in a reasonable agreement with the absorption coefficient at the band-edge. A more rigorous theoretical approach is outlined in Chapter 5.7, where we introduce the absorptance quantum according to Equation 5.3 as a ruler to quantify absorption spectra of semiconductors. Interestingly, since the transition matrix element to form exciton states can be written in terms of the matrix element $\langle\, c \,|\, \mathbf{x} \,|\, v \,\rangle$ to form free electron–hole pair states, this ruler approach can be extended to include electron–hole interaction by the formation of unbound excitons. In that case, we obtain a band-edge absorption coefficient of $(\pi\alpha/2r_\mathrm{X})\gamma^2$ with the correction factor $\gamma^2$ close to unity, see Supporting Information of ref 184. Clearly, such excitonic effects can contribute to the deviations of the band-edge absorption coefficient of specific semiconductors from the $m\pi\alpha/2r_\mathrm{X}$ reference line that is apparent in Figure 5.3f, in particular for semiconductors such as CdS with large effective masses and small dielectric constants. Otherwise, deviations could be caused by errors on the experimental data or uncertainties on the Bohr diameter.

Extending this approach to 0D QDs, it appears that the volume of a single optical transition is equivalently set by the QD diameter $d$ in the absence of any photonic effects. A QD superlattice monolayer would thus have an absorption coefficient $m\pi\alpha/d$ or an absorptance $m\pi\alpha$ for the band-edge transition; this is a conclusion in line with the experimental results shown in Figures 5.2c,d. In this case, however, the analysis is more complicated because the band-edge transition is heterogeneously broadened to yield an effective density of states $\rho_2(\hbar\omega)$. Considering a Gaussian broadening and writing the QD surface density as $n$, $\rho_2(\hbar\omega)$ reads

$$\rho_2(\hbar\omega) = n\frac{1}{\sqrt{2\pi\eta}}\mathrm{e}^{-\frac{(E-(E_\mathrm{c}-E_\mathrm{v}))^2}{2\eta^2}} \approx \frac{1}{d^2}\frac{1}{\sqrt{2\pi\eta}}\mathrm{e}^{-\frac{(E-(E_\mathrm{c}-E_\mathrm{v}))^2}{2\eta^2}}. \tag{5.5}$$

Using again the absorptance quantum as a ruler to quantify the integrated cross section (Equation 5.3), the absorptance of a QD superlattice monolayer is then obtained as

$$A = m\pi\alpha\frac{\pi\hbar^2}{\mu d^2}\frac{1}{\sqrt{2\pi\eta}}\mathrm{e}^{-\frac{(E-(E_\mathrm{c}-E_\mathrm{v}))^2}{2\eta^2}} \approx m\pi\alpha\frac{E_\mathrm{Q}}{(2\pi)^{3/2}\eta}\mathrm{e}^{-\frac{(E-(E_\mathrm{c}-E_\mathrm{v}))^2}{2\eta^2}}. \tag{5.6}$$

Here, we have introduced the quantization energy $E_Q$ in a QD according to the effective mass model. Interestingly, Equation 5.6 predicts that the band-edge absorptance will peak at $m\pi\alpha$ when the full width at half maximum of the exciton line is about one-sixth of the quantization energy; a result that agrees quite well with the experimental data shown in Figures 5.2c,d, and in fact also for most QD suspensions in which the size dispersion is kept to a minimum. Importantly, a more rigorous approach in which we use the known integrated cross section of the PbSe QDs enables us to predict very precisely the absorptance spectrum of the epitaxially connected QD films (see Figures 5.2c,d and Chapter 5.6). We thus conclude that the band-edge absorptance of 0D QDs will indeed peak at around $m\pi\alpha$ for a heterogeneous line broadening typically found with colloidal QDs.

## 5.3 Conclusion

The above observations have important consequences. While any 2D semiconductor exhibits the same absorptance $\pi\alpha$, the absorption coefficient of 3D semiconductors is inversely proportional to the Bohr diameter of the exciton (see Equation 5.4 and Figure 5.3f); the bulk exciton volume thus determines the widely varying absorption coefficient observed for bulk semiconductors, being the smallest for semiconductors with bands with low effective hole- and electron mass. The absorptance per crystal unit cell will thus increase the strongest for this type of semiconductors when considering the evolution from the 3D case to the 0D case. In practice, the enhanced absorption coefficient of small effective-mass QDs is often cloaked by pronounced dielectric screening. Incorporation of such QDs in a medium with high dielectric constant can therefore strongly enhance the absorptance of light at the band edge, a highly desirable property for their application as LED phosphor or infrared light absorber. The knowledge that a single QD in an appropriate dielectric medium and a semiconductor quantum well both have an absorptance in the range of $\pi\alpha$ is important for the engineering of luminescent light concentrators and photovoltaic devices. To highlight that even one QD monolayer shows sufficient absorption under normal incidence for optoelectronic applications, we present in Chapter 5.8 an infrared photodetector based on a honeycomb monolayer of PbSe QDs; this system has a sufficiently strong light absorptance and at the same time is conducting enough to act as a sensitive photodetector.

For monolayer transition metal dichalcogenide semiconductors, absorptances considerably above $\pi\alpha$ have been reported.[185] This is due the strongly enhanced exciton binding energy. We remark here that for low dimensional systems, the exciton-binding energy and thus also the enhancement of the absorptance above $\pi\alpha$, may strongly depend on the dielectric function of the environment.[186,187] In this respect, the absorptance of $\pi\alpha$ can be considered as the single particle basis to estimate the enhancement of light absorption if interactions play a role.

The experimental results and model calculations presented here definitely show that photons resonant with the band-edge transition have a probability close to $\pi\alpha$ to be absorbed for each Bohr exciton diameter pathlength in a semiconductor, independent of whether the exciton is confined in three dimensions, one dimension, or represents a bulk exciton. The heuristic framework that we present provides a basis to understand this compelling generalization. However, a more comprehensive understanding must exist for the observed generality in the absorption strength per exciton Bohr diameter. Also, the finding that for semimetals, such as graphene,[173] and plasmonic systems,[174] the absorptance is equal to πα in a very broad energy region further highlights this point.

## 5.4 Theory section – Light Absorption by a Two-Level system

*The transition rate from the initial to the final state from time-dependent perturbation theory.* We consider a two-level system with a ground state $|\,v\,\rangle$ and an excited state $|\,c\,\rangle$, characterized by the energies $E_\mathrm{v}$ and $E_\mathrm{c}$, respectively. Moreover, we will assume that the energy difference $E_\mathrm{c} - E_\mathrm{v}$ is described by a Gaussian distribution rather than a single number. This approach can reflect the unavoidable coupling of electronic states in solids or nanocrystals to lattice vibrations or to the surroundings (see Figure 5.4), or it may reflect heterogeneity in an ensemble of two-level systems. Taking this approach, the transition energy $E = E_\mathrm{c} - E_\mathrm{v}$ can be described by an effective density of states $\bar{\rho}(E)$ characterized by a broadening $\eta$ according to

$$\bar{\rho}(E) = \frac{1}{\sqrt{2\pi}\eta}\mathrm{e}^{-\frac{(E-(E_{\mathrm{c},0}-E_{\mathrm{v},0}))^2}{2\eta^2}}. \tag{5.7}$$

Note that according to Equation 5.7, the energy-integrated density of states is 1, *i.e.*, $\bar{\rho}(E)$ describes a single two-level system.

We calculate the transition rate of a two-level system from its initial (ground) state to its final (excited) state when exposed to electromagnetic radiation by time-dependent perturbation theory. Here, we assume that the two-level system is a point-like object. In that case, the operator $\mathbf{H}_\mathbf{r}$ describing the incident radiation can be included in the Hamiltonian operator of the two-level system as a harmonically oscillating electric potential. Assuming the incident light is linearly polarized with the electric field $E$ along the $x$-axis, we thus have

$$\mathbf{H}_\mathrm{r} = eE\mathbf{x}\sin(\omega t). \tag{5.8}$$

Note that the above expression assumes that the light is monochromatic. This approximation can be used when the spectral distribution of the incident light is narrower than the energy distribution of the transition.

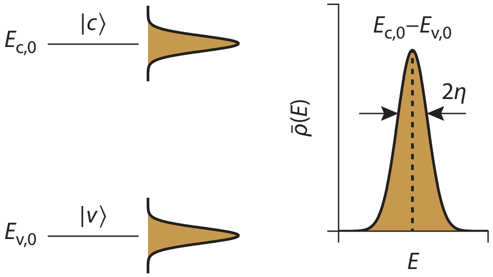

**Figure 5.4 |** Representation of a two-level system with fluctuating energy levels. The resulting distribution of transition energies $E_\mathrm{c} - E_\mathrm{v}$ can be represented by a Gaussian function with a width $\eta$.

By means of this sinusoidal perturbation, the transition rate $W$ from the initial to the final state is obtained as

$$W = \frac{\pi}{2\hbar} e^2 E^2 |\langle\, c \,|\, \mathbf{x} \,|\, v \,\rangle|^2 \bar{\rho}(\hbar\omega). \tag{5.9}$$

One readily shows that a similar expression can be obtained in the case of a narrow transition in combination with a broad spectral distribution of the incident radiation.[188] In that case, the density of state $\bar{\rho}(E)$ will be replaced by a distribution of the incident radiation over frequency or photon energy.

*The transition dipole matrix element.* Equation 5.9 shows that the properties of the two-level system determine the transition rate $W$ mostly through the dipole matrix element $\langle\, c \,|\, x \,|\, v \,\rangle$. For a single electron, $\langle\, c \,|\, \mathbf{x} \,|\, v \,\rangle$ is related to the matrix element of the momentum operator $\mathbf{p}_\mathrm{x}$. Writing the energy gap $E_{\mathrm{c},0} - E_{\mathrm{v},0}$ between both levels as $\hbar\omega_0$ and the mass of the electron as $m_\mathrm{e}$, the following relation applies[189]

$$\langle\, c \,|\, \mathbf{p}_\mathrm{x} \,|\, v \,\rangle = i m_\mathrm{e} \omega_0 \langle\, c \,|\, \mathbf{x} \,|\, v \,\rangle. \tag{5.10}$$

Hence, an alternative expression for the transition rate $W$ reads

$$W = \frac{\pi}{2\hbar} \frac{e^2 E^2}{m_\mathrm{e}^2 \omega_0^2} |\langle\, c \,|\, \mathbf{p}_\mathrm{x} \,|\, v \,\rangle|^2 \bar{\rho}(E). \tag{5.11}$$

An alternative approach to reach this expression for the transition rate is to include light matter interaction by replacing the momentum operator $\mathbf{p}$ by $\mathbf{p} + e\mathbf{A}$, where $\mathbf{A}$ is the vector potential describing the electromagnetic field.[189] In that case, the light–matter coupling is described by the Hamiltonian $\mathbf{H}'$ given by

$$\mathbf{H}' = -\frac{e}{m_\mathrm{e}} \mathbf{A} \cdot \mathbf{p}. \tag{5.12}$$

*The absorptance of a two-level system.* The absorptance $A$ is the ratio between the incident and the absorbed energy. The absorbed energy per unit time is equal to the product of the transition rate $W$ and the energy $E = \hbar\omega$ absorbed per transition. The incident energy per unit time, on the other hand, is more easily expressed as a power density $I$, *i.e.*, the energy passing per second through a unit surface. Indeed, writing the speed of light as $c$ and the permittivity of the vacuum as $\varepsilon_0$, the electric field $E$ is related to the power density as

$$I = \frac{c\varepsilon_0}{2} E^2. \tag{5.13}$$

To obtain a dimensionless absorptance, the incident power density should be compared to the power absorbed per unit of surface area. For this purpose, we write the number of two-level systems present per unit of surface area as $n$. With this definition, we obtain $A$ at the photon energy $\hbar\omega$ as

$$A(\hbar\omega) = \frac{W n \hbar\omega}{I} = \left(4\pi^2 \alpha |\langle\, c \,|\, \mathbf{x} \,|\, v \,\rangle|^2 \hbar\omega\right) \times n\bar{\rho}(\hbar\omega). \tag{5.14}$$

In the above expression, we have introduced the fine structure constant $\alpha$ as

$$\alpha = \frac{e^2}{4\pi\varepsilon_0 \hbar c}. \tag{5.15}$$

In addition, we have singled out in Equation 5.14 the product $n\rho(\hbar\omega)$ of the number of two-level systems and the density of states of a single two-level system at $E = \hbar\omega$ This combination in fact yields the number of transitions per energy range and per unit of surface area at $E = \hbar\omega$, a quantity we call the *effective* 2D density of states $\rho_2(\hbar\omega)$:

$$\rho_2(\hbar\omega) = n\bar{\rho}(\hbar\omega). \tag{5.16}$$

With this definition, an equivalent expression for the absorptance $A(\hbar\omega)$ is obtained as

$$A(\hbar\omega) = \left(4\pi^2\alpha|\langle\, c\,|\,\mathbf{x}\,|\,v\,\rangle|^2\hbar\omega\right) \times \rho_2(\hbar\omega). \tag{5.17}$$

Opposite from Equation 5.14, the expression for $A(\hbar\omega)$ given by Equation 5.17 can be readily applied to systems characterized by a density of transitions or a joint density of states — such as a bulk or a 2D semiconductor. Introducing the quantum of absorptance $\pi\alpha$, $A(\hbar\omega)$ can be normalized to yield

$$\frac{A(\hbar\omega)}{\pi\alpha} = 4\pi|\langle\, c\,|\,\mathbf{x}\,|\,v\,\rangle|^2\hbar\omega\,\rho_2(\hbar\omega). \tag{5.18}$$

*The absorption cross section and the oscillator strength.* By describing the transition energy for a two-level system through a distribution, the transition rate at a given energy $E = \hbar\omega$ will depend on the broadening $\eta$. However, what remains constant is the energy integrated transition rate. Intrinsic properties of a transition are therefore better expressed using quantities that reflect this integrated rate, rather than the transition rate at a given energy. Relevant quantities in this respect are the oscillator strength $f_{\mathrm{cv}}$ or the integrated cross section $\sigma_{\mathrm{i}}$ of a transition. Both are linked to the dipole matrix element $\langle\, c\,|\,\mathbf{x}\,|\,v\,\rangle$ of the transition.

For monochromatic light, the absorption cross section $\sigma(\omega)$ of a transition is the coefficient relating the transition rate $W$ to the incident photon flux $J_{\mathrm{N}} = I/(\hbar\omega)$:

$$W = \sigma(\omega)J_{\mathrm{N}}. \tag{5.19}$$

For the two-level system, we thus have:

$$\sigma(\omega) = 4\pi^2\alpha|\langle\, c\,|\,\mathbf{x}\,|\,v\,\rangle|^2\hbar\omega\bar{\rho}(\hbar\omega). \tag{5.20}$$

While $\sigma(\omega)$ indeed depends on the broadening of the line, the integrated cross section does not, provided that the line broadening is significantly smaller than the photon energy. For a line centered around $E = \hbar\omega_0$, we then obtain

$$\sigma_{\mathrm{i}} = 4\pi^2\alpha|\langle\, c\,|\,\mathbf{x}\,|\,v\,\rangle|^2\hbar\omega_0. \tag{5.21}$$

Hence, the absorptance $A$ of the layer can be written as (for $\eta \ll \hbar\omega_0$)

$$A(\hbar\omega) = \sigma_{\mathrm{i}}\,\rho_2(\hbar\omega). \tag{5.22}$$

*Interpretation.* According to Equation 5.19, $\sigma(\omega)$ has units $\mathrm{m}^2$ since it is a coefficient linking a transition rate ($\mathrm{s}^{-1}$) to a photon flux ($\mathrm{m}^{-2}\,\mathrm{s}^{-1}$). On the other hand, the absorption cross section is related to the absorptance, which can be seen as the probability that an incident photon is absorbed. Let us assume now that we have light incident on a medium that contains $n$ two-level systems per unit of surface area. In that case, we can assign each two-level system an area $S = 1/n$, and the ratio between the photons absorbed by each two-level system and the photons $N$ passing through the area $1/n$ can be expressed as

$$\frac{W}{N} = A(\omega) = \sigma(\omega)n. \tag{5.23}$$

Hence, we can represent a unit area of that medium by a set of $n$ adjacent squares, each having an area

$S = 1/n$ and characterized by an absorptance $A(\omega) = \sigma(\omega)n$ across that area, see Figure 5.5.

The correspondence with Equation 5.22 indicates that a similar interpretation applies in the case of a continuous distribution of final states, provided we focus on the integrated absorptance over an energy range $\Delta E$. Following Equation 5.22, this integrated absorptance is in first order given by

$$A(\hbar\omega)\Delta E = \sigma_i \rho_2(\hbar\omega)\Delta E. \tag{5.24}$$

*The oscillator strength.* Next to the integrated cross section, the transition between the initial and the final state of a two-level system can also be quantified by the oscillator strength $f_{cv}$. This is a dimensionless number, defined in terms of the transition angular frequency $\omega_0$ and the transition dipole moment

$$f_{cv} = \frac{2m_e}{\hbar}\omega_0 |\langle c | \mathbf{x} | v \rangle|^2. \tag{5.25}$$

Comparing Equation 5.21 and Equation 5.25, one sees that the integrated cross section and the oscillator strength indeed provide the same information on the optical transition, and both can be used to obtain an absorptance spectrum once the density of states is known.

*Corrections induced by dielectric material properties.* The previous equations for the absorption cross section and the absorptance only consider the response of the electrons involved in the resonant optical transitions. The response of the other electrons present in the studied systems and their environment can be described through the dielectric properties of the materials.

As shown in ref 172, when a semiconductor film or nanocrystals are mounted on a substrate of refractive index $n_s$, they experience both the incident electric field and the reflected one. This leads to a correction factor $4/(n_s + 1)^2$ that must be applied to $A(\hbar\omega)$ or $\sigma(\hbar\omega)$. See also Figure 5.1b.

There is an additional correction $|F|^2$ where $F = E_{in}/E$ coming from the fact that the local electric

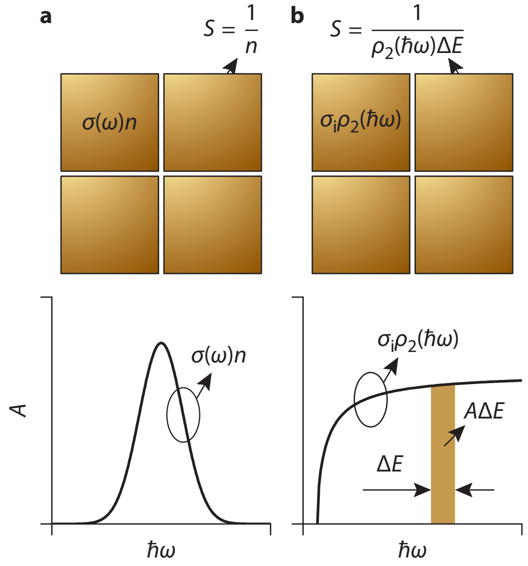

**Figure 5.5 |** (**a**) The absorptance of a medium having $n$ two-level systems per unit area can be represented by $n$ squares, covering each an area $S = 1/n$ and exhibiting absorptance $A(\omega) = \sigma(\omega)n$ across that area. (**b**) To obtain the integrated absorptance across an energy range $\Delta E$ of a medium having $\rho_2(\hbar\omega)$ transitions per unit of energy and area, the medium can be represented by $\rho_2(\hbar\omega)\Delta E$ squares per unit area, each providing an absorptance $\sigma_i\rho_2(\hbar\omega)$.

field $E_{\text{in}}$ seen by the two-electron system is screened compared to the bare one ($E$) due to the dielectric response of the semiconductor material itself. In the well-known case of a spherical system of dielectric constant $\varepsilon_{\text{in}}$ embedded in a medium of dielectric constant $\varepsilon_{\text{out}}$, the local-field factor is given by[190]

$$F = 3\varepsilon_{\text{out}}/(\varepsilon_{\text{in}} + 2\varepsilon_{\text{out}}). \tag{5.26}$$

In more complex situations, the local-field factor $F$ must be computed using numerical methods. In the case of semiconductor films or nanostructures deposited on a substrate, the total correction factor becomes $4|F|^2/(n_s + 1)^2$ where $F$ must account for the response of the substrate to the polarization charges induced in the semiconductor. The case of superlattices of epitaxially-connected QDs is discussed below.

*Final expression for the absorptance of a layer of two-level systems.* We can therefore summarize the results for an ensemble of two-level systems forming a 2D layer with a surface density $n = 1/S_0$ on a substrate with refractive index $n_s$. Combining the expressions given in the previous section, Equation 5.7, Equation 5.14, and Equation 5.25, we derive an analytical expression for the absorptance

$$A(\hbar\omega) = \frac{4|F|^2}{(n_s + 1)^2}\frac{\pi e^2 \hbar f}{2m_e c\varepsilon_0 S_0 \eta\sqrt{2\pi}} e^{-\frac{(\hbar\omega-\hbar\omega_0)^2}{2\eta^2}}. \tag{5.27}$$

leading to

$$A(\hbar\omega) = 0.438\frac{4|F|^2}{(n_s + 1)^2}\frac{f}{S_0\eta} e^{-\frac{(\hbar\omega-\hbar\omega_0)^2}{2\eta^2}}. \tag{5.28}$$

where $A$ is displayed in percentage, $S_0$ is given in nm$^2$ and $\eta$ in eV.

## 5.5 Theory section – The absorptance of a 2D semiconductor

*Theory within the effective mass approximation.* Using Equation 5.21, we can readily calculate the absorptance of a 2D direct band-gap semiconductor in the effective mass approximation, as shown in ref 172. For such a system, the *effective* 2D density of states $\rho_2$ corresponds to the actual joint density of states $\rho_{2D}$ of the 2D material. For a combination of a parabolic valence and conduction band (see Figure 5.6), we have

$$\rho_{2D} = \frac{\mu}{\pi\hbar^2}. \tag{5.29}$$

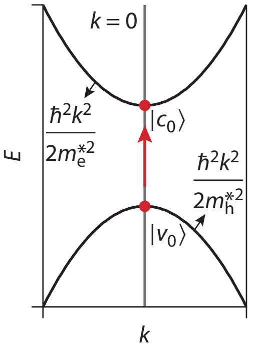

**Figure 5.6 |** Representation of a direct band-gap semiconductor with parabolic valence and conduction band. The states at the band extrema in the center of the Brillouin zone are indicated with red markers and labeled $|v_0\rangle$ and $|c_0\rangle$. The red arrow represents an optical transition between both states.

Here, $\mu$ is the reduced effective mass of the electron-hole pair

$$\mu = \frac{m_e^\star m_h^\star}{m_e^\star + m_h^\star}. \tag{5.30}$$

Combining Equations 5.11, 5.20, 5.21, and 5.29, the absorptance $A$ of a 2D semiconductor due to transitions between the valence-band state $|\, v \,\rangle$ and the conduction-band state $|\, c \,\rangle$ is obtained as

$$A_{2D} = 4\pi^2 \alpha |\langle\, c \,|\, \mathbf{p}_x \,|\, v \,\rangle|^2 \frac{\hbar}{m_e^2 \omega_0} \frac{\mu}{\pi\hbar^2}. \tag{5.31}$$

Within a two-band model, the effective masses $m_e^\star$ and $m_h^\star$ are related to the matrix element $\langle\, c_0 \,|\, \mathbf{p}_x \,|\, v_0 \,\rangle$ between the band-edge states $|\, v_0 \,\rangle$ and $|\, c_0 \,\rangle$ as defined in Figure 5.6

$$\frac{1}{m_e^\star} = \frac{1}{m_e} + \frac{2}{m_e^2} \frac{|\langle\, c_0 \,|\, \mathbf{p}_x \,|\, v_0 \,\rangle|^2}{E_g} \tag{5.32}$$

$$\frac{1}{m_h^\star} = -\frac{1}{m_e} + \frac{2}{m_e^2} \frac{|\langle\, c_0 \,|\, \mathbf{p}_x \,|\, v_0 \,\rangle|^2}{E_g}. \tag{5.33}$$

Here, $E_g$ is the bandgap of the corresponding bulk semiconductor. Summing both relations enables us to express $\langle\, c_0 \,|\, \mathbf{p}_x \,|\, v_0 \,\rangle$ as a function of $\mu$

$$\frac{1}{\mu} = \frac{4}{m_e^2} \frac{|\langle\, c_0 \,|\, \mathbf{p}_x \,|\, v_0 \,\rangle|^2}{E_g}. \tag{5.34}$$

Assuming that the transition dipole matrix element is independent of the wave vector, Equation 5.31 can thus be rewritten as

$$A_{2D} = \pi\alpha \frac{E_g}{\hbar\omega_0} \approx \pi\alpha. \tag{5.35}$$

Note that the quantum of absorptance is approximately obtained since the ratio $E_g/\hbar\omega_0$ will be somewhat smaller than 1 due to size quantization in a 2D semiconductor.

The finding that the absorptance of a 2D semiconductor boils down to the quantum of absorptance $\pi\alpha$ has been experimentally verified for the case of InAs quantum wells,[172] yet the above derivation stresses that this outcome is seemingly the result of a subtle balance between the transition dipole matrix element and the density of states.

*Tight binding calculations for a selection of 2D semiconductors.* In the following, we present tight binding calculations for InAs, CdSe, and PbSe (100) quantum wells. The absorptance is calculated using Equation 5.14 in which $|\, c \,\rangle$ and $|\, v \,\rangle$ are replaced by $|\, c, \mathbf{k} \,\rangle$ and $|\, v, \mathbf{k} \,\rangle$, the conduction and valence band states of wave-vector $\mathbf{k}$, respectively. The terms in Equation 5.14 are summed over the bands $c$ and $v$, and over the $\mathbf{k}$ vectors allowed for a sample of surface $S$ on which boundary conditions are applied ($n = 1/S$). Each transition line is broadened using Equation 5.7 in which $E_{c,0} - E_{v,0}$ is replaced by $E_c(\mathbf{k}) - E_v(\mathbf{k})$. Following refs 190,191, the dipole matrix elements are calculated from those of the momentum (Equation 5.10) which, in tight binding, can be deduced from the matrix elements of the Hamiltonian $H(\mathbf{k})$

$$\langle\, c, \mathbf{k} \,|\, p_x \,|\, v, \mathbf{k} \,\rangle \rightarrow \frac{m_0}{\hbar} \langle\, c, \mathbf{k} \,|\, \frac{\partial H(\mathbf{k})}{\partial k_x} \,|\, v, \mathbf{k} \,\rangle. \tag{5.36}$$

In the case of a quantum well irradiated perpendicularly, the external field is unscreened ($F = 1$). The correction to Equation 5.14 is thus limited to the factor describing the reflection of the light by the substrate (see Chapter 5.4).

Figure 5.1a presents calculations of the absorptance for InAs quantum wells. We used the tight-binding model of ref 192 and we assumed that surfaces are perfectly passivated, which is modeled by pseudo-hydrogen atoms saturating surface dangling bonds.[190] In order to compare with the experimental data of ref 172, we take into account the reflection of the light by the $CaF_2$ substrate ($n_s = 1.46$). We adjusted the thickness of the quantum wells to obtain the correct optical bandgap compared to experiments. The agreement between theory and experiments is good. The different steps, their position, their amplitude, and even their shape when they exhibit fine structures are very well described by the calculations. Each main step contributes as $4/(n_s+1)^2\pi\alpha$ to the absorptance. This agreement is quite remarkable, showing that excitonic effects are weak for this range of quantum well thickness. However, this is obtained assuming thinner quantum wells than the InAs membranes experimentally studied in ref 172. The reduction in thickness is of the order of 2 nm. This can be understood by band-bending effects which are well-known in the case of InAs surfaces, due to the pinning of the Fermi level by surface states.[193]

We have performed similar calculations for (100) CdSe quantum wells (Figure 5.7). We used the tight binding parameters of ref 194. We have chosen a thickness of 6 nm for which the excitonic effects should also be weak. Like in InAs, the calculated spectrum exhibits very clear steps at integer values of $\pi\alpha$. This is remarkable taking into account that CdSe is characterized by a much larger bandgap than InAs.

By comparison with InAs and CdSe, the case of PbSe is interesting since the bulk material is characterized in conduction and valence bands by four nonequivalent valleys at the L point of the Brillouin zone.[195] In a (100) quantum wells, these four valleys are projected at the two nonequivalent W points ($\pi/a[0, 1, 1]$) of the 2D Brillouin zone (Figure 5.8b), leading to almost twofold (fourfold with spin) degenerate sub-bands in each valley (there is small splitting due to inter-valley coupling).[195] Therefore we could expect absorptance steps of $4\pi\alpha$ if we consider that optical transitions are allowed only between sub-bands sharing the same quantum number (red arrows in Figure 5.8b).

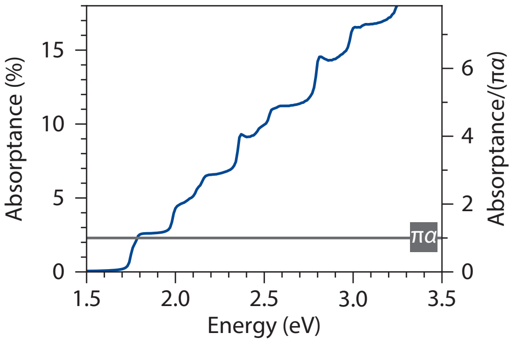

**Figure 5.7 |** Absorptance calculated for a CdSe quantum well with a thickness of 6.0 nm without local-field factor.

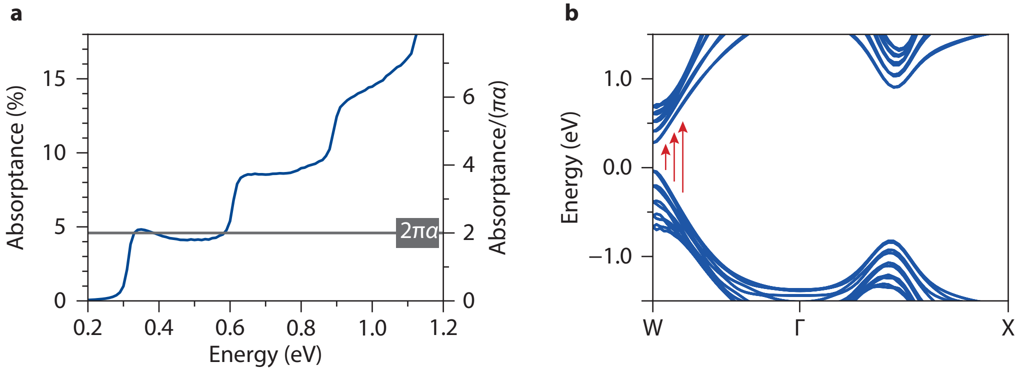

**Figure 5.8 |** (**a**) Absorptance calculated for a 6-nm-thick PbSe quantum well without local-field factor. (**b**) Lowest conduction bands and highest valence bands. The steps in the absorptance are associated to the transitions shown with the red arrows.

In absence of experimental data, we have performed calculations of the absorptance for a 6-nm-thick (100) PbSe quantum well using the tight-binding model of ref 195. The results, presented in Figure 5.8a, show that the absorptance is characterized by clear steps of height $2\pi\alpha$ (correction factor due to light reflection not included).

This behavior can be understood by the fact that the bands have quasi-linear dispersions as soon as one moves away from the band edges, and that the electronic states in the valence and conduction bands have very marked *p* character.[195] We then recover a situation close to that of graphene in which the absorptance amounts to $\pi\alpha/2$ in each valley.[173,196,197] In the case of (100) PbSe quantum wells, this gives a quantum of absorptance of 4 times $\pi\alpha/2 = 2\pi\alpha$, except in the energy regions where the sub-bands have a parabolic dispersion, *i.e.*, for transitions at sub-band edges which lead to visible bumps in the absorptance spectrum. This situation is very different from III−V or II−VI direct-gap semiconductors characterized by *s*–*p* type optical transitions and different band dispersions.

## 5.6 Epitaxially connected quantum-dot superlattices

*PbSe QD synthesis.* PbSe QDs were synthesized based on the methodology of Steckel *et al.*[43] For the lead precursor, a mixture of 4.77 g lead acetate (99.99%, Sigma-Aldrich), 10.35 g oleic acid (90%, Sigma-Aldrich) and 39.75 g 1-octadecene (90%, Sigma-Aldrich) was heated at 120 °C under vacuum for 5 hours. For the selenium precursor, 3.52 g selenium powder (99.99%, Alfa Aesar) was dissolved in a mixture of 46.59 mL trioctylphosphine (90%, Sigma-Aldrich) and 0.41 mL diphenylphosphine (98%, Sigma-Aldrich). Subsequently, 10.25 mL of the lead precursor was heated up to 180 °C at which 7.5 mL of the selenium precursor was swiftly injected. The mixture was kept at 150 °C for 70 seconds and the QD growth was quenched with 30 mL of a methanol/butanol mixture (1:2). The QD product dispersion was centrifuged and the QDs were redispersed in toluene. This concentrated dispersion of PbSe QDs was washed twice with methanol and the QDs were dissolved in toluene.

*Formation of square and honeycomb superlattices by means of oriented attachment.* The PbSe square superlattices were prepared by drop casting of a dispersion of PbSe QDs (size 6.2 nm) in toluene on the ethylene glycol (EG) substrate (see Figure 5.9).[175] The system is left for 45 minutes at 25 °C. The toluene evaporates and the PbSe square superlattices are formed by assembling PbSe QDs at the toluene/air interface after which the QDs attach via their four vertical [100] facets. Heating the system at 55 °C for 20 minutes leads to the formation of a square structure network with stronger atomic connections between the QDs.

To prepare honeycomb superlattices, an ultra-slow procedure was used as illustrated in Figure 5.9. A small Petri dish was filled with EG as a liquid substrate and placed in a bigger Petri dish that contained toluene. A dispersion of PbSe QDs in toluene was drop casted on the EG substrate. A beaker was placed on top of the Petri dishes to slow down the toluene evaporation. Under these conditions, the evaporation of the toluene solvent and the superlattice formation took around 16 hours. An atomically coherent buckled silicene-type honeycomb structure is formed by epitaxial attachment of the PbSe QDs via three of their six [100] facets.

*PbSe double layer superlattices.* To prepare double layer PbSe superlattices, we stamped the first monolayer of superlattices on the quartz substrates from EG. We dried the samples under vacuum for an hour and stamped the second layer of the superlattices on top of the first layer and dried again

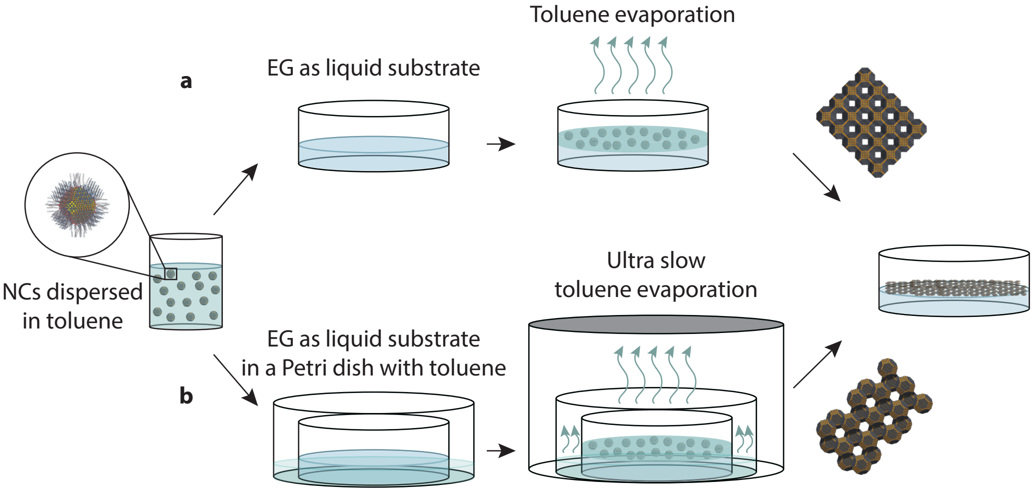

**Figure 5.9 | Experimental setup for self-assembly and oriented attachment of PbSe QDs.** A dispersion of PbSe QDs in toluene is prepared. (**a**) The QDs dispersion is drop casted on top of the ethylene glycol (EG) substrate, after which the toluene evaporates in about an hour. The PbSe square superlattices are formed by assembling PbSe QDs at the toluene/air interface after which the QDs attach via their four vertical 100 facets. (**b**) To form honeycomb superlattices, the EG substrate is put inside another Petri dish containing extra toluene. After drop casting the dispersion of PbSe QDs on top of the EG, a beaker was placed on top of the Petri dishes to slow down the toluene evaporation. After about 16 hours honeycomb superlattices are formed.

under vacuum.

*Transformation of PbSe square and honeycomb lattices to CdSe via a cation exchange reaction.* Silicon nitride TEM grids and quartz substrates with superlattices on top were kept in a 0.1 M cadmium oleate solution for 1h at 150 °C and then 175 °C for 10 minutes.[176] Afterwards, we cleaned the samples by immersing them in toluene, butanol/methanol (1:1), and methanol, respectively.

*Electron microscopy and electron diffraction.* Electron micrographs and selected area electron diffraction were recorded on a FEI Tecnai 20 operated at 200 kV. The HAADF-STEM measurements were performed using a double aberration corrected FEI Titan operated at 300 kV.

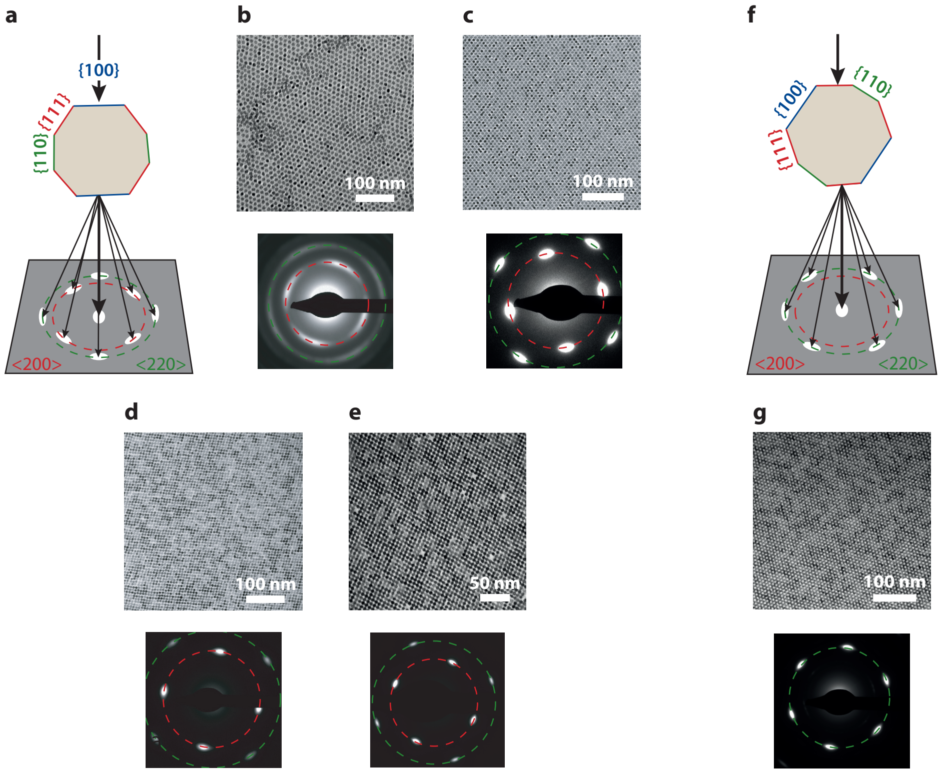

**Figure 5.10 | Electron diffraction tomography of superlattices.** (**a**) If the QDs are oriented with their {100} facets upwards, 4 spots on the <200> rings will be formed. (**b**) Most of the QDs are oriented with their {100} facets upwards, however, there are some with different orientations. As a result, a ring with four slightly sharper spots formed on <200> ring. (**c**) All the QDs are oriented with their {100} facets upwards. They are very well self-assembled, but without any atomic connection (attachment). Therefore, relatively thick 4 spots appear. (d) Atomic connections (necks) between the QDs in the square superlattices lead to narrower spots. (**e**) Thicker necks between the QDs result to very sharp and narrow spots. (**f**) If the QDs are oriented with their {111} facets upwards, 6 spots on the <220> ring will be formed. (**g**) In the case of silicene-type honeycomb superlattices, the {111} facets of the QDs are always upwards and the QDs are atomically connected. This results in very sharp and narrow 6 spots on the <220> ring.

*Optical characterization.* For the optical absorptance measurements, the superlattices on the quartz substrates were loaded in a custom-made sample holder inside an oxygen and water free glovebox. The optical absorption spectrum of the PbSe QDs dispersed in tetrachloroethylene was obtained on a PerkinElmer® LAMBDA$^{TM}$ 950 UV–vis–NIR spectrometer. The absorptance measurements of the PbSe superlattices were performed on a Bruker Vertex 70 FT-IR spectrometer or PerkinElmer® LAMBDA$^{TM}$ UV–vis–NIR spectrometer equipped with an integrating sphere. The absorptance spectra of the CdSe superlattices were obtained with a PerkinElmer® LAMBDA$^{TM}$ 900 UV–vis–NIR spectrometer equipped with an integrating sphere. The use of an integrating sphere reduces the contribution of scattered light to the measured transmission. For all measurements the transmission of the bare quartz substrate is subtracted.

*Absorptance measurements on CdSe samples.* Figure 5.12 shows absorptance measurements on the two different CdSe samples as for PbSe in Chapter 5.2; QDs in a honeycomb superlattice and square superlattice.

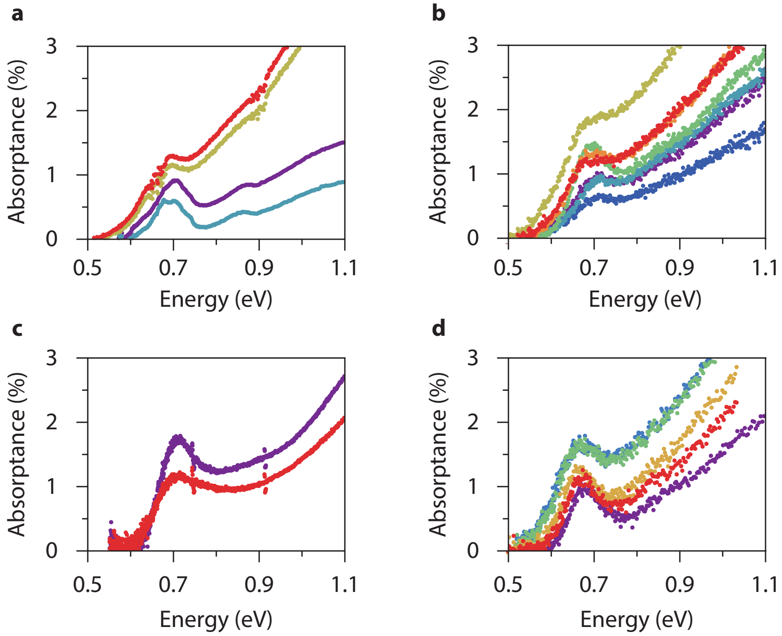

**Figure 5.11 | Overview of multiple absorptance measurements on the two PbSe superlattice samples performed by multiple research groups.** In Figures 5.2c,d representative measurements are used. (**a**) PbSe QD honeycomb superlattice, showing an average absorptance of 1.0% at 0.7 eV. The red and yellow spectra are prepared and measured in Utrecht and the purple and blue are prepared and measured in Delft. The difference between the two sets is caused by an integrating sphere used for the absorptance measurement in Delft, reducing the contribution of scattering in the measurement. **b**-**d** are all absorptance spectra on PbSe QD square superlattices prepared and measured in respectively Utrecht, Delft, and Ghent. The spectra show an average absorptance of 1.3% at 0.7 eV.

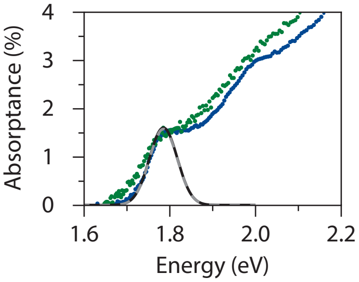

**Figure 5.12 | Absorptance spectra of the two types of CdSe QD samples as for PbSe in Chapter 5.2.** Absorptance spectra of CdSe QDs in a honeycomb superlattice (green) and square superlattice (blue). The absorptance at 2.0 eV is 1.6% for both superlattices. In black and gray the spectrum calculated using the oscillator strength of 6 nm QDs,[71] the superlattice parameter and the screening factor ( $|F|^2 = 0.66$ and $|F|^2 = 0.75$ respectively for honeycomb and square superlattice). See also Chapter 5.4 and Chapter 5.6.

*Dielectric screening in superlattices of epitaxially-connected QDs.* The local-field factor $F$ in square lattices of epitaxially-connected QDs was calculated using an atomistic approach in order to describe the effect of the epitaxial connections on the dielectric response. In this approach, the dielectric system is modeled as an ensemble of $N$ atoms. We define on each atom $i$ the average (energy) potential $V_i$ which is related to the variations of charge $\delta n_j$ on all atoms $j$, *i.e.*, the induced polarization charges. As described in refs 198,199, each physical quantity in this atomistic model is thus described by a matrix of size $N$. The bare potential $V_0$ induced by the external field $E$, the screened potential $V$, and the charges $\delta n$ are all defined by a column matrix of length $N$. The potentials and charges are linked by the linear relation $\delta n = \chi V$ where $\chi$ is the $N \times N$ polarization matrix that describes the noninteracting density response function. The screened potential, from which we derive $E_{\text{in}}$, is also given by $V = V_0 + v\delta n$ where the matrix $v$ represents electron-electron Coulomb interactions, *i.e.*, $v_{n,m} = e^2/|R_n - R_m|$ where $R_n$ is the position of atom $n$. Combining these equations leads to $V = \varepsilon^{-1} V_0$ where $\varepsilon$ is the $N \times N$ dielectric matrix equal to $I - v\chi$ where $I$ is the identity matrix. As described in ref 199, the non-diagonal terms of $\chi$ are restricted to nearest neighbors, and the bond polarizability is adjusted to give the correct dielectric constant $\varepsilon_{\text{in}}$ for the bulk semiconductor.

The superlattices are composed of tangent spheres of diameter $D$ connected by cylindrical necks of diameter $d$.[200] When the ratio $d/D$ increases, the local-field factor increases because a large part of polarization charges are repelled to infinity. In the extreme limit where all QDs would fuse to form a perfect 2D layer (quantum well), $F$ tends to unity, the external field is unscreened, all polarization charges are at infinity. The values of $F$ given in Chapter 5.2 were calculated for $d/D = 0.6$, $D = 5.5$ nm for PbSe, $D = 6.1$ nm for CdSe. We have checked that a ligand shell (represented by a dielectric shell) surrounding the superlattice has a minor effect on $F$, because polarization is dominated by the epitaxial connections between the QDs, polarization coming from ligands has a minor effect.

The methodology used to calculate the local-field factor $F$ in honeycomb superlattices is the same as for square ones. Again, each QD has a spherical shape and is connected to its three neighbors via cylindrical necks. However, the two QDs of the unit cell of the honeycomb lattice are not in the same plane since there is a 90° angle between bonds joining neighbor QDs.[176,201] The factor $F$ is found to be smaller in honeycomb superlattices than in square ones because, along the electric field direction, the QDs in the same plane are disconnected, connections are only present between QDs of different planes (chiral lattice). However, in this configuration, the dielectric response of the ligands becomes non negligible. As a consequence, the results were calculated for a honeycomb lattice fully embedded in a planar dielectric layer (thickness = 8.4 nm, dielectric constant = 3) that simulates the ligand shell.

*Modeling of the optical absorptance of lattices of QDs.* In this work, the band-edge absorption peak of the superlattices of QDs was calculated using the two-level model presented in Chapter 5.4. We assume that the total oscillator strength $f$, summed over all transitions contributing to this peak at the energy $\hbar\omega_0$, is the same as in single QDs. This assumption is based on the fact that, in superlattices of epitaxially-connected QDs, valence and conduction minibands are mainly derived from band-edge states of their constituent QDs.[200–202] The band-edge absorptance is given by Equation 5.27 and Equation 5.28 in which $f$ is deduced from optical cross sections measured on PbSe[203] and CdSe[71] QDs in solution. For the QD sizes considered in the present work, $f$ is 15 and 17 for respectively PbSe and CdSe.

*Parameters characterizing the absorptance of lattices of QDs.* Table 5.2 reports the different parameters that define the band-edge absorption of PbSe (CdSe) QDs in the different configurations studied in this work. The peak energy $\hbar\omega_0$ and the broadening energy $\eta$ are adjusted on experiments. The oscillator strengths are those of QDs in solution.[71,203] The values of $F$ for superlattices of epitaxially connected QDs were computed using the atomistic dielectric model described above. The $S_0$ values are obtained from TEM images. The good agreement between theoretical and experimental spectra, Figure 5.2 for PbSe, Figure 5.12 for CdSe, demonstrates that this model provides an accurate description of dielectric screening in superlattices of epitaxially connected QDs.

| Configuration | Compound | $f$ | $\hbar\omega_0$ (eV) | $\eta$ (eV) | $\lvert F\rvert^2$ | $S_0$ | Surrounding |
|---|---|---|---|---|---|---|---|
| Honeycomb superlattice | PbSe | 15 | 0.690 | 0.045 | 0.36 | $6.2^2\sqrt{3}/2$ | $4/(1.44+1)^2$ |
| Square superlattice | PbSe | 15 | 0.695 | 0.045 | 0.59 | $6.2^2$ | $4/(1.44+1)^2$ |
| Honeycomb superlattice | CdSe | 17 | 1.970 | 0.065 | 0.66 | $6.0^2\sqrt{3}/2$ | $4/(1.46+1)^2$ |
| Square superlattice | CdSe | 17 | 1.970 | 0.065 | 0.75 | $6.0^2$ | $4/(1.46+1)^2$ |

**Table 5.2 | Parameters characterizing the band-edge absorption for QDs in different configurations.** For QDs in lattices, $|F|^2$ is calculated using the atomistic dielectric model. These $|F|^2$ values and the correction factor for the surroundings (solvent or substrate) are used to generate the screening-free, *i.e.*, electronic contribution, absorptance at 0.7 eV and 2.0 eV for respectively PbSe and CdSe, shown in Figure 5.2. The values in this table are also used to generated the theoretical absorptance shown in Figures 5.3c,d and Figure 5.12 by using them in Equation 5.28.

## 5.6 Epitaxially connected quantum-dot superlattices

*The ruler principle.* For a 3D semiconductor, light absorption is best quantified using the absorption coefficient $a$ rather than the absorptance $A$. The absorption coefficient $a$ is defined in terms of the incident light intensity d$I$ that is absorbed by a material slab with a thickness d$x$:

$$\frac{\mathrm{d}I}{I} = -a\mathrm{d}x. \tag{5.37}$$

In what follows, we will write the slab thickness d$x$ in units of the exciton Bohr diameter $2r_\mathrm{X}$, hence $\mathrm{d}x = 2r_\mathrm{X}\mathrm{d}n$ with d$n$ the number of monolayers. Since the characteristic length for absorption ($1/a$) is in general much larger than $2r_\mathrm{X}$, the absorptance per Bohr diameter is given by the product $a$ times $2r_\mathrm{X}$. Moreover, the *effective* 2D density of states $\rho_2(E)$ at the transition energy $E$ of such a slab can be written as the product $2r_\mathrm{X}\rho_\mathrm{3D}(E)$ of the Bohr diameter and the 3D density of states. By means of Equation 5.22, the absorption coefficient of a semiconductor structure with a unit surface area and a thickness $2r_\mathrm{X}$ can then be written as

$$a = \frac{1}{2r_\mathrm{X}}\sigma_\mathrm{i}\rho_\mathrm{3D}2r_\mathrm{X}. \tag{5.38}$$

Since we know the absorptance of a 2D semiconductor, a more practical expression for the absorption coefficient of a semiconductor structure is obtained through the following approach:

- Normalize the density of states using the density of states of a 2D semiconductor.
- Introduce a correction factor $\gamma^2$ that takes differences in the integrated absorption cross section into account when comparing a given semiconductor structure with a 2D system.

As a result, we can rewrite Equation 5.38 as:

$$a = \frac{\sigma_\mathrm{i,2D}\rho_{2D}}{2r_\mathrm{X}}\left(\gamma^2\frac{\rho_\mathrm{3D}}{\rho_\mathrm{2D}}2r_\mathrm{X}\right) = \frac{\pi\alpha}{2r_\mathrm{X}}\Theta, \tag{5.39}$$

with

$$\Theta = \gamma^2\frac{\pi\hbar^2}{\mu}\rho_\mathrm{3D}(\hbar\omega)2r_\mathrm{X}. \tag{5.40}$$

In the supporting information of ref 184, we have shown that the entire correction factor $\Theta$ in Equation 5.39 is of the order of 1 for the band-edge transition of a bulk semiconductor. These results highlight that, as a good estimate, the band-edge absorption coefficient of a 3D semiconductor can be written as:

$$a \approx \frac{\pi\alpha}{2r_\mathrm{X}}. \tag{5.41}$$

**Figure 5.13 (right page) |** Absorption coefficient spectra for various bulk semiconductor materials of respectively GaAs,[180] GaSb,[204] InP,[205] InAs,[206] InSb,[181] PbS,[182] PbSe,[182] PbTe,[182] zb-CdS,[207] w-CdS,[208] zb-CdSe,[209] w-CdSe,[210] and CdTe.[211] The vertical gray line shows the band gap, the horizontal line the value of $m\pi\alpha/2r_\mathrm{X}$. The values for the bandgap ($E_\mathrm{g}$) and exciton Bohr radius ($r_\mathrm{X}$) are from ref 183. We can see that they often cross each other on the absorption coefficient spectra, indicating $a(E_\mathrm{g}) = m\pi\alpha/2r_\mathrm{X}$ as discussed in Chapter 5.2 and shown in Figure 5.3f.

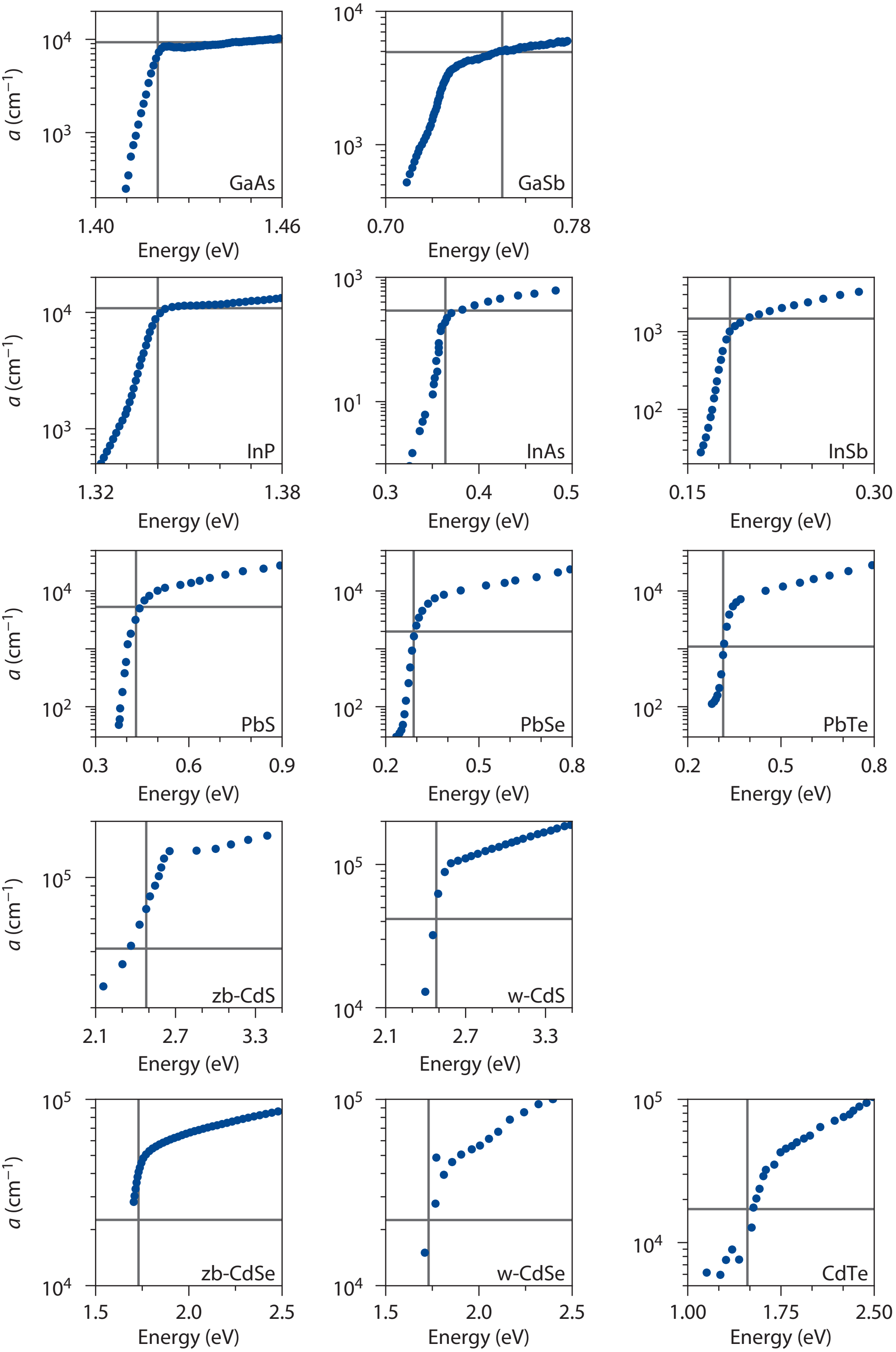
α (cm$^{-1}$)
Energy (eV)
GaAs
$10^4$
$10^3$
1.40
1.46
GaSb
$10^4$
$10^3$
0.70
0.78
InP
$10^4$
$10^3$
1.32
1.38
InAs
$10^3$
$10^1$
0.3
0.4
0.5
InSb
$10^3$
$10^2$
0.15
0.30
PbS
$10^4$
$10^2$
0.3
0.6
0.9
PbSe
$10^4$
$10^2$
0.2
0.5
0.8
PbTe
$10^4$
$10^2$
0.2
0.5
0.8
zb-CdS
$10^5$
2.1
2.7
3.3
w-CdS
$10^5$
$10^4$
2.1
2.7
3.3
zb-CdSe
$10^5$
$10^4$
1.5
2.0
2.5
w-CdSe
$10^5$
$10^4$
1.5
2.0
2.5
CdTe
$10^5$
$10^4$
1.00
1.75
2.50

## 5.6 The quantum of absorptance as a ruler to quantify absorption spectra of semiconductors

We incorporated a single PbSe honeycomb superlattice on top of interdigitated gold electrodes to form a photoconductor, see Figure 5.14. In order to do so, an atomically coherent PbSe honeycomb superlattice was assembled on the surface of the EG substrate, and then stamped onto the interdigitated electrodes, which feature a total electrode length of 34 cm and a gap of 25 µm gap between both electrodes. All measurements and device characterization were conducted with the sample being loaded in an airtight cell, prepared inside a glovebox to avoid oxidation of the sample. We analyzed the photoconductivity of the device by exciting the sample with light with energy-independent photon flux. The light intensity was modulated by a mechanical chopper within a frequency range from 1 to 500 Hz, and the resulting modulated photocurrent across the sample was measured. The illumination source was a halogen lamp, monochromatized by a SP-2150i Acton monochromator using a grating with 600 groves mm$^{-1}$ and a blaze wavelength of 1 µm. A silicon filter was placed directly after the monochromator exit. A Keithley 2614B supplied the voltage applied across the sample. A home-written software in LabView controlled spectral photoconductivity experiments. Current-voltage curves were measured using the Keithley 2614B SMU with and without illumination via a white light LED and controlled by a home-written software in Python.

Figure 5.14b presents the current-voltage curves in the dark and under illumination. The responsivity spectrum in Figure 5.14c measured with a modulation of 10 Hz closely reproduces the features of the absorptance spectrum observed for a PbSe honeycomb sample. However, the first and second optical transitions are more clearly observed than in an absorptance spectrum. This shows that the broadening of the absorptance resonances, and especially the onset at 0.5–0.6 eV is partially due to scattering. The signal-to-noise ratio in the responsivity spectra is excellent and shows the promise of such superlattices to be used in photodetectors. Also other 2D material platforms, such as monolayers of metal chalcogenides, have been reported for sensitive photodetection.[185] The superlattices that we propose here can be prepared from different semi-conductors and with a variable degree of quantum confinement as well, thus holding promise for cheap and sensitive photodetectors over a broad spectral region down to the mid-infrared.

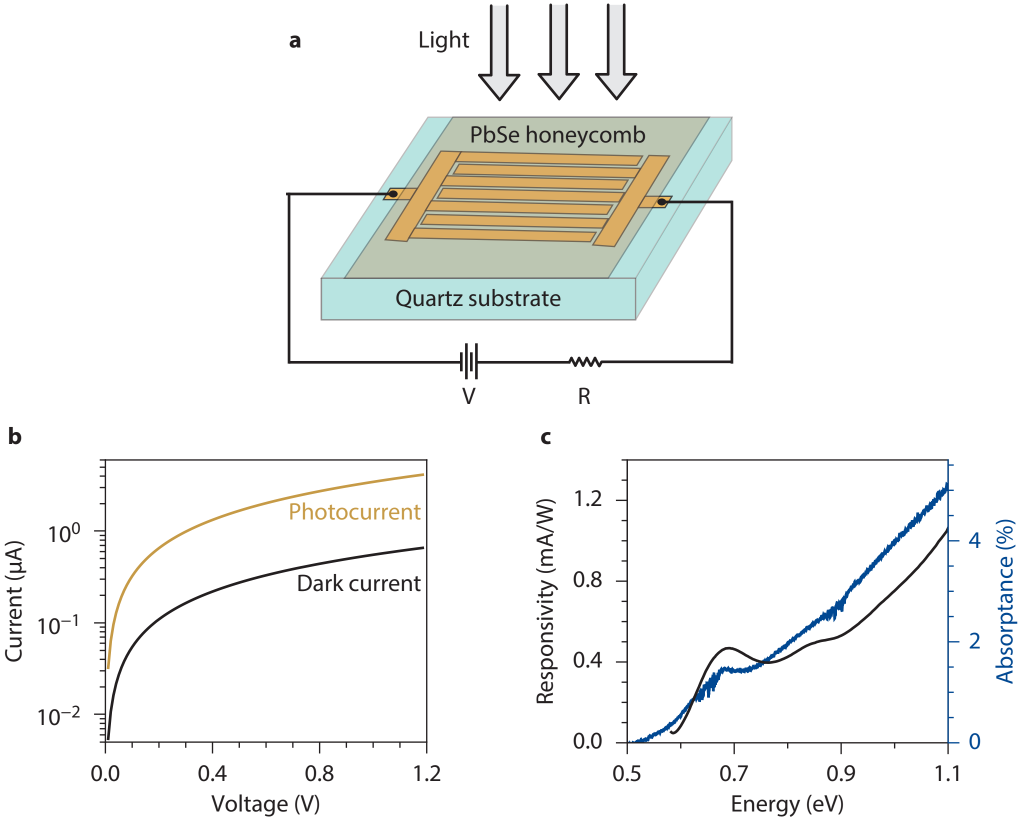

**Figure 5.14 | Photoconductivity measurements on PbSe honeycomb superlattices.** (**a**) A sketch of experimental arrangement for photoconductivity measurement on honeycomb superlattice. (**b**) The current-voltage curves of the PbSe QD honeycomb superlattice in the dark (black) and under illumination (yellow). (**c**) Responsivity spectrum for the PbSe QD monolayer honeycomb superlattice (black) reproducing the same features of the absorption spectrum (blue) but with more detail.

# Chapter 6

## Slow hole localization and fast electron cooling in Cu-doped InP/ZnSe quantum dots

Impurity doping of low-dimensional semiconductors is an interesting route towards achieving control over carrier dynamics and energetics, e.g., to improve hot carrier extraction, or to obtain strongly Stokes shifted luminescence. Such studies remain, however, underexplored for the emerging family of III–V colloidal quantum dots (QDs). Here, we show through a detailed global analysis of multiresonant pump–probe spectroscopy that electron cooling in copper-doped InP quantum dots (QDs) proceeds on subpicosecond time scales. Conversely, hole localization on Cu dopants is remarkably slow (1.8 ps), yet still leads to very efficient sub-bandgap emission. Due to this slow hole localization, common Auger assisted pathways in electron cooling cannot be blocked by Cu doping III–V systems, in contrast with the case of II–VI QDs. Finally, we argue that the structural relaxation around the Cu dopants, estimated to impart a reorganization energy of 220 meV, most likely proceeds simultaneously with the localization itself leading to efficient luminescence.

**Based on**

P.T. Prins, D.A.W. Spruijt, M.J.J. Mangnus, F.T. Rabouw, D.A.M. Vanmaekelbergh,
C. de Mello-Donegá, P. Geiregat

The Journal of Physical Chemistry Letters **13**, 9950–9956 (2022)

## 6.1 Introduction

Owing to rapid developments in the last 30 years, colloidal semiconductor nanocrystals (quantum dots, QDs) are currently applied as luminophores in displays and lighting.[7] The promise of QDs extends beyond these applications; QDs may form the active building blocks for solution-processable lasers,[212] bioimagers, luminescent solar concentrators (LSCs) and solar cells.[9] QDs combine a certain ease of processing with size- and shape-dependent optoelectronic properties as observed in both the energetics and dynamics of charge carriers. A key process in carrier dynamics is carrier cooling after nonresonant photoexcitation. In applications that rely on the extraction of hot carriers, such as non-conventional photovoltaics and photocatalysis, this cooling is undesired.[213,214] In many cases, however, fast cooling, *i.e.*, on a femtosecond time scale, is observed,[215] mostly facilitated by electron–hole coupled Auger mechanisms.[216–219] In II–VI QDs, this dominant Auger cooling pathway can be blocked by fast trapping valence band holes at doping-induced in-gap states leading to acclaimed multi-picosecond hot electron lifetimes.[220–222] Based on the above, the process of Cu doping may also be a means to slow down hot-electron cooling in the more environmentally friendly family of III–V QDs, such as InP. Cu doping in InP QDs was shown to cause quenching of the band-edge emission and concomitant appearance of a broader, sub-bandgap emission.[223–225] These changes in the steady state emission properties were ascribed to fast hole localization onto $Cu^+$ dopants, followed by a structural lattice relaxation of the atoms around the $Cu^{2+}$ site leading to strongly Stokes-shifted radiative recombination, similar to their II–VI counterparts.[224,226,227] Even though hole localization most likely occurs in III–V systems, for this to lead to a blocking of the Auger process critically depends on the time scale of electron–hole Auger coupling compared to the extraction of holes from the valence band by trapping. To date, the time scales of the assumed hole localization with respect to electron cooling remain unknown. It is therefore unclear whether the concept of slowing down electron cooling via doping also applies to the emerging family of III–V QDs with restricted toxicity.

Besides its effect on Auger electron–hole coupling, impurity doping enables sub-band gap luminescence.[228] The Stokes shift can be considerable and depends on the energetics and dynamics of the structural reorganization around the trapped carrier. Impurity-induced emission with a high quantum yield is much desired in LSCs in order to avoid photon losses by reabsorption in the QD luminophores.[229,230] In laser materials, the impurity level can result in population inversion and gain due to the large Stokes shift, similar to what is found in organic dyes.[231] So far, the understanding of charge-induced structural reorganization remains limited, in particular for III–V QDs.

In this chapter, we study the effect of Cu doping on the charge-carrier cooling dynamics in InP QDs. We use broadband and ultrafast pump–probe transient absorption (TA) spectroscopy with a range of different excitation wavelengths, chosen to be resonant with the relevant optical transitions. This method is ideally suited to investigate hot-carrier dynamics on the relevant time and energy scales.[232] However, as the simultaneous occurrence of transient bleaches, spectral shifts and induced absorptions observed in such experiments make data interpretation very difficult, we proceeded to employ an unbiased global-fit analysis method to identify excited states and quantify their dynamics in the context of cooling and structural reorganization.[233–238] As opposed to Cu-doped II–VI systems, we find that electron cooling in Cu:InP proceeds on ultrafast subpicosecond time scales whereas hole localization on $Cu^+$ in InP QDs occurs on a much slower, multiple picosecond, time scale. Hence, Cu dopants in InP quantum dots are most likely not able to prevent commonly observed Auger-assisted carrier cooling and are surprisingly ineffective as a strategy to slow down hot carriers. Hole localization onto $Cu^+$ leads to $Cu^{2+}$, which shows a strong reorganization energy. We do not observe this effect separately from the relaxation within our time resolution (about 150 fs), which suggests the process is extremely fast and most likely overlaps temporally with the hole localization itself, thereby finally leading to the observed efficient Stokes shifted emission.

## 6.2 Results and discussion

Cu-doped and undoped InP/ZnSe/$ZnSe_{0.5}S_{0.5}$/ZnS core/shell QDs, consisting of a ~3 nm InP core and a 3 monolayer shell, were prepared following a synthesis procedure adapted from literature,[223] see the methods in Chapter 6.4 and optical characterization of the InP cores in Figure 6.6. For simplicity, the explicit specification of the QD shells will be omitted hereafter. Inductively coupled plasma optical emission spectrometry (ICP-OES) on thoroughly washed core/shell samples shows that the Cu-doped InP QDs contain on average 30 Cu atoms per QD (SI). Both higher and lower doping levels were checked but results are always in line with what follows.

The absorption spectrum of the undoped InP QDs shows features at 2.2 and 2.7 eV (Figure 6.1a), which are assigned to transitions from the $1S_h$ and $1P_h$ level in the valence band (VB) to the $1S_e$ and $1P_e$ level in the conduction band (CB), respectively.[241] The emission spectrum shows band-edge emission at 2.1 eV with a broad tail to lower energies related to trap states[242,243] (Figure 6.1a). Upon Cu doping, the absorption peaks broaden and an absorption shoulder appears at lower energy, which is assigned to the excitation of $Cu^+$ d-electrons to the CB.[224,244,245] Such impurity-related absorption is often very low in oscillator strength, but can be clearly resolved here with an oscillator strength about 1 order of magnitude below the band edge absorption. Moreover, the band-edge emission is quenched, while a broad emission peak appears at 1.47 eV (Figure 6.1a). The resulting shift between the absorption peak at 2.2 eV and the emission is usually referred to as the apparent or global Stokes shift,[246,247] here 0.74 eV. The emission observed in Cu-doped InP QDs has a photoluminescence (PL) lifetime of 480 ns (Figures 6.1b and Figure 6.7a) with a quantum yield of 40%, which is much longer than that of the band-edge emission in undoped InP QDs (*viz.*, 40 ns, Figures 6.1b and Figure 6.7b). The ratio of the two lifetimes (480/40) matches the expected ratio of oscillator strengths obtained from absorption, being 1 order of magnitude, indicating little competition with nonradiative channels for the Cu-localized exciton. These observations are consistent with previous results on Cu-doped QDs[226] and allow us to assign the emission observed in Cu:InP QDs to the radiative recombination of a Cu-localized hole with a delocalized CB electron.

Figure 6.2a shows the normalized transient absorption ($\Delta A$) spectra for Cu-doped and undoped

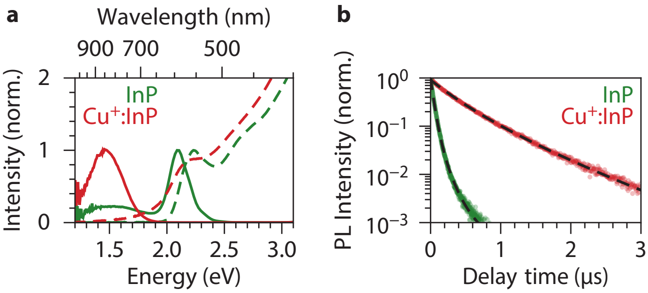

**Figure 6.1 | Linear Optical Properties.** (**a**) Absorption (dashed) and emission (solid) spectra of Cu-doped (red) and undoped InP (green) QDs. Both QDs have a ZnSe/$ZnSe_{0.5}S_{0.5}$/ZnS shell. The absorption spectra are normalized at 4.1 eV (Figure 6.6). The full width at half maximum of the emission from the Cu-doped and undoped QDs is 350 and 200 meV, respectively. (**b**) Photoluminescence decay curves of Cu-doped (red) and undoped InP (green) QDs under 515 nm excitation, taken at their respective emission maxima. The dashed lines show fits to a model for recombination between a delocalized electron and a localized hole[239] and a model of single exponential decay and delayed emission,[240] respectively (Figure 6.7).

InP QDs at 1 ns after excitation at 3.1 eV. At this delay time, all carriers have relaxed to their lowest excited state but have not yet recombined radiatively, as the PL decay time is much longer at 40 ns for undoped or 480 ns for doped QDs (Figure 6.1b). Both spectra show a negative signal (bleach) at 2.2 eV, matching the $1S_h$–$1S_e$ transition observed in the steady-state absorption spectra (Figure 6.1a). This transition is bleached in both the Cu-doped and undoped InP QDs; this can be understood by seeing that, in both cases, the lowest excited state has an electron-occupied $1S_e$ level. The TA spectrum of the Cu-doped InP QDs shows an additional bleach around 1.9 eV, which is absent in the TA spectrum of undoped QDs. This transition is also observed in the steady-state absorption spectrum of Cu-doped InP QDs, where it is assigned to the excitation of a $Cu^+$ d-electron to the $1S_e$ CB level, creating a $Cu^{2+}$–$1S_e$ excited state. Consequently, occupation of the $1S_e$ level bleaches this transition (Figure 6.2b). Besides negative signatures, both spectra also show a positive signal (photoinduced absorption) in the near-infrared region with a similar amplitude, from 1.0 to 1.7 eV (Figure 6.2a). This induced absorption is assigned to intraband transitions involving the excitation of the photogenerated electron and hole to higher CB and VB states, respectively.[248] The induced absorption does not show any significant kinetics on the time scale of the experiment (up to 3 ns) and appears instantly after excitation.

To determine the energies of the $1S_h$–$1S_e$ and the $Cu^{2+}$–$1S_e$ excited states, we fitted the bleach spectrum of the Cu-doped InP QDs to two Gaussians (Figure 6.2d). The transitions are broadened due to variations in size, shape, and composition of the QDs, surface imperfections that affect excited-state energies,[239] possible fine-structure splitting, and finally electron–phonon coupling.[249] The absorbing and emitting transitions between the ground state and the $Cu^{2+}$–$1S_e$ excited state are particularly broad (Figure 6.2d), mainly because the localized nature of the hole increases phonon coupling.[224] The shift between the maxima of the $Cu^+$ to $1S_e$ bleach (Figure 6.2d, orange dashed line)

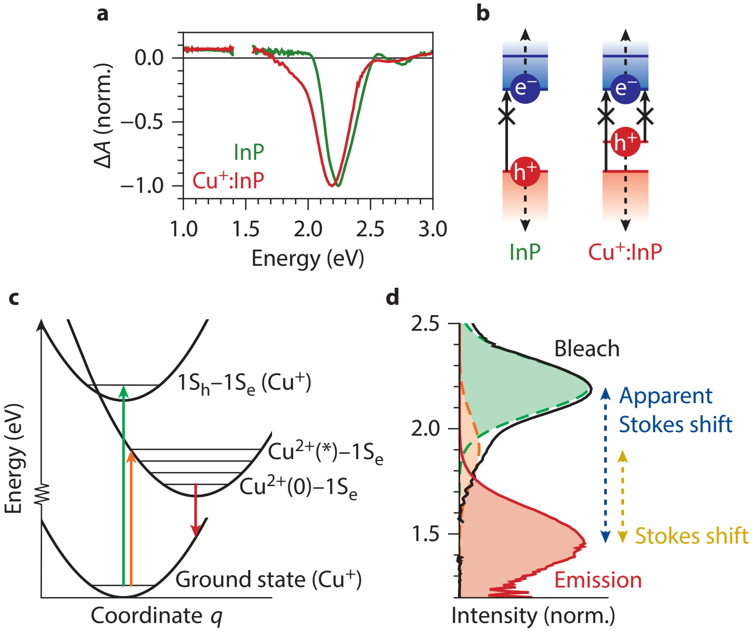

**Figure 6.2 | Energetics of absorption and emission.** (**a**) Normalized TA spectra of Cu-doped (red) and undoped InP QDs (green) after carrier cooling (1 ns delay time). (**b**) Schematic representation of the transitions that are blocked (solid arrows with cross) and new excited-state absorption transitions (dashed arrows). (**c**) Configurational diagrams of the ground and excited many-body states involved in excitation, cooling, trapping, and emission (not to scale and only some vibrational levels are shown). The coordinate *q* represents the environment around the Cu site. (**d**) The TA spectrum of the Cu-doped InP QDs decomposed into contributions of a VB to CB bleach (green) and a $Cu^+$ to CB bleach (orange). The emission spectrum is shown in red. The apparent and real Stokes shift are indicated with the blue and yellow arrows, they are 0.74 and 0.44 eV, respectively.

and the emission, *i.e.*, the Stokes shift, is 440 meV (Figure 6.2d, red line). Within the framework of a generalized Marcus model, this energy shift is twice the reorganization energy of the lattice for accommodating the change in the effective Cu oxidation state upon localization of the photogenerated hole. This reorganization energy of 220 meV is in line with reports on other Cu-containing QDs and DFT predictions on II–VI clusters.[224,244] The vibrational-zero level of the $Cu^{2+}(0)$–$1S_e$ excited state is in the middle between the maxima of absorption and emission, which is at 1.7 eV, see Figure 6.2d. We estimate the energy of the $1S_h$–$1S_e$ excited state from the energy of the maximum of the corresponding bleach feature (Figure 6.2d, green dashed line) at 2.2 eV.

By exciting the InP QDs with different pump wavelengths, we can create various excited-state configurations and follow their decay pathways. A pump pulse with an energy of 1.65 eV excites Cu-doped InP QDs selectively (resonantly) in the $Cu^+$-to-$1S_e$ transition (Figure 6.2c, orange arrow). Figure 6.3a shows the resulting TA spectra, measured at different delay times, −1 ps and between 0.1 and 7 ps (Figure 6.8a for 2D heatmap). The shape of the spectrum is independent of delay time and shows the absorption bleach of the $Cu^+ \rightarrow 1S_e$ and the $1S_h \rightarrow 1S_e$ transitions that we identified before (Figures 6.2c,d). This is consistent with instantaneous, *i.e.*, within our time resolution, formation of the $Cu^{2+}–1S_e$ excited state, from which radiative decay is slower than the time range of 3 ns available with our TA instrument (Figure 6.1b).

Shorter pump wavelengths produce TA spectra that change over the first few picoseconds after excitation (Figures 6.3b,c). Excitation with 2.18 eV, which matches the $1S_h$-to-$1S_e$ transition (Figure 6.2c, green arrow), results in minor spectral changes over the first few picoseconds, most notably in the tail of the absorption bleach at 1.9 eV (Figure 6.3b, Figure 6.8b for 2D heatmap). After a few picoseconds, the TA spectrum excited with 2.18 eV is the same as that excited with 1.65 eV (Figure 6.3a). We conclude that the dynamics in the first few picoseconds are most likely due to relaxation from the $1S_h–1S_e$ excited state to the $Cu^{2+}–1S_e$ excited state that we pumped in Figure 6.3a.

Continuing our systematic variation of pump wavelength, we excite nonresonantly at 3.1 eV. This results in an early time TA spectrum with multiple positive and negative signals (Figure 6.3c, Figure 6.8c for 2D heatmap). Within <1 ps, the spectrum converges to the early time spectrum that we saw before in Figure 6.3b, after which it changes further to resemble the spectra seen in Figure 6.3a. This is consistent with initial creation of an excited state with excess charge-carrier energy, which first relaxes to the $1S_h–1S_e$ excited state that we pumped in Figure 6.3b, and then further to the $Cu^{2+}–1S_e$ excited state that we created in Figure 6.3a.

When the spectral changes are as intricate as in Figure 6.3c, it is challenging to quantitatively

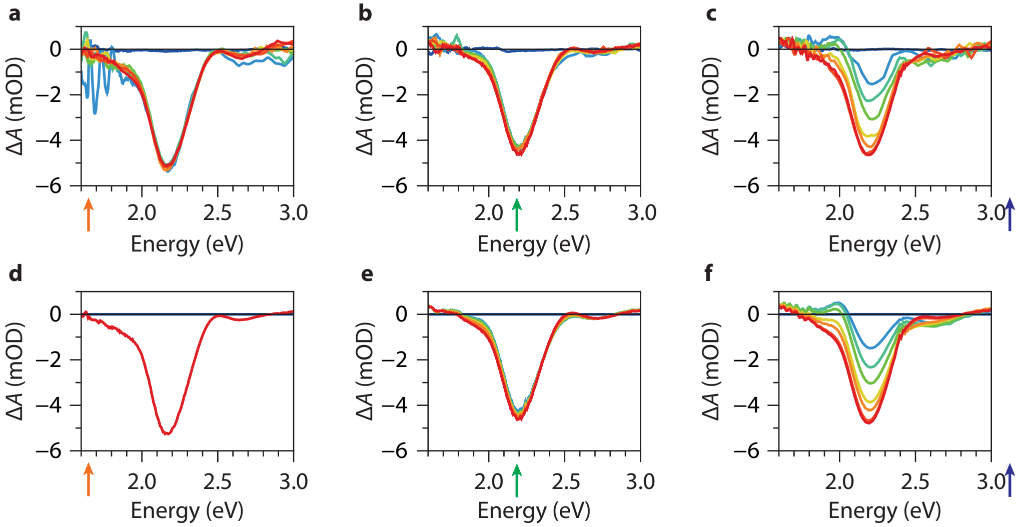

**Figure 6.3 | Multiresonant TA spectroscopy.** (**a–c**) Experimental transient absorption spectra of Cu-doped InP QDs at different delay times (–1, 0.1, 0.3, 0.5, 1, 1.5, 4, and 7 ps from blue to red) normalized for the absorbed fluence (see Chapter 6.5). The QDs are excited at (**a**) 1.65 eV, (**b**) 2.18 eV, and (**c**) 3.1 eV. (**d**–**f**) Global fit results from the data shown in panels **a**–**c**, using the model depicted in Figure 6.4. The arrows in the panels **a**–**c**, **d**–**f** indicate the excitation energy with the same color coding as in Figure 6.4.

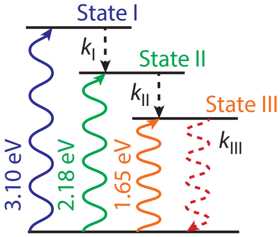

**Figure 6.4 |** An overview of the excited states created with the three different excitation energies, respectively blue, green, and orange. $k_I$ and $k_{II}$ are cooling processes and $k_{III}$ is the final radiative recombination (dashed red arrow).

understand the cooling dynamics from single-wavelength kinetic analysis. To retrieve the spectral signatures of the different excited states and quantify their lifetimes, we used an unbiased global fit analysis method with the kinetic model depicted in Figure 6.4 (see Chapter 6.7 for rate equations and fitting procedure). The spectra from the global fit are given in Figures 6.3e–g for the Cu-doped and undoped InP QDs, respectively. Comparing the experimental TA spectra (Figures 6.3a–c) to the fitted spectra (Figures 6.3e–g), we see that the agreement is excellent. Same, when we plot the data and global fit results as a function of time for specific energies, which can be found in Figure 6.9.

From our global-fit procedure, we can reconstruct the pure transient absorption spectra of the excited states involved. Important to note is that we do not input these spectra into the global fit but instead, they are an unbiased outcome of the fitting procedure. The spectra of the excited states of Cu-doped InP QDs for the three different excitation energies are shown in Figure 6.5a. The spectra of the excited state III are very comparable for the three different excitation energies (Figure 6.5a (lowest row), see also Figure 6.10). As discussed above, excited state III must be the $Cu^{2+}$–$1S_e$ state, which we create instantaneously when pumping at 1.65 eV (Figure 6.2c, orange arrow). This state could in principle be a vibrationally excited state of the $Cu^{2+}$, say $Cu^{2+}(*)$ in Figure 6.2c, or directly the vibrational ground state $Cu^{2+}(0)$. Both should be separated by the reorganization energy, but no such distinct set of spectra is obtained from the global fit. This indicates that the process of reorganization is faster than our time resolution, happening hence in concert with the hole localization itself. Arguing this reorganization is slower than our 3 ns time window is countered by the observation that the transient Stokes shifted PL build ups instantly, apart from the 150 ps time resolution, as is shown in Figure 6.7b.

The spectra of excited state II, which is the intermediate state under 3.1 eV excitation and the initial state under 2.18 eV excitation, are also remarkably similar for the two excitation wavelengths (Figure 6.5a (middle row), see also Figure 6.11). Note: in the 2.18 eV experiment we created 55% of excited state II and 45% of excited state III at $t = 0$, due to overlap of the absorbing transitions (Figure 6.2d, green and orange dashed lines). The striking similarity between the spectra confirms that after nonresonant excitation (3.1 eV excitation), the system initially relaxes to the same excited state that we create by excitation at 2.18 eV. We therefore interpret excited state II as the $1S_h$–$1S_e$ state, which we excite resonantly at 2.18 eV (Figure 6.2c, green arrow) and in which both the hole and electron occupy a delocalized band-edge level. We emphasize again that our global-fit procedure does not impose these similarities of the spectra a priori. The changes in the TA spectra between excited states II and III are induced by the hole localization on Cu which shows up as an extra bleach at 2.1 eV. Previous work on CdSe-based QDs has shown that a hole with excess energy can induce a photoinduced absorption on the lower energy side of the $1S_h$–$1S_e$ bleach (Figure 6.12).[250,251] Such a positive signal can partially cancel the bleach of the $Cu^+$ to $1S_e$ transition. The difference between the TA spectra of excited states II and III is likely due to the disappearance of such a type of additional induced absorption feature at 1.9 eV, because the hole cools, *i.e.*, loses its excess energy, when localizing on Cu. As argued above, we only observe one final state for the localized hole, indicating that any structural relaxation occurs either in concert with or faster than our time resolution.

The highest excited state I of Cu-doped InP QDs (Figure 6.5a (top row)) produces a derivative-like feature around the band gap energy at 2.1 eV and a bleach around 2.7 eV. This looks similar to the initial excited state we observe when performing the same measurement on the equally sized but undoped InP-based core/shell QDs (steady-state measurements in Figure 6.1a, TA measurements in Figure 6.13). The bleach at 2.7 eV matches well with the higher energy feature observed in the steady-state absorption spectrum (Figure 6.1a), which is assigned to a transition from the $1P_h$-level in the VB to the $1P_e$-level in the CB.[241] For this reason, we assign the highest excited state I populated under 3.1 eV to a situation where the electron occupies the $1P_e$ level. The electron occupation of the $1P_e$ level typically results in a red-shifted $1S_h \rightarrow 1S_e$ transition, resulting in the derivative-like feature in the differential absorption spectrum at 2.1 eV, as observed very clearly here.[232,250] Even though it is difficult to label exactly the hole level in the excited state, we can assume that the hole is delocalized over the dense hole manifold. For these reasons, we choose the label $h^*_{VB}$–$1P_e$ in Figure 6.5b, to indicate that the carriers are in the bands with excess energy compared to the band edge.

## 6.3 Conclusion

Our global-fit analysis for different excitation wavelengths unambiguously shows that hole localization from the VB edge ($1S_h$ state) to a $Cu^+$ dopant is remarkably slow (1.8 ps), in particular compared to typical time scales for hot-electron cooling from the 1P level (<500 fs).[252–256] Indeed, the time constant for hot-carrier cooling for our undoped InP-based core/shell QDs is 250 fs (see Figure 6.12). The photogenerated hole in both undoped and Cu-doped InP-based core/shell QDs therefore remains delocalized during the cooling process (Figure 6.5b). Hence, Cu doping cannot prevent any potential involvement of electron–hole Auger coupling in the cooling process. This explains why hot electrons created under 3.1 eV excitation relax in only 400 fs, comparable to the lifetime in the undoped InP QDs. This conclusion is in stark contrast with the earlier interpretation of TA data on Cu-doped CdSe QDs.[222] The authors of ref 222 attributed a slower component in the kinetics to slow electron cooling following ultrafast hole localization onto Cu. Our results based on a detailed global analysis, however, show that this strategy does not work for InP QDs. As to the microscopic nature of the very different coupling between the delocalized hole wave function and the Cu sites in II–VI *versus* III–V systems, we can only hypothesize at this point. A luminescence lifetime-fitting model,

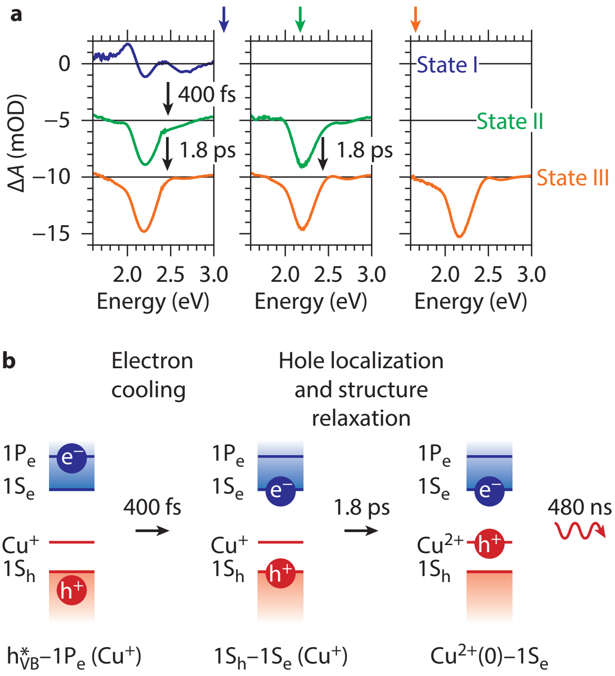

**Figure 6.5 | Global Fit Analysis.** (**a**) The transient absorption spectra of excited states I (blue), II (green), and III (orange) in Cu-doped InP QDs obtained from the global-fit analysis method for the three different excitation energies: blue arrow for 3.1 eV, green arrow for 2.18 eV, and orange arrow for 1.65 eV excitation. The spectra are shifted with −5 mOD for clarity. The black arrows show the fitted time constants for the transitions between the excited states. (**b**) Schematic representation of how we interpret the three excited states, $h^{*}_{VB}$–$1P_e$, $1S_h$–$1S_e$, and $Cu^{2+}(0)$–$1S_e$ respectively, and their lifetimes.

shown in Figure 6.7c, indicates that Cu atoms are most likely very uniformly distributed in large amounts throughout the InP core. Together with the dominantly type-I band alignment in InP/ZnSe, this suggests that strong spatial overlap exists between Cu sites and the initial band-edge hole wave function. If Cu dopants spread differently in the CdSe-based systems, one could expect a different degree of coupling leading to the observed fast hole localization. This thereby raises the question how electron cooling in the technologically relevant and environmentally friendly family of III–V materials can be slowed down. Combining Cu doping with other ways of reducing the Auger cooling rate, e.g., thick and/or type-II core–shell architectures,[257–260] might be key to significantly increase the lifetime of the hot electron.

To conclude, a rigorous analysis of multiresonant TA spectroscopic studies on Cu-doped and undoped InP-based core/shell QDs demonstrates that localization of the photogenerated hole in Cu-doped InP QDs is slow, with a time constant of 1.8 ps, thereby preventing any slowdown of carrier relaxation of hot electrons. Our results further identify that structural relaxation of the Cu site is most likely ultrafast with a reorganization energy of 220 meV.

## 6.4 Additional figures

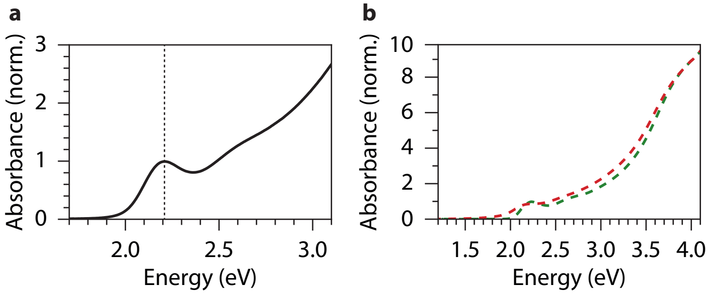

**Figure 6.6 |** (**a**) Steady-state absorption spectrum of the seed InP cores used for the copper doping and core/shell synthesis. The first absorption peak is at 2.21 eV (dashed line). Using the semi-empirical QD sizing function from ref 264 (specifically, equation 6 with parameters from table 2), we find a diameter of 3.0 nm. The bare InP cores do not show any emission upon photoexcitation. (**b**) Same absorption spectra as in Figure 6.1a but now zoomed out up to 4.1 eV, doped Cu-doped (red) and undoped InP (green) QDs. The spectra converge at higher energies, indicating that this is a good way of normalization, independent of copper doping.

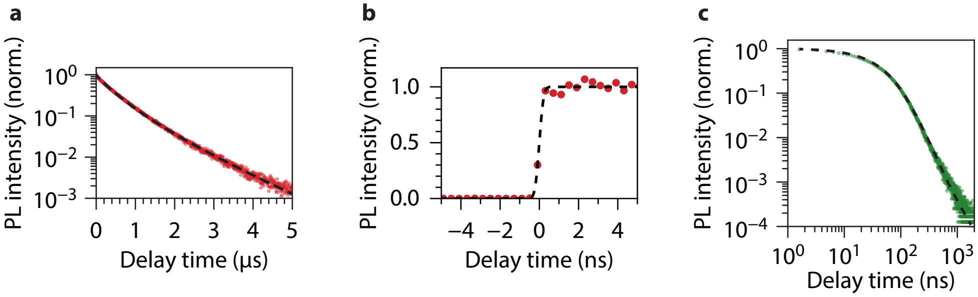

**Figure 6.7 | Same photoluminescence decay curves as shown in Figure 6.1b but now plotted individually.** (**a**) Decay curve of Cu-doped InP QDs under 515 nm excitation. The dashed line is a fit to a model for recombination between a delocalized electron and a localized hole as in ref 239. The parameter $r_{max}$ can be estimated from the ratio core diameter *versus* core/shell diameter. From the position of the absorption peak of the cores and the amount of shell material added we obtained a core diameter of 3 and a core/shell diameter of 4.7. This gives a $r_{max}$ of 0.640 nm. Subsequently the best fit yields a radiative lifetime of $\tau_0 = 248$ ns, which is the lifetime when the hole is localized directly in the center, *i.e.*, $r = 0$. Note that this model has as few fit parameters as a single exponential fit but still gives a good fit for multi-exponential behavior. The mean lifetime, *i.e.*, intensity reduced to 1/e, is 480 ns. (**b**) Zoom in on the decay curve of Cu-doped InP QDs (as shown in panel **a**), showing −5 to 5 ns. The dashed line is a fit to a step function convoluted with a Gaussian. The standard deviation of the Gaussian is ~170 ps, which is close to the instrument response of the set-up used to measure the decay curve. There is no indication of a rise in the intensity, *i.e.*, it appears instantly within the instrument response. (**c**) Decay curve of undoped InP QDs under 515 nm excitation plotted on a log-log scale to better visualize the slow component. The slow component follows power-law behavior, typical for delayed emission.[240] The dashed line is a fit to a model of single exponential decay and delayed emission as in ref 240. The best fit is obtained with a radiative lifetime of $\tau = 41.3$ ns, a trapping probability of $p = 14.7\%$, and a power exponent of $\alpha = 2.09$.

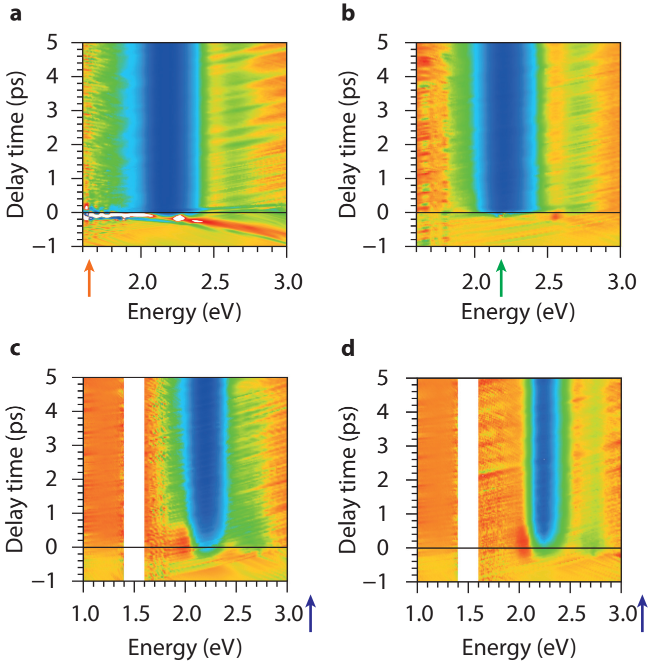

**Figure 6.8 |** Same data as in Figures 6.3a–c but here in 2D format: Panel (**a**) 1.65 eV excitation in Cu-doped InP, panel (**b**) 2.18 eV excitation in Cu-doped InP, and panel (**c**) 3.1 eV excitation in Cu-doped InP. (**d**) 3.1 eV in undoped InP. The intensity scales from blue ($\Delta A = -10$) to red ($\Delta A = 2$).

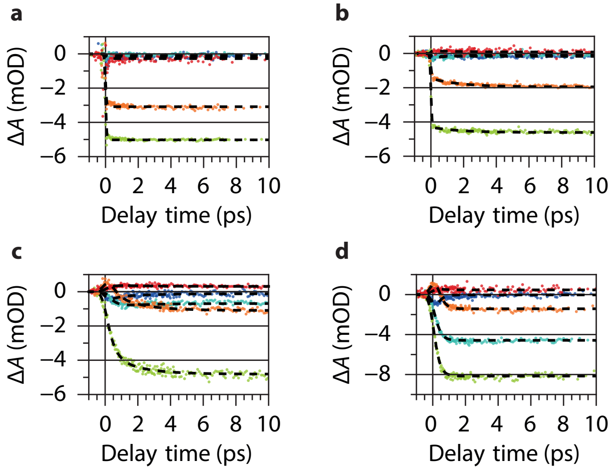

**Figure 6.9 |** Global fit results for time traces at energies throughout the entire spectrum. Spectral slices of the heat maps in Figure 6.8. The dashed lines are the global fit results. From (**a**–**d**), 1.65 eV excitation in Cu-doped InP, 2.18 eV excitation in Cu-doped InP, 3.1 eV in Cu-doped InP, and 3.1 eV in undoped InP.

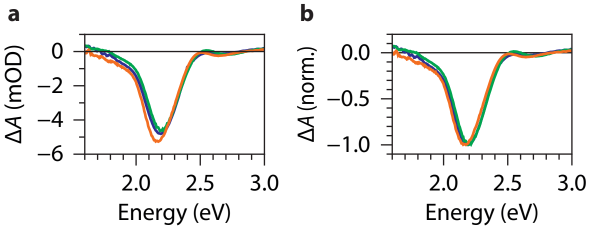

**Figure 6.10 |** Final transient absorption spectrum (excited state III) of the Cu-doped InP QDs for the three different excitation energies. The spectra of the final state only normalized for the absorbed fluence (**a**) and with additional normalization (**b**), for excitation into the $Cu^+$–CB (1.65 eV, orange), into the VB–CB (2.18 eV, green), and at 3.1 eV (blue). The normalization factor of the $Cu^+$ to CB excitation is more prone to errors due to the low absorption cross section at that energy. The small shifts can be attributed to slight differences between the excited populations due to inhomogeneity.

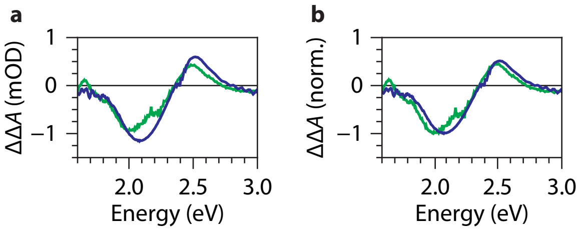

**Figure 6.11 |** Difference (Δ$\Delta A$) between the transient absorption spectra of excited state II and III for VB–CB (2.18 eV) excitation (green) and 3.1 eV excitation (blue) without additional normalization (**a**) and with (**b**). The blue Δ$\Delta A$ spectrum is obtained after subtracting state II from state III for the 3.1 eV excitation (Figure 6.5a, left row). The green Δ$\Delta A$ spectrum is the same but for the 2.18 eV excitation (Figure 6.5a, middle row). The interpretation of this Δ$\Delta A$ spectrum is difficult, as discussed above. The presence of a hot/delocalized hole shifts transitions, resulting in multiple bleaches and photo-induced absorption features. The additional normalization in panel **b** corrects for small errors made when normalizing the spectra for the absorbed fluence, similar as done in Figure 6.10b. The small shift can be attributed to a slight difference between the excited populations due to inhomogeneity.

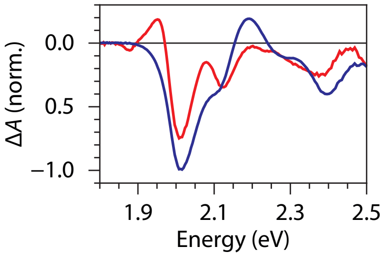

**Figure 6.12 |** Transient absorption spectroscopy measurement on high quantum yield CdSe/CdS/ZnS QDs with $2S_{3/2}$ excitation, *i.e.,* hot hole excitation (data from ref 251). The red spectrum is the transient absorption spectrum for a cold electron (in $1S_e$) and a hot hole (in $2S_{3/2}$), and the blue transient absorption spectrum is for a cold electron and a cold hole (in $1S_{3/2}$). The induced absorption at 1.95 eV originates from a lower biexciton energy when a hot hole is present compared to when a cold hole is present.[250]

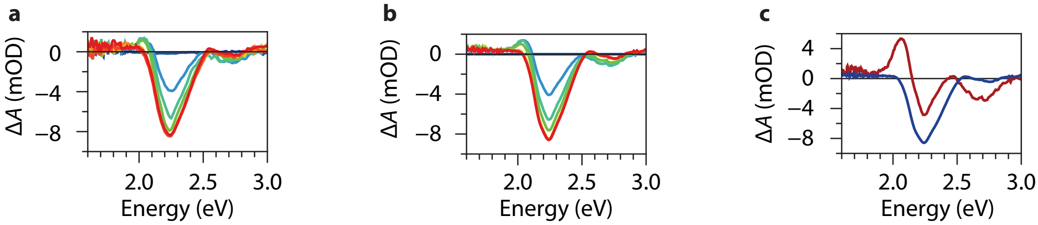

**Figure 6.13 |** Global fit results for undoped InP QDs. (**a**) Experimental transient absorption spectra of undoped InP QDs at different delay times (−1, 0.1, 0.3, 0.5, 1, 1.5, 4, and 7 ps from blue to red) normalized for the absorbed fluence. The QDs are excited at 3.1 eV. The heat map data can be found at Figure 6.8d and the time traces at certain energies at Figure 6.9d. (**b**) Global fit results from the data shown in panel **a**. (**c**) The transient absorption spectra of the two excited states obtained from the global-fit analysis method. The hot electron state (red), *i.e.*, electron populates the $1P_e$ level, decays into the cold state (blue) with a lifetime of 250 fs.

## 6.5 Methods

*Chemicals.* Stearic acid (SA, Sigma-Aldrich®, 95%), methanol (MeOH, Sigma-Aldrich®, 99.8%), tetramethylammonium hydroxide solution (TMAH, Sigma-Aldrich®, 25 wt% in methanol), copper(II) chloride ($CuCl_2$, Sigma-Aldrich®, 99%), 1-octadecene (ODE, Sigma-Aldrich®, 90%, degassed prior to use), indium(III) acetate ($InAc_3$, Sigma-Aldrich®, 99.99%), myristic acid (MA, Sigma-Aldrich®, ≥99%), tris(trimethylsilyl)phosphine ($P(TMS)_3$, ACROS Organics™, 98%), *n*-octylamine (Sigma-Aldrich®, 99%, degassed prior to use), zinc stearate ($ZnSt_2$, Sigma-Aldrich®, ≥95%), selenium (Se, Strem, -200 mesh, 99.99%), sulfur (S, Sigma-Aldrich®, 99.98%), trioctylphosphine (TOP, Sigma-Aldrich®, 97%), anhydrous acetone (VWR®, ≥99.8%), anhydrous ethanol (Sigma-Aldrich®, ≥99%), anhydrous toluene (Sigma-Aldrich®, 99.98%), and butylamine (Sigma-Aldrich®, 99,5%).

*Copper precursor.* Copper(II) stearate ($CuSt_2$) was prepared by a synthesis protocol adapted from literature.[261] 20 mmol (5.670 g) SA was dissolved in 38 mL MeOH by heating to 50 °C. After obtaining a clear solution, the reaction mixture was cooled down to room temperature. At room temperature, 20 mmol TMAH (7.292 g TMAH solution) was added, and the reaction mixture was kept stirring for 15 minutes. Subsequently, a solution of 10 mmol (1.345 g) $CuCl_2$ in 12.5 mL MeOH was added dropwise to the reaction mixture under vigorous stirring. A green precipitate of $CuSt_2$ slowly flocculated. After adding all the $CuCl_2$ in MeOH, the precipitate was washed with hot MeOH on a Büchner funnel, dried under vacuum, and stored in a glovebox. Before using $CuSt_2$ to dope the InP quantum dots (QDs) with copper, a 0.008 M solution of $CuSt_2$ in ODE was prepared by heating to 130 °C until the $CuSt_2$ was dissolved.

*Indium precursor.* The indium precursor for the InP core QDs synthesis was prepared in a large amount. 3.6 mmol (1.051 g) $InAc_3$, 15.75 mmol (3.597 g) MA, and 45 mL ODE was added to a round-bottom flask. The mixture was degassed on a Schlenk line at room temperature until all bubbles disappeared. Subsequently, the temperature was increased to 130 °C and degassed until a clear solution was obtained. Then the mixture was cooled down to room temperature and became turbid.

The mixture was stored in a glovebox.

*InP core QDs.* Inside a glovebox, one-ninth of the indium precursor was heated to 188 °C in a three-neck round-bottom flask equipped with a Vigreux condenser. To prepare the phosphor precursor, 0.2 mmol (58 µL) $P(TMS)_3$, 2.4 mmol (0.4 mL) *n*-octylamine, and 1 mL TOP were mixed in a vial inside a glovebox and transferred to a syringe. At 188 °C, the phosphor precursor was injected rapidly into the three-neck round-bottom flask while stirring vigorously. After injection, the temperature was set at 178 °C. The color of the reaction mixture changed from orange to dark red. After 30 minutes, the reaction was quenched by injecting 3 mL ODE. At room temperature, the reaction mixture was split into two equal parts. This synthesis procedure was adapted from refs 223,262.

*Cu-doped InP core QDs.* One part of the raw InP core QDs mixture was heated to 130 °C. Upon reaching this temperature, 2.5 mL of the copper precursor (0.02 mmol $CuSt_2$) was added dropwise. After addition, the temperature was increased to 220 °C with a heating rate of ~1 °C min$^{-1}$. When reaching 220 °C, the mixture was cooled down by removing the heating. This synthesis procedure was adapted from ref 223.

*Cu-doped and undoped InP QDs with a ZnSe/*$ZnSe_{0.5}S_{0.5}$*/ZnS shell.* The successive ion layer adsorption and reaction (SILAR) method was used for the growth of a thin and alloyed shell.[263] The shell exists of a ZnSe layer, a $ZnSe_{0.5}S_{0.5}$ layer, and a ZnS layer. The layers have the thickness of half a unit cell, also frequently called one monolayer. The zinc precursor was a 0.1 M solution of $ZnSt_2$ in ODE, degassed at 130 °C for an hour. The selenium/sulfur precursors were a 0.1 M solution of Se/S in TOP, sonicated until all material was dissolved. The specific amounts of material needed for SILAR depends on the InP QDs core size and number, respectively 3 nm and 140 nmol (in one half of the reaction mixture). In this case we added:

| Layer | Zinc precursor (mL) | Selenium precursor (mL) | Sulfur precursor (mL) |
|---|---|---|---|
| 1 | 0.33 | 0.33 | - |
| 2 | 0.46 | 0.23 | 0.23 |
| 3 | 0.63 | - | 0.63 |

The shell synthesis was done using the raw reaction mixture for the Cu-doped and undoped core InP QDs. The zinc precursor was added at 150 °C and allowed to react for 10 minutes. Next, the anionic precursor was added. Subsequently, the mixture was heated to 220 °C. After 30 minutes the reaction mixture was cooled down again to 150 °C and the same cycle was repeated twice. After the last cycle, the reaction was cooled down and the QDs were precipitated by adding acetone and ethanol until it became turbid. After redispersing in toluene, this washing step was repeated twice. The final sample was stored in a high concentration in toluene in the glovebox.

*Linear Absorption and Luminescence Spectroscopy.* For optical measurements, the samples were diluted with toluene in the glovebox and stored in 10-mm pathlength quartz cuvettes. Absorption spectra were measured on a PerkinElmer® LAMBDA$^{TM}$ 950 UV–vis–NIR spectrometer. Photoluminescence (PL) spectra were recorded on a fiber-coupled spectrometer (Ocean Optics USB4000-FL-395) using a 395-nm LED as excitation source. By placing a 400-nm longpass filter before the spectrometer, the excitation light was filtered out. The wavelength-dependent detection efficiency of the spectrometer and filter was corrected for, using a calibrated light source (Avantes AvaLight-DH-CAL). PL decay measurements were obtained on an Edinburgh Instruments FLS920 fluorescence spectrometer equipped with a 375-nm diode laser (Edinburgh Instruments EPL-375, 100 kHz repetition rate) as excitation source and a photomultiplier tube (Hamamatsu H7422) for detection. A PicoQuant TimeHarp 260 Pico was used for time-correlated single photon counting (TCSPC). The PL photon rate was below 1 kHz in all PL decay measurements.

*Transient Absorption Spectroscopy.* For the transient absorption (TA) spectroscopy measurements, the samples were diluted with toluene in the glovebox and stored in 2-mm pathlength quartz cuvettes. A titanium-doped sapphire laser was used to generate 800 nm light with 110-fs pulses with a repetition rate of 80 MHz (Spectra-Physics® Mai Tai® HP). The pulses were recompressed to 110-fs at 1 kHz using a regenerative amplifier (Spectra-Physics® Spitfire® Ace™ with a 527 nm Spectra-Physics® Empower® seed laser). From this beam, 95% was coupled into a traveling wave optical parametric amplifier (LIGHT CONVERSION TOPAS-PRIME), to generate the light used to pump the QDs, *i.e.,* 3.1, 2.18, and 1.65 eV. Before the pump reached the sample, the pump was chopped to 500 Hz. The pump profile was determined using a beam profiler (Thorlabs BC106N-VIS/M). The profile represents a two-dimensional Gaussian with $\sigma_x$ and $\sigma_y$ respectively 431 and 396 µm. The remaining five percent of the 800 nm beam was used to generate the broadband probe from 350 to 800 nm ($CaF_2$) or 850 to 1600 nm (YAG crystal). The probe beam was ~10 times smaller than the pump beam and aligned to the middle of the pump beam. The arrival of the probe pulse was delayed relative to the pump using an automated two-folded delay stage (Newport™ TAS) with a maximum delay of 3 ns. The probe spectrum was measured on a fiber-coupled spectrometer. To avoid effects of photocharging and sample degradation the samples were stirred during the measurements. All TA data used in this work is corrected for dispersion in the probe light (chirp)[232] by fitting a polynomial function to the solvent response of toluene. Additionally, the TA data is normalized by the total number of excitations per area per pulse and the average number of excitons $\langle N \rangle$ is always below 0.15 (see Chapter 6.5 and Chapter 6.6).

*Inductively coupled plasma optical emission spectrometry (ICP-OES).* Before performing the measurements, the QDs were washed three more times with toluene, acetone, and ethanol (v/v 1:1:16). To facilitate the removal of the stearates, 25 µL butylamine was added during the third washing step. After the last centrifugation, the QDs were dried under vacuum and subsequently dissolved overnight in 65% nitric acid (ultrapure for trace metal analysis). This mixture was diluted with ultrapure water to ~1 µg $mL^{-1}$ In in 5% nitric acid. The emission of the samples was measured using a PerkinElmer® Optima™ 8300DV and compared to a calibration curve prepared from diluting a standard (PerkinElmer® Multi-Element Standard 3). The obtained Cu to In ratio is 0.1. In a 3-nm spherical zinc-blende InP QD are ~300 In atoms. So, there are ~30 Cu atoms per QD.

## 6.6 Normalization TA data by total number of excitations per area per pulse

Often, the differential absorbance is normalized for the average number of excitations per QD per pulse:

$$\langle N \rangle = \sigma_p J_p, \tag{6.1}$$

With $\sigma_p$ the absorption cross section per QD (cm$^2$), $J_p$ the average fluence in photons per area per pulse (cm$^{-2}$) at the excitation energy $p$. $J_p$ is the average fluence corrected for absorption throughout the cuvette according to:

$$J_p = \frac{1 - 10^{-A_p}}{A_p \ln 10} J_{0,p}, \tag{6.2}$$

with $A_p$ the absorbance and $J_{0,p}$ the measured fluence. However, since $\sigma_p$ is not easily experimentally accessible, we followed ref 265:

$$\sigma_p = \frac{A_p \ln 10}{n}, \tag{6.3}$$

with $n$ the (projected) number density per area (cm$^{-2}$). If we plug Equation 6.3 in Equation 6.1, we obtain:

$$\langle N \rangle = \frac{A_p \ln 10}{n} \frac{1 - 10^{-A_p}}{A_p \ln 10} J_{0,p}. \tag{6.4}$$

We used $n\langle N \rangle$ to normalize the differential absorbance:

$$n\langle N \rangle = A_p \ln 10 \frac{1 - 10^{-A_p}}{A_p \ln 10} J_{0,p} = (1 - 10^{-A_p}) J_{0,p}. \tag{6.5}$$

Here, $n\langle N \rangle$ corresponds to the average number of excitations per area per pulse (cm$^{-2}$).

$A_p$ was determined from the steady-state absorption spectrum measured on the samples for TA. $J_{0,p}$ was calculated from a laser power measurement and a beam profile measurement by:

$$J_{0,p} = \frac{P}{fES}, \tag{6.6}$$

with $P$ the power (J s$^{-1}$), $f$ the frequency (s$^{-1}$), $E$ the energy of the photons used for excitation (J), and $S$ the area of the beam (cm$^2$).

$S$ was calculated from the width of the beam using:

$$S = 2\pi\sigma_x\sigma_y, \tag{6.7}$$

with $\sigma_x$ and $\sigma_y$ the standard deviation in the $x$ and $y$ direction from a two-dimensional Gaussian fitted to the beam profile.

## 6.7 Estimation $\langle N \rangle$

The average number of excitons $\langle N \rangle$ is still important to estimate the amount of multiexcitons. In our work we wanted to study the cooling of single excitons, for that reason the number of multiexcitons must be negligible. To calculate the number of excitons we need to know the absorption cross section (Equation 6.1). Good practice has shown that one can estimate the absorption cross section at higher energy by using bulk parameters and taking into account dielectric screening.[116] Following the methodology from ref 266 and the bulk values from Adachi[267] we find an absorption cross section of $8 \cdot 10^{-15}\ \mathrm{cm}^{-2}$ at 300 nm. We subsequently scale the absorption cross section with the absorption spectrum to obtain the absorption cross section at the excitation energies used in this work. In all our experiments $\langle N \rangle < 0.15$. The excitons are distributed according to the Poisson distribution. The probability that a QD contains $N$ excitons is:

$$P(N) = \frac{\langle N \rangle^{N} \mathrm{e}^{-\langle N \rangle}}{N!}. \tag{6.8}$$

The ratio $P(2)/P(1)$ is equal to $\langle N \rangle/2$. Hence, the contribution of biexcitons in our experiments is below 7.5%.

## 6.8 Global fit analysis of TA data

For *three* excited states, *i.e.*, 3.1 eV excitation of Cu-doped InP QDs:

$$\frac{\mathrm{d}N_1}{\mathrm{d}t} = -k_1 N_1(t) \tag{6.9}$$

$$\frac{\mathrm{d}N_2}{\mathrm{d}t} = k_1 N_1(t) - k_2 N_2(t) \tag{6.10}$$

$$\frac{\mathrm{d}N_3}{\mathrm{d}t} = k_2 N_2(t) - k_3 N_3(t). \tag{6.11}$$

Using the conditions at $t = 0$, $N_1(0) = 1$, $N_2(0) = 0$, $N_3(0) = 0$, we can solve the Equations 6.9–6.11. Additionally, we set $k_3$ to 0 (this is the radiative decay rate which can be ignored because for cooling we only look at the data up to 100 ps). We get the following equations:

$$N_1(t) = \mathrm{e}^{-k_1 t} \tag{6.12}$$

$$N_2(t) = -\frac{k_1(\mathrm{e}^{-k_1 t} - \mathrm{e}^{-k_2 t})}{k_1 - k_2} \tag{6.13}$$

$$N_3(t) = \frac{k_1 - k_1 \mathrm{e}^{-k_2 t} - k_2(1 - \mathrm{e}^{-k_1 t})}{k_1 - k_2}. \tag{6.14}$$

For *two* excited states with the same conditions at $t = 0$, *i.e.*, 3.1 eV excitation of undoped InP QDs, the rate equations are equal to Equation 6.12 and Equation 6.13 with $k_2$ set to zero.

For *two* excited states but with different conditions at $t = 0$, *i.e.*, 2.18 eV excitation of Cu-doped InP QDs:

$$\frac{\mathrm{d}N_1}{\mathrm{d}t} = -k_1 N_1(t) \tag{6.15}$$

$$\frac{\mathrm{d}N_2}{\mathrm{d}t} = k_1 N_1(t) - k_2 N_2(t). \tag{6.16}$$

Using the conditions at $t = 0$, $N_1(0) = f_0$, and $N_2(0) = 1 - f_0$, we can solve Equation 6.15 and Equation 6.16. Additionally, we set the radiative decay rate $k_2$ to 0 again. We get the following equations:

$$N_1(t) = f_0 \mathrm{e}^{-k_1 t} \tag{6.17}$$

$$N_2(t) = f_0(1 - \mathrm{e}^{-k_1 t}). \tag{6.18}$$

All rate equations are convoluted with the instrument response function (IRF). The instrument response function is taken as a Gaussian. The equations used for the global fit analysis are:

$$N_x^{\mathrm{IRF}}(t) = \int_{-\infty}^{\infty} \left\{ \begin{array}{ll} 0 & \tau \leq t_0 \\ N_x(\tau - t_0) & \tau > t_0 \end{array} \right\} \frac{1}{\sqrt{2\pi}\delta} \mathrm{e}^{-\frac{(t-\tau)^2}{2\delta^2}} \mathrm{d}\tau. \tag{6.19}$$

A time trace at one specific energy for three excited states can be described by:

$$I_E(t) = A_E N_1^{\mathrm{IRF}}(t) + B_E N_2^{\mathrm{IRF}}(t) + C_E N_3^{\mathrm{IRF}}(t). \tag{6.20}$$

For the global fit we sum over all time traces in the data set and use a least square fitting method to find the best fit parameters. Plotting $A_E$, $B_E$, and $C_E$ as function of energy we get the excited state spectra as shown in Figure 6.5.

# References

# References

1. Montanarella, F. & Kovalenko, M. V. Three Millennia of Nanocrystals. *ACS Nano* **16**, 5085–5102 (2022).
2. Walter, P. *et al.* Early Use of PbS Nanotechnology for an Ancient Hair Dyeing Formula. *Nano Lett.* **6**, 2215–2219 (2006).
3. Freestone, I., Meeks, N., Sax, M. & Higgitt, C. The Lycurgus Cup — A Roman nanotechnology. *Gold Bull.* **40**, 270–277 (2007).
4. Faraday, M. X. The Bakerian Lecture. —Experimental relations of gold (and other metals) to light. *Philos. Trans. R. Soc. London* **147**, 145–181 (1857).
5. Hvolbæk, B. *et al.* Catalytic activity of Au nanoparticles. *Nano Today* **2**, 14–18 (2007).
6. Bawendi, M. G., Steigerwald, M. L. & Brus, L. E. The Quantum Mechanics of Larger Semiconductor Clusters ('Quantum Dots'). *Annu. Rev. Phys. Chem.* **41**, 477–496 (1990).
7. Won, Y.-H. *et al.* Highly efficient and stable InP/ZnSe/ZnS quantum dot light-emitting diodes. *Nature* **575**, 634–638 (2019).
8. Murray, C. B., Norris, D. J. & Bawendi, M. G. Synthesis and characterization of nearly monodisperse CdE (E = sulfur, selenium, tellurium) semiconductor nanocrystallites. *J. Am. Chem. Soc.* **115**, 8706–8715 (1993).
9. Kovalenko, M. V. *et al.* Prospects of Nanoscience with Nanocrystals. *ACS Nano* **9**, 1012–1057 (2015).
10. Nasilowski, M., Mahler, B., Lhuillier, E., Ithurria, S. & Dubertret, B. Two-Dimensional Colloidal Nanocrystals. *Chem. Rev.* **116**, 10934–10982 (2016).
11. Campos, M. P. *et al.* A Library of Selenourea Precursors to PbSe Nanocrystals with Size Distributions near the Homogeneous Limit. *J. Am. Chem. Soc.* **139**, 2296–2305 (2017).
12. Bourzac, K. Quantum dots go on display. *Nature* **493**, 283–283 (2013).
13. Luo, Z., Xu, D. & Wu, S. Emerging Quantum-Dots-Enhanced LCDs. *J. Disp. Technol.* **10**, 526–539 (2014).
14. Shimizu, K. T. *et al.* Toward commercial realization of quantum dot based white light-emitting diodes for general illumination. *Photonics Res.* **5**, A1 (2017).
15. Shirasaki, Y., Supran, G. J., Bawendi, M. G. & Bulović, V. Emergence of colloidal quantum-dot light-emitting technologies. *Nat. Photonics* **7**, 13–23 (2012).
16. Malinowski, P. *et al.* Thin-Film Quantum Dot Photodiode for Monolithic Infrared Image Sensors. *Sensors* **17**, 2867 (2017).
17. Rauch, T. *et al.* Near-infrared imaging with quantum-dot-sensitized organic photodiodes. *Nat. Photonics* **3**, 332–336 (2009).
18. Sun, B. *et al.* Pseudohalide-Exchanged Quantum Dot Solids Achieve Record Quantum Efficiency in Infrared Photovoltaics. *Adv. Mater.* **29**, 1700749 (2017).
19. Tang, J. *et al.* Colloidal-quantum-dot photovoltaics using atomic-ligand passivation. *Nat. Mater.* **10**, 765–771 (2011).
20. Meinardi, F. *et al.* Large-area luminescent solar concentrators based on 'Stokes-shift-engineered' nanocrystals in a mass-polymerized PMMA matrix. *Nat. Photonics* **8**, 392–399 (2014).
21. Wu, K., Li, H. & Klimov, V. I. Tandem luminescent solar concentrators based on engineered quantum dots. *Nat. Photonics* **12**, 105–110 (2018).
22. Kwon, S. G. & Hyeon, T. Formation Mechanisms of Uniform Nanocrystals via Hot-Injection and Heat-Up Methods. *Small* **7**, 2685–2702 (2011).
23. Park, J., Joo, J., Kwon, S. G., Jang, Y. & Hyeon, T. Synthesis of Monodisperse Spherical Nanocrystals. *Angew. Chemie Int. Ed.* **46**, 4630–4660 (2007).
24. Sugimoto, T. Preparation of monodispersed colloidal particles. *Adv. Colloid Interface Sci.* **28**, 65–108 (1987).
25. Yin, Y. & Alivisatos, A. P. Colloidal nanocrystal synthesis and the organic–inorganic interface. *Nature* **437**, 664–670 (2005).
26. Murray, C. B., Kagan, C. R. & Bawendi, M. G. Synthesis and Characterization of Monodisperse Nanocrystals and Close-Packed Nanocrystal Assemblies. *Annu. Rev. Mater. Sci.* **30**, 545–610 (2000).
27. Reiss, P., Carrière, M., Lincheneau, C., Vaure, L. & Tamang, S. Synthesis of Semiconductor Nanocrystals, Focusing on Nontoxic and Earth-Abundant Materials. *Chem. Rev.* **116**, 10731–10819 (2016).
28. Thanh, N. T. K., Maclean, N. & Mahiddine, S. Mechanisms of Nucleation and Growth of Nanoparticles in Solution. *Chem. Rev.* **114**, 7610–7630 (2014).
29. Wang, Y., He, J., Liu, C., Chong, W. H. & Chen, H. Thermodynamics versus Kinetics in Nanosynthesis. *Angew. Chemie Int. Ed.* **54**, 2022–2051 (2015).
30. Bullen, C. R. & Mulvaney, P. Nucleation and Growth Kinetics of CdSe Nanocrystals in Octadecene. *Nano Lett.* **4**, 2303–2307 (2004).

31. LaMer, V. K. & Dinegar, R. H. Theory, Production and Mechanism of Formation of Monodispersed Hydrosols. *J. Am. Chem. Soc.* **72**, 4847–4854 (1950).
32. Dirksen, J. A. & Ring, T. A. Fundamentals of crystallization: Kinetic effects on particle size distributions and morphology. *Chem. Eng. Sci.* **46**, 2389–2427 (1991).
33. Reiss, H. The Growth of Uniform Colloidal Dispersions. *J. Chem. Phys.* **19**, 482–487 (1951).
34. Peng, X., Wickham, J. & Alivisatos, A. P. Kinetics of II−VI and III−V Colloidal Semiconductor Nanocrystal Growth: "Focusing" of Size Distributions. *J. Am. Chem. Soc.* **120**, 5343–5344 (1998).
35. Rempel, J. Y., Bawendi, M. G. & Jensen, K. F. Insights into the Kinetics of Semiconductor Nanocrystal Nucleation and Growth. *J. Am. Chem. Soc.* **131**, 4479–4489 (2009).
36. Whitehead, C. B., Özkar, S. & Finke, R. G. LaMer's 1950 model of particle formation: a review and critical analysis of its classical nucleation and fluctuation theory basis, of competing models and mechanisms for phase-changes and particle formation, and then of its application to silver halide, semiconductor, metal, and metal-oxide nanoparticles. *Mater. Adv.* **2**, 186–235 (2021).
37. Watzky, M. A. & Finke, R. G. Transition Metal Nanocluster Formation Kinetic and Mechanistic Studies. A New Mechanism When Hydrogen Is the Reductant: Slow, Continuous Nucleation and Fast Autocatalytic Surface Growth. *J. Am. Chem. Soc.* **119**, 10382–10400 (1997).
38. Mozaffari, S. *et al.* Colloidal nanoparticle size control: experimental and kinetic modeling investigation of the ligand–metal binding role in controlling the nucleation and growth kinetics. *Nanoscale* **9**, 13772–13785 (2017).
39. Handwerk, D. R., Shipman, P. D., Whitehead, C. B., Özkar, S. & Finke, R. G. Mechanism-Enabled Population Balance Modeling of Particle Formation en Route to Particle Average Size and Size Distribution Understanding and Control. *J. Am. Chem. Soc.* **141**, 15827–15839 (2019).
40. Franke, D. *et al.* Continuous injection synthesis of indium arsenide quantum dots emissive in the short-wavelength infrared. *Nat. Commun.* **7**, 12749 (2016).
41. Achorn, O. B., Franke, D. & Bawendi, M. G. Seedless Continuous Injection Synthesis of Indium Phosphide Quantum Dots as a Route to Large Size and Low Size Dispersity. *Chem. Mater.* **32**, 6532–6539 (2020).
42. Liu, H., Owen, J. S. & Alivisatos, A. P. Mechanistic Study of Precursor Evolution in Colloidal Group II−VI Semiconductor Nanocrystal Synthesis. *J. Am. Chem. Soc.* **129**, 305–312 (2007).
43. Steckel, J. S., Yen, B. K. H., Oertel, D. C. & Bawendi, M. G. On the Mechanism of Lead Chalcogenide Nanocrystal Formation. *J. Am. Chem. Soc.* **128**, 13032–13033 (2006).
44. Abe, S., Čapek, R. K., De Geyter, B. & Hens, Z. Tuning the Postfocused Size of Colloidal Nanocrystals by the Reaction Rate: From Theory to Application. *ACS Nano* **6**, 42–53 (2012).
45. Owen, J. S., Chan, E. M., Liu, H. & Alivisatos, A. P. Precursor Conversion Kinetics and the Nucleation of Cadmium Selenide Nanocrystals. *J. Am. Chem. Soc.* **132**, 18206–18213 (2010).
46. Hendricks, M. P., Campos, M. P., Cleveland, G. T., Jen-La Plante, I. & Owen, J. S. A tunable library of substituted thiourea precursors to metal sulfide nanocrystals. *Science* **348**, 1226–1230 (2015).
47. Tessier, M. D., Dupont, D., De Nolf, K., De Roo, J. & Hens, Z. Economic and Size-Tunable Synthesis of InP/ZnE (E = S, Se) Colloidal Quantum Dots. *Chem. Mater.* **27**, 4893–4898 (2015).
48. Qu, L., Peng, Z. A. & Peng, X. Alternative Routes toward High Quality CdSe Nanocrystals. *Nano Lett.* **1**, 333–337 (2001).
49. Wu, L., Fournier, A. P., Willis, J. J., Cargnello, M. & Tassone, C. J. In Situ X-ray Scattering Guides the Synthesis of Uniform PtSn Nanocrystals. *Nano Lett.* **18**, 4053–4057 (2018).
50. Wu, L. *et al.* High-temperature crystallization of nanocrystals into three-dimensional superlattices. *Nature* **548**, 197–201 (2017).
51. Abécassis, B. *et al.* Real-Time in Situ Probing of High-Temperature Quantum Dots Solution Synthesis. *Nano Lett.* **15**, 2620–2626 (2015).
52. Narayanan, T. *et al.* A multipurpose instrument for time-resolved ultra-small-angle and coherent X-ray scattering. *J. Appl. Crystallogr.* **51**, 1511–1524 (2018).
53. Flores-Rojas, G. G., López-Saucedo, F. & Bucio, E. Gamma-irradiation applied in the synthesis of metallic and organic nanoparticles: A short review. *Radiat. Phys. Chem.* **169**, 107962 (2020).
54. McMurtry, B. M. *et al.* Continuous Nucleation and Size Dependent Growth Kinetics of Indium Phosphide Nanocrystals. *Chem. Mater.* **32**, 4358–4368 (2020).
55. Maes, J. *et al.* Size and Concentration Determination of Colloidal Nanocrystals by Small-Angle X-ray Scattering. *Chem. Mater.* **30**, 3952–3962 (2018).
56. Talapin, D. V., Rogach, A. L., Haase, M. & Weller, H. Evolution of an Ensemble of Nanoparticles in a Colloidal Solution: Theoretical Study. *J. Phys. Chem. B* **105**, 12278–12285 (2001).
57. Thessing, J., Qian, J., Chen, H., Pradhan, N. & Peng, X. Interparticle Influence on Size/Size Distribution Evolution of Nanocrystals. *J. Am. Chem. Soc.* **129**, 2736–2737 (2007).

58. Thomä, S. L. J., Krauss, S. W., Eckardt, M., Chater, P. & Zobel, M. Atomic insight into hydration shells around facetted nanoparticles. *Nat. Commun.* **10**, 995 (2019).

59. Zobel, M., Neder, R. B. & Kimber, S. A. J. Universal solvent restructuring induced by colloidal nanoparticles. *Science* **347**, 292–294 (2015).

60. Spagnoli, D., Gilbert, B., Waychunas, G. A. & Banfield, J. F. Prediction of the effects of size and morphology on the structure of water around hematite nanoparticles. *Geochim. Cosmochim. Acta* **73**, 4023–4033 (2009).

61. Kwon, S. G. *et al.* Kinetics of Monodisperse Iron Oxide Nanocrystal Formation by "Heating-Up" Process. *J. Am. Chem. Soc.* **129**, 12571–12584 (2007).

62. Vetter, T., Iggland, M., Ochsenbein, D. R., Hänseler, F. S. & Mazzotti, M. Modeling Nucleation, Growth, and Ostwald Ripening in Crystallization Processes: A Comparison between Population Balance and Kinetic Rate Equation. *Cryst. Growth Des.* **13**, 4890–4905 (2013).

63. Bøjesen, E. D. & Iversen, B. B. The chemistry of nucleation. *CrystEngComm* **18**, 8332–8353 (2016).

64. Handwerk, D. R., Shipman, P. D., Whitehead, C. B., Özkar, S. & Finke, R. G. Particle Size Distributions via Mechanism-Enabled Population Balance Modeling. *J. Phys. Chem. C* **124**, 4852–4880 (2020).

65. Berti, D. & Palazzo, G. *Colloidal Foundations of Nanoscience*. (Elsevier, 2014).

66. Singh, S. *et al.* Colloidal CdSe Nanoplatelets, A Model for Surface Chemistry/Optoelectronic Property Relations in Semiconductor Nanocrystals. *J. Am. Chem. Soc.* **140**, 13292–13300 (2018).

67. Drijvers, E., De Roo, J., Martins, J. C., Infante, I. & Hens, Z. Ligand Displacement Exposes Binding Site Heterogeneity on CdSe Nanocrystal Surfaces. *Chem. Mater.* **30**, 1178–1186 (2018).

68. Mozaffari, S. *et al.* The role of nanoparticle size and ligand coverage in size focusing of colloidal metal nanoparticles. *Nanoscale Adv.* **1**, 4052–4066 (2019).

69. Riedinger, A. *et al.* An intrinsic growth instability in isotropic materials leads to quasi-two-dimensional nanoplatelets. *Nat. Mater.* **16**, 743–748 (2017).

70. van Embden, J., Chesman, A. S. R. & Jasieniak, J. J. The Heat-Up Synthesis of Colloidal Nanocrystals. *Chem. Mater.* **27**, 2246–2285 (2015).

71. Čapek, R. K. *et al.* Optical Properties of Zincblende Cadmium Selenide Quantum Dots. *J. Phys. Chem. C* **114**, 6371–6376 (2010).

72. Boesecke, P. Reduction of two-dimensional small- and wide-angle X-ray scattering data. *J. Appl. Crystallogr.* **40**, s423–s427 (2007).

73. Dreiss, C. A., Jack, K. S. & Parker, A. P. On the absolute calibration of bench-top small-angle X-ray scattering instruments: a comparison of different standard methods. *J. Appl. Crystallogr.* **39**, 32–38 (2006).

74. Momma, K. & Izumi, F. VESTA 3 for three-dimensional visualization of crystal, volumetric and morphology data. *J. Appl. Crystallogr.* **44**, 1272–1276 (2011).

75. Guinier, A. & Fournet, G. *Small-angle scattering of X-rays*. (John Wiley & Sons, Inc., 1955).

76. Huang, D., Simon, S. L. & McKenna, G. B. Chain length dependence of the thermodynamic properties of linear and cyclic alkanes and polymers. *J. Chem. Phys.* **122**, 084907 (2005).

77. Sedlak, S. M., Bruetzel, L. K. & Lipfert, J. Quantitative evaluation of statistical errors in small-angle X-ray scattering measurements. *J. Appl. Crystallogr.* **50**, 621–630 (2017).

78. Abe, S., Capek, R. K., De Geyter, B. & Hens, Z. Reaction Chemistry/Nanocrystal Property Relations in the Hot Injection Synthesis, the Role of the Solute Solubility. *ACS Nano* **7**, 943–949 (2013).

79. Flamee, S. *et al.* Fast, High Yield, and High Solid Loading Synthesis of Metal Selenide Nanocrystals. *Chem. Mater.* **25**, 2476–2483 (2013).

80. Nakonechnyi, I., Sluydts, M., Justo, Y., Jasieniak, J. & Hens, Z. Mechanistic Insights in Seeded Growth Synthesis of Colloidal Core/Shell Quantum Dots. *Chem. Mater.* **29**, 4719–4727 (2017).

81. De Nolf, K. *et al.* Controlling the Size of Hot Injection Made Nanocrystals by Manipulating the Diffusion Coefficient of the Solute. *J. Am. Chem. Soc.* **137**, 2495–2505 (2015).

82. Peng, X. *et al.* Shape control of CdSe nanocrystals. *Nature* **404**, 59–61 (2000).

83. Chen, Z., Nadal, B., Mahler, B., Aubin, H. & Dubertret, B. Quasi-2D Colloidal Semiconductor Nanoplatelets for Narrow Electroluminescence. *Adv. Funct. Mater.* **24**, 295–302 (2014).

84. Estrada, D. *et al.* 32-1: On-chip Red Quantum Dots in White LEDs for General Illumination. *SID Symp. Dig. Tech. Pap.* **49**, 405–408 (2018).

85. Mangum, B. D., Landes, T. S., Theobald, B. R. & Kurtin, J. N. Exploring the bounds of narrow-band quantum dot downconverted LEDs. *Photonics Res.* **5**, A13 (2017).

86. Tessier, M. D., Javaux, C., Maksimovic, I., Loriette, V. & Dubertret, B. Spectroscopy of Single CdSe Nanoplatelets. *ACS Nano* **6**, 6751–6758 (2012).

87. Reiss, P., Carayon, S., Bleuse, J. & Pron, A. Low polydispersity core/shell nanocrystals of CdSe/ZnSe and CdSe/ZnSe/ZnS type: preparation and optical studies. *Synth. Met.* **139**, 649–652 (2003).

88. Cui, J. *et al.* Direct probe of spectral inhomogeneity reveals synthetic tunability of single-nanocrystal spectral linewidths. *Nat. Chem.* **5**, 602–606 (2013).

89. Ithurria, S. & Dubertret, B. Quasi 2D Colloidal CdSe Platelets with Thicknesses Controlled at the Atomic Level. *J. Am. Chem. Soc.* **130**, 16504–16505 (2008).

90. Ithurria, S., Bousquet, G. & Dubertret, B. Continuous Transition from 3D to 1D Confinement Observed during the Formation of CdSe Nanoplatelets. *J. Am. Chem. Soc.* **133**, 3070–3077 (2011).

91. Yeltik, A. *et al.* Experimental Determination of the Absorption Cross-Section and Molar Extinction Coefficient of Colloidal CdSe Nanoplatelets. *J. Phys. Chem. C* **119**, 26768–26775 (2015).

92. Geiregat, P. *et al.* Localization-limited exciton oscillator strength in colloidal CdSe nanoplatelets revealed by the optically induced stark effect. *Light Sci. Appl.* **10**, 112 (2021).

93. Di Giacomo, A., Rodà, C., Khan, A. H. & Moreels, I. Colloidal Synthesis of Laterally Confined Blue-Emitting 3.5 Monolayer CdSe Nanoplatelets. *Chem. Mater.* **32**, 9260–9267 (2020).

94. Ouyang, J. *et al.* Multiple Families of Magic-Sized CdSe Nanocrystals with Strong Bandgap Photoluminescence via Noninjection One-Pot Syntheses. *J. Phys. Chem. C* **112**, 13805–13811 (2008).

95. Chen, Y., Chen, D., Li, Z. & Peng, X. Symmetry-Breaking for Formation of Rectangular CdSe Two-Dimensional Nanocrystals in Zinc-Blende Structure. *J. Am. Chem. Soc.* **139**, 10009–10019 (2017).

96. Liu, Y. *et al.* Colloidal CdSe 0-Dimension Nanocrystals and Their Self-Assembled 2-Dimension Structures. *Chem. Mater.* **30**, 1575–1584 (2018).

97. Liu, Y. *et al.* Photoluminescent Colloidal Nanohelices Self-Assembled from CdSe Magic-Size Clusters via Nanoplatelets. *J. Phys. Chem. Lett.* **10**, 2794–2801 (2019).

98. Lyashchova, A. *et al.* Optical absorption, induced bleaching, and photoluminescence of CdSe nanoplatelets grown in cadmium octanoate matrix. *Nanoscale Res. Lett.* **9**, 88 (2014).

99. Castro, N. *et al.* Insights into the Formation Mechanism of CdSe Nanoplatelets Using in Situ X-ray Scattering. *Nano Lett.* **19**, 6466–6474 (2019).

100. Prins, P. T. *et al.* Extended Nucleation and Superfocusing in Colloidal Semiconductor Nanocrystal Synthesis. *Nano Lett.* **21**, 2487–2496 (2021).

101. Bertrand, G. H. V., Polovitsyn, A., Christodoulou, S., Khan, A. H. & Moreels, I. Shape control of zincblende CdSe nanoplatelets. *Chem. Commun.* **52**, 11975–11978 (2016).

102. Achtstein, A. W. *et al.* Linear Absorption in CdSe Nanoplates: Thickness and Lateral Size Dependency of the Intrinsic Absorption. *J. Phys. Chem. C* **119**, 20156–20161 (2015).

103. Geiregat, P. *et al.* Thermodynamic Equilibrium between Excitons and Excitonic Molecules Dictates Optical Gain in Colloidal CdSe Quantum Wells. *J. Phys. Chem. Lett.* **10**, 3637–3644 (2019).

104. Jiang, Y. *et al.* Synthesis of CdSe Nanoplatelets without Short-Chain Ligands: Implication for Their Growth Mechanisms. *ACS Omega* **3**, 6199–6205 (2018).

105. Scott, R. *et al.* A comparative study demonstrates strong size tunability of carrier–phonon coupling in CdSe-based 2D and 0D nanocrystals. *Nanoscale* **11**, 3958–3967 (2019).

106. van der Bok, J. C., Dekker, D. M., Peerlings, M. L. J., Salzmann, B. B. V. & Meijerink, A. Luminescence Line Broadening of CdSe Nanoplatelets and Quantum Dots for Application in w-LEDs. *J. Phys. Chem. C* **124**, 12153–12160 (2020).

107. Failla, M. *et al.* Observation of the quantized motion of excitons in CdSe nanoplatelets. *Phys. Rev. B* **102**, 195405 (2020).

108. Jana, S. *et al.* Stacking and Colloidal Stability of CdSe Nanoplatelets. *Langmuir* **31**, 10532–10539 (2015).

109. She, C. *et al.* Low-Threshold Stimulated Emission Using Colloidal Quantum Wells. *Nano Lett.* **14**, 2772–2777 (2014).

110. Tanford, C. Micelle shape and size. *J. Phys. Chem.* **76**, 3020–3024 (1972).

111. Małecka, B. Thermal decomposition of $Cd(CH_3COO)_2 \cdot 2H_2O$ studied by a coupled TG-DTA-MS method. *J. Therm. Anal. Calorim.* **78**, 535–544 (2004).

112. Martínez-Casado, F. J. *et al.* Unraveling the Decomposition Process of Lead(II) Acetate: Anhydrous Polymorphs, Hydrates, and Byproducts and Room Temperature Phosphorescence. *Inorg. Chem.* **55**, 8576–8586 (2016).

113. van der Stam, W. *et al.* In Situ Probing of Stack-Templated Growth of Ultrathin $Cu_{2-x}S$ Nanosheets. *Chem. Mater.* **28**, 6381–6389 (2016).

114. Knüsel, P. N. *et al.* Experimental Evidence for Two-Dimensional Ostwald Ripening in Semiconductor Nanoplatelets. *Chem. Mater.* **32**, 3312–3319 (2020).

115. Jiang, Y., Chen, H., Mu, X. & He, Z. Thermal decomposition of magnesium acetate in nitrogen. *J. Phys. Conf. Ser.* **1653**, 012057 (2020).

116. Hens, Z. & Moreels, I. Light absorption by colloidal semiconductor quantum dots. *J. Mater. Chem.* **22**, 10406–10415 (2012).

117. Lindner, P. & Zemb, T. *Neutron, X-ray and light scattering : introduction to an investigative tool for colloidal and polymeric systems*. (Elsevier, 1991).

118. Renaud, G., Lazzari, R. & Leroy, F. Probing surface and interface morphology with Grazing Incidence Small Angle X-Ray Scattering. *Surf. Sci. Rep.* **64**, 255–380 (2009).

119. Vetrone, F. *et al.* Intracellular imaging of HeLa cells by non-functionalized $NaYF_4:Er^{3+},Yb^{3+}$ upconverting nanoparticles. *Nanoscale* **2**, 495–8 (2010).

120. Gargas, D. J. *et al.* Engineering bright sub-10-nm upconverting nanocrystals for single-molecule imaging. *Nat. Nanotechnol.* **9**, 300–305 (2014).

121. Yang, Y. *et al.* Hydrothermal synthesis of $NaLuF_4:{}^{153}Sm,Yb,Tm$ nanoparticles and their application in dual-modality upconversion luminescence and SPECT bioimaging. *Biomaterials* **34**, 774–783 (2013).

122. Kim, W. J., Nyk, M. & Prasad, P. N. Color-coded multilayer photopatterned microstructures using lanthanide(III) ion co-doped $NaYF_4$ nanoparticles with upconversion luminescence for possible applications in security. *Nanotechnology* **20**, 185301 (2009).

123. Lu, Y. *et al.* Tunable lifetime multiplexing using luminescent nanocrystals. *Nat. Photonics* **8**, 32–36 (2014).

124. Zou, W., Visser, C., Maduro, J. A., Pshenichnikov, M. S. & Hummelen, J. C. Broadband dye-sensitized upconversion of near-infrared light. *Nat. Photonics* **6**, 560–564 (2012).

125. Wang, J. *et al.* Photon energy upconversion through thermal radiation with the power efficiency reaching 16%. *Nat. Commun.* **5**, 5669 (2014).

126. Zhou, B., Shi, B., Jin, D. & Liu, X. Controlling upconversion nanocrystals for emerging applications. *Nat. Nanotechnol.* **10**, 924–936 (2015).

127. Homann, C. *et al.* $NaYF_4:Yb,Er/NaYF_4$ Core/Shell Nanocrystals with High Upconversion Luminescence Quantum Yield. *Angew. Chemie Int. Ed.* **57**, 8765–8769 (2018).

128. Würth, C., Fischer, S., Grauel, B., Alivisatos, A. P. & Resch-Genger, U. Quantum Yields, Surface Quenching, and Passivation Efficiency for Ultrasmall Core/Shell Upconverting Nanoparticles. *J. Am. Chem. Soc.* **140**, 4922–4928 (2018).

129. Krämer, K. W. *et al.* Hexagonal Sodium Yttrium Fluoride Based Green and Blue Emitting Upconversion Phosphors. *Chem. Mater.* **16**, 1244–1251 (2004).

130. Boyer, J.-C. & van Veggel, F. C. J. M. Absolute quantum yield measurements of colloidal $NaYF_4:Er^{3+}$, $Yb^{3+}$ upconverting nanoparticles. *Nanoscale* **2**, 1417–9 (2010).

131. Brechbühler, R. *et al.* Two-Dimensional Drexhage Experiment for Electric- and Magnetic-Dipole Sources on Plasmonic Interfaces. *Phys. Rev. Lett.* **121**, 113601 (2018).

132. Zhang, Z., Chen, Y. & Zhang, Y. Self-Assembly of Upconversion Nanoparticles Based Materials and Their Emerging Applications. *Small* **18**, 2103241 (2022).

133. Heer, S., Kömpe, K., Güdel, H. U. & Haase, M. Highly efficient multicolour upconversion emission in transparent colloids of lanthanide-doped $NaYF_4$ nanocrystals. *Adv. Mater.* **16**, 2102–2105 (2004).

134. Mai, H.-X. *et al.* High-Quality Sodium Rare-Earth Fluoride Nanocrystals: Controlled Synthesis and Optical Properties. *J. Am. Chem. Soc.* **128**, 6426–6436 (2006).

135. Rinkel, T., Raj, A. N., Dühnen, S. & Haase, M. Synthesis of 10 nm $\beta$-$NaYF_4:Yb,Er/NaYF_4$ Core/Shell Upconversion Nanocrystals with 5 nm Particle Cores. *Angew. Chemie Int. Ed.* **55**, 1164–1167 (2016).

136. Voß, B., Nordmann, J., Uhl, A., Komban, R. & Haase, M. Effect of the crystal structure of small precursor particles on the growth of $\beta$-$NaREF_4$ (RE = Sm, Eu, Gd, Tb) nanocrystals. *Nanoscale* **5**, 806–812 (2013).

137. Deng, R. *et al.* Temporal full-colour tuning through non-steady-state upconversion. *Nat. Nanotechnol.* **10**, 237–242 (2015).

138. Wang, F. & Liu, X. Upconversion Multicolor Fine-Tuning: Visible to Near-Infrared Emission from Lanthanide-Doped $NaYF_4$ Nanoparticles. *J. Am. Chem. Soc.* **130**, 5642–5643 (2008).

139. Johnson, N. J. J., Korinek, A., Dong, C. & van Veggel, F. C. J. M. Self-Focusing by Ostwald Ripening: A Strategy for Layer-by-Layer Epitaxial Growth on Upconverting Nanocrystals. *J. Am. Chem. Soc.* **134**, 11068–11071 (2012).

140. Fischer, S., Bronstein, N. D., Swabeck, J. K., Chan, E. M. & Alivisatos, A. P. Precise Tuning of Surface Quenching for Luminescence Enhancement in Core–Shell Lanthanide-Doped Nanocrystals. *Nano Lett.* **16**, 7241–7247 (2016).

141. Bastian, P. U., Nacak, S., Roddatis, V. & Kumke, M. U. Tracking the Motion of Lanthanide Ions within Core–Shell–Shell $NaYF_4$ Nanocrystals via Resonance Energy Transfer. *J. Phys. Chem. C* **124**, 11229–11238 (2020).

142. Liu, L. *et al.* Elemental Migration in Core/Shell Structured Lanthanide Doped Nanoparticles. *Chem. Mater.* **31**, 5608–5615 (2019).

143. Voss, B. & Haase, M. Intrinsic Focusing of the Particle Size Distribution in Colloids Containing Nanocrystals of Two Different Crystal Phases. *ACS Nano* **7**, 11242–11254 (2013).

144. Suter, J. D., Pekas, N. J., Berry, M. T. & May, P. S. Real-Time-Monitoring of the Synthesis of β-$NaYF_4$:17%Yb,3%Er Nanocrystals Using NIR-to-Visible Upconversion Luminescence. *J. Phys. Chem. C* **118**, 13238–13247 (2014).

145. Radunz, S. *et al.* Evolution of Size and Optical Properties of Upconverting Nanoparticles during High-Temperature Synthesis. *J. Phys. Chem. C* **122**, 28958–28967 (2018).

146. Zhao, M.-L. *et al.* Sequential Growth of High Quality Sub-10 nm Core–Shell Nanocrystals: Understanding the Nucleation and Growth Process Using Dynamic Light Scattering. *Langmuir* **35**, 489–494 (2019).

147. May, P. B., Suter, J. D., May, P. S. & Berry, M. T. The Dynamics of Nanoparticle Growth and Phase Change During Synthesis of β-$NaYF_4$. *J. Phys. Chem. C* **120**, 9482–9489 (2016).

148. van der Bok, J. C. *et al.* In Situ Optical and X-ray Spectroscopy Reveals Evolution toward Mature CdSe Nanoplatelets by Synergetic Action of Myristate and Acetate Ligands. *J. Am. Chem. Soc.* **144**, 8096–8105 (2022).

149. Homann, C., Bolze, J. & Haase, M. Colloidal Crystals of $NaYF_4$ Upconversion Nanocrystals Studied by Small-Angle X-Ray Scattering (SAXS). *Part. Part. Syst. Charact.* **36**, 1800391 (2019).

150. Rinkel, T., Nordmann, J., Raj, A. N. & Haase, M. Ostwald-ripening and particle size focussing of sub-10 nm $NaYF_4$ upconversion nanocrystals. *Nanoscale* **6**, 14523–14530 (2014).

151. Rabouw, F. T. *et al.* Quenching Pathways in $NaYF_4$:$Er^{3+}$,$Yb^{3+}$ Upconversion Nanocrystals. *ACS Nano* **12**, 4812–4823 (2018).

152. Smith, A. J. *et al.* I22: SAXS/WAXS beamline at Diamond Light Source – an overview of 10 years operation. *J. Synchrotron Radiat.* **28**, 939–947 (2021).

153. Roy, D. M. & Roy, R. Controlled Massively Defective Crystalline Solutions with the Fluorite Structure. *J. Electrochem. Soc.* **111**, 421 (1964).

154. Perera, S. S., Amarasinghe, D. K., Dissanayake, K. T. & Rabuffetti, F. A. Average and Local Crystal Structure of β-Er:Yb:$NaYF_4$ Upconverting Nanocrystals Probed by X-ray Total Scattering. *Chem. Mater.* **29**, 6289–6297 (2017).

155. Bressler, I., Pauw, B. R. & Thünemann, A. F. McSAS : software for the retrieval of model parameter distributions from scattering patterns. *J. Appl. Crystallogr.* **48**, 962–969 (2015).

156. Breßler, I. & Pauw, B. R. McSAS. *BAMresearch* (2022). Available at: https://github.com/bamresearch/mcsas.

157. Garvie, R. C. Stabilization of the tetragonal structure in zirconia microcrystals. *J. Phys. Chem.* **82**, 218–224 (1978).

158. Thoma, R. E., Insley, H. & Hebert, G. M. The Sodium Fluoride-Lanthanide Trifluoride Systems. *Inorg. Chem.* **5**, 1222–1229 (1966).

159. Li, C. *et al.* A simple method to clean ligand contamination on TEM grids. *Ultramicroscopy* **221**, 113195 (2021).

160. Hammouda, B. A new Guinier–Porod model. *J. Appl. Crystallogr.* **43**, 716–719 (2010).

161. Dhaene, E., Billet, J., Bennett, E., Van Driessche, I. & De Roo, J. The Trouble with ODE: Polymerization during Nanocrystal Synthesis. *Nano Lett.* **19**, 7411–7417 (2019).

162. Yaws, C. L. *Yaws' Handbook of Thermodynamic and Physical Properties of Chemical Compounds*. (Knovel, 2003).

163. Lhuillier, E. *et al.* Two-Dimensional Colloidal Metal Chalcogenides Semiconductors: Synthesis, Spectroscopy, and Applications. *Acc. Chem. Res.* **48**, 22–30 (2015).

164. Coropceanu, I. & Bawendi, M. G. Core/Shell Quantum Dot Based Luminescent Solar Concentrators with Reduced Reabsorption and Enhanced Efficiency. *Nano Lett.* **14**, 4097–4101 (2014).

165. Lim, J., Park, Y.-S. & Klimov, V. I. Optical gain in colloidal quantum dots achieved with direct-current electrical pumping. *Nat. Mater.* **17**, 42–49 (2018).

166. Yang, Z., Pelton, M., Fedin, I., Talapin, D. V. & Waks, E. A room temperature continuous-wave nanolaser using colloidal quantum wells. *Nat. Commun.* **8**, 143 (2017).

167. Keuleyan, S., Lhuillier, E., Brajuskovic, V. & Guyot-Sionnest, P. Mid-infrared HgTe colloidal quantum dot photodetectors. *Nat. Photonics* **5**, 489–493 (2011).

168. Whitham, K. *et al.* Charge transport and localization in atomically coherent quantum dot solids. *Nat. Mater.* **15**, 557–563 (2016).

169. Rodina, A. V. & Efros, A. L. Effect of dielectric confinement on optical properties of colloidal nanostructures. *J. Exp. Theor. Phys.* **122**, 554–566 (2016).

170. Geiregat, P., Justo, Y., Abe, S., Flamee, S. & Hens, Z. Giant and Broad-Band Absorption Enhancement in Colloidal Quantum Dot Monolayers through Dipolar Coupling. *ACS Nano* **7**, 987–993 (2013).

171. Szkopek, T. The fine structure constant determines spontaneous emission rates from semiconductors. *Appl. Phys. Lett.* **98**, 211117 (2011).

172. Fang, H. *et al.* Quantum of optical absorption in two-dimensional semiconductors. *Proc. Natl. Acad. Sci.* **110**, 11688–11691 (2013).

173. Nair, R. R. *et al.* Fine Structure Constant Defines Visual Transparency of Graphene. *Science* **320**, 1308–1308 (2008).

174. Kravets, V. G., Schedin, F. & Grigorenko, A. N. Fine structure constant and quantized optical transparency of plasmonic nanoarrays. *Nat. Commun.* **3**, 640 (2012).

175. Evers, W. H. *et al.* Low-Dimensional Semiconductor Superlattices Formed by Geometric Control over Nanocrystal Attachment. *Nano Lett.* **13**, 2317–2323 (2013).

176. Boneschanscher, M. P. *et al.* Long-range orientation and atomic attachment of nanocrystals in 2D honeycomb superlattices. *Science* **344**, 1377–1380 (2014).

177. Sandeep, C. S. S. *et al.* Epitaxially Connected PbSe Quantum-Dot Films: Controlled Neck Formation and Optoelectronic Properties. *ACS Nano* **8**, 11499–11511 (2014).

178. Walravens, W. *et al.* Setting Carriers Free: Healing Faulty Interfaces Promotes Delocalization and Transport in Nanocrystal Solids. *ACS Nano* **13**, 12774–12786 (2019).

179. Peters, J. L. *et al.* Mono- and Multilayer Silicene-Type Honeycomb Lattices by Oriented Attachment of PbSe Nanocrystals: Synthesis, Structural Characterization, and Analysis of the Disorder. *Chem. Mater.* **30**, 4831–4837 (2018).

180. Dell, J. M., Joyce, M. J., Usher, B. F., Yoffe, G. W. & Kemeny, P. C. Unusually strong excitonic absorption in molecular-beam-epitaxy-grown, chemically lifted GaAs thin films. *Phys. Rev. B* **42**, 9496–9500 (1990).

181. Moss, T. S., Smith, S. D. & Hawkins, T. D. F. Absorption and Dispersion of Indium Antimonide. *Proc. Phys. Soc. Sect. B* **70**, 776–784 (1957).

182. Scanlon, W. W. Recent advances in the optical and electronic properties of PbS, PbSe, PbTe and their alloys. *J. Phys. Chem. Solids* **8**, 423–428 (1959).

183. Madelung, O. *Semiconductors: Data Handbook*. (Springer, 2004).

184. Prins, P. T. *et al.* The Fine-Structure Constant as a Ruler for the Band-Edge Light Absorption Strength of Bulk and Quantum-Confined Semiconductors. *Nano Lett.* **21**, 9426–9432 (2021).

185. Mak, K. F., Lee, C., Hone, J., Shan, J. & Heinz, T. F. Atomically Thin $MoS_2$: A New Direct-Gap Semiconductor. *Phys. Rev. Lett.* **105**, 136805 (2010).

186. Chernikov, A. *et al.* Exciton Binding Energy and Nonhydrogenic Rydberg Series in Monolayer $WS_2$. *Phys. Rev. Lett.* **113**, 076802 (2014).

187. Li, Y. *et al.* Measurement of the optical dielectric function of monolayer transition-metal dichalcogenides: $MoS_2$, $MoSe_2$, $WS_2$, $WSe_2$. *Phys. Rev. B* **90**, 205422 (2014).

188. Griffiths, D. J. *Introduction to quantum mechanics*. (Cambridge University Press, 2017).

189. Merzbacher, E. *Quantum Mechanics*. (John Wiley and Sons Ltd., 1970).

190. Delerue, C. & Lannoo, M. *Nanostructures*. (Springer Berlin Heidelberg, 2004).

191. Graf, M. & Vogl, P. Electromagnetic fields and dielectric response in empirical tight-binding theory. *Phys. Rev. B* **51**, 4940–4949 (1995).

192. Boykin, T. B., Klimeck, G., Bowen, R. C. & Oyafuso, F. Diagonal parameter shifts due to nearest-neighbor displacements in empirical tight-binding theory. *Phys. Rev. B* **66**, 125207 (2002).

193. Petrovykh, D. Y., Yang, M. J. & Whitman, L. J. Chemical and electronic properties of sulfur-passivated InAs surfaces. *Surf. Sci.* **523**, 231–240 (2003).

194. Dufour, M. *et al.* Doping as a Strategy to Tune Color of 2D Colloidal Nanoplatelets. *ACS Appl. Mater. Interfaces* **11**, 10128–10134 (2019).

195. Allan, G. & Delerue, C. Confinement effects in PbSe quantum wells and nanocrystals. *Phys. Rev. B* **70**, 245321 (2004).

196. Mak, K. F. *et al.* Measurement of the Optical Conductivity of Graphene. *Phys. Rev. Lett.* **101**, 196405 (2008).

197. Stauber, T., Peres, N. M. R. & Geim, A. K. Optical conductivity of graphene in the visible region of the spectrum. *Phys. Rev. B* **78**, 085432 (2008).

198. Delerue, C., Lannoo, M. & Allan, G. Calculations of the electron-energy-loss spectra of silicon nanostructures and porous silicon. *Phys. Rev. B* **56**, 15306–15313 (1997).

199. Allan, G. & Delerue, C. Energy transfer between semiconductor nanocrystals: Validity of Förster's theory. *Phys. Rev. B* **75**, 195311 (2007).

200. Delerue, C. From semiconductor nanocrystals to artificial solids with dimensionality below two. *Phys. Chem. Chem. Phys.* **16**, 25734–25740 (2014).

201. Delerue, C. & Vanmaekelbergh, D. Electronic band structure of zinc blende CdSe and rock salt PbSe semiconductors with silicene-type honeycomb geometry. *2D Mater.* **2**, 034008 (2015).

202. Kalesaki, E., Evers, W. H., Allan, G., Vanmaekelbergh, D. & Delerue, C. Electronic structure of atomically coherent square semiconductor superlattices with dimensionality below two. *Phys. Rev. B* **88**, 115431 (2013).

203. Moreels, I. *et al.* Composition and size-dependent extinction coefficient of colloidal PbSe quantum dots. *Chem. Mater.* **19**, 6101–6106 (2007).

204. Ghezzi, C. *et al.* Optical absorption near the fundamental absorption edge in GaSb. *Phys. Rev. B* **52**, 1463–1466 (1995).

205. Turner, W. J., Reese, W. E. & Pettit, G. D. Exciton Absorption and Emission in InP. *Phys. Rev.* **136**, A1467–A1470 (1964).

206. Dixon, J. R. & Ellis, J. M. Optical Properties of n-Type Indium Arsenide in the Fundamental Absorption Edge Region. *Phys. Rev.* **123**, 1560–1566 (1961).

207. Cardona, M., Weinstein, M. & Wolff, G. A. Ultraviolet Reflection Spectrum of Cubic CdS. *Phys. Rev.* **140**, A633–A637 (1965).

208. Ninomiya, S. & Adachi, S. Optical properties of wurtzite CdS. *J. Appl. Phys.* **78**, 1183–1190 (1995).

209. Gupta, T. K. & Doh, J. Optical properties of polycrystalline CdSe films. *J. Mater. Res.* **7**, 1243–1246 (1992).

210. Ninomiya, S. & Adachi, S. Optical properties of cubic and hexagonal CdSe. *J. Appl. Phys.* **78**, 4681–4689 (1995).

211. Adachi, S., Kimura, T. & Suzuki, N. Optical properties of CdTe: Experiment and modeling. *J. Appl. Phys.* **74**, 3435–3441 (1993).

212. Geiregat, P., Van Thourhout, D. & Hens, Z. A bright future for colloidal quantum dot lasers. *NPG Asia Mater.* **11**, 41 (2019).

213. Clavero, C. Plasmon-induced hot-electron generation at nanoparticle/metal-oxide interfaces for photovoltaic and photocatalytic devices. *Nat. Photonics* **8**, 95–103 (2014).

214. Grimaldi, G. *et al.* Hot-electron transfer in quantum-dot heterojunction films. *Nat. Commun.* **9**, 2310 (2018).

215. Rabouw, F. T. & de Mello Donega, C. Excited-State Dynamics in Colloidal Semiconductor Nanocrystals. *Top. Curr. Chem.* **374**, 58 (2016).

216. Efros, A. L., Kharchenko, V. A. & Rosen, M. Breaking the phonon bottleneck in nanometer quantum dots: Role of Auger-like processes. *Solid State Commun.* **93**, 281–284 (1995).

217. Klimov, V. I. & McBranch, D. W. Femtosecond 1P-to-1S Electron Relaxation in Strongly Confined Semiconductor Nanocrystals. *Phys. Rev. Lett.* **80**, 4028–4031 (1998).

218. Guyot-Sionnest, P., Shim, M., Matranga, C. & Hines, M. Intraband relaxation in CdSe quantum dots. *Phys. Rev. B* **60**, R2181–R2184 (1999).

219. Klimov, V. I., Mikhailovsky, A. A., McBranch, D. W., Leatherdale, C. A. & Bawendi, M. G. Mechanisms for intraband energy relaxation in semiconductor quantum dots: The role of electron-hole interactions. *Phys. Rev. B* **61**, R13349–R13352 (2000).

220. Maiti, S. *et al.* Electrochemical Evaluation of Dopant Energetics and the Modulation of Ultrafast Carrier Dynamics in Cu-Doped CdSe Nanocrystals. *J. Phys. Chem. C* **121**, 27233–27240 (2017).

221. Dutta, A., Bera, R., Ghosh, A. & Patra, A. Ultrafast Carrier Dynamics of Photo-Induced Cu-Doped CdSe Nanocrystals. *J. Phys. Chem. C* **122**, 16992–17000 (2018).

222. Wang, L. *et al.* Observation of a phonon bottleneck in copper-doped colloidal quantum dots. *Nat. Commun.* **10**, 4532 (2019).

223. Xie, R. & Peng, X. Synthesis of Cu-Doped InP Nanocrystals (d-dots) with ZnSe Diffusion Barrier as Efficient and Color-Tunable NIR Emitters. *J. Am. Chem. Soc.* **131**, 10645–10651 (2009).

224. Knowles, K. E., Nelson, H. D., Kilburn, T. B. & Gamelin, D. R. Singlet–Triplet Splittings in the Luminescent Excited States of Colloidal $Cu^+$:CdSe, $Cu^+$:InP, and $CuInS_2$ Nanocrystals: Charge-Transfer Configurations and Self-Trapped Excitons. *J. Am. Chem. Soc.* **137**, 13138–13147 (2015).

225. Mundy, M. E., Eagle, F. W., Hughes, K. E., Gamelin, D. R. & Cossairt, B. M. Synthesis and Spectroscopy of Emissive, Surface-Modified, Copper-Doped Indium Phosphide Nanocrystals. *ACS Mater. Lett.* **2**, 576–581 (2020).

226. Knowles, K. E. *et al.* Luminescent Colloidal Semiconductor Nanocrystals Containing Copper: Synthesis, Photophysics, and Applications. *Chem. Rev.* **116**, 10820–10851 (2016).

227. Hassan, A., Zhang, X., Liu, C. & Snee, P. T. Electronic Structure and Dynamics of Copper-Doped Indium Phosphide Nanocrystals Studied with Time-Resolved X-ray Absorption and Large-Scale DFT Calculations. *J. Phys. Chem. C* **122**, 11145–11151 (2018).

228. Norris, D. J., Efros, A. L. & Erwin, S. C. Doped Nanocrystals. *Science* **319**, 1776–1779 (2008).

229. Bradshaw, L. R., Knowles, K. E., McDowall, S. & Gamelin, D. R. Nanocrystals for Luminescent Solar Concentrators. *Nano Lett.* **15**, 1315–1323 (2015).

230. Sadeghi, S. *et al.* High-Performance, Large-Area, and Ecofriendly Luminescent Solar Concentrators Using Copper-Doped InP Quantum Dots. *iScience* **23**, 101272 (2020).

231. Geiregat, P. *et al.* Continuous-wave infrared optical gain and amplified spontaneous emission at ultralow threshold by colloidal HgTe quantum dots. *Nat. Mater.* **17**, 35–42 (2017).

232. Klimov, V. I. & McBranch, D. W. Femtosecond high-sensitivity, chirp-free transient absorption spectroscopy using kilohertz lasers. *Opt. Lett.* **23**, 277–279 (1998).

233. McArthur, E. A., Morris-Cohen, A. J., Knowles, K. E. & Weiss, E. A. Charge Carrier Resolved Relaxation of the First Excitonic State in CdSe Quantum Dots Probed with Near-Infrared Transient Absorption Spectroscopy. *J. Phys. Chem. B* **114**, 14514–14520 (2010).

234. Knowles, K. E., McArthur, E. A. & Weiss, E. A. A Multi-Timescale Map of Radiative and Nonradiative Decay Pathways for Excitons in CdSe Quantum Dots. *ACS Nano* **5**, 2026–2035 (2011).

235. Ashner, M. N., Winslow, S. W., Swan, J. W. & Tisdale, W. A. Markov Chain Monte Carlo Sampling for Target Analysis of Transient Absorption Spectra. *J. Phys. Chem. A* **123**, 3893–3902 (2019).

236. Labrador, T. & Dukovic, G. Simultaneous Determination of Spectral Signatures and Decay Kinetics of Excited State Species in Semiconductor Nanocrystals Probed by Transient Absorption Spectroscopy. *J. Phys. Chem. C* **124**, 8439–8447 (2020).

237. van Stokkum, I. H. M., Larsen, D. S. & van Grondelle, R. Global and target analysis of time-resolved spectra. *Biochim. Biophys. Acta - Bioenerg.* **1657**, 82–104 (2004).

238. Ruckebusch, C., Sliwa, M., Pernot, P., de Juan, A. & Tauler, R. Comprehensive data analysis of femtosecond transient absorption spectra: A review. *J. Photochem. Photobiol. C Photochem. Rev.* **13**, 1–27 (2012).

239. Hinterding, S. O. M. *et al.* Unusual Spectral Diffusion of Single $CuInS_2$ Quantum Dots Sheds Light on the Mechanism of Radiative Decay. *Nano Lett.* **21**, 658–665 (2021).

240. Rabouw, F. T. *et al.* Delayed Exciton Emission and Its Relation to Blinking in CdSe Quantum Dots. *Nano Lett.* **15**, 7718–7725 (2015).

241. Fu, H. & Zunger, A. Excitons in InP quantum dots. *Phys. Rev. B* **57**, R15064–R15067 (1998).

242. Guzelian, A. A. *et al.* Synthesis of Size-Selected, Surface-Passivated InP Nanocrystals. *J. Phys. Chem.* **100**, 7212–7219 (1996).

243. Mićić, O. I., Sprague, J., Lu, Z. & Nozik, A. J. Highly efficient band-edge emission from InP quantum dots. *Appl. Phys. Lett.* **68**, 3150–3152 (1996).

244. Nelson, H. D., Li, X. & Gamelin, D. R. Computational Studies of the Electronic Structures of Copper-Doped CdSe Nanocrystals: Oxidation States, Jahn–Teller Distortions, Vibronic Bandshapes, and Singlet–Triplet Splittings. *J. Phys. Chem. C* **120**, 5714–5723 (2016).

245. Nelson, H. D. *et al.* Mid-Gap States and Normal vs Inverted Bonding in Luminescent $Cu^+$- and $Ag^+$-Doped CdSe Nanocrystals. *J. Am. Chem. Soc.* **139**, 6411–6421 (2017).

246. Fuhr, A., Yun, H. J., Crooker, S. A. & Klimov, V. I. Spectroscopic and Magneto-Optical Signatures of $Cu^{1+}$ and $Cu^{2+}$ Defects in Copper Indium Sulfide Quantum Dots. *ACS Nano* **14**, 2212–2223 (2020).

247. Berends, A. C., Mangnus, M. J. J., Xia, C., Rabouw, F. T. & de Mello Donega, C. Optoelectronic Properties of Ternary I–III–$VI_2$ Semiconductor Nanocrystals: Bright Prospects with Elusive Origins. *J. Phys. Chem. Lett.* **10**, 1600–1616 (2019).

248. Guyot-Sionnest, P. & Hines, M. A. Intraband transitions in semiconductor nanocrystals. *Appl. Phys. Lett.* **72**, 686–688 (1998).

249. Cui, J. *et al.* Evolution of the Single-Nanocrystal Photoluminescence Linewidth with Size and Shell: Implications for Exciton–Phonon Coupling and the Optimization of Spectral Linewidths. *Nano Lett.* **16**, 289–296 (2016).

250. Hwang, Y.-N., Je, K.-C., Kim, D. & Park, S.-H. Observation of enhanced biexcitonic effect in semiconductor nanocrystals. *Phys. Rev. B* **64**, 041305 (2001).

251. Grimaldi, G. *et al.* Spectroscopic Evidence for the Contribution of Holes to the Bleach of Cd-Chalcogenide Quantum Dots. *Nano Lett.* **19**, 3002–3010 (2019).

252. Ellingson, R. J. *et al.* Excitation Energy Dependent Efficiency of Charge Carrier Relaxation and Photoluminescence in Colloidal InP Quantum Dots. *J. Phys. Chem. B* **106**, 7758–7765 (2002).

253. Blackburn, J. L., Ellingson, R. J., Mićić, O. I. & Nozik, A. J. Electron Relaxation in Colloidal InP Quantum Dots with Photogenerated Excitons or Chemically Injected Electrons. *J. Phys. Chem. B* **107**, 102–109 (2003).

254. Richter, A. F. *et al.* Fast Electron and Slow Hole Relaxation in InP-Based Colloidal Quantum Dots. *ACS Nano* **13**, 14408–14415 (2019).

255. Nguyen, A. T., Jen-La Plante, I., Ippen, C., Ma, R. & Kelley, D. F. Extremely Slow Trap-Mediated Hole Relaxation in Room-Temperature InP/ZnSe/ZnS Quantum Dots. *J. Phys. Chem. C* **125**, 4110–4118 (2021).

256. Kim, T., Won, Y., Jang, E. & Kim, D. Negative Trion Auger Recombination in Highly Luminescent InP/ZnSe/ZnS Quantum Dots. *Nano Lett.* **21**, 2111–2116 (2021).

257. Pandey, A. & Guyot-Sionnest, P. Slow Electron Cooling in Colloidal Quantum Dots. *Science* **322**, 929–932 (2008).

258. Cragg, G. E. & Efros, A. L. Suppression of Auger Processes in Confined Structures. *Nano Lett.* **10**, 313–317 (2010).

259. Bae, W. K. *et al.* Controlled Alloying of the Core–Shell Interface in CdSe/CdS Quantum Dots for Suppression of Auger Recombination. *ACS Nano* **7**, 3411–3419 (2013).

260. Rabouw, F. T. *et al.* Dynamics of Intraband and Interband Auger Processes in Colloidal Core–Shell Quantum Dots. *ACS Nano* **9**, 10366–10376 (2015).

261. Srivastava, B. B., Jana, S. & Pradhan, N. Doping Cu in Semiconductor Nanocrystals: Some Old and Some New Physical Insights. *J. Am. Chem. Soc.* **133**, 1007–1015 (2011).

262. Xie, R., Battaglia, D. & Peng, X. Colloidal InP Nanocrystals as Efficient Emitters Covering Blue to Near-Infrared. *J. Am. Chem. Soc.* **129**, 15432–15433 (2007).

263. Li, J. J. *et al.* Large-Scale Synthesis of Nearly Monodisperse CdSe/CdS Core/Shell Nanocrystals Using Air-Stable Reagents via Successive Ion Layer Adsorption and Reaction. *J. Am. Chem. Soc.* **125**, 12567–12575 (2003).

264. Aubert, T. *et al.* General Expression for the Size-Dependent Optical Properties of Quantum Dots. *Nano Lett.* **22**, 1778–1785 (2022).

265. Boehme, S. C. *et al.* Electrochemical Control over Photoinduced Electron Transfer and Trapping in CdSe-CdTe Quantum-Dot Solids. *ACS Nano* **8**, 7067–7077 (2014).

266. De Geyter, B. & Hens, Z. The absorption coefficient of PbSe/CdSe core/shell colloidal quantum dots. *Appl. Phys. Lett.* **97**, 161908 (2010).

267. Adachi, S. *Optical Constants of Crystalline and Amorphous Semiconductors*. (Springer US, 1999).

# Samenvatting in het Nederlands

Licht, straling in de vorm van *fotonen*, is essentieel voor het leven. Het dient zo lang als we ons herinneren meerdere doeleinden, zoals het geven van warmte, zorgen voor de productie van zuurstof en suikerhoudende materialen in planten, geven van ons dag-en nachtritme en het stelt ons in staat onze omgeving waar te nemen. Onze eerste en nog steeds belangrijkste bron van licht is de zon, maar tegenwoordig kunnen we ons geen wereld zonder kunstlicht voorstellen. We gebruiken het om de wereld te verlichten wanneer de zon onder is en zelfs wanneer deze op is, voor communicatie en voor verschillende andere activiteiten. Kunstlicht werd mogelijk door de vaardigheid om nieuwe materialen te synthetiseren die niet in de natuur voorkomen. We hebben ook materialen ontdekt die de energie van zonlicht kunnen benutten om elektriciteit op te wekken voor onze apparaten. Eerst was de synthese (het maken) van deze materialen vaak een kwestie van uitproberen en geluk. Door de juiste *atomen*, onze bouwstenen, te combineren, kunnen materialen de gewenste eigenschappen krijgen. Ons begrip van dit proces breidt zich steeds verder uit, waardoor we materiaaleigenschappen kunnen voorspellen en materialen kunnen synthetiseren op een meer rationele basis.

## Creatie en eigenschappen van fotoactieve nanomaterialen

Er zijn verschillende methodes voor het maken van fotoactieve nanomaterialen. De specifieke technieken die worden gebruikt zijn afhankelijk van het gewenste materiaal en de beoogde toepassing ervan. De synthese van nanomaterialen en het begrip van hun optische eigenschappen zijn cruciaal om hun potentieel optimaal te benutten.

In deze scriptie ligt onze primaire focus op nanomaterialen en nanodeeltjes, deze hebben doorgaans afmetingen variërend van 1 tot 100 nanometer. Ter referentie, een nanometer (nm) komt overeen met een miljardste van een meter (zie ook Figuur 1a). Wanneer nanodeeltjes een vaste structuur vertonen die is georganiseerd in een geordend atoompatroon, vallen ze in de categorie die bekend staat als nanokristallen. Nanokristallen vertonen vaak afwijkende eigenschappen in vergelijking met grotere kristallen van hetzelfde materiaal. Deze unieke eigenschappen hebben al eeuwenlang mensen gefascineerd, dit gaat terug tot de tijd van de Egyptische farao's (haarverf, Figuur 1b) en Romeinse keizers (Lycurgusbeker, Figuur 1c).

Laten we bijvoorbeeld goud in zijn grootschalige, macroscopische vorm nemen. Het staat bekend om zijn gele kleur, reflecterende eigenschappen en weerstand tegen corrosie. Maar wanneer de grootte van het goudkristal wordt verkleind tot de nanoschaal, ondergaat het een aanzienlijke verandering in eigenschappen. Goudnanokristallen kunnen verschillende kleuren vertonen, afhankelijk van hun grootte, variërend van rood tot paars (Figuur 1d). Dit geeft de rode kleur aan het licht dat door de Lycurgusbeker schijnt. Met afmetingen op de nanometerschaal hebben goudkristallen ook een verhoogde reactiviteit en worden daarom ook gebruikt als katalysator in chemische reacties.

Halfgeleidermaterialen op nanometerschaal, ook wel bekend als 'quantum dots', hebben het begrip en de toepassing van halfgeleidermaterialen op revolutionaire wijze veranderd. Een macroscopisch halfgeleiderkristal heeft een vaste energiekloof tussen zijn valentie- en geleidingsbanden. Wanneer een lichtdeeltje (foton) een energie draagt die groter is dan deze bandkloof, kan het een elektron van de valentieband naar de geleidingsband brengen, waarbij een gat in de valentieband achterblijft. De halfgeleider is daardoor geleidend. Het aangeslagen elektron–gat paar kan zich gedragen als twee vrije ladingdragers. Het kan ook een door Coulomb-aantrekking gebonden toestand vormen, genaamd een exciton (Figuur 1e). In een zonnepaneel wordt het aangeslagen elektron–gat paar omgezet in elektrische arbeid in een uitwendig circuit. Anderzijds kan het elektron ook recombineren met het gat, resulterend in de emissie van een foton.

In het verleden vereiste het wijzigen van de bandkloof van halfgeleiders het veranderen van het type atomen waaruit het materiaal bestaat. Met quantum dots hebben we echter de mogelijkheid om de bandkloof af te stemmen door de grootte van de quantum dots aan te passen (Figuur 1f). Dit grootte-afhankelijke fenomeen staat bekend als het kwantum-opsluitingseffect. In macroscopische materialen wordt de grootte van een exciton (bekend als de Bohrstraal) bepaald door het samenspel van elektron–gat aantrekking en de kinetische energie van elektron en gat. Wanneer de fysieke grootte van een quantum dot kleiner is dan de Bohrstraal, wordt het exciton beperkt door de afme-

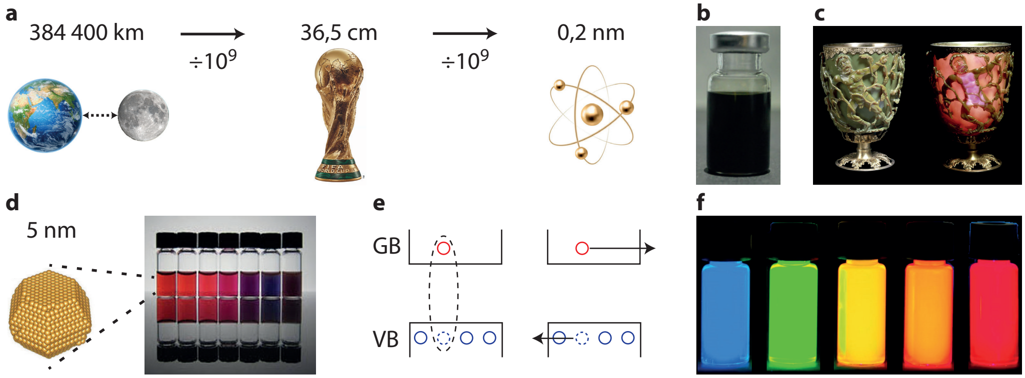

**Figuur 1 | Het uiterlijk van nanokristallen en hun interactie met licht.** (**a**) Drie verschillende groottes om weer te geven wat een nanometer is. De FIFA® wereldbeker is ongeveer een miljard keer kleiner dan de afstand tussen de aarde en de maan. Een goud atoom is dan weer ongeveer een miljard keer kleiner dan de wereldbeker. (**b**) Meer dan 4000 jaar geleden gebruikten de Egyptenaren loodzouten om hun haar te verven. Ze hadden geen idee dat de zwarte kleur kwam door de 5 nm loodsulfide-nanokristallen in hun haar. De foto toont een vloeistof met loodsulfide-nanokristallen. (**c**) De Romeinse Lycurgusbeker uit de $4^e$ eeuw na Christus. De beker lijkt groen wanneer hij van voren verlicht wordt en rood of roze wanneer hij van achteren verlicht wordt. Dit effect wordt gegenereerd door de lichtabsorptie van goud nanokristallen die in het glas zitten. (**d**) Het verschil tussen macroscopisch goud en goud nanokristallen. Een goud nanokristal van 5 nm heeft een rode kleur, zo'n deeltje bevat ongeveer vierduizend goud atomen. De grootte van de goud nanokristallen neemt toe van links naar rechts, resulterend in een kleurverandering van rood naar paars. (**e**) Situatie nadat een foton is geabsorbeerd door een halfgeleidermateriaal. Het foton heeft een elektron van de valentieband (VB) naar de geleidingsband (GB) gebracht. Het elektron (rood) laat een elektron gat (blauwe stippellijn) achter in de valentieband. Als het elektron en elektron gat gebonden zijn heet dat een exciton (links, zwarte stippellijn). Als het elektron terugvalt in het gat komt er een foton vrij. In het geval van zonnepanelen, kan het elektron–gat paar worden omgezet in elektrische arbeid (rechts). (**f**) Quantum dots onder een ultraviolette lamp. De emissie is blauw voor 2 nm quantum dots en verschuift naar rood wanneer de quantum dots 6 nm zijn. Deze grootteafhankelijkheid is te wijten aan het kwantum-opsluiting effect en maakt verschillende emissiekleuren mogelijk zonder de samenstelling van de quantum dots te veranderen.

tingen van het nanokristal, en neemt de energie van het exciton toe in omgekeerde verhouding tot het kwadraat van de diameter van het kristal. Het kwantum-opsluitingseffect leidt tot de instelbare emissie-eigenschappen van quantum dots. Bijvoorbeeld, Samsungs QLED-televisies gebruiken op indiumfosfide gebaseerde quantum dots voor zowel groene als rode emissie, maar met verschillende diameters van respectievelijk 2 nm en 3,5 nm.

De mogelijkheid om verschillende groottes quantum dots te maken werd decennia geleden bereikt door factoren zoals temperatuur en het gebruik van specifieke moleculaire reageermiddelen te variëren. Echter, het vormingsproces van deze nanokristallen uit hun moleculaire beginstoffen bleef onduidelijk. Er werd tot nu toe gesuggereerd dat het proces snelle nucleatie omvat, waarbij meerdere atomen samenklonteren, gevolgd door langzame groei door toevoeging van enkele atomen. De synthese werd geoptimaliseerd door verschillende opties te proberen, met als doel een eindproduct te produceren dat voornamelijk bestaat uit quantum dots met een specifieke grootte, resulterend in een specifieke emissiekleur. Dit is cruciaal omdat specifiekere en nauwere emissie zorgt voor hogere kleurzuiverheid waardoor de televisie nauwkeuriger kleuren kan weergeven.

## Overzicht van het onderzoek beschreven in dit proefschrift

Hoofdstuk 2 presenteert een onderzoek naar de synthese van cadmiumselenide (CdSe) quantum dots met behulp van *in situ* Röntgenverstrooiing. Voor het eerst is de experimentele opstelling die in de synchrotron werd gebruikt vergelijkbaar met die in het laboratorium voor de synthese van deze nanokristallen. In tegenstelling tot het eerder voorspelde mechanisme van explosieve nucleatie en groei beperkt door diffusie, tonen onze bevindingen trage nucleatie en reactiebeperkte groei. Hiermee samenhangend observeren we een afnemende groeisnelheid met toenemende nanokristalradius, wat leidt tot "superfocussering" en de synthese van nanokristallen met een specifieke grootte.

Hoofdstuk 3 richt zich op de synthese van anisotrope (niet ronde) CdSe-nanokristallen, namelijk nanoplaatjes. Deze nanoplaatjes hebben een gedefinieerde grootte in één dimensie, wat resulteert in een specifiekere en smallere emissie in vergelijking met isotrope nanokristallen. Net als in Hoofdstuk 2 gebruikten we een kwantitatieve benadering om informatie over de grootte en concentratie van de nanokristallen te verzamelen tijdens de synthese. Ons onderzoek biedt inzichten in de oorsprong van de anisotrope vorm en de aanwezigheid van bijproducten in de vorm van isotrope CdSe-nanokristallen. We identificeren ook een kleine populatie mini-nanoplaatjes in het mengsel, waarvan de groei aanzienlijk wordt versterkt wanneer korte coördinerende moleculen worden geïntroduceerd.

In Hoofdstuk 4 onderzochten we de synthese van niet-geleidende natrium yttrium fluoride ($NaYF_4$) nanokristallen gedoteerd met fotoactieve lanthanide-ionen, specifiek erbium ($Er^{3+}$) en ytterbium ($Yb^{3+}$), in tegenstelling tot halfgeleider nanokristallen. Lanthanide-ionen vertonen nog nauwere emissielijnen dan halfgeleider nanokristallen en faciliteren een fenomeen dat bekend staat als upconversion, een proces waarbij twee infrarode fotonen worden omgezet in één groen foton. We richtten ons op de synthese van hexagonale fase $NaYF_4$:$Er^{3+}$,$Yb^{3+}$-nanokristallen uit nanodeeltjes met een kubische fase, wat een kristalfaseovergang met zich meebrengt. Deze overgang komt overeen met een herstructurering van de atomen binnen het kristallijne rooster. Tijdens de synthese observeerden we een bimodale verdeling, bestaande uit twee verdelingen: een van kleine deeltjes en een van grote deeltjes. In tegenstelling tot eerdere aannames waarin de fase-overgang werd beschouwd als de kritieke factor in het vormingsmechanisme en de splitsing van de deeltjesverdeling, tonen onze bevindingen aan dat de samenstelling van de kubische fase nanodeeltjes de groeisnelheden van de nanodeeltjes bepaalt en daarmee de overgang van een unimodale naar een bimodale grootteverdeling. Vervolgens ondergaat de grotere subset in de bimodale verdeling van kubische fase nanodeeltjes een fase-overgang naar de hexagonale fase. Deze overgang wordt gevolgd door de groei van hexagonale fase nanokristallen en het oplossen van de kubische fase nanodeeltjes. Uiteindelijk leidt dit proces tot een unimodale populatie van hexagonale fase nanokristallen met een smalle verdeling.

Hoofdstuk 5 gaat in op de basisprincipes van foton-absorptie door halfgeleider(nano)materialen. We ontdekten een intrigerende relatie tussen de kans op absorptie van een resonant foton, een foton met een energiepakket gelijk aan de bandkloof, en de grootte van het exciton. Of we nu kijken naar nuldimensionale nanokristallen, tweedimensionale nanokristalsuperstructuren of driedimensionale bulkmaterialen, de waarschijnlijkheid van resonante lichtabsorptie per tijdseenheid en per exciton Bohrdiameter is (nagenoeg) gelijk aan $\pi\alpha$ (=0,023), waarbij $\alpha$ staat voor de fijnstructuurconstante (een fundamentele constante die veel voorkomt in natuurverschijnselen). Als gevolg hiervan neemt de waarschijnlijkheid van foton-absorptie toe bij exciton-opsluiting; quantum dots hebben dus een sterkere absorptie per volume-eenheid in vergelijking met bulkmaterialen. Echter, quantum dots zijn meestal verspreid in een medium met een lage diëlektrische constante, wat resulteert in diëlektrische afscherming van het elektromagnetische veld van het licht, wat dan weer de absorptiekans van een resonant foton vermindert. Daarom zou het interessant zijn om de quantum dots te verspreiden in een medium met een hoge diëlektrische constante om de lichtabsorptie per materiaal te optimaliseren, bijvoorbeeld bij het gebruik van quantum dots als fosfor voor lampen en beeldschermen, en in zonnepanelen.

In Hoofdstuk 6 richtte ons onderzoek zich op de snelle relaxatieprocessen die plaatsvinden na de absorptie van fotonen door halfgeleider nanokristallen. Normaal gesproken, wanneer een foton overtollige energie boven de bandkloof draagt, gaat deze overtollige energie verloren als warmte. Deze beperking op het potentiële rendement van zonnepanelen staat algemeen bekend als de Shockley-Queisserlimiet, die voor silicium op 30% is vastgesteld. Een van de factoren die de efficiënte onttrekking van ladingdragers belemmert, is de snelle afkoeling van foto-opgewekte ladingdragers door zogenaamde Augerkoeling, die plaatsvindt binnen een tijdsbestek van minder dan een picoseconde (een biljoenste van een seconde). In onze studie hebben we een vergelijking gemaakt van ladingdragerkoeling in koper (Cu) gedoteerde indiumfosfide (InP) nanokristallen en ongedoteerde InP-nanokristallen. Door gebruik te maken van ultrasnelle tijdsafhankelijke absorptiespectroscopie hebben we de verrassende waarneming gedaan dat het elektron sneller energie verliest en afkoelt in vergelijking met het gat. Deze bevinding suggereert dat de lokalisatie van gaten op koper de Augerkoeling in Cu gedoteerde InP-nanokristallen niet belemmert. Er zijn dus andere methodes nodig om de overtollige energie te kunnen benutten.

# List of publications

publications this thesis was based on are highlighted in green
$^{+}$both authors contributed equally

## 2023

25. **Probing nearby molecular vibrations with lanthanide-doped nanocrystals**
M.J.J. Mangnus, V.R.M. Benning, B. Baumgartner, P.T. Prins, T.P. van Swieten, A.J.H. Dekker, A. van Blaaderen, B.M. Weckhuysen, A. Meijerink, F.T. Rabouw
Nanoscale **15**, 16601–16611 (2023)

24. **Which Ion Dominates the Temperature and Pressure Response of Halide Perovskites and Elpasolites?**
L.A. Muscarella, H.J. Jöbsis, B. Baumgartner, P.T. Prins, D.N. Maaskant, A.V. Petukhov, D. Chernyshov, C.J. McMonagle, E.M. Hutter
The Journal of Physical Chemistry Letters **14**, 9042–9051 (2023)

23. **Operando time-gated Raman spectroscopy of solid catalysts**
R. Vogel, P.T. Prins, F.T. Rabouw, B.M. Weckhuysen
Catalysis Science & Technology **13**, 6366–6376 (2023)

22. **The role of water in carbon dioxide adsorption in porphyrinic metal-organic frameworks**
B. Baumgartner, P.T. Prins, J.N. Louwen, M. Monai, B.M. Weckhuysen
ChemCatChem **15**, e202300722 (2023)

21. **Dielectric and optical properties of superlattices of epitaxially connected nanocrystals**
C. Delerue, P.T. Prins, D.A.M. Vanmaekelbergh, Z. Hens
Physical Review B **107**, 245413 (2023)

20. **The formation of $NaYF_4:Er^{3+},Yb^{3+}$ nanocrystals studied by *in situ* X-ray scattering: phase transition and size focusing** (Chapter 4)
P.T. Prins,$^{+}$ J.C. van der Bok,$^{+}$ T.P. van Swieten, S.O.M. Hinterding, A.J. Smith, A.V. Petukhov, A. Meijerink, F.T. Rabouw
Angewandte Chemie International Edition **62**, e202305086 (2023)

19. **Analysis of the 1-year outdoor performance of quantum dot luminescent solar concentrators**
T.A. de Bruin,$^{+}$ R. Terricabres-Polo,$^{+}$ A. Kaul,$^{+}$ N.K. Zawacka, P.T. Prins, T.F.J. Gietema, A.C. de Waal, D.K.G. de Boer, D.A.M. Vanmaekelbergh, P. Leblans, S. Verkuilen, Z. Hens, C. de Mello-Donegá, W.G.J.H.M. van Sark
Solar RRL **7**, 2201121 (2023)

18. **Growth and self-assembly of $CsPbBr_3$ nanocrystals in the TOPO/$PbBr_2$ synthesis as seen with X-ray scattering**
F. Montanarella, Q.A. Akkerman, D. Bonatz, M.M. van der Sluijs, J.C. van der Bok, P.T. Prins, M. Aebli, A. Mews, D.A.M. Vanmaekelbergh, M.V. Kovalenko
Nano Letters **23**, 667–676 (2023)

## 2022

17. **Bifunctional europium for operando catalyst thermometry in an exothermic chemical reaction**
B.J.P. Terlingen, T. Arens, T.P. van Swieten, F.T. Rabouw, P.T. Prins, M.M. de Beer, A. Meijerink, M.P. Ahr, E.M. Hutter, C.E.J. van Lare, B.M. Weckhuysen
Angewandte Chemie International Edition **134**, e202211991 (2022)

16. **Slow hole localization and fast electron cooling in Cu-doped InP/ZnSe quantum dots** (Chapter 6)
P.T. Prins, D.A.W. Spruijt, M.J.J. Mangnus, F.T. Rabouw, D.A.M. Vanmaekelbergh, C. de Mello-Donegá, P. Geiregat
The Journal of Physical Chemistry Letters **13**, 9950–9956 (2022)

15. **Optically detected magnetic resonance spectroscopy of Cu-doped CdSe/CdS and $CuInS_2$ colloidal quantum dots**
A. Harchol,+ Y. Barak,+ K.E. Hughes, K.H. Hartstein, H.J. Jöbsis, P.T. Prins, C. de Mello-Donegá, D.R. Gamelin, E. Lifshitz
ACS Nano **16**, 12866–12877 (2022)

14. ***In situ* optical and X-ray spectroscopy reveals evolution toward mature CdSe nanoplatelets by synergetic action of myristate and acetate ligands** (Chapter 3)
J.C. van der Bok,+ P.T. Prins,+ F. Montanarella, D.N. Maaskant, F.A. Brzesowsky, M.M. van der Sluijs, B.B.V. Salzmann, F.T. Rabouw, A.V. Petukhov, C. De Mello-Donegá, D.A.M. Vanmaekelbergh, A. Meijerink
Journal of the American Chemical Society **144**, 8096–8105 (2022)

13. **Universality of optical absorptance quantization in two-dimensional group-IV, III–V, II–VI, and IV–VI semiconductors**
M. Lannoo, P.T. Prins, Z. Hens, D.A.M. Vanmaekelbergh, C. Delerue
Physical Review B **105**, 035421 (2022)

## 2021

12. **The fine-structure constant as a ruler for the band-edge light absorption strength of bulk and quantum-confined semiconductors** (Chapter 5)
P.T. Prins,+ M. Alimoradi Jazi,+ N.A. Killilea, W.H. Evers, P. Geiregat, W. Heiss, A.J. Houtepen, C. Delerue, Z. Hens, D.A.M. Vanmaekelbergh
Nano Letters **21**, 9426–9432 (2021)

11. **Extended nucleation and superfocusing in colloidal semiconductor nanocrystal synthesis** (Chapter 2)
P.T. Prins,+ F. Montanarella,+ K. Dümbgen, Y. Justo, J.C. van der Bok, S.O.M. Hinterding, J.J. Geuchies, J. Maes, K. De Nolf, S. Deelen, H. Meijer, T. Zinn, A.V. Petukhov, F.T. Rabouw, C. de Mello-Donegá, D.A.M. Vanmaekelbergh, Z. Hens
Nano Letters **21**, 2487–2496 (2021)

10. **Unraveling the growth mechanism of magic-sized semiconductor nanocrystals**
A.S. Mule,+ S. Mazzotti,+ A.A. Rossinelli, M. Aellen, P.T. Prins, J.C. van der Bok, S.F. Solari, Y.M. Glauser, P.V. Kumar, A. Riedinger, D.J. Norris
Journal of the American Chemical Society **143**, 2037–2048 (2021)

9. **Unusual spectral diffusion of single $CuInS_2$ quantum dots sheds light on the mechanism of radiative decay**
S.O.M. Hinterding, M.J.J. Mangnus, P.T. Prins, H.J. Jöbsis, S. Busatto, D.A.M. Vanmaekelbergh, C. de Mello- Donegá, F.T. Rabouw
Nano Letters **21**, 658–665 (2021)

## 2020

8. **Should anisotropic emission or reabsorption of nanoparticle luminophores be optimized for increasing luminescent solar concentrator efficiency?**
P. Moraitis, D.K.G. de Boer, P.T. Prins, C. de Mello-Donegá, K. Neyts, W.G.J.H.M. van Sark
Solar RRL **4**, 2000279 (2020)

## 2018

7. **Reply to "Overtone vibrational transition-induced lanthanide excited-state quenching in $Yb^{3+}/Er^{3+}$-doped upconversion nanocrystals"**
   F.T. Rabouw, P.T. Prins, P. Villanueva-Delgado, M. Castelijns, R.G. Geitenbeek, A. Meijerink
   ACS Nano **12**, 10576–10577 (2018)

6. **Exciton fine structure and lattice dynamics in InP/ZnSe core/shell quantum dots**
   A. Brodu, M.V. Ballottin, J. Buhot, E.J. Van Harten, D. Dupont, A. La Porta, P.T. Prins, M.D. Tessier, M.A.M. Versteegh, V. Zwiller, S. Bals, Z. Hens, F.T. Rabouw, P.C.M. Christianen, C. de Mello-Donegá, D.A.M. Vanmaekelbergh
   ACS Photonics **5**, 3353–3362 (2018)

5. **Crystallization of nanocrystals in spherical confinement probed by *in situ* X-ray scattering**
   F. Montanarella, J.J. Geuchies, T. Dasgupta, P.T. Prins, C. van Overbeek, R. Dattani, P. Baesjou, M. Dijkstra, A.V. Petukhov, A. van Blaaderen, D.A.M. Vanmaekelbergh
   Nano Letters **18**, 3675–3681 (2018)

4. **Quenching pathways in $NaYF_4:Er^{3+},Yb^{3+}$ upconversion nanocrystals**
   F.T. Rabouw, P.T. Prins, P. Villanueva-Delgado, M. Castelijns, R.G. Geitenbeek, A. Meijerink
   ACS Nano **12**, 4812–4823 (2018)

3 **Near-infrared-emitting $CuInS_2/ZnS$ dot-in-rod colloidal heteronanorods by seeded growth**
C. Xia, N. Winckelmans, P.T. Prins, S. Bals, H.C. Gerritsen, C. de Mello-Donegá
Journal of the American Chemical Society **140**, 5755–5763 (2018)

## 2017

2 **$NaYF_4:Er^{3+},Yb^{3+}/SiO_2$ core/shell upconverting nanocrystals for luminescence thermometry up to 900 K**
R.G. Geitenbeek, P.T. Prins, W. Albrecht, A. van Blaaderen, B.M. Weckhuysen, A. Meijerink
The Journal of Physical Chemistry C **121**, 3503–3510 (2017)

## 2016

1. **Europium-doped $NaYF_4$ nanocrystals as probes for the electric and magnetic local density of optical states throughout the visible spectral range**
   F.T. Rabouw, P.T. Prins, D.J. Norris
   Nano Letters **16**, 7254–7260 (2016)

# List of presentations

## 2020

***In situ* study of the formation mechanism of nanocrystals** (oral)
in the group of Prof. David Norris, ETH Zürich, Switzerland
2020/03/24

***In situ* X-ray scattering studies on the formation mechanism of nanoparticles** (poster)
at the DUBBLE-ESRF User Meeting, Brussels, Belgium
2020/03/06

***In situ* study of the formation mechanism of nanocrystals** (oral)
at the weekly 'nanoseminar' of all nanomaterials research groups at Utrecht University, The Netherlands
2020/02/21

## 2019

**Extended nucleation and superfocusing in colloidal nanocrystal synthesis** (oral)
at the MRS Fall meeting, Boston, United States of America
2019/12/05

**Doping InP quantum dots with copper slows down hot electron cooling** (poster)
at the MRS Fall meeting, Boston, United States of America (best poster award nominee)
2019/12/05

**Linearly polarized emission from CdSe/CdS dot-in-rod heterostructures** (oral)
in the group of Dr. Katerina Newell, University of Amsterdam, The Netherlands
2019/04/04

## 2018

**Doping InP quantum dots with copper slows down hot electron cooling** (oral)
at the NanoGe Fall Meeting, Torremolinos, Spain
2018/10/22

# About the author

Tim Prins was born in Ermelo, The Netherlands, on February 10, 1992. He graduated from Christelijk College Groevenbeek in Ermelo in 2010. In the same year, he started studying 'science and innovation management' at Utrecht University. During his bachelor's program, he took additional chemistry courses, which allowed him to start with the 'nanomaterials: chemistry and physics' master's program, also at Utrecht University, after obtaining his bachelor's degree in 2014. His master's research focused on the synthesis of silica-coated lanthanide-doped nanocrystals for high-temperature thermometry and the investigation of the mechanisms behind the luminescence quenching of these nanocrystals. This work was conducted under the supervision of Robin Geitenbeek and Andries Meijerink in the Condensed Matter and Interfaces group. For his internship, he went to ETH in Zürich, Switzerland, to study the photonic effects on lanthanide-doped nanocrystals, supervised by Freddy Rabouw and David Norris. He obtained his master's degree in 2016.

Tim started as a PhD researcher in the Condensed Matter and Interfaces group at Utrecht University in October 2016, under the supervision of Daniël Vanmaekelbergh, Celso de Mello-Donegá, and Wilfried van Sark. The primary findings of his research are described in this thesis and have been published in peer-reviewed scientific journals and presented at international conferences. Throughout his PhD, Tim supervised twelve bachelor and master students and was a teaching assistant for first- and second-year courses on organic and analytical lab skills. Additionally, he successfully obtained measurement time at three different synchrotrons by writing three proposals, which significantly contributed to the results presented in this thesis.

In May 2021, Tim started working as a research technician in the Inorganic Chemistry and Catalysis group led by Bert Weckhuysen at Utrecht University.